Investigating the Reinforcement Architecture Dependency of Failure for Composites

A

Dissertation

Presented to

the faculty of the School of Engineering and Applied Science

University of Virginia

in partial fulfillment

of the requirements for the degree

Doctor of Philosophy

by

Frederick Michael Heim

August 2020

APPROVAL SHEET

This

Dissertation

is submitted in partial fulfillment of the requirements
for the degree of

Doctor of Philosophy

Author: Frederick Michael Heim

This Dissertation has been read and approved by the examing committee:

Advisor: Xiaodong (Chris) Li

Advisor:

Committee Member: Baoxing Xu, PhD

Committee Member: Elizabeth Opila, PhD

Committee Member: Osman Ozbulut, PhD

Committee Member: David Green, PhD

Committee Member:

Committee Member:

Accepted for the School of Engineering and Applied Science:

Craig H. Benson, School of Engineering and Applied Science

August 2020

Abstract

The properties of composites are tunable via the constituents, but failure is often related to nonuniformity of the constituents, including irregular size, shape, density or orientation. Textile composites featuring continuous fiber reinforcements, bundled into tows, are set to replace many metallic structural components to extend performance and safety in extreme material applications. The intricate manufacturing process of braided and woven composites produces inconsistency in both the microstructure and mechanical properties, particularly, along the length of long components. Some of this variability is attributed to nonuniform tow placement, producing systematic and stochastic distortions in the tow trajectories, causing unit cells of irregular shape and size, and ultimately, influencing stress redistribution behavior. Much information about these nonperiodic defects is unknown, including how they are spatially distributed at the macroscale, how the specific braid/weave architecture or local geometry influences their development, and how they dictate mechanical failure. To address this need, stereoscopic digital image correlation was utilized in an unconventional manner to develop a multitude of scalable systems to quantify nonuniform reinforcement distributions and investigate the reinforcement architecture dependency of failure for textile composites.

In this dissertation, a brief literature review of fundamental background information on the targeted ceramic and polymer matrix composite systems and stereoscopic digital image correlation is given. In the second chapter, an overview is given of preceding work utilizing customized reinforcement phase manufacturing to improve mechanical performance in aluminum matrix composites, which served as the inspiration for the pursuit of the work completed for textile composites. In the third chapter, a scalable system to triangulate the surface of complexly shaped materials or objects is developed and evaluated using a series of fundamental and computational

experiments. In the fourth chapter, the scalable system is applied separately to both carbon fiber and silicon carbide fiber braided composite systems to reveal the first measurements of long-range tow spacing variability and through a comparison of two braids, the spatial influence of each tow orientation family. In the fifth chapter, targeted mechanical experiments and numerical simulations are performed on carbon fiber braided composites to quantify the influence of tow structure irregularity on local stress/strain concentration leading to failure. In the sixth chapter, novel stereoscopic digital image correlation techniques and tow location segmentation schemes developed in previous chapters are applied to braided and woven silicon carbide fiber / silicon carbide matrix composites to assess the influence of underlying tow structure on hermetic seal and cracking behavior during mechanical loading. In the final chapter, a summary is given of the completed research as well as several recommendations for future pursuits and applications to additional material systems. The investigation detailed herein is expected to reveal new fundamental information on tow trajectory deviations in textile composites and their critical implications on mechanical performance, which will serve to guide manufacturing improvements of defect sensitive composite materials.

Table of Contents

Acknowledgments

I would like to thank my advisor Professor Xiaodong (Chris) Li for his guidance and patience throughout my PhD study. His mentoring philosophy coupled with his enthusiasm for research has been inspirational to my development as a researcher. I would also like to thank my committee members, Prof. Baoxing Xu, Prof. Elizabeth Opila, Prof. Osman Ozbulut, and Prof. David Green for their valuable time and knowledge.

I would also like to thank the manifold members of the Li Research Group whose pursuit for knowledge has been forged with my own: Dr. Yunya Zhang, Dr. Zan Gao, Dr. Ningning Song, Dr. Brendan Croom, Clifton Bumgardner, Oliver Holzmond, Jamison Bartlett, Yosyp Schwab, Alex Jarama, David Roche, Jiajun He, Dr. Liwen Zhang, Dr. Jiadeng Zhu, Victor Shen, Diane Burden, Yucheng Zhou, Tyler Daspit, Rouxi Chen, Kenneth Brown, Morgan Price, Cole Love-Baker, Ryan Cordier, and Dr. Tim Harrell.

My parents Fred and Angie Heim have kindled my passion for understanding, and I thank them for their long-lasting support throughout all my ventures both big and small. Most importantly, I would like to thank my wife, Gabrielle Heim for her joy, sacrifice, and strength during my study. Furthermore, I must recognize my son Will Heim, who despite his love for typing with my keyboard, has been a treasured companion during the compilation of this work.

Finally, I appreciate and acknowledge my sources of funding throughout this effort. Financial support was provided by the U.S. National Science Foundation (CMMI- 1537021), the Commonwealth Center for Advanced Manufacturing (CCAM D-073), Westinghouse Electric Company LLC (PO 4500695139), and the U.S. Department of Energy's Nuclear Energy University Program (Project 17-13080). Furthermore, I acknowledge the support of Jorie Walters, Benjamin Maier, Roger Lu, Peng Xu, and Ed Lahoda of the Westinghouse Electric Company and Christian Deck of General Atomics who provided critical insight and guidance for this research.

List of Figures

List of Tables

CHAPTER 1: INTRODUCTION

1. Importance of reinforcement architecture defects

Continuous fiber-reinforced composites have been become increasingly popular as they offer exciting performance benefits over conventional isotropic materials and are widely applicable to numerous markets, ranging from nuclear fuel claddings to sporting goods. While these braided or woven composites exhibit excellent mechanical properties, their performance is affected by nonuniformity in their tow architecture, which leads to "unit cells" (Fig. 1.1) [1] of irregular size and shape.[2–4] Such nonperiodic deviations, similar to fiber waviness, are intrinsic to the textile processing used in composite manufacturing and present an additional challenge to computational modeling efforts.[5–7] This architectural distortion is particularly critical in demanding composite applications that require certification of the material (e.g., aerospace or nuclear industries), such that the irregularity in the composite braid/weave and its effects on the mechanical properties are well understood.[8,9] Particularly this work complements a large body of experiments and numerical simulations that have shown the effect of multiscale porosity, [10] fiber clustering within tows,[11,12] tow trajectories within a single unit cell,[7,13] and fabric-scale variation in tow placement.[14–16] In particular, this work focuses on quantifying the long-range variation in reinforcement placement at the macroscale and unit cell level for braided and woven composite, as well as studying their effects on mechanical performance.

Of particular interest, woven and braided (Fig. 1) ceramic matrix composites (CMCs) [6,17–19] and carbon-fiber reinforced polymers (CFRP) [20–22] exhibit mechanical properties that are sensitive to defects in tow arrangement and fiber waviness. Particularly, irregular tow spacing likely contributes to altered elasticity, strength and failure characteristics. The interlocked nature of braided/woven composites means that a single misplaced tow influences the position of all neighboring tows, which creates systematic distortions in the composite architecture. These defects are intrinsic to the manufacturing process,[22,23] but it is unclear how they are spatially distributed in braided/woven composites, or how the specific type of architecture or local geometry (e.g., bends) influences their development.

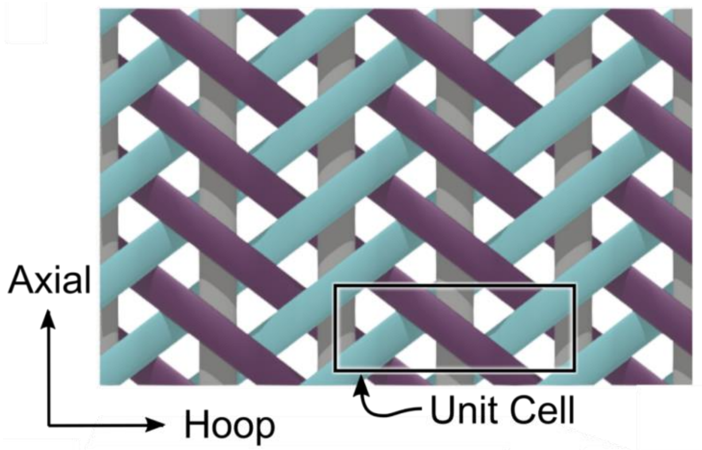

Fig. 1.1. Ideal unit cell in the tow architecture of a triaxial braid.[1]

Numerous experiments have demonstrated that the seemly stochastic positioning of tows causes stress localization and alters damage and failure propagation.[3,14,22,24,25] Given that the arrangement of reinforcing tows can predict some of the statistical variation in observed mechanical and failure properties, there is great interest in understanding the stochastic and spatial characteristics of such composite architectures. Because the textile process can produce very long, complex-shaped composites, a scalable method for quantifying tow architecture nonuniformity must be established.[18] This system is necessary to ensure that the tow placement and mechanical properties are uniform along the length of the part.

Surface metrology techniques hold promise for quantifying the full-field disorder in tow architecture and the long-range tow level deformation of the external layer at the macroscale.[14,26] The undulations of tows in woven or braided composites [19] create a rough surface, such that surface profilometry techniques are a viable approach to measure the tow placement. Local peaks on the surface correspond to the apex of a surface tow as it crosses over other underlying tows (*i.e.*, the tow "crown"). Non-contact measurement techniques such as laser profilometry and digital image correlation (DIC), therefore, hold promise for quantifying the disorder of tow architecture and can be used for *in situ* monitoring during the braiding/weaving process or *ex situ* inspection of manufactured parts.[14,20,21] In fact, DIC has recently been used to quantify the tow geometry in (2D) woven composite panels.[15,22]

2. Overview of model composites

Continuous fiber reinforced composites are the primary interest of this work and can be simplified into three basic constituents: matrix, fiber, and interface.[27] Numerous architectural designs exist, including stitched, woven, non-woven, braided, and multi-axial warp knit.[28] Particularly, the interlocking nature of woven and braided designs works to improve bulk mechanical performance and is the focus of this work. In these types, fibers with micron sized diameters are bundled into tows and are two- dimensionally (2D) or three-dimensionally (3D) woven or braided together, often using conventional textile procedures.[29,30] Common types of reinforcement fibers include glass, carbon, and silicon carbide. After the tow architecture is formed either the matrix or a special interface coating can be applied. Desired interface properties vary per composite composition, type, and purpose. Emphasis in this dissertation is placed on tubular style composites, but some planar composites were also examined. Axis symmetric, tubular composites present new challenges for experimentalist and often exhibit stress redistribution and complex failure.[31] Currently, a vast majority of tubular composites exist as polymer matrix composites (PMC) and ceramic matrix composites (CMC), so these two material platforms will be the material subject of this dissertation. A brief background and overview of each model composite composition is given in the following sections.

2.1. SiC/SiC composites and claddings

2.1.1. **Significance**

Due to the current need to bridge the gap between fossil fuels and lower energy output renewable sources, nuclear energy is being reinvestigated for more efficient and safer reactor designs.[32,33] Many of the leading alternative reactor designs rely on significantly increased operating temperatures or exposing structural materials to corrosive salts.[34–36] Past materials were incapable of surviving long-term exposure to such an extreme and irradiative environment while maintaining ductility and strength.[37–39] Furthermore, following recent nuclear disasters, emphasis is being placed on increasing the reliability and cost efficiency of legacy reactors, which would benefit from structural material advances within stringent nuclear energy requirements.[33,40,41]

Specific to CMC nuclear fuel claddings, which are hermetically sealed tubes that contain radioactive fuel pellets and helium gas coolant, a multitude of fiber/tow architectures have been explored.[42] Furthermore, the various braid architectural designs tend to influence performance and manufacturability. It has been found that general “looseness” of high initial density braids is needed to ensure proper matrix infiltration of these crucial materials.[43–45] However, this looseness potentially degrades mechanical and environmental resistance properties. Not only does a loose braid promote irregular tow placement, it has greater implications on the gas tightness of the CMC fuel cladding.[46,47]Nonuniform coating and trapped internal pores are common and can additionally affect hermetic and failure performance.[45,48] The effects of these nonideal microstructure features need to be evaluated for CMC claddings.

Furthermore, SiC/ SiC CMCs are being regarded for accident tolerant fuel (ATF) claddings and structural materials, including both braided and woven CMCs, for current light water nuclear reactors and next-generation reactor designs. In accident conditions, these CMCs are expected to withstand temperatures up to 1200 °C while still maintaining mechanical and hermetic seal integrity.[49] Adding complexity, the potential effects of the pressurized helium coolant with the cladding at these temperatures are not well established.

2.1.2. Description

Born out of the need for a future generation of materials that are capable of withstanding extreme conditions, SiC/SiC is one of the more promising tough, ceramic solutions. SiC/SiC CMCs are applicable to a wide range of new high-temperature and highly-corrosive environments, including aircraft engines and nuclear reactors.[45,50–52] CMCs can be separated into three main components: matrix, fiber, and interphase.[51] Often the fibers are bundled into tows (Fig. 1.2b) and woven or braided into a preform, typically sheets or tubes. These high-tensile strength fibers are coated in a relatively weak carbon or boron nitride interface layer, which separates the fibers from the SiC matrix. This interface is crucial to the slowed failure or pseudo-plasticity of an otherwise brittle SiC material. Fig. 1.2c-d shows a fracture surface of a SiC/SiC CMC tube loaded in bending. Here, the fibers and grown SiC can be seen.

For nuclear reactor applications, high purity SiC is necessary to avoid swelling and other negative effects incurred by irradiation. Therefore, chemical vapor infiltration (CVI) is the preferred method for matrix deposition to achieve β-phase SiC, which has good irradiation resistance. [44,45] Typically, Hi-Nicalon type S fibers, braided or woven over a preform, are infiltrated with a methyltrichlorosilane (CH_3SiCl_3) precursor, which is mixed with hydrogen to form SiC, according to:

$$CH_3SiCl_3 + H_2 \rightarrow SiC + 3HCl + H_2 \tag{1.1}$$

The carbon interface and SiC matrix are effectively grown layer wise from the fiber preform. Deposition rate and infiltration time are two key variables that must be balanced to avoid entrapped porosity and impractically long infiltration durations. Typically, infiltration duration is on the order of hundreds of hours. [45]

Of importance to this dissertation, CVI has benefits for nuclear application, but it has proven challenging / impractical to achieve full densification of CMCs via this processing route. Typical densities range from 70 to 90 % theoretical, which indicates significant internal porosity and gaps (Fig. 1.2a). More critically, fiber preforms are often braided or woven in a comparatively loose fashion to enable proper infiltration. This looseness of the preform would allow the tow architecture to vary considerably, potentially on both a local and global scale. It is expected that both internal pores/gaps and nonuniformity of the reinforcement preform influence failure behavior.[16,25] The SiC/SiC CMCs used throughout this dissertation were found to exhibit ultimate strengths ranging from 150 to 300 MPa with fracture strains ranging from 0.2 to 0.6 %. An optical image of the triaxially braided SiC/SiC CMCs studied in Chapter 4 is presented in Fig. 1.2e. An optical image of the biaxially braided SiC/SiC CMCs with a SiC outer coating studied in Chapter 6 is presented in Fig. 1.2f.

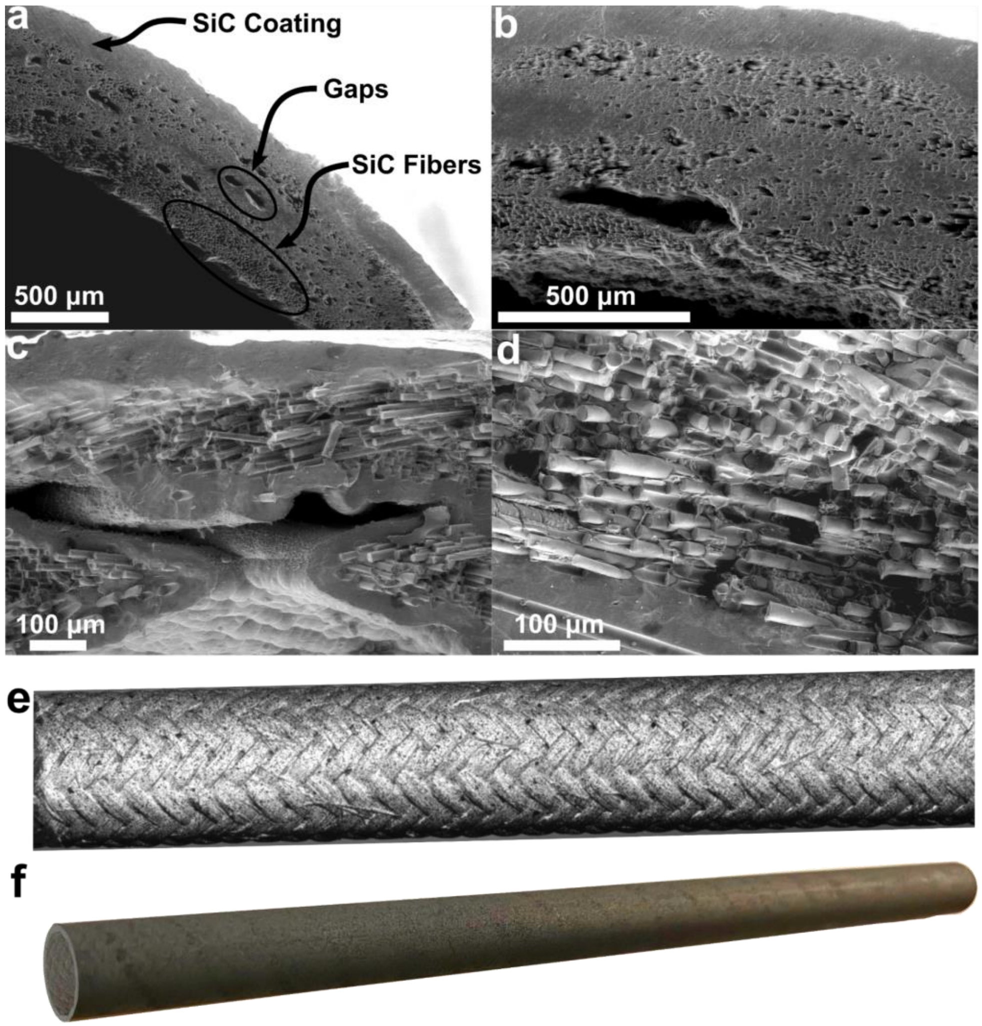

Fig. 1.2. SEM and optical images of SiC/SiC CMC. (a-b) Cut cross-section of biaxially braided CMC cladding. (c-d) Fracture cross-section of biaxially braided CMC. (e) Triaxial braid CMC studied in Chapter 4. (f) Biaxial braid CMC with SiC coating studied in Chapter 6.

2.2. Braided carbon fiber reinforced polymer matrix composites

2.2.1. **Significance**

Tubular braided composites benefit from conventional textile manufacturing, including maypole and radial braiding procedures. When combined with relatively low-cost polymer infiltration, carbon fiber reinforced polymers offer a potentially throughput and robust material solution for a range of applications where light-weight, high strength, and high stiffness are needed. Particularly targeted application in this dissertation include wind turbine blades and pressure-vessels. Both of which are necessary for the Department of Energy's mission of electricity production from wind, natural gas, and hydrogen.

2.2.2. **Description**

Reinforced polymer composites have become common over the past few decades. Typical reinforcement fibers include glass and carbon; however, new plant-based fibers are being explored for reduced environmental impact.[53] Beyond unidirectional fiber composites, fibers are either filament wound or bundled into tows to be woven or braided along a preform or compressed in a mold. Typical braid configurations include, diamond, regular, and Hercules patterns.[54] Fiber reinforced polymers are often impregnated with a thermoset epoxy resin, serving as the matrix, and are subsequentially compressed or placed into an autoclave.[55,56] Generally, a strong matrix-fiber bond is desired for polymer matrix composites (PMCs).[57] This enables a transfer-of-load mechanism, where the fibers endure most of the load, greatly increasing composite strengths beyond that of the polymer/epoxy matrix. An image of the carbon fiber reinforced polymer (CFRP) tubes utilized in Chapter 4 and Chapter 5 is provided in Fig. 1.3.

Fig. 1.3. Picture of biaxially braided CFRP tubes studied in Chapter 4 and 5.

3. Principles of three-dimensional digital image correlation

3.1. Overview

Spatial measurements by three-dimensional digital image correlation (3D-DIC) provide the basis for surface strain and displacement analysis for the composites under investigation. It also serves as the basis of the mosaic digital image correlation technique developed in this dissertation. 3D-DIC is commonly used for collecting *in-situ* deformation measurements during dynamic loading and is uniquely capable of measuring nonhomogeneous strains. [58–60] It is simultaneously capable of measuring the shape of 3D surfaces with exceptional accuracy; out-of-plane measurements have been shown accurate to 1/20,000th of camera-sample distance.[61–63] In this section, a technical background on the 3D-DIC technique is provided, which was used extensively in this effort.

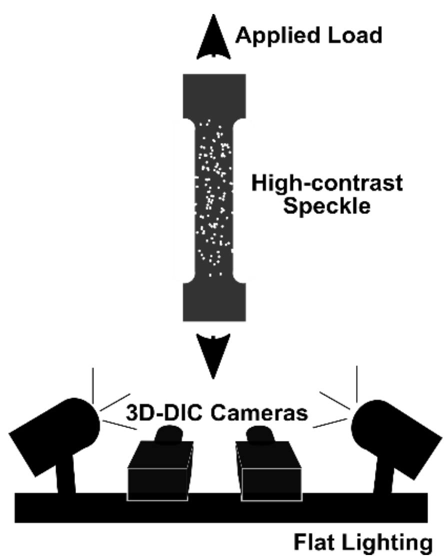

Fig. 1.4. Typical 3D-DIC setup.

In conventional applications, 3D-DIC measurements are used to track the local surface deformation during mechanical testing (Fig. 1.4). The key elements of accurate DIC measurements include: a high-contrast surface pattern, a pair of high-resolution digital cameras, bright/flat lighting, accurate calibration to geometrically relate images from the two cameras, and a robust DIC algorithm to compute 3D position. These elements are discussed as follows.

The specimen must have some type of random, high contrast surface pattern. This pattern can be the natural grain of the material or an applied coating of paint, which is used to quantitatively track the deformation of the specimen. Because images are distance invariant, DIC is applicable across multiple length scales, including the nanoscale via high resolution transmission electron microscopy (HRTEM) imaging,[64] the microscale via scanning electron microscopy (SEM)[65] and/or optical microscopy imaging,[66] and a macroscale with digital imaging.[67] Across these scales, DIC typically requires uniform illumination and a non-reflective surface pattern as glare and shadows can produce under/oversaturated regions and reduce contrast. To obtain the best measurements, this surface pattern should have the widest contrast range as possible. When recorded by the digital cameras, an ideal pattern will effectively use the full range of gray-scale values and minimize the error associated with digitizing a real pattern.

A pair of cameras is positioned in front of the sample, and both are angled inwards, towards the specimen, to have overlapping fields of view. The lens of each camera must be brought into focus on the specimen and aperture adjusted to maximize apparent contrast of the pattern on the specimen. To obtain the best measurements, the highest resolution cameras should be employed to allow for finer speckles (where ideally three to four pixels will contain a single speckle), creating a more accurate digital representation. The information collected by the cameras is digitized into gray-scale values that are read onto a computer to extract the displacements from the images using 3D-DIC software.

The 3D coordinates of the specimen surface are triangulated between images from two cameras to calculate 3D local displacements. If a specimen is viewed by two cameras from different perspectives, each location on the specimen can be found in each of the two recorded digital images. If the positions of the cameras relative to each other, magnification of the lenses, and imaging parameters are all known, then the 3D coordinate points of any location in the imaging space can be calculated by triangulation; therefore, a complete 3D map of the specimen surface can be constructed. This 3D map is generated for each image pair, and when compared to the reference state, it is used to compute 3D deformations from the change in surface shape to a high degree of accuracy. To obtain all of the information about the setup needed to accomplish this, a calibration process must be done. Triangulation between the two cameras is enabled by a calibration procedure completed prior to every test. Calibration is completed by recording the 3D motion of a set of known, high contrast, and uniform grid patterns. The dimensional distances between the grids are known precisely, and the orientation of the grid can be found by nonuniform dots placed outside of the standard grid. It is important to note that the calibration process is what effectively determines the physical dimensions of the specimen in the DIC calculation, as this information is not ascertainable from 2D images alone.

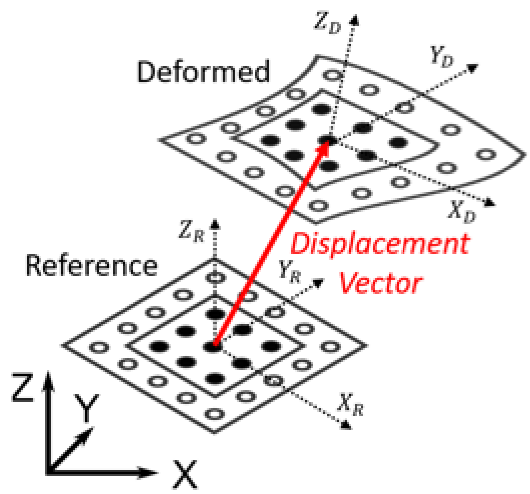

Fig. 1.5. Illustration of 3D-DIC displacement vector between un-deformed and deformed subsets. Inspired from [58].

Once the two cameras are calibrated, the 3D-DIC algorithm can be used to track the deformation of the surface via quantitative displacement measurements of the speckle pattern. The local displacement of the speckles is tracked in groups called subsets, as seen in Fig. 1.5. The size of the subset needs to be chosen in accordance with average speckle diameter; if a subset contains only one large speckle, it will be indiscernible from other subsets and contain little information to track through the time lapse of images. Therefore, choosing a subset size will always be a compromise because breaking the images into larger subsets will decrease the noise in the measurements at the cost of minor increased computational time and decreased spatial resolution. Conversely, a too small subset size will typically result in a failed correlation between the reference images and the deformed images. The displacement vector of each subset is calculated by a DIC algorithm to a theoretical accuracy of better than 0.01 pixels.

3.2. Accuracy

Like all measurement systems, DIC intrinsically has errors; these are associated with the image digitization process / camera setup and the calibration process. An extensive study done by Sandia National Laboratories effectively separated these errors into image correlation and calibration errors (Fig. 1.6).[68,69] The digitalization of the physical surface into grayscale valued images adds random noise to DIC measurements; poor speckle pattern quality will increase this noise level. A poorly setup camera system can decrease the measurement precision by significantly increasing situationally added noise, such as glare, having the lenses out of focus, lens distortion or insufficient camera angles. A poor calibration will also induce systematic errors that will decrease the accuracy of the DIC measurements; movement of the cameras after calibration or changes in the environment will also induce systematic errors. Lastly, the robustness and quality of DIC algorithm used and the input of all of these errors will affect the 3D surface reconstruction.

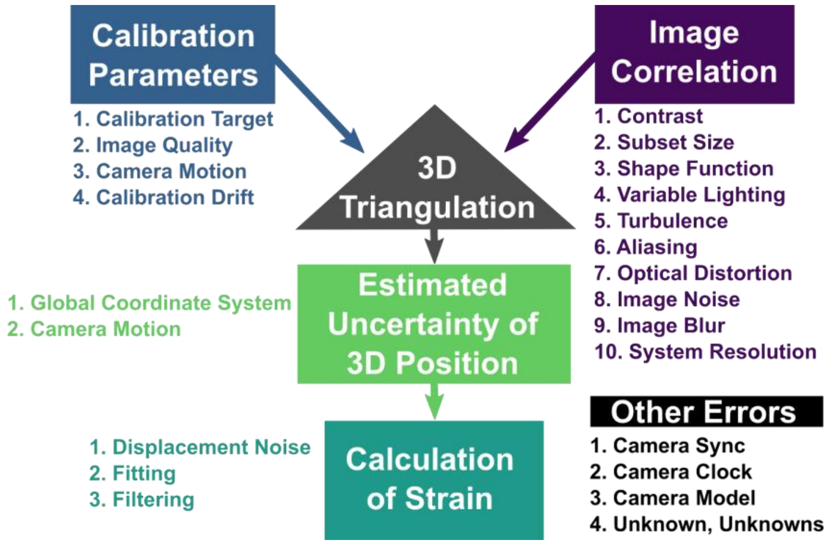

Fig. 1.6. 3D-DIC intrinsic errors can be categorized into image correlation and calibration errors; listed are some of the things that affect each. Recreated from [68].

It is clear that to obtain spatial deformation measurements with the best possible accuracy and precision, these intrinsic errors within the 3D-DIC system need to be minimized. It is necessary to understand the origins of these errors to minimize them. Most sources of error, during this work, were minimized simply by experience, ensuring proper setup of the cameras, selection of magnifying lenses, selection of a calibration grid size, a well-defined calibration routine, a high-contrast and homogenous speckle pattern sized to complement expected strain features, selection of an appropriate subset size, *etc*. For others, the use of cutting-edge correlation software with refined features, such as a hybrid, two-step calibration or lens distortion correction, helped to minimize traditionally significant errors.

4. Research plan and objectives

Within this dissertation, work is carried out to investigate the effects of reinforcement architecture on mechanical performance. In particular, for fiber-tow based composite systems a method to quantify braid and weave architecture for complexly-shaped geometries in a manner capable of detecting and tracking distortion in unit cell dimensions was implemented. By extending common DIC techniques, a full-field surface metrology system was developed capable of efficiently quantifying tow placement and trajectories for the purpose of studying systematic manufacturing induced irregularities and short-range braid/weave intrinsic defects at the unit cell level. It was hypothesized that braid/weave specific patterns influence non-periodic, non-stochastic behavior in tow placement, and these spatial defects could be quantified and measured during full-scale mechanical loading to correlate with the evolution of local failure performance. Work was directed at identifying key braid/weave architecture deviations that substantially affected performance via experimental and computational means to aid in targeted quality control certification in the field of extreme composite operations. Specific materials to be examined include biaxially braided tubular CFRP composites, triaxially braided tubular SiC/SiC CMCs, biaxially braided tubular SiC/SiC CMCs, and plain weave planar SiC/SiC CMCs. The broad goals of this dissertation are to understand architectural defects that arise in current braided/woven composites, to investigate their effects on performance, and to determine if a correlation can be made to predicted failure performance and improve the safety and efficiency of these components.

The objective of this work is to understand the long-range and short-range architectural defects present in the reinforcement architectural pattern of biaxial and triaxial braids as well as plain weave composites and their effects on mechanical and environmental resistance performance. This goal encompasses four scientific objectives.

(I) Little work has been done on quantifying architectural irregularity in tubular and other complex-shaped composites [4]; therefore, a system to gather tow placement and tow trajectory information must be developed. Such a system should be scalable, robust, and potentially applicable for gauging other scientifically desirable surface defects, for example, welds, threads or pits.

(II) The effects of global and local architectural irregularities for braids and weaves on mechanical performance are unknown, which is of critical importance to carbon and silicon carbide composites.[25] Using the previously developed system, spatial surface tow locations can be measured during composite deformation. Then, a relationship between strain concentration and distorted tow structure dimensions can be determined as well as a macroscale relationship between average distortions and bulk performance over a range of loading conditions.

(III) It is common in computational simulations to geometrically model composites as periodic propagations of an ideal, uniform unit cell.[5–7] While it is known this ideal geometry is inaccurate, incorporating the true geometry is challenging, with respect to both quantifying the real geometry as well as actually incorporating and meshing the realistic architecture into a virtual model. Furthermore, preferably, only architectural defects proven to have an influence on performance would be modeled. If the true tow architecture was measured and a relationship between distorted unit cell dimensions and strain concentration could be experimentally determined, numerical simulations with targeted realistic tow trajectories could be developed to systematically probe which configurations of unit cell distortion have a substantial influence on mechanical performance.

(IV) In the case of nuclear fuel cladding and other tubular composite pressure vessel structures, the unique, anisotropic microstructural properties of composites can lead to a highly convoluted definition of failure, including matrix cracking, loss of gas-tightness (hermeticity), reinforcement fiber fracture, and loss of load-bearing capability. For SiC/SiC CMC braided fuel cladding tubes, these behaviors are unknown as their complex shape and experimental nature makes them difficult to mechanically evaluate.[46,47] Using a coupled suite of sensors including noncontact, spatial strain measurements, a relevant helium gas detection probe, and acoustic emissions, critical strain values at matrix failure, hermetic failure, fiber failure, and loss of load-bearing capability must be determined to assist in the development of safe design protocols for such materials. Furthermore, the cracking behavior exhibited by the brittle constituents must be well understood prior to implementation in nuclear reactors or other extreme applications.

5. References

[1] Heim FM, Croom BP, Bumgardner C, Li X. Scalable measurements of tow architecture variability in braided ceramic composite tubes. J Am Ceram Soc 2018;101. doi:10.1111/jace.15564.

[2] Pankow M, Justusson B, Riosbaas M, Waas AM, Yen CF. Effect of fiber architecture on tensile fracture of 3D woven textile composites. Compos Struct 2019;225. doi:10.1016/j.compstruct.2019.111139.

[3] Berbon MZ, Rugg KL, Dadkhah MS, Marshall DB. Effect of Weave Architecture on Tensile Properties and Local Strain Heterogeneity in Thin-Sheet C-SiC Composites. J Am Ceram Soc 2002;85:2039–48. doi:10.1111/j.1151-2916.2002.tb00401.x.

[4] Elhajjar R, Grant P, Ashforth C. Composite Structures: Effects of Defects. 2018. doi:10.1002/9781118997710.

[5] Vanaerschot A, Cox BN, Lomov S V, Vandepitte D. Multi-scale modelling strategy for textile composites based on stochastic reinforcement geometry. Comput Methods Appl Mech Eng 2016;310:906–34. doi:https://doi.org/10.1016/j.cma.2016.08.007.

[6] Cox BN, Bale HA, Begley M, Blacklock M, Do B-C, Fast T, et al. Stochastic Virtual Tests for High-Temperature Ceramic Matrix Composites. Annu Rev Mater Res 2014;44:479–529. doi:10.1146/annurev-matsci-122013-025024.

[7] Rinaldi RG, Blacklock M, Bale H, Begley MR, Cox BN. Generating virtual textile composite specimens using statistical data from micro-computed tomography: 3D tow representations. J Mech Phys Solids 2012;60:1561–81. doi:10.1016/j.jmps.2012.02.008.

[8] Lightfoot JS, Wisnom MR, Potter K. Defects in woven preforms: Formation mechanisms and the effects of laminate design and layup protocol. Compos Part A Appl Sci Manuf 2013;51:99–107. doi:10.1016/J.COMPOSITESA.2013.04.004.

[9] Mills A. Automation of carbon fibre preform manufacture for affordable aerospace applications. Compos Part A Appl Sci Manuf 2001;32:955–62. doi:10.1016/S1359-

835X(00)00154-8.

[10] Larson NM, Zok FW. Insights from in-situ X-ray computed tomography during axial impregnation of unidirectional fiber beds. Compos Part A Appl Sci Manuf 2018;107:124–34. doi:10.1016/j.compositesa.2017.12.024.

[11] Czabaj M, Riccio M, Whitacre W. Numerical reconstruction of graphite/epoxy composite microstructure based on sub-micron resolution X-ray computed tomography. Compos Sci Technol 2014;105. doi:10.1016/j.compscitech.2014.10.017.

[12] Sherman S, Simmons J, Przybyla C. Mesoscale characterization of continuous fiber reinforced composites through machine learning: Fiber chirality. Acta Mater 2019;181:447–59. doi:10.1016/J.ACTAMAT.2019.10.001.

[13] Bale H, Blacklock M, Begley MR, Marshall DB, Cox BN, Ritchie RO. Characterizing Three-Dimensional Textile Ceramic Composites Using Synchrotron X-Ray Micro-Computed-Tomography. J Am Ceram Soc 2012;95:392–402. doi:10.1111/j.1551-2916.2011.04802.x.

[14] Rossol MN, Rajan VP, Zok FW. Effects of weave architecture on mechanical response of 2D ceramic composites. Compos Part A Appl Sci Manuf 2015;74:141–52. doi:10.1016/j.compositesa.2015.04.003.

[15] Rossol MN, Shaw JH, Bale H, Ritchie RO, Marshall DB, Zok FW. Characterizing Weave Geometry in Textile Ceramic Composites Using Digital Image Correlation. J Am Ceram Soc 2013;96:2362–5. doi:10.1111/jace.12468.

[16] Heim FM, Croom BP, Bumgardner C, Li X. Scalable measurements of tow architecture variability in braided ceramic composite tubes. J Am Ceram Soc 2018;101:4297–307. doi:10.1111/jace.15564.

[17] Chen M, Blacklock M, Zhang D, Gong J. Effects of stochastic tow waviness on stiffness and strength of plain-weave ceramic matrix composites. Adv Mech Eng 2017;9:1–10. doi:10.1177/1687814017727973.

[18] Gowayed Y, Ojard G, Prevost E, Santhosh U, Jefferson G. Defects in ceramic matrix composites and their impact on elastic properties. Compos Part B Eng 2013;55:167–75. doi:10.1016/J.COMPOSITESB.2013.06.026.

[19] Dai S, Cunningham PR, Marshall S, Silva C. Influence of fibre architecture on the tensile, compressive and flexural behaviour of 3D woven composites. Compos Part A Appl Sci Manuf 2015;69:195–207. doi:10.1016/J.COMPOSITESA.2014.11.012.

[20] Mandell JF, Samborsky DD, Wang L-S. EFFECTS OF FIBER WAVINESS ON

COMPOSITES FOR WIND TURBINE BLADES, 2003.

[21] Pottavathri SB, Nair R, Asmatulu R. Effect of In-Plane Fiber Tow Waviness Upon the Tensile Strength Characteristics of Fiber Reinforced Composites of Carbon/Epoxy AS4/3501-6. vol. Volume 9:, 2015. doi:10.1115/IMECE2015-52366.

[22] Belnoue JP-H, Mesogitis T, Nixon-Pearson OJ, Kratz J, Ivanov DS, Partridge IK, et al. Understanding and predicting defect formation in automated fibre placement pre-preg laminates. Compos Part A Appl Sci Manuf 2017;102:196–206. doi:10.1016/J.COMPOSITESA.2017.08.008.

[23] Boisse P, Hamila N, Madeo A. Modelling the development of defects during composite reinforcements and prepreg forming. Philos Trans A Math Phys Eng Sci 2016;374:20150269. doi:10.1098/rsta.2015.0269.

[24] Yang QD, Rugg KL, Cox BN, Marshall DB. Evaluation of Macroscopic and Local Strains in a Three-Dimensional Woven C/SiC Composite. J Am Ceram Soc 2005;88:719–25. doi:10.1111/j.1551-2916.2005.00156.x.

[25] Croom BP, Li X, Deck CP, Xu P, Lahoda EJ. Quantifying the three-dimensional damage and stress redistribution mechanisms of braided SiC/SiC composites by in situ volumetric digital image correlation. Scr Mater 2016;130:238–41. doi:10.1016/j.scriptamat.2016.12.021.

[26] Duboust N, Ghadbeigi H, Pinna C, Ayvar-Soberanis S, Collis A, Scaife R, et al. An optical method for measuring surface roughness of machined carbon fibre-reinforced plastic composites. J Compos Mater 2017;51:289–302. doi:10.1177/0021998316644849.

[27] Ansar M, Xinwei W, Chouwei Z. Modeling strategies of 3D woven composites: A review. Compos Struct 2011;93:1947–63. doi:10.1016/J.COMPSTRUCT.2011.03.010.

[28] Behera BK, Dash BP. Mechanical behavior of 3D woven composites. Mater Des 2015;67:261–71. doi:10.1016/J.MATDES.2014.11.020.

[29] Kyosev Y, editor. 1 - Introduction: the main types of braided structure using maypole braiding technology. Braid. Technol. Text., Woodhead Publishing; 2015, p. 1–25. doi:https://doi.org/10.1533/9780857099211.1.

[30] Kyosev Y, editor. 2 - Patterning of braided products. Braid. Technol. Text., Woodhead Publishing; 2015, p. 29–46. doi:https://doi.org/10.1533/9780857099211.1.29.

[31] Melenka GW, Carey JP. Experimental analysis of diamond and regular tubular braided composites using three-dimensional digital image correlation. J Compos Mater 2017;51:3887–907. doi:10.1177/0021998317695418.

[32] Ruth M, Antkowiak M, Gossett S. Nuclear and Renewable Energy Synergies Workshop: Report of Proceedings 2011. doi:10.2172/1031396.

[33] Karoutas Z, Brown J, Atwood A, Hallstadius L, Lahoda E, Ray S, et al. The maturing of nuclear fuel: Past to Accident Tolerant Fuel. Prog Nucl Energy 2018;102:68–78. doi:10.1016/j.pnucene.2017.07.016.

[34] Ramana M V, Hopkins LB, Glaser A. Licensing small modular reactors. Energy 2013;61:555–64. doi:https://doi.org/10.1016/j.energy.2013.09.010.

[35] Ingersoll DT. Deliberately small reactors and the second nuclear era. Prog Nucl Energy 2009;51:589–603. doi:https://doi.org/10.1016/j.pnucene.2009.01.003.

[36] Serp J, Allibert M, Beneš O, Delpech S, Feynberg O, Ghetta V, et al. The molten salt reactor (MSR) in generation IV: Overview and perspectives. Prog Nucl Energy 2014;77:308–19. doi:https://doi.org/10.1016/j.pnucene.2014.02.014.

[37] McCoy HE. An Evaluation of the Molten-Salt Reactor Experiment Hastelloy N Surveillance Specimens - Fourth Group. Oak Ridge Natl Lab 1971;ORNL-TM-30.

[38] Ouyang F-Y, Chang C-H, Kai J-J. Long-term corrosion behaviors of Hastelloy-N and Hastelloy-B3 in moisture-containing molten FLiNaK salt environments. J Nucl Mater 2014;446:81–9. doi:https://doi.org/10.1016/j.jnucmat.2013.11.045.

[39] Cheng T, Keiser JR, Brady MP, Terrani KA, Pint BA. Oxidation of fuel cladding candidate materials in steam environments at high temperature and pressure. J Nucl Mater 2012;427:396–400. doi:https://doi.org/10.1016/j.jnucmat.2012.05.007.

[40] Hirano M, Yonomoto T, Ishigaki M, Watanabe N, Maruyama Y, Sibamoto Y, et al. Insights from review and analysis of the Fukushima Dai-ichi accident. J Nucl Sci Technol 2012;49:1–17. doi:10.1080/18811248.2011.636538.

[41] Kurata M. Research and Development Methodology for Practical Use of Accident Tolerant Fuel in Light Water Reactors. Nucl Eng Technol 2016;48:26–32. doi:10.1016/j.net.2015.12.004.

[42] Sauder C. Ceramic Matrix Composites: Nuclear Applications. Ceram. Matrix Compos., John Wiley & Sons, Ltd; 2014, p. 609–46. doi:10.1002/9781118832998.ch22.

[43] Lackey WJ. Review, Status, and Future of the Chemical Vapor Infiltration Process for Fabrication of Fiber-Reinforced Ceramic Composites. A Collect. Pap. Present. 13th Annu. Conf. Compos. Adv. Ceram. Mater. Ceram. Eng. Sci. Proc., John Wiley & Sons, Ltd; 2008, p. 577–84. doi:10.1002/9780470310557.ch1.

[44] Katoh Y, Ozawa K, Shih C, Nozawa T, Shinavski RJ, Hasegawa A, et al. Continuous SiC fiber, CVI SiC matrix composites for nuclear applications: Properties and irradiation effects. J Nucl Mater 2014;448:448–76. doi:10.1016/j.jnucmat.2013.06.040.

[45] Deck CP, Khalifa HE, Sammuli B, Hilsabeck T, Back CA. Fabrication of SiC–SiC composites for fuel cladding in advanced reactor designs. Prog Nucl Energy 2012;57:38–45. doi:10.1016/J.PNUCENE.2011.10.002.

[46] Katoh Y, Kishimoto H, Kohyama A. The influences of irradiation temperature and helium production on the dimensional stability of silicon carbide. J Nucl Mater 2002. doi:10.1016/S0022-3115(02)01062-0.

[47] Katoh Y, Hu X, Koyanagi T, Singh GP. Determination of He and D permeability of neutron-irradiated SiC tubes to examine the potential for release due to micro-cracking. Oak Ridge, TN (United States): 2017. doi:10.2172/1394374.

[48] Zhuo W, Niu F, Zhao Y, Qi H, Hao Z, Hao P. Helium Permeability Measurement of SiC Ceramic Composites for Advanced Reactor Application. Int. Conf. Nucl. Eng. Proceedings, ICONE, vol. 1, 2013. doi:10.1115/ICONE21-15525.

[49] Choi SR, Bansal NP, Verrilli MJ. Delayed failure of ceramic matrix composites in tension at elevated temperatures. J Eur Ceram Soc 2005;25:1629–36. doi:10.1016/J.JEURCERAMSOC.2004.05.024.

[50] Yvon P, Carré F. Structural materials challenges for advanced reactor systems. J Nucl Mater 2009;385:217–22. doi:10.1016/j.jnucmat.2008.11.026.

[51] Deck CP, Jacobsen GM, Sheeder J, Gutierrez O, Zhang J, Stone J, et al. Characterization of SiC-SiC composites for accident tolerant fuel cladding. J Nucl Mater 2015;466:667–81. doi:10.1016/j.jnucmat.2015.08.020.

[52] DiCarlo JA, Yun H-M, Morscher GN, Bhatt RT. SiC/SiC Composites for 1200°C and Above. In: Bansal NP, editor. Handb. Ceram. Compos., Boston, MA: Springer US; 2005, p. 77–98. doi:10.1007/0-387-23986-3_4.

[53] Bruni-Bossio B, Ayranci C, Carey JP, Omonov T, Curtis J. Experimental testing of the tensile elastic properties of cellulose braided composites. Compos Part B Eng 2019;166:542–8. doi:10.1016/J.COMPOSITESB.2019.02.052.

[54] Carey JP. 1 - Introduction to braided composites. In: Carey JP, editor. Handb. Adv. Braided Compos. Mater., Woodhead Publishing; 2017, p. 1–21. doi:https://doi.org/10.1016/B978-0-08-100369-5.00001-5.

[55] Jamin T, Dubé M, Lebel LL. Effect of stamp-forming parameters and bend radius on the mechanical performance of curved beam carbon fiber/polyphenylene sulfide specimens. J Compos Mater 2016;50:1213–25. doi:10.1177/0021998315590261.

[56] Hassan MH, Othman AR, Kamaruddin S. A review on the manufacturing defects of complex-shaped laminate in aircraft composite structures. Int J Adv Manuf Technol 2017;91:4081–94. doi:10.1007/s00170-017-0096-5.

[57] Jesson DA, Watts JF. The Interface and Interphase in Polymer Matrix Composites: Effect on Mechanical Properties and Methods for Identification. Polym Rev 2012;52:321–54. doi:10.1080/15583724.2012.710288.

[58] Sutton MA. Three-dimensional digital image correlation to quantify deformation and crack-opening displacement in ductile aluminum under mixed-mode I/III loading. Opt Eng 2007;46:051003. doi:10.1117/1.2741279.

[59] Schreier H, Orteu JJ, Sutton MA. Image correlation for shape, motion and deformation measurements: Basic concepts, theory and applications. Springer US; 2009. doi:10.1007/978-0-387-78747-3.

[60] Ivanov D, Ivanov S, Lomov S, Verpoest I. Strain mapping analysis of textile composites. Opt Lasers Eng 2009;47:360–70. doi:10.1016/J.OPTLASENG.2008.05.013.

[61] Helm JD, McNeill SR, Sutton MA. Improved three-dimensional image correlation for surface displacement measurement. Opt Eng 1996;35:1911–20. doi:10.1117/1.600624.

[62] Rossol MN, Shaw JH, Bale H, Ritchie RO, Marshall DB, Zok FW. Characterizing weave geometry in textile ceramic composites using digital image correlation. J Am Ceram Soc 2013;96:2362–5. doi:10.1111/jace.12468.

[63] Sutton MA, Orteu JJ, Schreier HW. Image Correlation for Shape, Motion and Deformation Measurements. Boston, MA: Springer US; 2009. doi:10.1007/978-0-387-78747-3.

[64] Sun Y, Liu J, Blom D, Koley G, Duan Z, Wang G, et al. Atomic-scale imaging correlation on the deformation and sensing mechanisms of SnO2 nanowires. Appl Phys Lett 2014;105:243105. doi:10.1063/1.4904912.

[65] Guo S, Sutton M, Li X, Li N, Wang L. SEM-DIC based nanoscale thermal deformation studies of heterogeneous material. Conf Proc Soc Exp Mech Ser 2014;3:145–50. doi:10.1007/978-3-319-00768-7_17.

[66] Bumgardner C, Croom BP, Li X. High-temperature delamination mechanisms of thermal barrier coatings: in-situ digital image correlation and finite element analyses. Acta Mater

2017;128:54–63. doi:10.1016/j.actamat.2017.01.061.

[67] Croom BP, Bumgardner C, Li X. Unveiling residual stresses in air plasma spray coatings by digital image correlation. Extrem Mech Lett 2016. doi:10.1016/j.eml.2016.02.013.

[68] Reu PL, Miller TJ. DIC Uncertainty Quantification for Large Scale Outdoor Testing 2014.

[69] Balcaen R, Reu PL, Lava P, Debruyne D. Stereo-DIC Uncertainty Quantification based on Simulated Images. Exp Mech 2017;57. doi:10.1007/s11340-017-0288-9.

CHAPTER 2: CUSTOM COMPOSITE ARCHITECTURE FOR THE IMPROVEMENT OF STRENGTH AND TOUGHNESS IN ALUMINUM MATRIX COMPOSITES

This dissertation is focused on studying the structure of the reinforcement phase in composites and how this influences failure. Inspiration for this topic was developed via preliminary experiments with metal matrix composites, where I used the principles core to composite performance to plan an ideal reinforcement phase microstructure in an aluminum matrix, which could be done within a laboratory with low-cost equipment. To achieve this designed microstructure a novel manufacturing method had to be developed to intrinsically induce the desired intermetallic phases with coordinated locations. This ideal microstructure was derived from biological inspiration, namely from sea shell containing nacre, which is a widely reported exceptional armor utilizing a multitude of multiscale toughening mechanisms.[1] Full details of this work can be found in *Heim et al.* [2]. Scanning electron microscopy (SEM), Transmission electron microscopy (TEM), X-ray diffraction (XRD), and nanoindentation measurements were performed with the assistance of *Zhang*.

1. Introduction

With added emphasis on efficiency and reduced carbon pollutants many industries are pushing materials development in search of new micro and nano scale microstructure mechanisms that can be programmed and customized to form composites with an enhanced combination of mechanical properties, such as higher strength, toughness, and stiffness with lower weight. In metal matrix composites, aluminum matrix composites (AMC) are attractive because Al is abundant, light-weight, ductile, corrosion resistant, and compatible with many other key structural metals. Intermetallic reinforcements formed from Al have demonstrated superior particle-matrix interfaces, specifically compounds with nickel[3–8] and titanium[9–13]. These intermetallic phases are gaining attention because of their relative high strength, low weight, high performance in extreme environments, and excellent cohesion with the Al matrix due to solid-state reactions.[14–19] In general, it is well demonstrated that the toughness behavior of reinforced composites are highly sensitive to the reinforcement characteristics, involving size, volume fraction, and clustering.[20,21]

Studies like that of *A. Ayyar and N. Chawla* [20] that have carefully modeled and studied the effect of reinforcement phase architecture; specifically, variables such as particle size/shape and level of particle clustering, in particle reinforced composites, were used to show that rectangular or elongated particles aligned perpendicular to a crack tip exhibited superior crack shielding abilities and work to improve the toughness of composites. They also concluded that, while clusters of large particles often hurt toughness, the complex stress state surrounding clusters of small particles has a similar crack deflection effect as that of a single large particle and with certain particle shapes, can work to significantly increase the roughness of the crack path, indicating enhanced degrees of crack deflection. By creating layer-wise organized elongated or rectangular-like intermetallic particle reinforcements for a given matrix material, there is potential to overcome the classical low toughness limitations of particulate (typically SiC or alumina) reinforced metal composites by architecturally inducing crack deflection mechanisms.

2. Experimental methods

2.1. Material preparation

Due to the precedent of this manufacturing method and subsequent unique distribution and shape of reinforcing particles, I have named this process the Rolling of Randomly Orientated Layer-wise Materials (RROLM) method (Fig. 2.1a). Commercial grade aluminum foil was used with nickel titanium (NiTi) particles purchased from SkySpring Nanomaterials Inc. with a size range of 80-60 nm and a composition of 50/50 atomic % in shape-memory alloy (SMA) form. Composites were made with a prescribed 10 % by weight of NiTi nanoparticles, 90 % by weight Al foil.

The Al foil was coated with NiTi nanoparticles and folded to a few layers. Before application to the foil surface, the NiTi nanoparticles were distributed in acetone via an ultrasonic bath for approximately 10 minutes; this material was then spread evenly, as possible, over the surface of the Al foil using a synthetic fiber brush. By minimizing the contact area of the brush and rinsing with additional acetone, the amount of nanoparticles lost to the brush was minimized.

This sandwich of materials was then crumpled into approximately a sphere. This ball was compressed into a 25.4 mm diameter cylinder by a pressure of 160 MPa. These compressed coins were then clamped tightly and heated by 5 °/min (machine limited) in a MTI GSL-1800X tube furnace with argon flow protection to a temperature of 630 °C for 4 hours duration; the furnace was then allowed to cool to ambient temperature, which took about 4 hours. These coins were then mechanically cold rolled for a reduction in thickness of eighty-five percent. Pre-rolled coin thicknesses were limited by the rolling machine (< 5 mm); thereby limiting the resulting samples to submillimeter thicknesses. The materials created in this fashion with NiTi nanoparticles and Al foil will hence forth be called NiTi-Al foil composites. The same process was used for the construction of Ni-Al foil samples with 99.9% Ni 20 nm nanoparticles also purchased from SkySpring Nanomaterials Inc. for a comparison considering a single-phase reinforcement; additionally, control samples were fabricated without the addition of any nanoparticles, and these will be called Al foil composites.

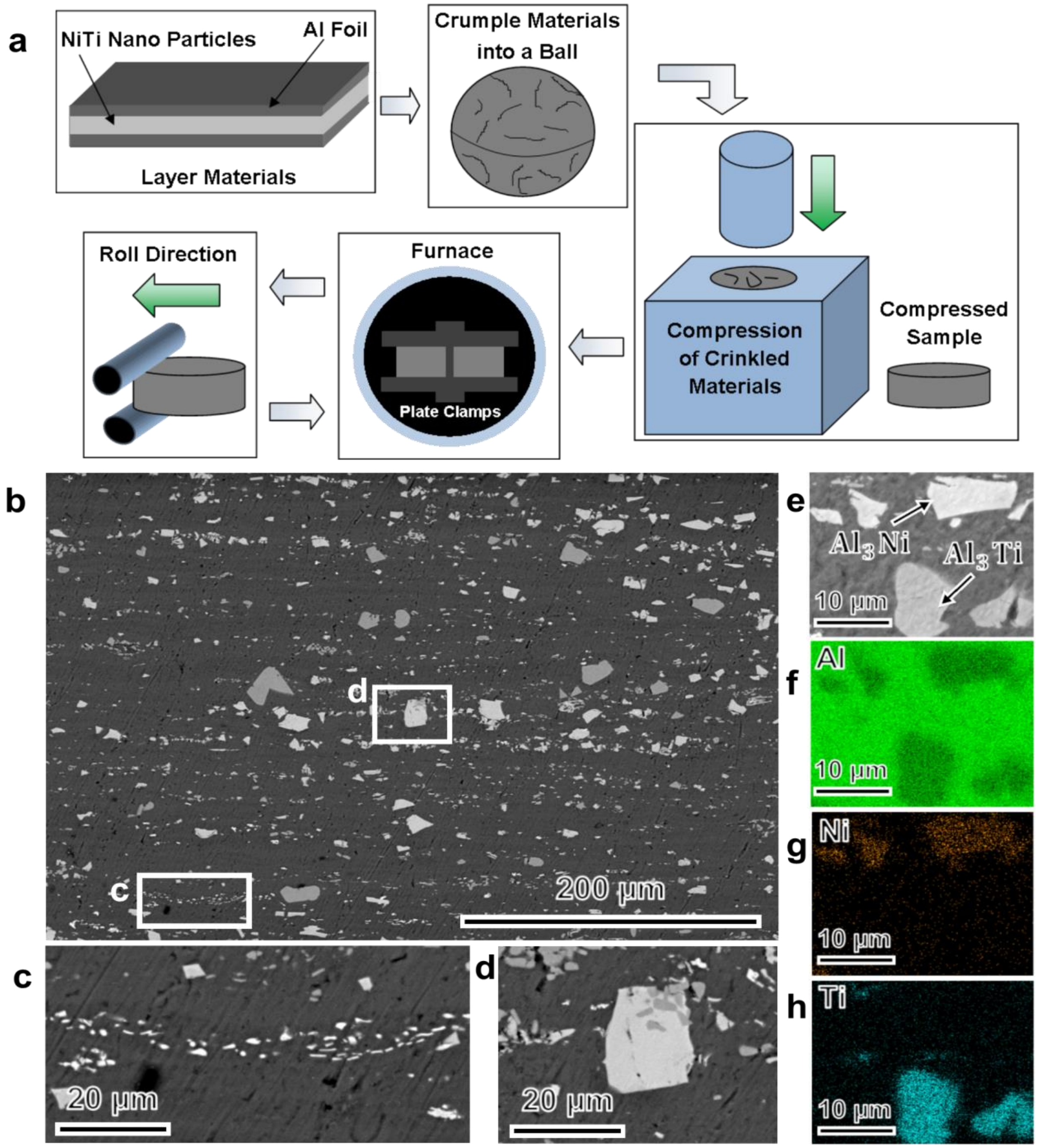

Fig. 2.1. (a) Schematic illustrating the steps taken in the RROLM manufacturing process. (b) Circular Backscatter Detector (CBS) image of the layered organization throughout the composite containing regions (c) and (d). (c) Higher magnification CBS view of the smaller reinforcing particles. (d) Higher magnification CBS view of a larger rectangular reinforcing particle exhibiting two phases. (e) Higher magnification CBS view of intermediate sized reinforcing particles. (f-h) Energy dispersive spectrometer elemental mappings of (e) corresponding to Al, Ni, and Ti elements respectively.

2.2. Microstructure and composition characterization

Samples for examination were mechanically polished using standard metallurgical procedures. The microstructure and local composition of the composites were characterized by means of a FEI Quanta 650 Scanning Electron Microscope (SEM) with an energy dispersive spectrometer (EDS) and Circular Backscatter Detector (CBS). The matrix, reinforcing particles, and corresponding interfaces were studied via a FEI Titan Transmission Electron Microscope (TEM). X-ray diffraction (XRD, a PANalytical X'Pert Pro Multi-Purpose Diffractometer (MPD) equipped with Cu K_α radiation (λ = 0.15406 nm)) was used to characterize the chemical phases present in the scanning range (2Θ) of 20° to 80°. The XRD data was post-processed to remove the background noise; additionally, a ten-sample moving filter of was applied to this modified signal to distinguish stronger peaks. Nanoindentation was performed with a Micro Materials NanoTest Vantage equipped with a diamond Berkovich tip. Twenty indentations separated by 3 µm were made in a continuous line to a load of 20 mN for each particle tested

MATLAB was used to process acquired CBS images and uncover the intermetallic particle size distribution. Ten images over various parts of the cross-section of a NiTi-Al foil sample were used in this analysis. Magnifications levels in these images were varied from 260x to 2000x, where the majority were at 1000x to prevent a bias in the reported areas due to limited resolution of low magnification images, while still being able to account for a large proportion of the sample surface. In CBS images particles appear much brighter in intensity than the matrix; by sectioning each image into sub regions and doing local thresholding to convert to a binary image, a clear distinction between particles and matrix can be made. After isolating the particles in a binary image, MATLAB has several built-in functions to detect continuous edges and, subsequently, find the area contained within these edges. Another method in MATLAB leveraging the relative intensities for different compounds observable in CBS images was used to find the approximate area fraction of the three phases present (Al, Al_3Ni, Al_3Ti). The area fraction is then projected into the third dimension to estimate volume fraction. Figure S1 in the Supporting Information of the published article *Heim et al.* [22] highlights these three distinct intensity peaks.

2.3. Mechanical Testing

To quantify the improvements in mechanical performance of composites made in this fashion, tensile tests were performed. These were done for NiTi-Al foil composites, Ni-Al foil composites, Al foil composites (control), and high purity Al. Tensile test samples were cut and mechanically ground from larger, bulk rolled sheets into the dimensions seen in Fig. 2.3a. Tensile tests were performed with an Admet eXpert 2611 table-top, universal testing machine with an Admet 1210AJ-2K-B, 8.9 kN load cell. All reported results were done at a strain rate of 1 mm / min. Ultimate engineering tensile strength was defined according to:

$$\sigma_{UTS} = \max\left(\frac{F}{w*t}\right) \tag{2.1}$$

where F is load recorded by the Admet, *w* is the initial sample width, and *t* is the initial sample thickness. Toughness for each sample was calculated according to:

$$T = \int_0^{\varepsilon_f} \sigma d\varepsilon \tag{2.2}$$

where σ is engineering stress and ε is engineering strain, integrated over the initial and final engineering strain.

A three-point bending test was performed *in situ* under SEM to observe crack formation and growth through the cross-section of a NiTi-Al foil sample. A rectangular sample of dimensions 25 mm x 5 mm x 0.5 mm was fabricated from the same NiTi-Al foil bulk materials used to make tensile test samples. A notch was cut along the sample width, via a razor blade, at the center of the greatest dimension. This was then mounted in a MTII SEMtester 1000 modified to perform three-point flexural tests. Displacement of the center pin was incrementally controlled manually outside of the SEM via a laptop, as the sample had to remain completely stationary while the surface was scanned. A FEI Quanta 650 Scanning Electron Microscope (SEM) with a Circular Backscatter Detector (CBS) was used to obtain images of the cross section. High contrast CBS images during crack progression were taken to later calculate the 2D local strain gradients over the cross-section as the crack progressed. These images were analyzed via VIC-2D 2009 Digital Image Correlation (DIC) software, which is able to isolate and remove rigid body motion between each image to reveal surface deformation by tracking high-contrast particles or in this case, intermetallic particles. A subset size of 45 and step size of 12 were used for the DIC strain analysis.

3. Results

3.1. Microstructure and composition characterization

Circular Backscatter Detector (CBS) images taken via SEM are used to highlight the elemental differences in the NiTi-Al foil composites. The intermetallic compounds are predominantly aligned within clusters parallel to the rolling direction of the sample (Fig. 2.1b). Many of the particles have a rectangular-biased shape with jagged edges. By the unique RROLM process local NiTi and Al interactions during heating form a layered Al- intermetallic structure; however globally, the orientation of these layers were still mostly random and unorganized. During rolling, these layers fragment into much smaller, elongated particles that are then aligned by rolling. This was likely effective because the initial random orientation of the layered intermetallics prevented through thickness, unstable brittle fracture along any consistently oriented Al-intermetallic layers during the subsequent rolling process.

As seen in Fig. 2.1b and 2.1c many of the smaller and intermediate particles are clustered into locally horizontal orientated veins. Additionally, most of the larger particles appear by CBS imaging to be a single phase, but as seen in Fig. 2.1d this is not always the case. Inspection of the

CBS images (Fig. 2.1e) indicates that there are two dominate intermetallic phases present; these were confirmed by EDS mapping (Fig. 2.1f-1h) and XRD measurements to be Al_3Ni and Al_3Ti. An imaging analysis of the CBS images indicated that the area fraction of each intermetallic is around 3-4 %, for a total intermetallic area fraction of around 6-8 %. Given the concentration of Ni (5 % wt.) and Ti (5% wt.) relative to Al (90% wt.), the size of the NiTi particles, and the duration of heating it is not unreasonable that only two phases were found; as the Al-Ni-Ti ternary phase diagram[23] as well as literature[15,23–31] confirm that Al_3Ni and Al_3Ti are the most stable compounds formed around these temperatures. At temperatures around 630 °C it is often found that the NiTi phase is unstable, which initiates the reaction between Ni and Ti with Al.[32] Solid-state reactions between Ti[27,28] and Ni[24,31] with Al have been shown to be rather quick, especially once the Al side oxide layer is broken down; therefore there is little uncertainty that the NiTi nanoparticles have reacted full and settled into these two equilibrium phases.

A nanoindentation study, was done for both Al_3Ni (nanohardness / modulus of 6.17 / 130 GPa) and Al_3Ti (nanohardness / modulus of 1.4 / 79.7 GPa) particles, which unveiled the bi-level reinforcing potential enabled by the utilization of NiTi nanoparticles (Fig. 2.2a-2d). These results, which can be compared to that of [19], indicate that under mechanical loading the two intermetallic phases will likely fail at separate instances, thereby working to delay unstable fracture and improve the mechanical performance over a mono-phase particulate reinforced composite.

An image processing analysis uncovering the resultant particulate area was done over a random subset of the NiTi-Al foil cross-section, observed under SEM. Particles sizes can be discretized into three categories by area: small particles (<12 μm^2), larger particles (> 65 μm^2), and intermediate sized particles between the two ranges. Each of these categories makes up a third of the total particulate area; the average particle area was 5 μm^2, indicating that the majority of particles were quite small (Fig. 2.2e).

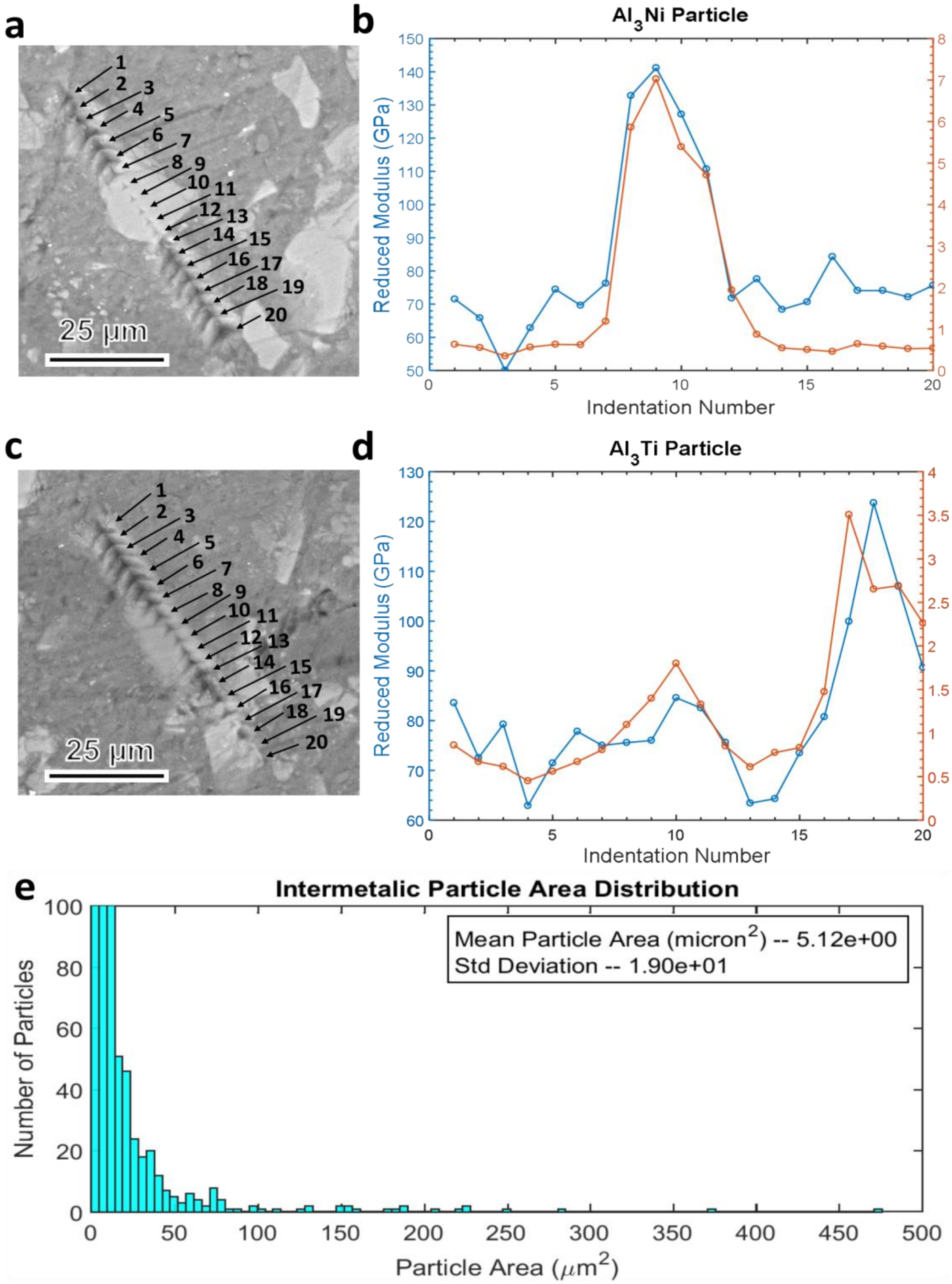

Fig. 2.2. Nanoindentation results of an Al_3Ni and Al_3Ti particle, respectively. (a) SEM image of an indentation trail passing through an Al_3Ni particle. (b) Recorded reduced modulus and nanohardness for the corresponding Al_3Ni particle. (c) SEM image of an indentation trail passing through an Al_3Ti particle. (d) Recorded reduced modulus and nanohardness for the

corresponding Al_3Ti particle. (e) Particle area distribution; the first three columns correspond to particles under 12 μm^2 and rise to about 2860, 330, and 100 counts respectively.

3.2. Mechanical performance

To evaluate the engineered improvements in properties made possible by the layer-wise organized, dual Al-intermetallic reinforcements, tensile tests were carried out. For comparison, Ni-Al foil samples with a single reinforcement Al_3Ni phase (confirmed via XRD and EDS), control samples fabricated from solely Al foil, and samples made with 99.9% pure Al are compared to the performance of NiTi-Al foil samples (Fig. 2.3). It is clear that all samples suffered from a reduction in ductility compared to that of pure Al. The toughness of the NiTi-Al foil, Ni-Al foil and Al foil composites were, respectively, 3.3 MJ / m^3, 0.78 MJ / m^3, and 1.7 MJ / m^3 (Fig. 2.3b), calculated from the area under the tensile curve. The apparent improvement in toughness over the Al foil control was around 94%, while the Ni-Al foil sample presents a drastic reduction in toughness. This behavior is anticipated to be a result of the tailored microstructure induced by mechanical rolling and the RROLM process as well as the critically smaller phase structure of the NiTi-Al foil composites over the Ni-Al foil composites, likely induced from the rapid formation of two separate phases in a similar local volume, respectively.

A marked 71% increase in UTS was observed over the control samples (Fig. 2.3b), with a reasonable 265 MPa. The strength of the Ni-Al foil composites was higher than that of the control (~17%) likely due to some load transfer to the large Al_3Ni phase particles. SEM images of the fracture surface morphology for the NiTi-Al composites (Fig. 2.3c) indicate, through elongated dimples, a non-uniform stress distribution and failure by shear stress along the greater dimension of the particles. This is noteworthy as this indicates the particles interrupt and alter the local stress distribution in the matrix material causing critical changes in the mode of fracture along the crack tip; this crack deflection mechanism has the potential to increase the toughness of these materials.

Brittle fracture of the intermetallic compounds (Fig. 2.3d) is evident by the relatively clean cleavage of the reinforcement surface. Zooming out from the surface, (Fig. 2.3e) it becomes apparent that the size of the dimples varies significantly, corresponding to the variation in reinforcement size, which can be clearly distinguished by CBS imaging. In this image, the horizontal orientation bias in the coalescence of voids is apparent.

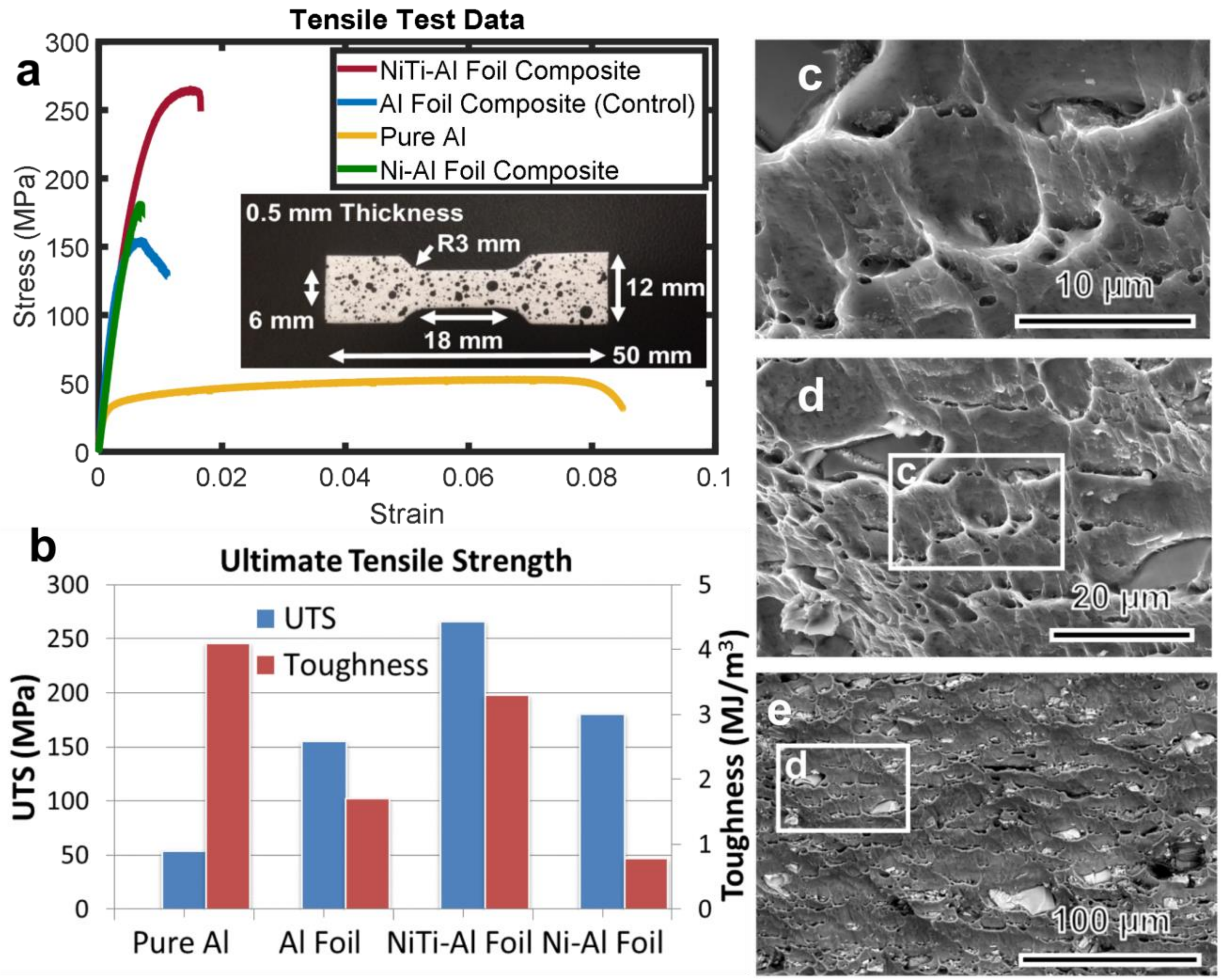

Fig. 2.3. (a) Tensile test results and sample dimensions (strain rate of 1 mm/min) for three materials in a strain hardened state (85 % reduced by cold work). (b) Comparison of ultimate tensile strength (UTS) and toughness. (c) SEM image of an elongated dimpled surface morphology. (d) Highlights the fracture surface of the intermetallic particles. (e) CBS image displaying a layered orientation bias in the development of micro voids. All SEM images of NiTi-Al Foil composite.

An *in situ* SEM, three-point bend test on a NiTi-Al foil composite was performed to uncover several intrinsic toughening mechanisms. Fig. 2.4a shows four SEM images of the progression of an initial crack through the cross-section. Initially there are two possible primary crack fronts, but as strain was increased the left crack was halted and the right crack proceeded, becoming the main crack. However, long before this distinction was made, it was clear that the response of the material impacted an expansive area of the cross-section as countless particles cracked with increasing strain; this will be discussed in more detail later. The majority of these widespread cracks did not self-propagate; in Fig. 2.4b a closer view of a cracked large particle can be seen slowly turning into a large void. It was interesting that this large crack opened up to about half the width of the original particle before eventually linking up with other smaller voids. The bond between the particle and matrix appeared exceptionally strong, and the presence of many microcracks within the particles indicated exceptional load transfer from matrix to particle. As the main crack progressed it followed a tumultuous path. Main crack growth between images was highly stable, and in the right-most image an enormous amount of crack tip widening is visible (Fig. 2.4a). The energy absorbed by redirection and blunting of the crack tip as well as the microcracking of the many particles is expected to have aided in improving the toughness of this composite over the control (Al Foil).

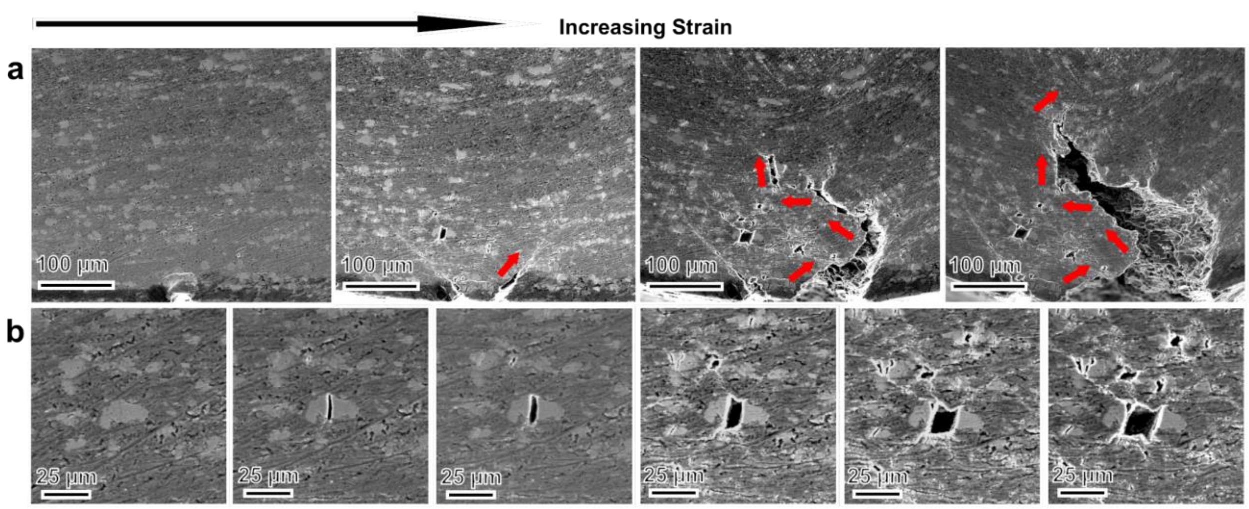

Fig. 2.4. *In situ* SEM images of the cross-section of a NiTi-Al foil in a three-point bending

configuration with an initial notch. (a) Four SEM images over increased strain that highlight the unusual path of the primary crack and the general blunting of the crack tip. (b) Six SEM images over increased strain that highlight the intermetallic particles' resistance to decohesion with the matrix and resistance to crack propagation.

Because of the elemental contrast between the matrix and particles it was possible to track the local deformation of the matrix and particles via DIC between consecutive CBS images. As this sample was less than a millimeter thick, the following analysis can be considered under a plane stress constraint. Additionally, strain fields displayed are relative to the previous CBS image taken, which corresponds to a 0.1 mm displacement of the center support.

Fig. 2.5 exhibits the first principal strain profile that took place before any noticeable crack propagation. To the trained eye this profile should look suspiciously large; however, this is a result of how DIC smooths spatial strains. This strain field indicates a large degree of microcracking, which would appear as large and highly localized strains, but as the strains are filtered to remove potentially noisy data, the highly concentrated deformation gets spread over the local region, exaggerating the strain profile. As the global strain increases and the main crack begins to propagate (Fig. 2.5b) the stress zone becomes less symmetrical as the particles on the left side appear to dissipate the strain energy more effectively, as indicated by the expanded size of the leftward strain profile. This leads to the primary crack proceeding on the right side of the plastic zone. After this point, the degree of ongoing wide spread microcracking declines as many of the particles have already cracked; this is indicated by the decrease in apparent size of the plastic zone. However, Fig. 2.5c also shows a high degree of localized void growth, as the strain fields below the crack surface are almost as high as on the crack front. From Fig 2.5c, it can be seen that the strain field increases along the underside of the local cluster of intermetallic particles with a grouping length of around 75 µm; By comparing the crack between Fig. 2.5c and Fig. 2.5d, it can be noticed that the crack was deflected by this visible local cluster of 5-20 µm sized particles, forcing it around this cluster, similar to the behavior modeled by *A. Ayyar and N. Chawla*.[20] Additionally, in Fig. 2.5d, it can be seen that another local horizontally orientated vein with a length around 100 μm, consisting predominantly of 2-5 μm sized particles similarly shielded the matrix material behind them from the crack tip. As seen in the last progression of the main crack in Fig. 2.4a, which occurs shortly after Fig.2.5d, there is a large blunting of the crack tip until the expected local stress levels are raised sufficiently to finally break around this cluster. As the crack progressed through the consecutively layered clusters of reinforcement it was often deflected (Fig. 2.5c) and stalled (Fig. 2.5d). I*n situ* and post-mortem observations indicated that the Al_3Ni phase often cracked before the Al_3Ti phase; however, it was difficult to decouple this observation from particle size. The dominate contributor to the first principal strains was the bending strain this is likely related to the expansion of voids along this direction. These *in situ* observations and measurements can be used to present some apparent toughening mechanisms.

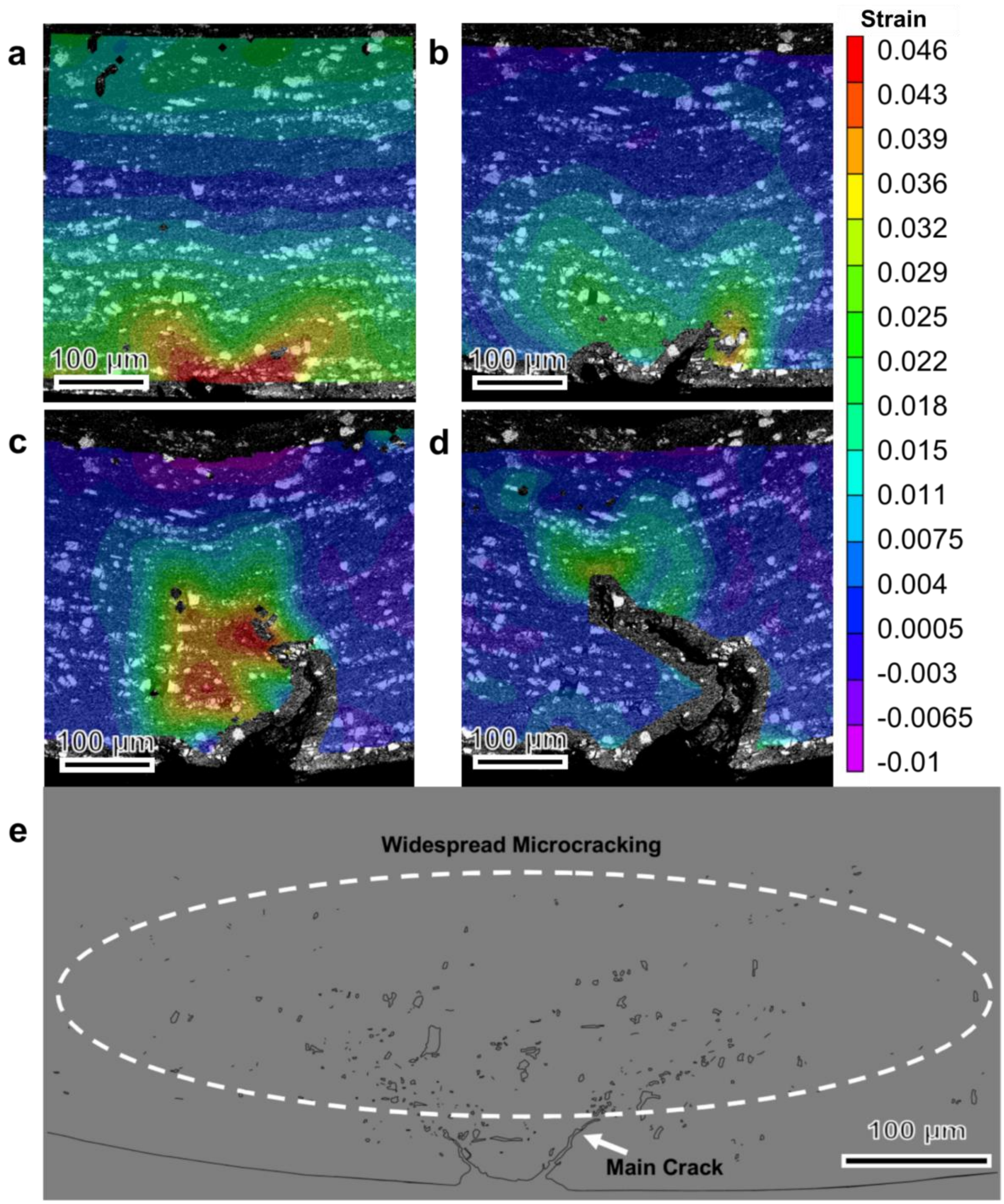

Fig. 2.5. DIC analysis of high-contrast CBS images taken during *in situ* three-point flexure test. (a-d) Local first principle strains as the crack progressed. The displayed units of strain are unity. (e) Schematic highlighting the formed cracks in (b).

Image processing was used to find and trace the crack edges and allowed the extent of the initial microcracking to be easily investigated (Fig. 2.5e); this schematic corresponds to the strain state as seen in Fig. 2.5b. Microcracks formed in excess of 200 µm away from the primary crack;

illustrating that the particle structure induces an intrinsic microcracking toughening mechanism that works to shield the crack. Energy is absorbed by the cracking of these intermetallic particles and stresses are relieved ahead of the crack tip by this mechanism.[33] It was observed by SEM that many of the intermediate sized particles cracked in several places with few penetrating deep into the matrix material.

4. Discussion

While the NiTi-Al foil composites are strengthened by the reinforcing particles, nano precipitates and low energy dislocation structures (observed via TEM),[22] these are less novel compared to the intrinsic toughening mechanisms apparent from the *in situ* crack growth and fracture surface observations. Typically at the cost of reduced ductility and toughness, particle reinforced composites often only improve the strength of the matrix material.[21,33] Crack deflection and subsequent extension is a powerful toughening mechanism; however classical small homogenous particulate reinforcements do little to redirect primary cracks.[20] Small particulates rarely fracture, hence reducing microvoid formation, but because of their small size, they can do little to substantially redirect cracks (Fig. 2.6). Large circular particulates on the other hand will often fracture or detach from the matrix and because of their random orientation, often do minimal crack deflection and actually reduce toughness by forming large microvoids that enhance crack progression (Fig. 2.6b).

The NiTi-Al foil composites studied in this research present a useful preference for cracking that helped to redirect cracks. Fig. 2.3b, seen previously, displayed the marked increase in both UTS and toughness of the NiTi-Al foil over control samples (Al Foil), which is a trait not typically found in particulate reinforced composites. The combined effect of a strong interface between the intermetallic phases and Al matrix as well as the aligned, roughly rectangular, shape of the particulates greatly enhanced the probability of their failure through fracture. The microvoids created by these microcracks were often small and contained by the high interface strength and ductility of the matrix. The toughening effects of these microcracks were twofold; breaking of the strong intermetallic particles released energy and promoted a highly irregular avenue for the primary crack (Fig. 2.6c). Variation in the area of the reinforcements worked to enhance this deflection, as observations indicated that a crack preferred to redirect through a close-by microvoid than contest a large particle. A successive time-lapse of increasing strain taken by SEM during the *in situ* three-point flexural observations highlighted this crack deflection (Fig. 2.6d-f). The primary crack approached an orientated cluster of intermetallic particles (Fig. 2.6d) and was redirected around this cluster. This happened several times as the crack progressed (Fig. 2.6f). With each successive alteration of the crack direction, changes in the relative mixed modes of fracture changed how the material experienced loading and consumed large quantities of energy.

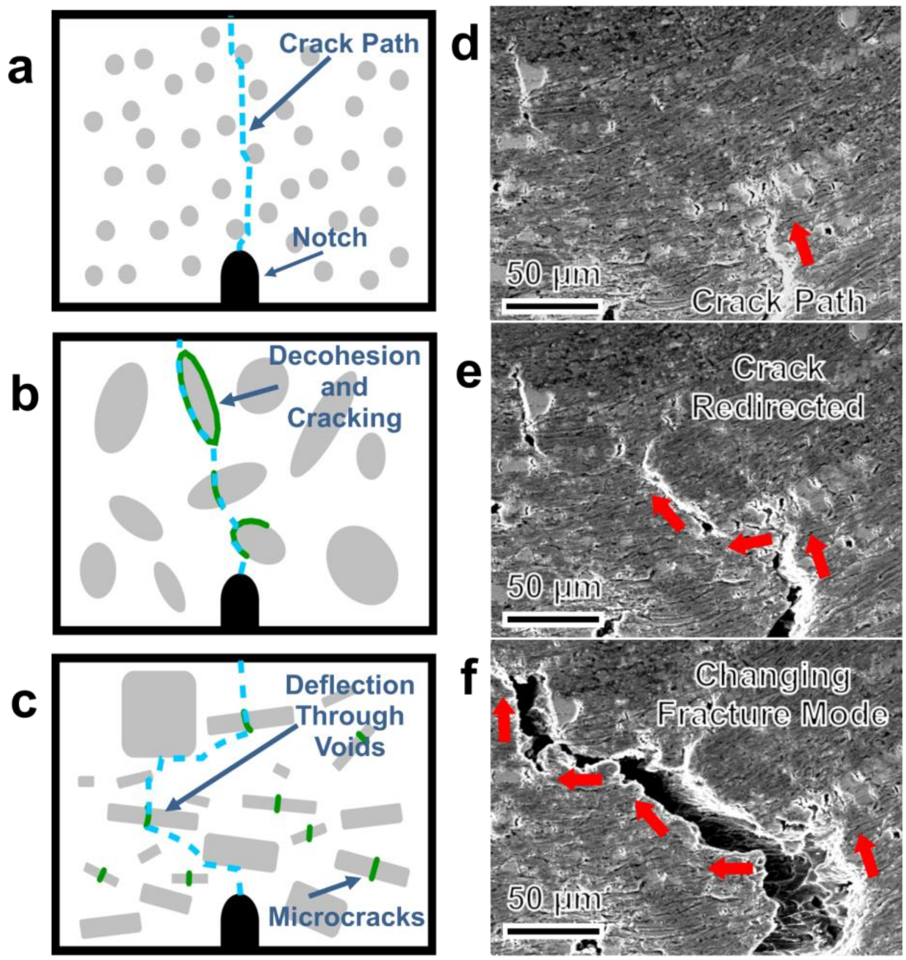

Fig. 2.6. Schematics illustrating the typical crack propagation of particulate reinforced metal matrix composites and successive SEM images showing intermetallic particles redirecting a main crack. (a) Rigid small spherical particles do little to redirect cracks. (b) Large particles often create unstable large voids that lower toughness. (c) NiTi-Al foil composites leverage a combination of layer-wise orientated elongated particles to absorb energy and redirect cracks. (d) Crack approaches a vein of intermetallic particles. (e) Crack redirects around vein to a weaker location. (f) Crack redirects again; each redirection results in a change in the relative modes of mixed mode facture.

5. *Conclusions*

By using a fresh approach to manufacture particle reinforced composites, it was possible to form specially shaped (mean of 5 µm^2) and distributed intermetallic particles having bi-level mechanical properties (reduced modulus of 130 GPa and 80 GPa for Al_3Ni and Al_3Ti, respectively) and excellent cohesion with the ductile Al matrix. The RROLM process was specifically designed to intrinsically enable the production of this organized microstructure to augment the balance of strength and toughness typically exhibited by traditional metal composites. This was demonstrated successfully with improvements in strength (~70%) and toughness (~90%) relative to the control samples. The strength (265 MPa) was found to be enhanced by a multi-scale synergy of precipitates, low energy dislocation structure formation, and large particles induced by the original NiTi nanoparticles. The likely cause of the displayed increase in toughness (3.3 MJ / m^3) was observed by an *in situ* three-point bending test under SEM. The composite exhibited massive, widespread microcracking ahead of the crack tip, relieving internal stresses and shielding the crack, as well as a significant crack deflection mechanism, steering cracks around local veins of intermetallic particles. The results of this study are in excellent agreement with the work done by *Ayyar and N. Chawla*,[20] indicating that local clusters of small rectangular-like particles organized perpendicular to a crack are exceptionally effective for increasing crack deflection and do enable improvements to toughness of particle reinforced composites.

6. References

[1] Li X, Chang W-C, Chao YJ, Wang R, Chang M. Nanoscale Structural and Mechanical Characterization of a Natural Nanocomposite Material: The Shell of Red Abalone. Nano Lett 2004;4:613–7. doi:10.1021/nl049962k.

[2] Heim FM, Zhang Y, Li X. Uniting Strength and Toughness of Al Matrix Composites with Coordinated Al3Ni and Al3Ti Reinforcements. Adv Eng Mater 2018;20. doi:10.1002/adem.201700605.

[3] Miranda G, Carvalho O, Soares D, Silva FS. Properties assessment of nickel particulate-reinforced aluminum composites produced by hot pressing. J Compos Mater 2015;50:523–31. doi:10.1177/0021998315577148.

[4] Choi YB, Matsugi K, Sasaki G. Development of Intermetallic Compounds Reinforced Al Alloy Composites Using Reaction of Porous Nickel and Aluminum. Mater Trans 2013;54:595–8. doi:10.2320/matertrans.MBW201214.

[5] Fogagnolo JB, Pallone EMJA, Martin DR, Kiminami CS, Bolfarini C, Botta WJ. Processing of Al matrix composites reinforced with Al–Ni compounds and Al2O3 by reactive

milling and reactive sintering. J Alloys Compd 2009;471:448–52. doi:https://doi.org/10.1016/j.jallcom.2008.03.125.

[6] Qian J, Li J, Xiong J, Zhang F, Lin X. In situ synthesizing Al3Ni for fabrication of intermetallic-reinforced aluminum alloy composites by friction stir processing. Mater Sci Eng A 2012;550:279–85. doi:https://doi.org/10.1016/j.msea.2012.04.070.

[7] Alexander DJ, Sikka VK. Mechanical properties of advanced nickel aluminides. In: WHANG SH, POPE DP, LIU CTBT-HTA and I, editors., Oxford: Elsevier; 1992, p. 114–9. doi:https://doi.org/10.1016/B978-1-85166-822-9.50022-4.

[8] Moussa SO, El-Shall MS, Alexander DJ, Sikka VK, Qian J, Li J, et al. In situ synthesizing Al3Ni for fabrication of intermetallic-reinforced aluminum alloy composites by friction stir processing. Mater Trans 1992;550:114–9. doi:10.2320/matertrans.MBW201214.

[9] Moussa SO, El-Shall MS. Fabrication of nanostructured nickel and titanium aluminides starting from elemental nanopowders. Mater Chem Phys 2008;112:1015–20. doi:https://doi.org/10.1016/j.matchemphys.2008.06.071.

[10] Wang F, Eskin D, Mi J, Connolley T, Lindsay J, Mounib M. A refining mechanism of primary Al3Ti intermetallic particles by ultrasonic treatment in the liquid state. Acta Mater 2016;116:354–63. doi:https://doi.org/10.1016/j.actamat.2016.06.056.

[11] Milman YV, Miracle DB, Chugunova SI, Voskoboinik I V, Korzhova NP, Legkaya TN, et al. Mechanical behaviour of Al3Ti intermetallic and L12 phases on its basis. Intermetallics 2001;9:839–45. doi:https://doi.org/10.1016/S0966-9795(01)00073-5.

[12] Yamaguchi M, Umakoshi Y. The deformation behaviour of intermetallic superlattice compounds. Prog Mater Sci 1990;34:1–148. doi:https://doi.org/10.1016/0079-6425(90)90002-Q.

[13] Abbasi Chianeh V, Madaah Hosseini HR, Nofar M. Micro structural features and mechanical properties of Al–Al3Ti composite fabricated by in-situ powder metallurgy route. J Alloys Compd 2009;473:127–32. doi:https://doi.org/10.1016/j.jallcom.2008.05.068.

[14] Nakamura M, Kimura K. Elastic constants of TiAl3 and ZrAl3 single crystals. J Mater Sci 1991;26:2208–14. doi:10.1007/BF00549190.

[15] Rohatgi A, Harach DJ, Vecchio KS, Harvey KP. Resistance-curve and fracture behavior of Ti–Al3Ti metallic–intermetallic laminate (MIL) composites. Acta Mater 2003;51:2933–57. doi:https://doi.org/10.1016/S1359-6454(03)00108-3.

[16] Wu JM, Zheng SL, Li ZZ. Thermal stability and its effects on the mechanical properties of rapidly solidified Al-Ti alloys. Mater Sci Eng A 2000;289:246–54.

doi:https://doi.org/10.1016/S0921-5093(00)00886-8.

[17] Grabel J V, Cost JR. Ultrasonic velocity measurement of elastic constants of Al-Al3Ni unidirectionally solidified eutectic. Metall Mater Trans B 1972;3:1973–8. doi:10.1007/BF02642587.

[18] Matsumuro M, Kitsudo T. Fabrication of In-Situ Intermetallic Compound Dispersed Aluminum Matrix Composites by Addition of Metal Powders. Mater Trans 2006;47:2972–9. doi:10.2320/matertrans.47.2972.

[19] Miranda G, Madeira S, Silva FS, Carvalho O. A nanoindentation study on Al3Ni interface of Ni reinforced aluminum-silicon composite. Mech Adv Mater Struct 2017;24:871–4. doi:10.1080/15376494.2016.1196790.

[20] Ayyar A, Chawla N. Microstructure-based modeling of crack growth in particle reinforced composites. Compos Sci Technol 2006;66:1980–94. doi:https://doi.org/10.1016/j.compscitech.2006.01.007.

[21] Clyne TW, Withers PJ. An Introduction to Metal Matrix Composites. Cambridge: Cambridge University Press; 1993. doi:DOI: 10.1017/CBO9780511623080.

[22] Heim FM, Zhang Y, Li X. Uniting Strength and Toughness of Al Matrix Composites with Coordinated Al3Ni and Al3Ti Reinforcements. Adv Eng Mater 2018;20:1700605. doi:10.1002/adem.201700605.

[23] Lee KJ, Nash P. The Al-Ni-Ti system (Aluminum-Nickel-Titanium). J Phase Equilibria 1991;12:551–62. doi:10.1007/BF02645068.

[24] Kovalev OB, Belyaev V V. Mathematical modeling of metallochemical reactions in a two-species reacting disperse mixture. Combust Explos Shock Waves 2013;49:563–74. doi:10.1134/S0010508213050080.

[25] van Loo FJJ, Rieck GD. Diffusion in the titanium-aluminium system—I. Interdiffusion between solid Al and Ti or Ti-Al alloys. Acta Metall 1973;21:61–71. doi:https://doi.org/10.1016/0001-6160(73)90220-4.

[26] Sujata M, Bhargava S, Sangal S. On the formation of TiAl3 during reaction between solid Ti and liquid Al. J Mater Sci Lett 1997;16:1175–8. doi:10.1007/BF02765402.

[27] Oh J, Lee WC, Pyo SG, Park W, Lee S, Kim NJ. Microstructural analysis of multilayered titanium aluminide sheets fabricated by hot rolling and heat treatment. Metall Mater Trans A 2002;33:3649–59. doi:10.1007/s11661-002-0239-6.

[28] Xu L, Cui YY, Hao YL, Yang R. Growth of intermetallic layer in multi-laminated Ti/Al diffusion couples. Mater Sci Eng A 2006;435–436:638–47. doi:https://doi.org/10.1016/j.msea.2006.07.077.

[29] Zhu K, Yu W, Aman Y, Jing T. Synthesis, microstructure and mechanical properties of a bio-inspired Ti-intermetallic multi-layered/SiCf-reinforced Ti-matrix hybrid composite. J Mater Sci 2016;51:8747–60. doi:10.1007/s10853-016-0139-6.

[30] Mishin Y, Herzig C. Diffusion in the Ti–Al system. Acta Mater 2000;48:589–623. doi:https://doi.org/10.1016/S1359-6454(99)00400-0.

[31] Huang W, Chang YA. A thermodynamic analysis of the Ni□Al system. Intermetallics 1998;6:487–98. doi:https://doi.org/10.1016/S0966-9795(97)00099-X.

[32] Frenzel J, George EP, Dlouhy A, Somsen C, Wagner MF-X, Eggeler G. Influence of Ni on martensitic phase transformations in NiTi shape memory alloys. Acta Mater 2010;58:3444–58. doi:https://doi.org/10.1016/j.actamat.2010.02.019.

[33] Hertzberg RW, Hauser FE. Deformation and Fracture Mechanics of Engineering Materials. J Eng Mater Technol 1977;99:96. doi:10.1115/1.3443416.

CHAPTER 3: MOSAIC DIGITAL IMAGE CORRELATION

1. Introduction

Often it is difficult to fully and statistically assess the structure of a composite's reinforcement phase when it is encased in matrix material, as in the case of the previously discussed metal matrix composites. However, textile composites often exhibit a textured outer surface with tow crowns extending from the surface, which contains information about the tow architecture of the outer layer (Fig. 3.1). In some composite systems with one or a few layers of braided or woven material it is potentially possible to get a statistical measure of the reinforcing tow architecture and thus, tow architecture irregularity or defects.

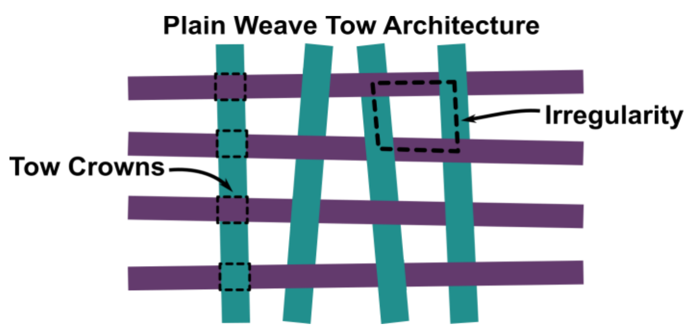

Fig. 3.1. Schematic of plain weave tow structure, highlighting tow peak or "crowns" and irregular tow contact and orientations.

Woven and braided ceramic matrix composites (CMCs) [1–4] and carbon-fiber reinforced polymers (CFRP) [5–7] exhibit mechanical properties that are very sensitive to defects in tow arrangement and fiber waviness; particularly, irregular tow spacing contributes to altered elasticity, strength and failure characteristics (Fig. 3.1). These defects are produced during the manufacturing process,[7,8] but it is unclear how they can be mitigated. Because the textile process can produce very long, intricate materials, a scalable method enabling a statistical measurement of tow architecture nonuniformity is needed.[18] This system is necessary to ensure that the tow placement and mechanical properties are uniform along the length of the part.

To enable full-field measurements of complex shaped composite surfaces a high resolution, high accuracy, and noncontact surface metrology solution must be developed to detect subtle, changes in geometry, over potentially large (> 4 m) lengths. Three-dimensional digital image correlation (3D-DIC) involves a calibration step which enables a robust geometric relationship between the two stereoscopic cameras and the ability to triangulate surface topology.[13] To quantify the full-field tow variability of complex-shaped and cylindrical components, it is necessary to combine multiple local measurements into a single, global coordinate system. A new technique called "Mosaic DIC" (M-DIC) was developed that automates this process by efficiently and robustly computing the spatial transformations required to tile multiple local 3D-DIC measurements into a single, comprehensive "mosaic" of the entire surface profile. Provided that there exists some overlap in the image pairs (Fig. 3.2) corresponding to adjacent local measurements, and the sample undergoes strictly rigid body motion, 3D-DIC displacement measurements can be decomposed into translation and rotation components that relate the multiple frames of reference. This technique is valid for arbitrary motion between frames and can be used to efficiently reconstruct (Fig. 3.3) and measure intricate geometric shapes, including cylinders. By performing 3D-DIC analysis in sections, versus a traditional, single measurement, the resolution of this stereo optical technique can be extensively enhanced to meet the need of a robust, quick, precise, and accurate surface metrology solution for large, high aspect ratio surfaces.

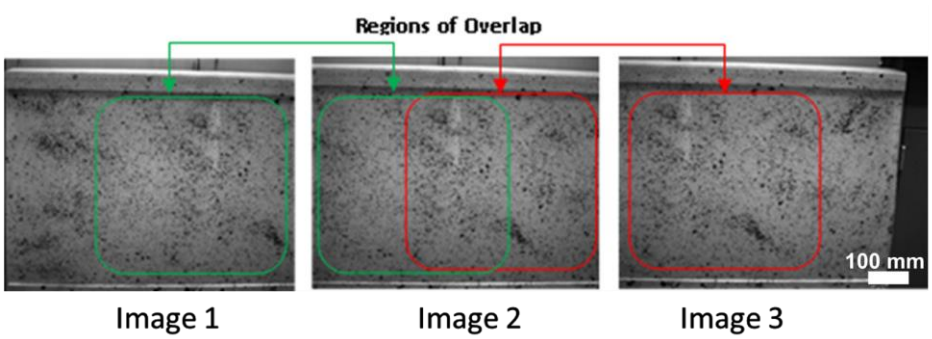

Fig. 3.2. Schematic of how regions of overlap relate for consecutive DIC images.

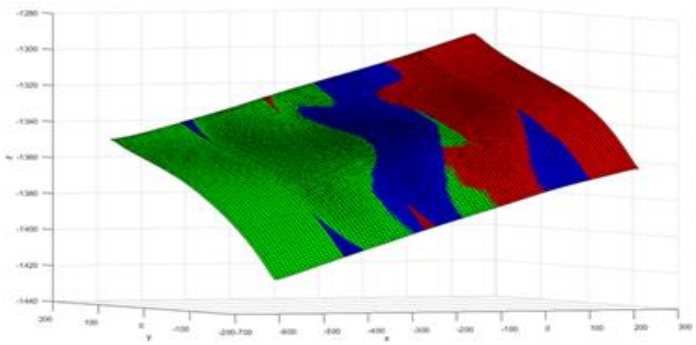

Fig. 3.3. Red, blue, and green represent separate local 3-D surfaces combined into a continuous composite surface profile.

2. M-DIC testbed

The scalability of DIC measurements allows for laboratory-scale experiments to be used to quantify the magnitudes of errors in the proposed surface metrology solution. These experiments were carried out over several testbeds, each contributing uniquely to a specific end goal; their specific functions and end deliverables will be discussed later. Errors intrinsic to 3D-DIC and errors unique to our solution have been considered and collected into three categories: system error, spatial distortion error, and transformation error. Improving the resolution of the M-DIC solution will involve finding techniques of minimizing these errors; this is discussed in detail here. By performing analysis of these controllable testbeds, it is possible to study and find methods to reduce the three different error categories, and a superior measurement system can be developed.

Multiple testbeds, shown in Fig. 3.4, were developed to demonstrate and characterize the accuracy, precision, and robustness of the proposed 3D-DIC measurement technique. Collectively, they demonstrated the ability to measure 3D surfaces, enabled the development of a technique to combine local 3D surface data, allowed for the assessment of the intrinsic accuracy of 3D-DIC, and provided grounds to improve the accuracy of a compiled 3D-DIC solution.

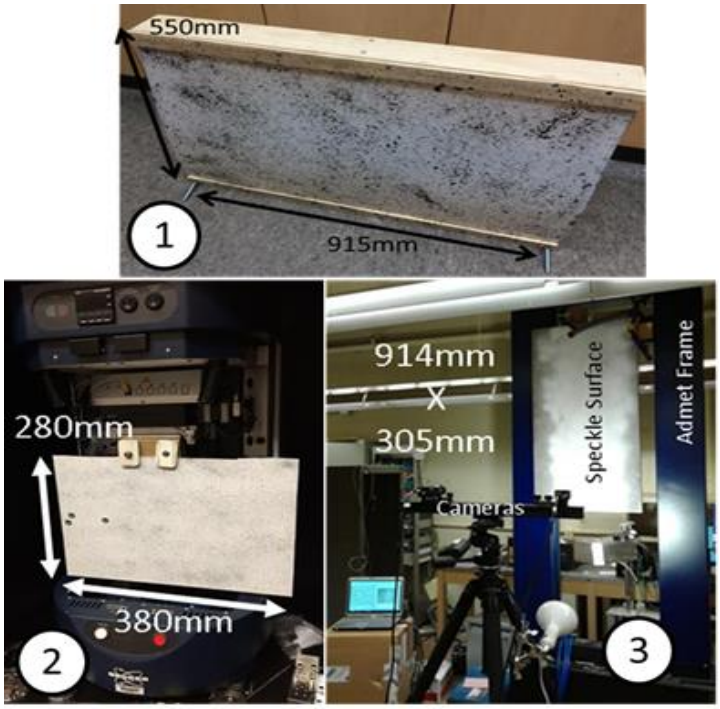

Fig. 3.4. Setup of three constructed testbeds.

Testbed 1 consisted of a rectangular wooden frame securing a sheet of white nylon. This surface was used to demonstrate the feasibility of reconstructing a complete surface profile from three image pairs and corresponding DIC analyses to create the surface seen previously in Fig. 3.3. Twenty images were taken at the center of the speckle pattern to reveal the artificial displacements detected by the DIC system with zero actual displacement. The surface was coated with two different speckle patterns, one with a speckle diameter of approximately 18 mm and the second with speckles near 9 mm in diameter to assess the effects of speckle size and subset size on the standard deviation of the recorded displacements. This testbed was also used to initially detect the existence of significant spatial distortion in the DIC recorded displacements.

Testbed 2 was constructed with the desire to accurately study the spatial distortion present in the DIC measurements and develop a complete model to correct the distortion generated by 3-D rigid body motion of the speckled surface. To accurately model the distortion, the speckled surface needed to be rigid and heavy to reduce potential vibrations and to be precisely translated in all three directions of motion. The setup was contained in a Bruker Tribometer that had a displacement accuracy of approximately 0.001 mm and consisted of an aluminum plate that carried the speckle pattern, with nominal diameter of 1 mm, and a steel weight bolted to the plate to reduce vibrations. The tribometer allowed for 75 mm of displacement in the horizontal and vertical directions and 100 mm of displacement for the out of plane direction. With this testbed a systematic approach for creating distortion models in all three directions of motion was accomplished.

Testbed 3 was constructed to study the effects of image overlap on the accuracy of the composite surface profile. The speckled surface consisted of a sheet of glass that was chosen for its stiffness and high relative flatness. This surface was speckled with a nominal diameter of 1 mm and was carefully hung from the arm of an Admet universal testing machine, with displacement accuracy of 0.5 mm, and imaged in sections. This testbed enabled an experimental study of the effects of percent overlap between the consecutive images on a known shape geometry. The Admet also allowed for a reliable single translation direction, which enabled a single direction of motion distortion model to be constructed for the glass surface.

3. Results and discussion

3.1. Assessment of M-DIC errors

To obtain robust composite tow architecture information, the accuracy and precision of M-DIC must be methodically tested and all sources of measurement error be accounted for. The first step toward this is to determine magnitudes of the main error sources. Fortunately, for a solution whose core relies on digital images and a surface speckle pattern, scaling the measurement process is as simple as scaling the speckle size with the pixel height of the images taken. However, this may actually be more challenging in practical applications as errors will increase in size and other situational errors may become more prominent, such as camera and surface vibrations. With that research scope consideration, the current key research challenge presented by larger (>4 m) surfaces is that an increase in measured surface dimensions will also increase the magnitudes of error, and as surfaces get longer more local surfaces will need to be combined together, which will increase errors that propagate.

These scalable errors can be separated into three categories: system error, spatial distortion error, and transformation error. Errors intrinsic to DIC measurements will be lumped into system error; this will include errors induced by many sources, including the cameras, DIC algorithm, lighting, speckle quality, and lens focus. Spatial distortion error is the variation in the apparent displacement measurements between DIC image pairs; this is mostly dependent on the choice of lenses and their setup parameters, such as focus and aperture. Errors associated with the numerical computation of the transformation between consecutive surfaces are categorized under transformation error. In this section, the order of magnitude of each error relative to each source is found according to Table 3.1. Finding methods to reduce these errors and understanding how they will propagate will be the main focus of the following section.

Table 3.1. Relative importance of each M-DIC error source.

Error type	Relative order of magnitude
System	10
Spatial Distortion	100
Transformation	1

3.1.1. System error

Noise detected in DIC measurements is of great concern to the research community, who commonly uses this technology for surface-wide strain measurements;[13–15] therefore, much research on this topic has already been completed.[16,17] Here we are defining system error as the artificial displacements outputted by DIC when multiple images of the same target sample are taken with zero actual displacement; these have a Gaussian distribution. From literature, it is clear that the DIC correlation related errors that are present in any DIC system can be separated into systematic errors and statistical errors.[18,19]

Systematic errors are typically small in magnitude and are typically overshadowed by statistical errors. They are a result of the method in which the true speckle pattern is converted into CCD pixels by the cameras and the limited accuracy of the linear distortion model for subsets, which is worse for heavily curved surfaces or surfaces with large dimensional gradients.[19] Systematic errors, typically called the mean-bias error, have a sinusoidal shape as a function of sub-pixel displacement; the amplitude of this error has a relationship with speckle pattern quality and calibration scores.[18–20] If a high-quality speckle pattern and calibration are used, systematic errors can be minimized.

The statistical errors are random and occur largely because of the limited number of pixels in an image and the limited range of available gray values that correspond to a speckle.[19] To reduce statistical errors, a high contrast speckle pattern is desired to increase the span of available gray values and high-resolution images to increase the number of pixels composing a speckle. Statistical errors can also be reduced by adjusting the subset size; standard deviation of displacements will decrease exponentially with increases in subset size (Fig. 3.5). However, there is a trade off when adjusting subset size, which relates to the size of the chunks that the images are split into and analyzed. Too large will result in less spatial resolution as local deformation will be smoothed, and too small will result in large noise in the measurements.

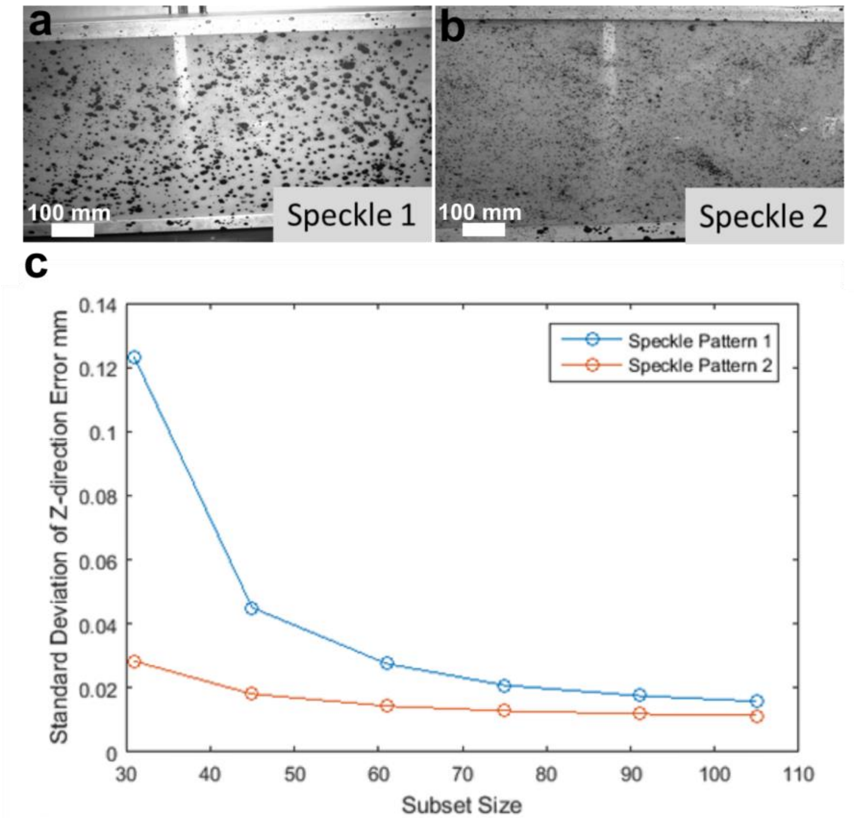

Fig. 3.5. Relationship between speckle quality, standard deviation of out of plane displacement, and subset size. (a) Coarse speckle pattern, with nominal diameter of 18 mm. (b) Fine speckle pattern, with nominal diameter of 9 mm. (c) Comparison plot.

System error is, therefore, dependent mostly on the cameras, subset size, and speckle pattern. The Point Grey cameras used are a constant in all experiments performed and are considered to be sufficient to minimize the error they add into the DIC system. Speckle pattern quality is considered to be a variable that will need to be controlled to develop a robust surface metrology system; since the system error predominantly depends on pixel information, estimates of the magnitude of the system error can be easily scaled up from a few millimeters to tens of meters. A unit pixel represents some physical measurement, and the size of this physical measurement can be increased without any change to the how the pixel is analyzed by the DIC software. Therefore, if the artificial displacements are normalized by the physical height of a sample, they can be directly scaled to estimate the system error of a larger sample with an identical speckle pattern quality.

3.1.2. Spatial distortion error

Imaging with lenses will result in lens distortion artifacts in the recorded images. The magnitude and shape of the spatial distortion changes with different lenses, aperture settings, and focal planes. For a system that tracks the location of speckles from image to image, distortion affects the accuracy of displacement fields detected. This is most apparent in rigid body translations of a sample (Fig. 3.6). VIC-3D from Correlated Solutions (the DIC software used exclusively in this dissertation) contains distortion correction models that significantly reduce the magnitude of the spatial distortion, but there is still residual distortion present (Fig. 3.6) even after implementing VIC-3D's best correction.

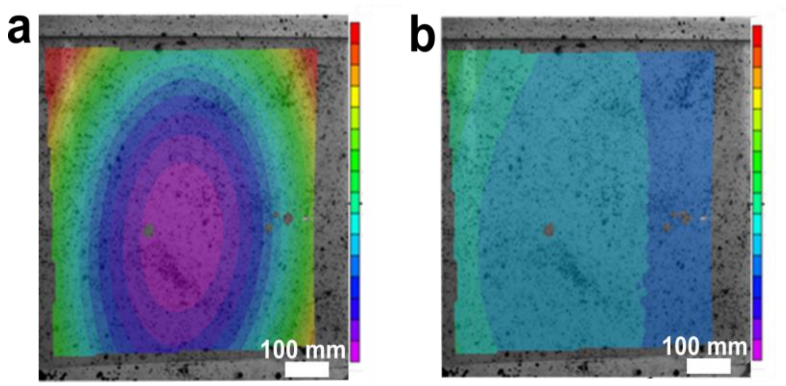

Fig. 3.6. Rigid body translation to the left results in significant distortion in the recorded spatial displacement. (a) Horizontal displacement with no applied distortion model. (b) Horizontal displacement with VIC-3D's third order distortion model applied. Note: color bar scales are the same for both images.

Spatial distortion in DIC measurements has distortion components in each direction of motion and each direction of motion will cause distortion in the other two (Fig. 3.7); therefore, for complete 3-D motion, there are nine components of distortion, which can be combined into a single model for each direction. Examples of these distortion fields can be seen in Fig. 3.7 for an in-plane, horizontal translation. Because the shape and magnitude of distortion depend on many situational variables it is impractical to predict how each will affect the distortion fields. However, it is easy to consider that if the lenses, aperture settings, and focal plane all remain physically the same for a given camera system and the speckle patterns are of identical quality the distortion magnitude will scale with image dimensional height. This will likely never be the case in practical applications, but it serves as a useful estimation for the scaling of these errors from small to larger surfaces.

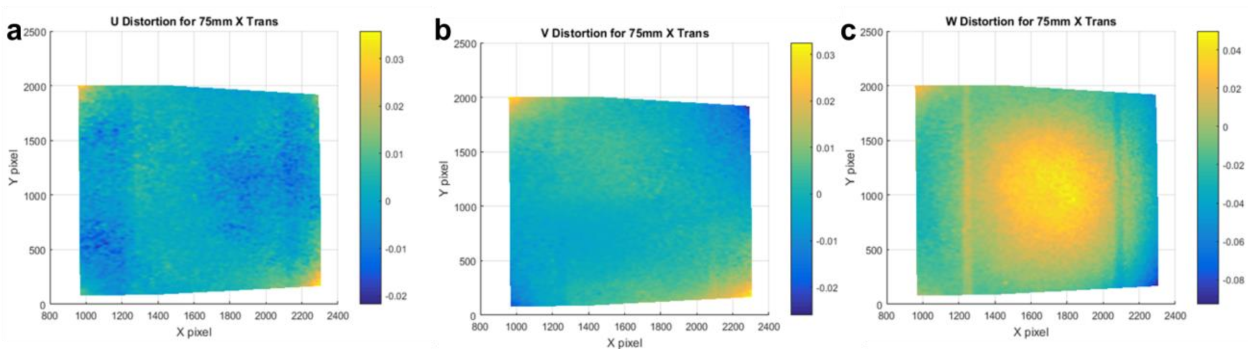

Fig. 3.7. The X, Y, and Z distortion error in mm, respectively, for a 75 mm translation in the X direction for a sample of height 225 mm. (a) U distortion. (b) V distortion. (c) W distortion.

3.1.3. Transformation error

To construct a complete surface profile of a tubular, high aspect ratio, or other complexly shaped sample, multiple images and DIC analyses are done along the greater sample dimension. The DIC analyses are done progressively along the long dimension, creating consecutive 3-D maps of the corresponding surface. These are then combined together into a single coordinate system to create a continuous surface profile. To do this requires coordinate transformations. Reference and deformed coordinates are correlated by the DIC system; practically, these would be used after spatial distortion correction. These two lists of data coordinates are then feed into a least-squares transformation function using a singular value decomposition technique. The methodology used stemmed from Arun[21] and Challis[22] and was programed in MATLAB. A brief description of the procedure taken in this function follows; a mathematical representation of this procedure is given in Chapter 4.

First the two point clouds are read into MATLAB, and their centroids are found. The covariance matrix is then computed by shifting both centroids to the origin. This leaves the difference between the two point clouds as a rotation. The covariance matrix is then decomposed using singular value decomposition. Two components of decomposition are then used to construct the best rotation matrix, in which considerations must be made for a special reflection case to prevent mirroring. With the rotation matrix found, the translation matrix is simply found by rotating the deformed centroid by the rotation matrix and then finding the difference between this and the reference centroid.

The accuracy of the transformations computed will be affected by the number of data points in each cloud. For stitching together local surface profiles, this means that the percentage of overlap between the consecutive images will affect the accuracy of the transformation. To quantify this effect a numerical study was done in MATLAB to model the effects of percent overlap, displacement magnitude, and inputted Gaussian noise.

First a given set of coordinate data is generated based on a function that approximates a real, curved surface. This data set is then rotated and translated by an input rotation and translation matrix; Gaussian noise with a particular user defined standard deviation is then added. This creates a set of coordinate points that represents a deformed surface with noise from the DIC system. The aspect ratios of the data sets were varied to reveal how the effective percentage of overlap in corresponding real images is affected by random noise. For a particular magnitude of added Gaussian noise, 2000 transformations were computed. The standard deviation of the 2000 computed translation matrices was then computed and compared with the inputted Gaussian noise and the percent of data set overlap. The results of this study, normalized by the height of the undeformed data set can be seen in Fig. 3.8. This study showed that the standard deviation of the translation matrices increases linearly with inputted standard deviation of Gaussian noise. The slopes of the linear trends are inversely proportional to the square root of the percentage of overlap as seen in Fig. 3.8b. This trend indicates that more percent overlap results in more tolerance to data noise for the computed transformation.

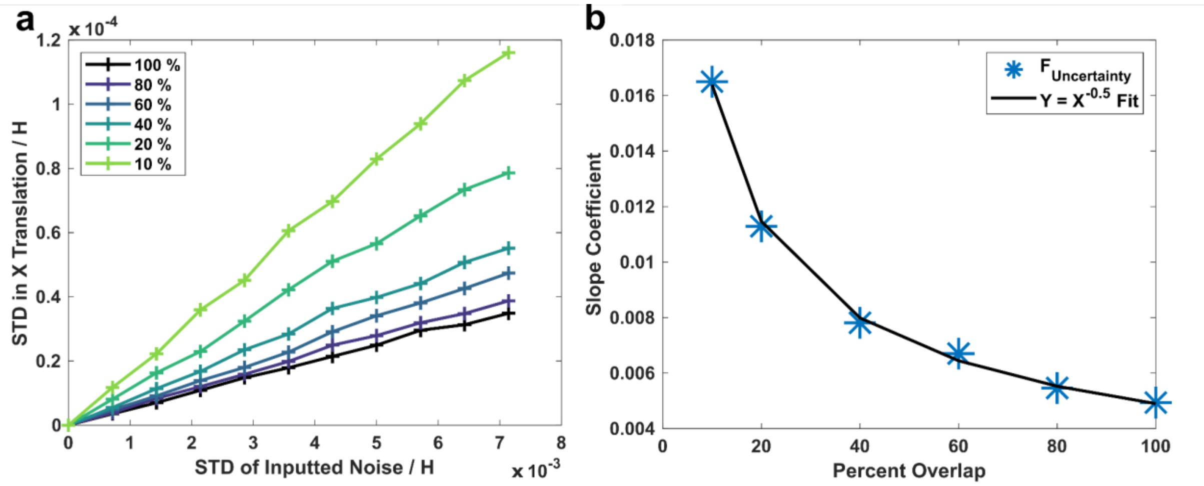

Fig. 3.8. Plots of overlap study. (a) Plot of the relationship between data noise and the noise in the computed transformation for multiple percent overlaps between consecutive images. (b) Plot of relationship between percent overlap and rate at which increases in data noise increases transformation noise.

Critically, the standard deviation found in the translation matrix is almost two orders of magnitude smaller than the standard deviation of the added random noise. The error induced by the transformation is much smaller than the errors induced by the DIC system and spatial distortion. However, the error in the transformation is a function of the magnitude of the other two errors as inputted noise, and as those two errors scale up with larger sample surfaces, error in the computed transformation will also scale up in magnitude.

3.2. Evaluation of M-DIC error reduction schemes

A DIC surface profiling solution with high resolution necessitates that multiple smaller, local surface profiles be precisely combined to compose the full surface. For high aspect ratio profiles, it is expected, and later demonstrated, that the error compounded by combining the surfaces will be greatly lower than the effective resolution if the profile were constructed from a single image pair. Therefore, it is of critical interest to investigate methods of reducing the other two sources of error (system and spatial distortion), to in effect reduce the error in computed transformations, which would potentially compound as multiple surfaces are stitched together. The goal is to improve the precision and accuracy of the DIC measurements so that sub-millimeter features can be detected.

3.2.1. Reduction of system error

System error that depends predominantly on the quality of speckle pattern will scale directly with the physical height of a recorded sample. It is desired to reduce the magnitude of this error to improve the precision of DIC generated surface measurements and to reduce the noise affecting the calculated transformations used in combining these local surfaces. A simple improvement of speckle quality can reduce the system error for the same subset size significantly; shown here with a ~60 % reduction (Fig. 3.9).

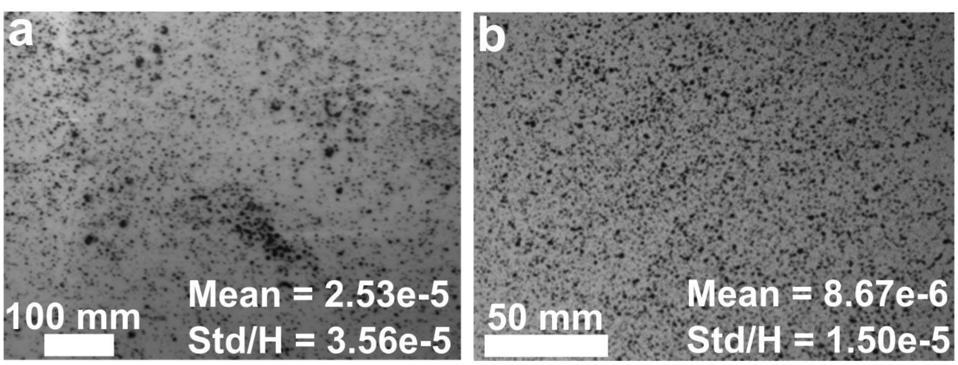

Fig. 3.9. Images of speckle patterns. (a) Represents a speckle of moderate quality, with nominal diameter of 9 mm. (b) Represents a speckle of high quality, with nominal diameter of 1 mm. Significant improvements (~60 % reduction) in the image height normalized standard deviation can be accomplished by improving speckle quality.

The majority of the system error is statistical in nature, so averaging multiple DIC outputs of identical, “zero” displacement conditions is effective at reducing random noise. This can be accomplished by taking multiple stereoscopic images of the same location on a sample. Instead of averaging the gray-scale values of the images, it is preferred to average the DIC outputs associated with each left and right image pair as this will minimize the noise from the complete DIC system, including the DIC algorithm.

The DIC outputs of the same location are not necessarily in the same order and typically have a slightly different number of data points, so care must be taken in finding the average of each data point. All of the DIC outputs can be related by creating an index with the reference data coordinates; matching this index throughout the outputs ensures that the same locations are being averaged together regardless of the order of the data points in the DIC output files. The relationship between the standard deviation of the displacements of the averaged DIC output and number of outputs included in the averaging can be seen in Fig. 3.10.

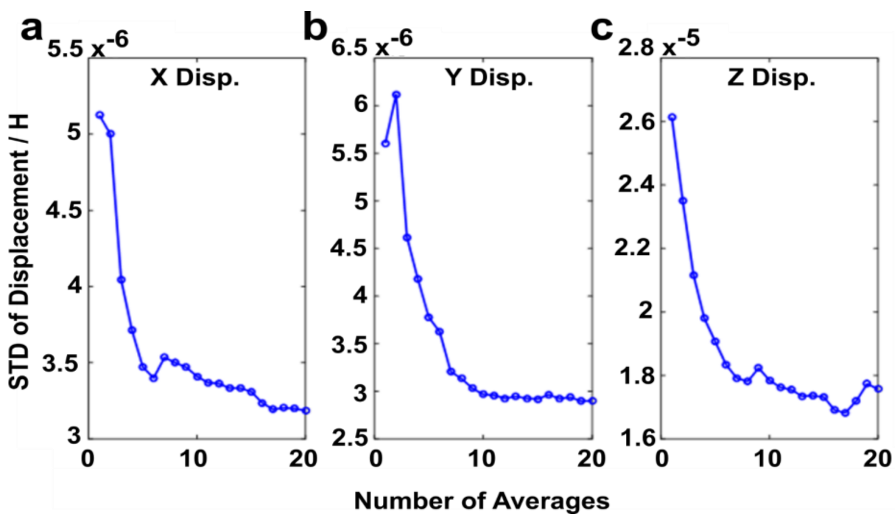

Fig. 3.10. Standard deviations normalized by sample height for “zero” displacement DIC correlations are reduced by averaging. (a) X, (b) Y, (c) Z.

Because increasing the number of images will proportionally increase imaging time, computing time, and required data storage space, it is necessary to balance the increased benefits with the additional resources needed. With this in mind, the results displayed in Fig. 3.10 indicate that an average of around ten DIC outputs is sufficient to get the majority of the benefits from averaging, which is a reduction of the standard deviation by about forty percent. It is important to note that noise in the out-of-plane direction or Z direction is about an order of magnitude larger than that of the other two directions. Reducing the system error is crucial for improving the precision and accuracy of a DIC solution, because the noise in the DIC measurements reduces the resolution in the Z direction. The contrast and quality of the speckle pattern will also play a large role in affecting the noise of the DIC measurements, so to minimize the noise before averaging an optimal speckle pattern should always be used.

3.2.2. **Reduction of distortion error**

For purely rigid body motion the DIC recorded displacements should be completely uniform over the entire correlated surface. As shown previously, this is not typically the case because of lens distortion. The VIC-3D software used exclusively in this research has a built-in distortion model that is calculated during the calibration process; this is usually sufficient to remove the majority of distortion. However, with the use of wide-angle lenses residual distortion may be significant, and since distortion will affect the accuracy of M-DIC, it must be studied and potentially minimized further. A common technique to develop a model of the distortion affecting digital imaging systems is to apply a known magnitude of rigid body motion to a sample, and then study the shape of the apparent displacement field.[23–25] True rigid body motion should result in a planar displacement field. With the magnitude of the actual displacement known, rigid body motion can be subtracted from the apparent displacements and what remains will be the distortion in the system. The methodology used to find, model, and remove spatial distortion was largely inspired by *Kammers et al.* [24], which explains, the procedure to remove drift and spatial distortion from SEM images. An explanation of the developed procedure follows.

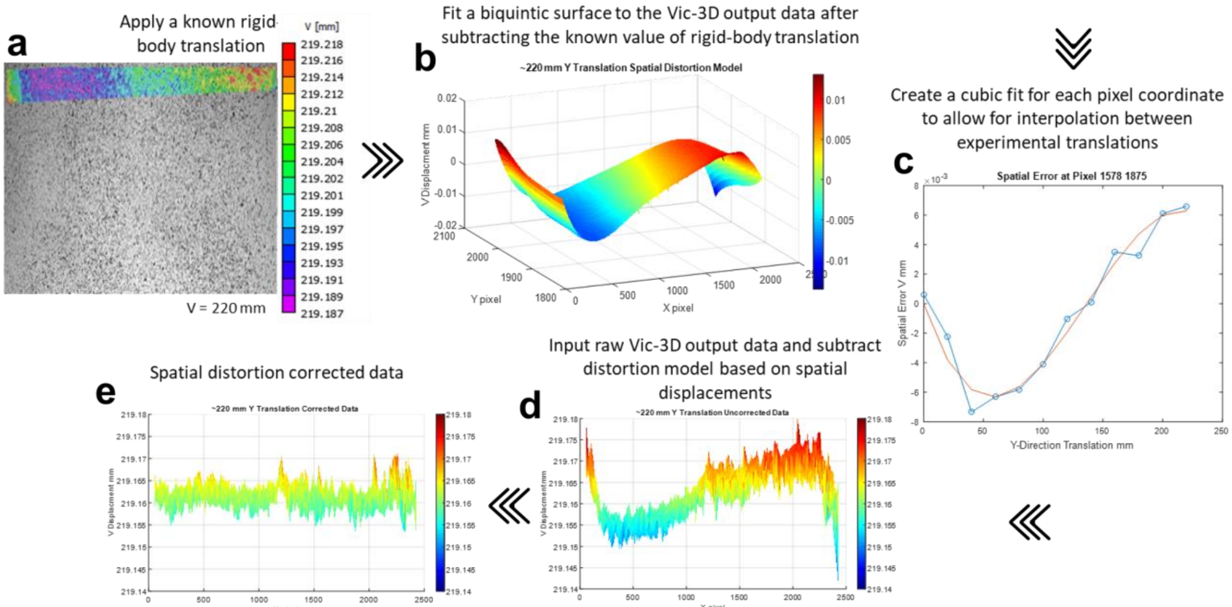

Fig. 3.11. Illustration of the process used to correct the Y displacement field for a Y direction displacement of 78 % of the image, sample height. (a) Correlate rigid body transformation dataset. (b) Generate surface fit of given translation field. (c) Generate interpolation between translations per pixel coordinate. (d) Input experimental dataset for correction. (e) Obtain spatial distortion corrected dataset.

First, data for creating a distortion model must be collected (Fig. 3.11a); Testbeds 2 and 3 enabled accurate displacements to be imposed on a speckled sample. For a complete model for all ranges of motion, the sample must be displaced incrementally and imaged in all three directions of motion. Multiple image pairs can be taken at each imposed displacement for averaging of the DIC outputs. With data collection completed, this information will be analyzed by VIC-3D in one step for each direction of motion; this results in spatial displacement measurements from the original reference image. The DIC outputs are averaged for the same imposed displacement to reduce statistical noise in the model. For each displacement field, with the known rigid body motion removed via a planar fit, the spatial data points are plotted with respect to the X and Y pixel coordinates. A biqunitic surface is then fit to each of these displacement fields (Fig. 3.11b). This results in a distortion value for each pixel coordinate for all the known, imposed displacements. At each pixel the relationship between displacement magnitude and distortion magnitude can be fit to a cubic line (Fig. 3.11c). This will allow for interpolation between the imposed displacements. This must be done for each direction of motion desired; therefore, resulting in a total of nine distortion values for each pixel, three coming from each direction of motion. The nine distortion values can later be summed with respect to the displacement direction in which the correction needs to be applied, resulting in three complete distortion models, one for each direction of motion. This complete model, in the form of nine cubic fit coefficient vectors for each pixel can then be saved and used to correct a full surface imaged by the exact same camera setup (Fig. 3.11d). This will be done by subtracting the combined distortion model for each pixel from the displacement measurements. Therefore, at each pixel, each displacement in all directions of motion will be corrected for spatial distortion (Fig. 3.11e). These corrected displacements are then added to the original reference data coordinates to obtain corrected “deformed” data coordinates, which are used to compute the necessary transformations to combine local surface profiles.

The distortion model creation process adds many steps in the M-DIC measurement technique, but the added improvement in the surface measurements is potentially substantial in the case of wide-angle lenses (Fig. 3.12a). The effective deviation from the rigid body displacement value has been effectively reduced by an additional ~85% from VIC-3D’s third order reduction for a displacement field in the same direction as the main translation that occurred (Fig. 13.12b). This correction helps to remove distortion that will affect each local surface measurement and will likely propagate in transformation error as the transformation uses edge information, which is what is typically distorted the most. It should be noted that when applied to higher magnification, narrow angled lens, such as the “50 mm” lens, the improvements become marginal considering the extra experimental and computational time needed to perform this correction. The 50 mm lenses, with specific details in the methods section of each Chapter, were used for the nearly all other measurements in this dissertation.

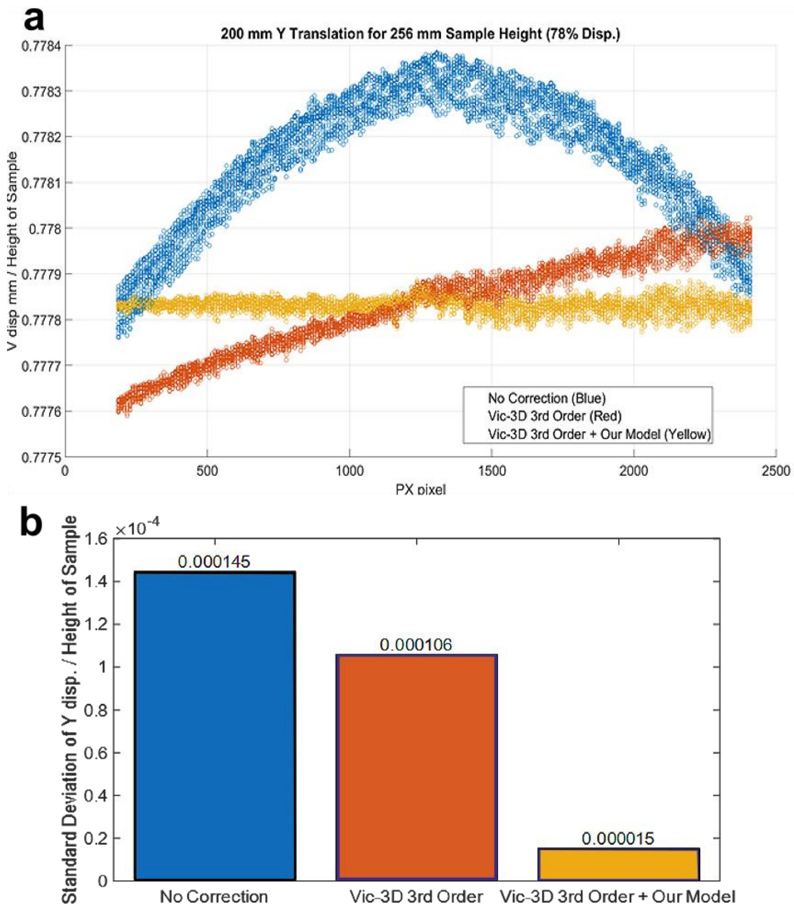

Fig. 3.12. Comparison of distortion models. (a) Comparison plot of the Y direction (V) displacement field for local surface measurements made with no correction, VIC-3D’s third order correction, and VIC-3D’s third order correction with the addition of the developed model. (b) Bar chart of the normalized by image height standard deviation of the Y direction displacement field for a 78 % image height displacement in the Y direction (200 mm of 256 mm). All shown displacement fields have been averaged over 5 DIC outputs to reduce statistical noise and were measured with a 35 mm lens.

3.2.3. Reduction of transformation error propagation

As shown in the previous sections, the error in the DIC measurements is dominated by the system error and spatial distortion error, but it is necessary to understand how the transformation error will propagate over several transformations. Numerical simulations and testbed experiments were done to understand this phenomenon. The procedure outlined in Fig. 3.13 represents the methodology used in the numerical simulations.

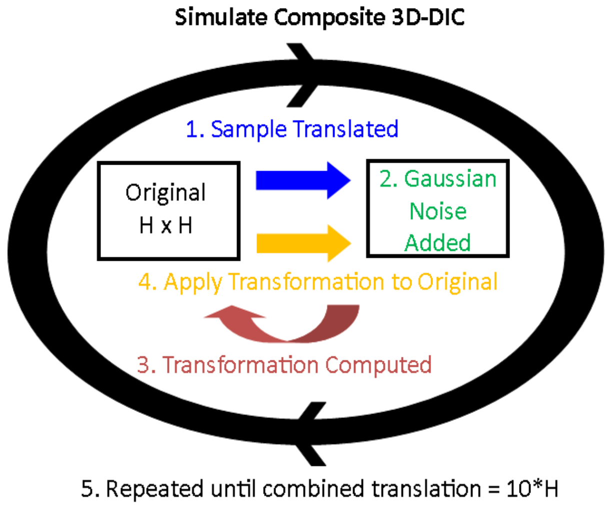

Fig. 3.13. Illustration of the procedure used to simulate the effects of the transformation error on M-DIC composited surfaces.

The original sample shape used in this study was a three-dimensional, flat square plane, so deviations from expected values would be clearly defined. The procedure stated in Fig. 3.13 was repeated for Gaussian noise inputs with a standard deviation ranging from zero to one, in 0.1 increments. This procedure was then repeated 2000 times to gain a statistical understanding of how the combined surface will deviate from the true surface as more transformations are used to bring surface coordinates into a global coordinate system. A schematic explanation of the desired result can be seen in Fig. 3.14. This was done for 80, 60, 40, 20, and 10 percent overlap regions to effectively study how the number of needed transformations to achieve a certain compiled sample length affected the total standard deviation of the composite surface. In other words, do the benefits of increased percent overlap induce less noise over a M-DIC combined surface, with an aspect ratio of ten, or is less total error induced by fewer transformations being applied?

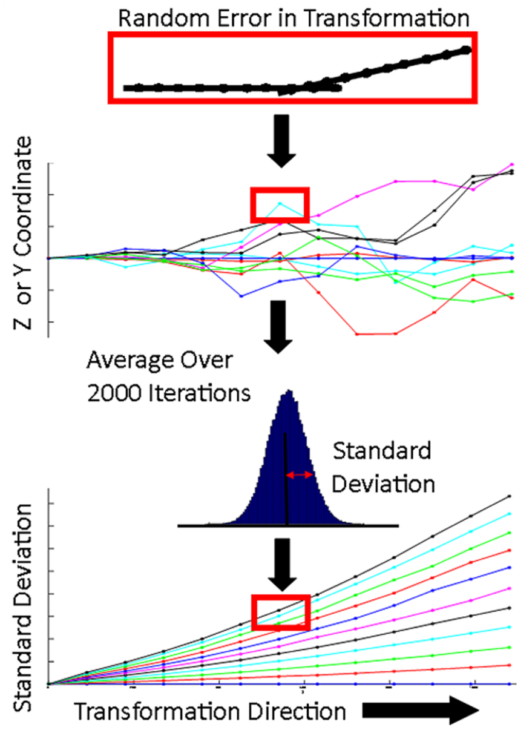

Fig. 3.14. Random error in each transformation will cause a random deviation from the expected planar shape. This deviation always has a random direction and, therefore, has a Gaussian distribution if combined over 2000 iterations. The standard deviation of this distribution can then be used to understand the expected magnitude of deviation as more transformations are done on a set of data coordinates.

The results of these simulations are summarized in Fig. 3.15; for clarity, only one data point from the planar surface is displayed. The shape of the X direction is a horizontal parabola (Fig. 3.15a) and the shapes of the Y and Z direction normalized standard deviation are vertical parabolas (Fig. 3.15 b-c). The necessary conclusions drawn from this study are that the Z (out-of-plane) direction, for all percent overlaps (Fig. 3.15c) and all inputted noise levels, has the largest magnitude relative to X and Y; this comparison is displayed in Fig. 3.15a-c, which displays X, Y, and Z normalized standard deviations for 40 percent overlap. Additionally, for all X, Y and Z directions the higher the percent overlap, the higher the normalized standard deviation; this comparison is displayed in Fig. 3.5d-f, which displays the Z direction normalized standard deviation for 80, 60, and 20 percent overlaps. This indicates that if DIC measurements have significant noise, it is better to decrease the percent overlap.

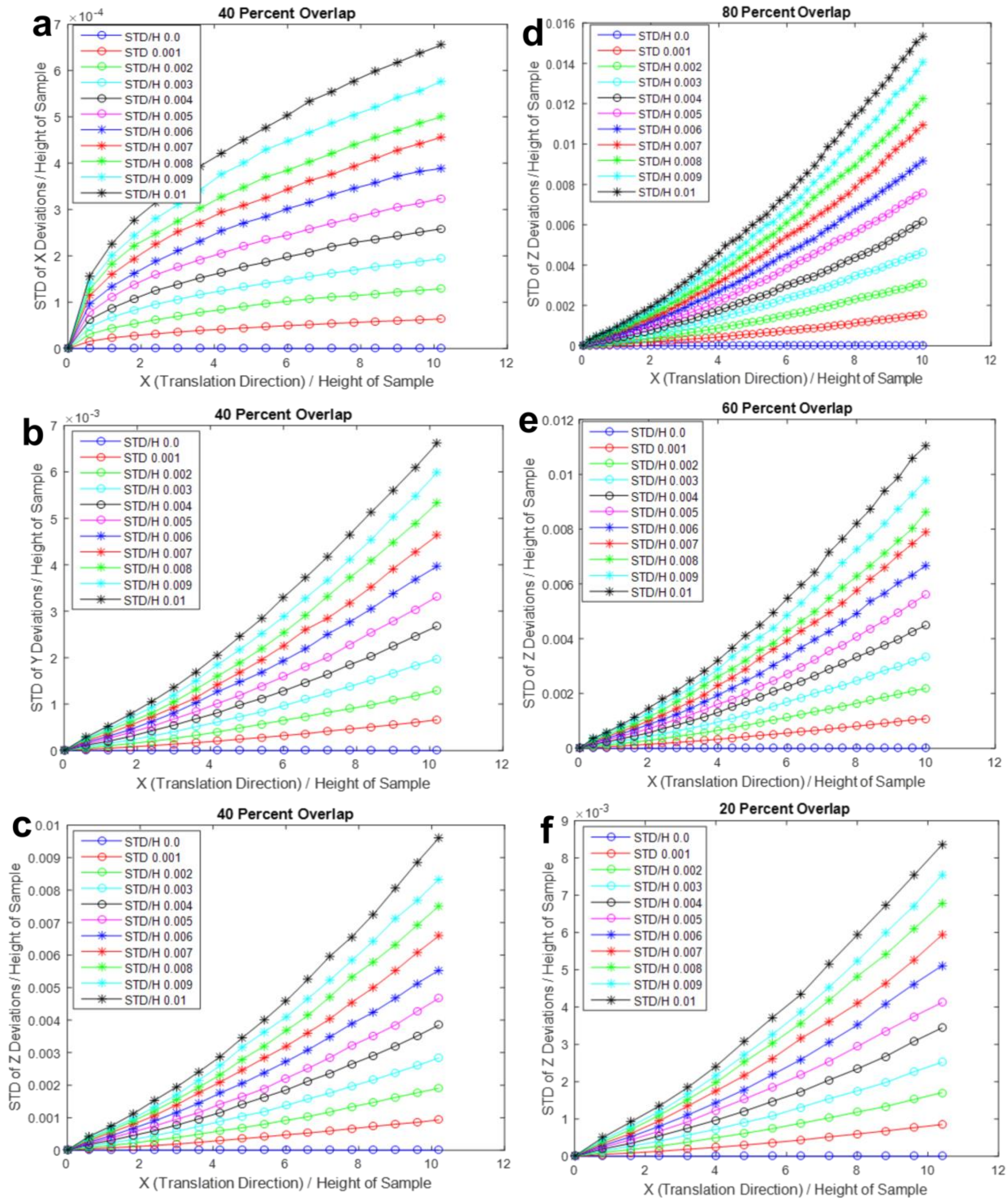

Fig. 3.15. Summarized plots of transformation error study. (a-c) Represent the X, Y, Z normalized standard deviation for 40 % overlap, respectively. (d-f) Represent the Z normalized standard deviation for 80, 60, and 20 % overlap regions, respectively.

An experimental study, completed separately from the numerical simulations, was also done. Testbed 3, which was a flat glass pane, was used for this, in which 83, 65, 47, and 29 percent overlap regions were studied (Fig. 3.16a). All results are seen in Fig. 3.16a for both no correction and a 3rd order correction applied in Vic-3D. Summarized, more pertinent results are presented in Fig. 3.16b. An analytical model of the bending of the glass, due to being hung from the arm of the Admet universal tester, is presented as an exact physical model of the glass shape (Fig. 3.16b). A single image reconstruction of the whole surface is also presented to demonstrate the improvement in resolution of a composite surface over a single image surface with the same speckle pattern. These results indicate that the smaller overlap regions result in a more accurate model, with a maximum difference of 0.07 mm (Fig. 3.16b), of the complete surface; this result is in agreement with the numerical simulations performed. In summary, for both numerical and experimental studies, this indicates for M-DIC measurements, the out-of-plane surface height dimension is most affected by the transformation error, and the selected percent overlap between the images should be minimized to reduce the number of transformations applied to combine the local surface profiles, which minimizes the error in the complete surface profile.

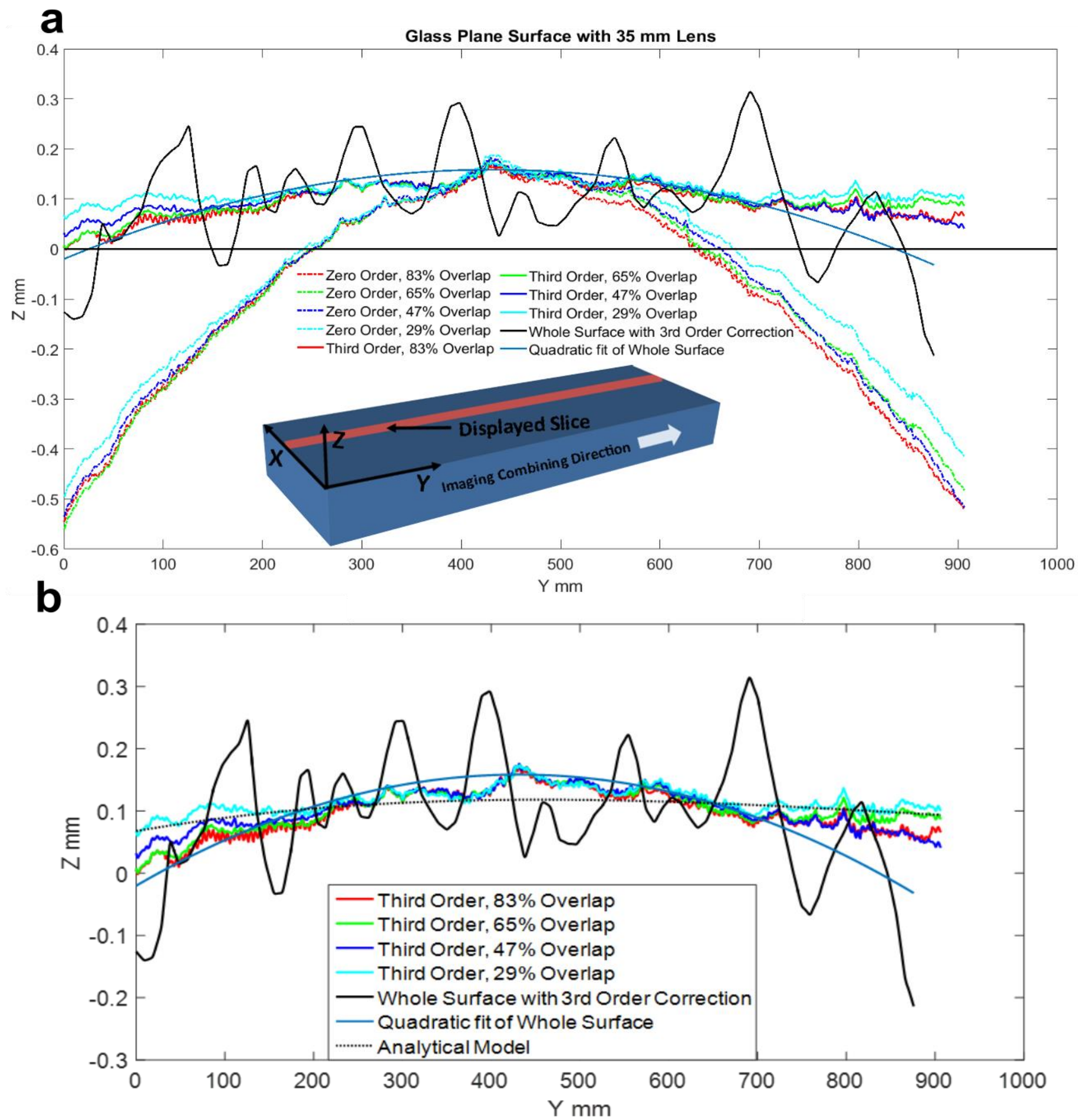

Fig. 3.16. Comparison plots of the surface as constructed with different percent overlaps. (a) All results. (b) most pertinent results. Each of the generated composite surfaces was constructed with an average of 5 DIC outputs; the whole surface was constructed with an average of 15 DIC outputs.

3.3. Development of surface-pattern quality assessments

Previously shown results indicate that with low distortion lenses and with radial distortion models, spatial distortion in DIC measurements can be significantly reduced. Therefore, system error becomes the dominate source of error. Shown results demonstrated the importance of speckle quality for reducing system error. Therefore, finding a quantification of speckle quality is of importance to all DIC research tasks.

The quality of a speckle pattern depends on numerous physical characteristics, such as average speckle size, uniformity, the number of speckles, and the digital recording of that pattern, which is affected by situational parameters such as the grade of camera, lighting, and lens focus. Literature has provided many examples of researchers doing comprehensive studies on how the accuracy of DIC measurements is affected by speckle quality. Pan *et al*. [20,26] demonstrated both a local and global quality parameter named the sum of square of subset intensity gradients (SSSIG) and mean intensity gradient (MIG), respectively, that indicate speckle quality. The two parameters are closely related as the MIG is a scaled-up version of the SSSIG. It is therefore easy to apply the MIG both locally or globally; therefore, it is the parameter of choice that will be utilized to develop a surface pattern quality assessment function. The mean intensity gradient is defined as:

$$MIG = \sum_{i=1}^{W} \sum_{j=1}^{H} \frac{\left| \sqrt{f_x(x_{ij})^2 + f_y(x_{ij})^2} \right|}{W\ x\ H} \tag{3.1}$$

where W and H are the image height and width in units of pixels, $f_x(x_{ij})$ and $f_y(x_{ij})$ are the X- and Y-directional intensity derivatives at pixel (x_{ij}). These are computed in MATLAB using a Sobel gradient operator. The MIG is averaged over an inputted section of width and height within the image; it is therefore possible to calculate multiple MIGs from a single image, if the image and calculations are sectioned up. This enables some adjustments to how sensitive the measured MIGs are to the non-uniformity of the speckle pattern. Pan et al. showed that the MIG value is related to the DIC mean-bias error and standard deviation of measured displacements, in which higher MIG value consistently corresponded to a smaller mean-bias error and smaller standard deviation in recorded displacement as seen in Fig. 3.17.

Speckle pattern	A	B	C	D	E
Mean intensity gradient	34.6444	21.5143	20.0398	12.3400	9.0379

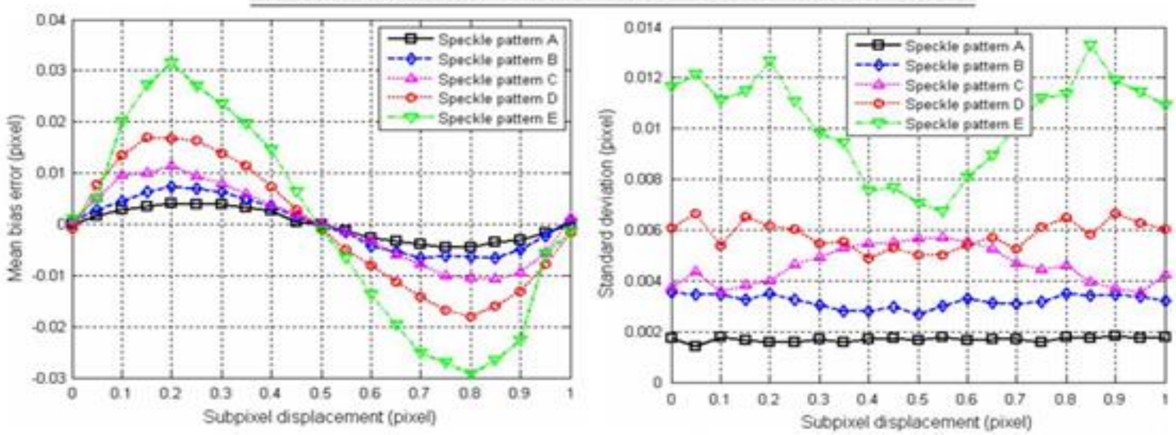

Fig. 3.17 Speckle patterns with higher MIG values have less mean bias error and lower standard deviations in recorded displacements. Results shown for a subset size of 31. From ref [20].

It is clear that a higher MIG is desired to obtain more precise and accurate measurements. The question now becomes, how high the MIG needs to be to obtain sufficient quality measurements. This can be accomplished by relating the MIG values to metrics of noise and standard deviations obtained from VIC-3D outputs. The VIC-3D software developed by Correlated Solution contains a parameter simply called sigma that is defined as one standard deviation confidence in the match in units of pixel; in other words, it is a spatial metric of how confident the match between the left and right image is for a particular subset size. Locations with high sigma values indicate regions with poor correlation due to high noise or excessive intensity gradients; this can be due to a number of reasons, such as glare or a lack of contrast within the nearby subsets, in the case of an abnormally large speckle or lack of speckle. Sigma is a useful parameter within the DIC software for determining the spatial quality of measurements that will be made. Relating sigma and the MIG will allow a user to get an estimation of how the DIC software will perceive the quality of the speckle pattern and images without the need for actually implementing the license. The relationship was found in MATLAB by breaking inputted images with a wide range of speckle sizes and qualities into 256 small rectangles then computing the MIG for each section and relating the average sigma value over that region as recorded by the DIC system for a particular subset size. As expected, there is a strong relationship between the MIG and sigma as seen in Fig. 3.18a. The sigma value exponentially decreases with increases in MIG. This indicated that selecting a minimum MIG of 80 ensures that the majority of the benefits of a higher MIG value have been obtained.

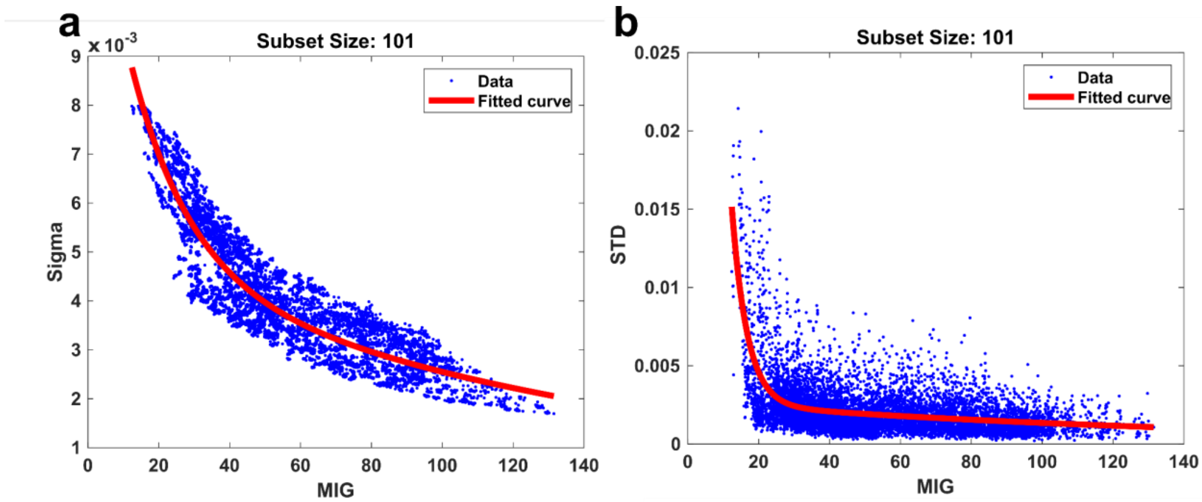

Fig. 3.18. Sample and fitted curve plots. (a) The relationship between VIC-3D's sigma value and the MIG value. (b) The relationship between the standard deviation of displacements and MIG values.

Pan *et al*. demonstrated that a relationship between the MIG and the recorded displacements existed; however, the study was limited by 5 speckle patterns and only a narrow range of MIG values was considered. For higher quality speckle patterns, this study was extended. The relationship was found using the same method as for the sigma relationship and can be seen in Fig. 3.18b. The standard deviation exponentially decreases with increases in the MIG, which was expected as sigma has a similar relation. These two relationships, if combined over several subset sizes, can be used to obtain estimates of the quality of DIC measurements that will be gained from a particular MIG value with a particular subset size. Therefore, the above procedure was repeated for eight different subset sizes and is plotted as surfaces in Fig. 3.19. The MIG is easily obtainable from the applied speckle prior to mechanical loading or DIC correlation; so, with Fig.

3.19, a rapid estimate of system error can be found with minimal time or computational resources.

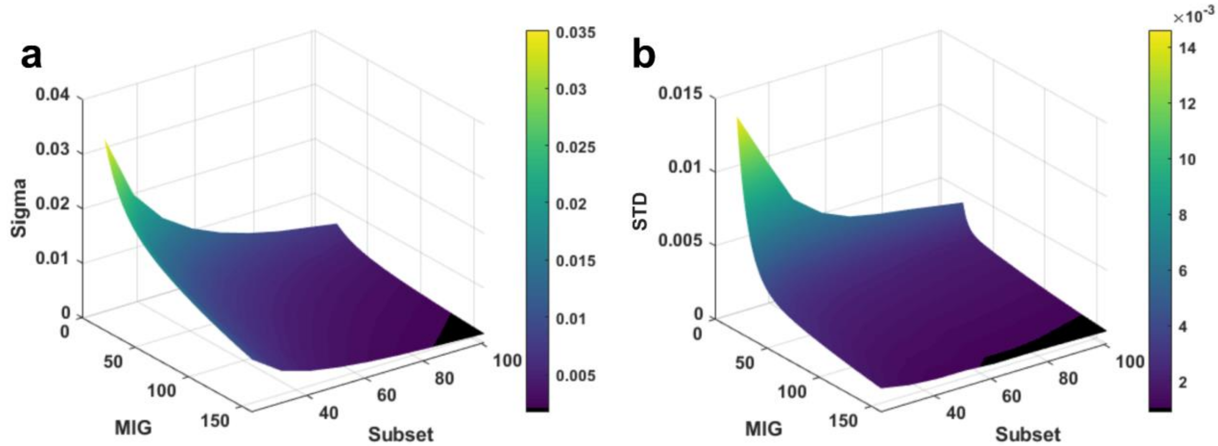

Fig. 3.19. Three variable relationship plots. (a) Three-dimensional relationship between VIC-3D's sigma value, MIG, and subset size. (b) Three-dimensional relationship between the standard deviation (STD) of the recorded displacements, MIG, and subset size.

4. Conclusions

The completed research has demonstrated the feasibility of M-DIC surface measurements. It has been shown that a mosaic surface profile comprised of higher resolution, local measurements is superior in accuracy to a single surface generated by a typical 3D-DIC measurement for a high aspect ratio surface (either natively planar or an unwrapped cylinder). Sources of error were classified into system, spatial distortion, and transformation error. The magnitude of these sources was quantified and reduction measures were investigated. Because system error is the dominant source of error after reductions and is highly dependent on speckle quality. A rapid quantifiable measure of speckle quality was investigated and can be used to predict system error prior to mechanical loading or DIC correlations. Based on the work of M-DIC error sources, the following conclusion were made.

- System error, associated with the physical setup and intrinsic inaccuracies of 3D-DIC, can be reduced significantly ($\leq$ 75 %) by improvements of speckle pattern and averaging.

- Spatial error, associated with lens distortion, can be modeled for each direction of motion and significantly reduced (≤ 85 %) for a single image pair by several additional steps in the experimental measurement technique.
- Transformation error, associated with the numerical back-tracking of the transformation from noisy data points, is the smallest error source (~ 1/100th of inputted noise), but propagation of this error down the length of a mosaic surface results in a desire to minimize the number of necessary transformations by reducing the percentage of overlap between consecutive stereo images.
- The MIG parameter can be used as a metric to predict the error in 3D-DIC measured displacements.
- A high MIG will help to ensure the imaged speckle pattern is high contrast, in-focus, and contains an appropriate speckle diameter in relation to image size for optimal M-DIC measurements.

5. References

[1] Cox BN, Bale HA, Begley M, Blacklock M, Do B-C, Fast T, et al. Stochastic Virtual Tests for High-Temperature Ceramic Matrix Composites. Annu Rev Mater Res 2014;44:479–529. doi:10.1146/annurev-matsci-122013-025024.

[2] Chen M, Blacklock M, Zhang D, Gong J. Effects of stochastic tow waviness on stiffness and strength of plain-weave ceramic matrix composites. Adv Mech Eng 2017;9:1–10. doi:10.1177/1687814017727973.

[3] Gowayed Y, Ojard G, Prevost E, Santhosh U, Jefferson G. Defects in ceramic matrix composites and their impact on elastic properties. Compos Part B Eng 2013;55:167–75. doi:10.1016/J.COMPOSITESB.2013.06.026.

[4] Dai S, Cunningham PR, Marshall S, Silva C. Influence of fibre architecture on the tensile, compressive and flexural behaviour of 3D woven composites. Compos Part A Appl Sci Manuf 2015;69:195–207. doi:10.1016/J.COMPOSITESA.2014.11.012.

[5] Mandell JF, Samborsky DD, Wang L-S. EFFECTS OF FIBER WAVINESS ON COMPOSITES FOR WIND TURBINE BLADES, 2003.

[6] Pottavathri SB, Nair R, Asmatulu R. Effect of In-Plane Fiber Tow Waviness Upon the Tensile Strength Characteristics of Fiber Reinforced Composites of Carbon/Epoxy AS4/3501-6. vol. Volume 9:, 2015. doi:10.1115/IMECE2015-52366.

[7] Belnoue JP-H, Mesogitis T, Nixon-Pearson OJ, Kratz J, Ivanov DS, Partridge IK, et al. Understanding and predicting defect formation in automated fibre placement pre-preg laminates. Compos Part A Appl Sci Manuf 2017;102:196–206. doi:10.1016/J.COMPOSITESA.2017.08.008.

[8] Boisse P, Hamila N, Madeo A. Modelling the development of defects during composite reinforcements and prepreg forming. Philos Trans A Math Phys Eng Sci 2016;374:20150269. doi:10.1098/rsta.2015.0269.

[9] Berbon MZ, Rugg KL, Dadkhah MS, Marshall DB. Effect of Weave Architecture on Tensile Properties and Local Strain Heterogeneity in Thin-Sheet C-SiC Composites. J Am Ceram Soc 2002;85:2039–48. doi:10.1111/j.1151-2916.2002.tb00401.x.

[10] Yang QD, Rugg KL, Cox BN, Marshall DB. Evaluation of Macroscopic and Local Strains in a Three-Dimensional Woven C/SiC Composite. J Am Ceram Soc 2005;88:719–25. doi:10.1111/j.1551-2916.2005.00156.x.

[11] Rossol MN, Rajan VP, Zok FW. Effects of weave architecture on mechanical response of 2D ceramic composites. Compos Part A Appl Sci Manuf 2015;74:141–52. doi:10.1016/j.compositesa.2015.04.003.

[12] Croom BP, Li X, Deck CP, Xu P, Lahoda EJ. Quantifying the three-dimensional damage and stress redistribution mechanisms of braided SiC/SiC composites by in situ volumetric digital image correlation. Scr Mater 2016;130:238–41. doi:10.1016/j.scriptamat.2016.12.021.

[13] Sutton MA. Three-dimensional digital image correlation to quantify deformation and crack-opening displacement in ductile aluminum under mixed-mode I/III loading. Opt Eng 2007;46:051003. doi:10.1117/1.2741279.

[14] Helm JD, McNeill SR, Sutton MA. Improved three-dimensional image correlation for surface displacement measurement. Opt Eng 1996;35:1911–20. doi:10.1117/1.600624.

[15] Schreier H, Orteu JJ, Sutton MA. Image correlation for shape, motion and deformation measurements: Basic concepts, theory and applications. Springer US; 2009. doi:10.1007/978-0-387-78747-3.

[16] Reu PL, Miller TJ. DIC Uncertainty Quantification for Large Scale Outdoor Testing 2014.

[17] Balcaen R, Reu PL, Lava P, Debruyne D. Stereo-DIC Uncertainty Quantification based on Simulated Images. Exp Mech 2017;57. doi:10.1007/s11340-017-0288-9.

[18] Pan B, Yu L, Wu D, Tang L. Systematic errors in two-dimensional digital image correlation due to lens distortion. Opt Lasers Eng 2013;51:140–147. doi:10.1016/j.optlaseng.2012.08.012.

[19] Becker T, Splitthof K, Siebert T, Kletting P. Error estimations of 3D digital image correlation measurements. Proc.SPIE, vol. 6341, 2006. doi:10.1117/12.695277.

[20] Pan B, Lu Z, Xie H. Mean intensity gradient: An effective global parameter for quality assessment of the speckle patterns used in digital image correlation. Opt Lasers Eng 2010;48:469–77. doi:https://doi.org/10.1016/j.optlaseng.2009.08.010.

[21] Arun KS, Huang TS, Blostein SD. Least-Squares Fitting of Two 3-D Point Sets. IEEE Trans Pattern Anal Mach Intell 1987;PAMI-9:698–700. doi:10.1109/TPAMI.1987.4767965.

[22] Challis JH. A procedure for determining rigid body transformation parameters. J Biomech 1995;28:733–7. doi:https://doi.org/10.1016/0021-9290(94)00116-L.

[23] Gioi RG von, Monasse P, Morel J-., Tang Z. Towards high-precision lens distortion correction. 2010 IEEE Int. Conf. Image Process., 2010, p. 4237–40. doi:10.1109/ICIP.2010.5651928.

[24] Kammers AD, Daly S. Digital Image Correlation under Scanning Electron Microscopy: Methodology and Validation. Exp Mech 2013;53:1743–61. doi:10.1007/s11340-013-9782-x.

[25] Sutton MA, Li N, Garcia D, Cornille N, Orteu JJ, McNeill SR, et al. Metrology in a scanning electron microscope: theoretical developments and experimental validation. Meas Sci Technol 2006;17:2613–22. doi:10.1088/0957-0233/17/10/012.

[26] Pan B, Xie H, Wang Z, Qian K, Wang Z. Study on subset size selection in digital image correlation for speckle patterns. Opt Express 2008;16:7037–48. doi:10.1364/OE.16.007037.

CHAPTER 4: MOSAIC DIC FOR MEASUREMENTS OF TOW ARCHITECTURE VARIABILITY OF BRAIDED COMPOSITES TUBES

1. Introduction

While continuous fiber-reinforced, braided composites exhibit exceptional mechanical properties, their performance is intrinsically affected by their tow architecture.[1–3] Past work for braid composites has demonstrated the effects of tow configuration and braid angle on mechanical properties.[4–6] However, they also tend to contain local variations in tow placement, which will also contribute to and limit performance.[7]

The undulations of tows in woven or braided composites [18,19] create a rough surface (Fig. 4.1a), such that surface profilometry techniques are a viable approach to measure the tow placement. Local peaks on the surface correspond to the apex of a surface tow as it crosses over other underlying tows, *i.e.* the tow "crown" (Fig. 4.1b). Digital Image Correlation (DIC) has been used to quantify the as-manufactured tow geometry in (2D) woven composite panels [20,21] and has been used extensively to study strain inhomogeneities, characteristic of composite materials. [4,6,22,23] The Mosaic DIC (M-DIC) approach, previously explored, can be used to map the surface profile of large, non-planar components through the automatic combination of multiple smaller surface measurements into a single, high-resolution reconstruction of the composite surface.

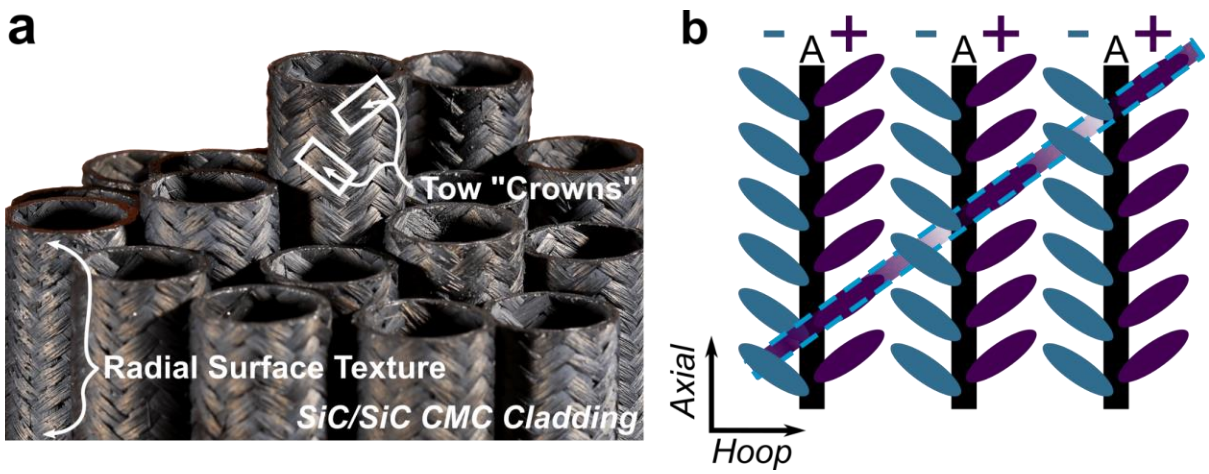

Fig. 4.1. (a) Image of SiC/SiC CMC cladding tubes with ~10 mm outer diameter, highlighting surface texture and tow crown locations, adapted from Oak Ridge National Laboratory. (b) Schematic definition of negative, positive, axial tows.

In particular, this chapter focuses on the variation of tow placement, which leads to "unit cells" of irregular size and shape, in both braided carbon-fiber reinforced polymer (CFRP) tubes and SiC/SiC ceramic matrix composites (CMCs). The separate study of these two cases was completed for several reasons. First, each contained a unique braid type, including a biaxial braid for the CFRPs and a triaxial braid for the CMCs; therefore, the influence of each tow family on systematic manufacturing/braiding defects could be isolated. Second, CFRPs are more widely distributed, are more mature, contain typical composite properties, and can be explored as a fundamental case study. SiC/SiC present a more practical and specific case but are still rapidly evolving.

This chapter has three main objectives: (i) present algorithms necessary for full-scale measurements of tow irregularity of braided, tubular composites. (ii) show and compare results for both composite systems to provide a scientific understanding of tow architecture irregularity. (iii) demonstrate a route towards improved, defect modeling of braided composites through experiment-based measurements.

2. *Background for CMC practical case*

Ceramic matrix composites exhibit exceptional strength and toughness compared to monolithic ceramics due to the deliberate arrangement of strong fibers within an otherwise brittle matrix, which makes them appealing high-temperature structural materials for aerospace and nuclear energy applications. The mechanical properties of CMCs are very sensitive to defects in tow arrangement, with irregular tow spacing contributing to altered elastic, strength and fracture characteristics.[11,24] Numerous experiments and models have demonstrated that the stochastic positioning of tows causes stress localization and alters damage and failure propagation.[2,25,26] Recent *in situ* experiments have suggested that irregular tow spacing in chemical vapor infiltration densified, braided CMCs is correlated with the location of composite failure.[27]

Given that the arrangement of tows within CMCs can predict some of the statistical variation in observed mechanical properties, there is great interest in understanding the stochastic properties of such composite architectures. This is particularly valuable for nuclear energy applications, where the hermeticity of fuel cladding could be influenced by variation in tow spacing. To this end, various microstructural characterization techniques are used to determine tow characteristics throughout the composite over multiple length scales. High-resolution techniques such as X-ray computed tomography (XCT) can extract high-frequency variation in tow geometry and position over ~1 mm length scales,[28–30] while lower-resolution techniques such as stereoscopic digital image correlation (3D-DIC) can measure (surface) variation over much larger length scales (>1 cm).[31] Measurements from these two regimes could be combined to generate statistically-accurate virtual composite representations,[32,33] which would allow efficient computational screening of mechanical properties by finite element techniques.[11]

For a comparative example from literature, measurements of a flat CMC panel of woven architecture were obtained by 3D-DIC using the following workflow:[31] (i) 3D-DIC based height measurement of overlapping sub regions of flat CMC panel. (ii) semi-manual stitching of multiple DIC measurements, yielding single dataset for entire panel. (iii) segmentation of crowns of individual tows by height thresholding. (iv) extraction of crown centroids. (v) statistical analysis of tow trajectories.

This approach exhibits several limitations: (i) measurement is only possible for quasi-planar specimens, (ii) the accuracy of the coordinate transformations is limited by human precision, and (iii) thresholding can yield inaccurate tow position measurements. Furthermore, this technique is wholly inapplicable to composite tubes or any 3D geometry since less than half of the component is visible in a single image. Even in regions that could be analyzed from a single perspective, significant variations in crown height combined with close packing could cause some tows to be missed during segmentation, and neighboring crowns to be merged into a single feature.

3. Framework of Mosaic DIC for tubular composites

To quantify the full-field tow variability of braided components, it is necessary to combine multiple local 3D-DIC measurements into a single, global coordinate system. Here, a technique developed in the past chapter, called M-DIC is used, which automates this process by efficiently and robustly computing the spatial transformations required to tile multiple local measurements into a single, comprehensive “mosaic” of the entire surface. Provided that there exists some overlap in the image pairs corresponding to adjacent local measurements, and the sample undergoes strictly rigid body motion, 3D-DIC displacement measurements can be decomposed into translation and rotation components that relate the multiple frames of reference. This technique is valid for arbitrary motion between frames and can be used to efficiently reconstruct and measure intricate geometric shapes, including cylinders.

Implementation of the M-DIC technique is schematically depicted in Fig. 4.2. After calibrating the 3D-DIC system, partially overlapping measurements of the entire composite surface are acquired, yielding image pairs $I_1, I_2, \dots, I_n$ in the local coordinate systems $P^1, P^2, \dots, P^n$. This is achieved by applying *rigid body motion* to the specimen between imaging, here, accomplished via mounting stage rotation in a Bruker tribometer.

To concisely derive the mathematical framework for M-DIC, a DIC operator is introduced to describe the results for 3D-DIC analysis,

$$x_j^i = x_i^i + u_{i\to j}^i\left(x_i^i\right) = \mathrm{DIC}(I_i, I_j) \tag{4.1}$$

where images I_i and I_j are the reference and "deformed" images, x_i^i are the extracted surface coordinates in the reference state, x_j^i are the corresponding coordinates in the deformed state, and $u_{i\to j}^i\left(x_i^i\right)$ is the displacement field that relates the two. x_i^i, x_j^i and $u_{i\to j}^i$ are $(3 \times N)$ lists of coordinates and displacements. Note that throughout this section concerning data sets, superscripts correspond to the current frame of reference, and subscripts correspond to originating images.

Each image pair is correlated *twice* to provide detailed shape measurements in the local frame P^i as well as displacement between frames P^i and P^{i+1}.

$$x_i^i = \mathrm{DIC}(I_i, I_i) \text{ for } i = 1 \dots n \tag{4.2}$$

$$x_{i+1}^i = x_i^i + u_{i\to i+1}^i\left(x_i^i\right) = \mathrm{DIC}(I_i, I_{i+1}) \text{ for } i = 1 \dots n-1 \tag{4.3}$$

By nature of the measurement, the rigid body motion $u_{i\to i+1}^i$ can be expressed as a combination of rotation and translation,

$$x_{i+1}^i = [R_{i\to i+1}]x_i^i + \bar{u}_{i\to i+1}^i \tag{4.4}$$

where $[R_{i\to i+1}]$ is a proper and orthogonal rotation matrix, and $\bar{u}_{i\to i+1}^i$ is the average displacement vector. Both $[R_{i\to i+1}]$ and $\bar{u}_{i\to i+1}^i$ are found by singular value decomposition (SVD) according to methods outlined by Arun.[34] In brief, the SVD yields,

$$[U][S][V]^T = \left(x_i^i - \bar{x}_i^i\right)\left(x_{i+1}^i - \bar{x}_{i+1}^i\right)^T \tag{4.5}$$

where $\bar{x}_i^i$ and $\bar{x}_{i+1}^i$ are the centroids of the reference and deformed coordinates. With some manipulation, the coordinate transformation is obtained,

$$[R_{i\to i+1}] = [V][U]^T \tag{4.6}$$

$$\bar{u}_{i\to i+1}^i = \left(x_{i+1}^i - \bar{x}_{i+1}^i\right) - [R_{i\to i+1}]\left(x_i^i - \bar{x}_i^i\right) \tag{4.7}$$

It can be shown that Eq. 4.4 allows the transformation of *any* data acquired in frame P^{i+1} into the prior frame P^i,

$$x_{i+1}^i = [R_{i\to i+1}]^T\left(x_{i+1}^{i+1} - \bar{u}_{i\to i+1}^i\right) \tag{4.8}$$

In this way, the multiple local measurements can be combined into a single global coordinate system by iteratively transforming coordinates $x_i^i \to x_i^{i-1} \to \cdots \to x_i^1$.

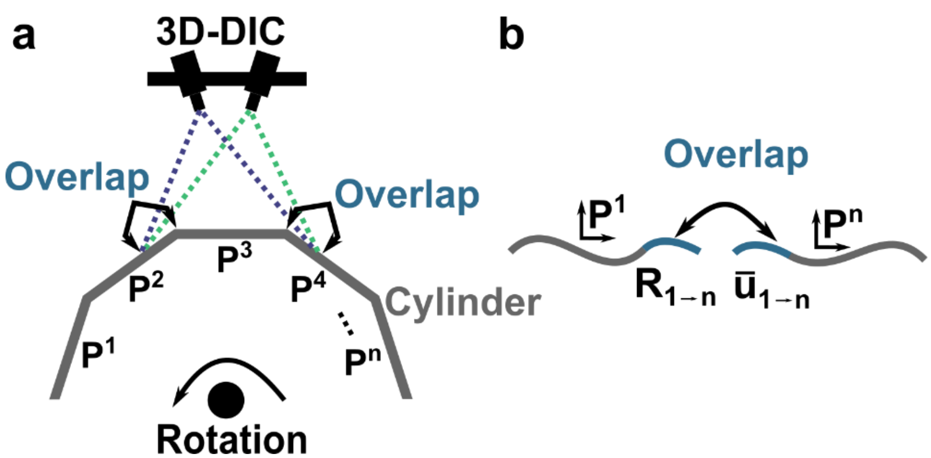

Fig. 4.2. Mosaic DIC technique. (a) Local 3D surface profiles are captured by 3D-DIC in coordinate frames $P^1, P^2, \ldots, P^n$. (b) Regions of overlap between consecutive measurements allow computation of the transformation parameters $[R_{i\to i+1}]$ and $\bar{u}_{i\to i+1}^i$, enabling local measurements to be combined.

3.1. Validation of Mosaic DIC for tubular geometry

The final Mosaic shape measurement for an Aluminum validation specimen is summarized in Fig. 4.3, which confirmed that M-DIC accurately captured the cylindrical geometry. The radius was measured to be $10 \pm 0.03\ mm$, which closely matched the variation measured by calipers.

The height map revealed circumferential grooves due to machining, as well as three axial bands due to irregular paint thickness, which was associated with the white undercoat for the DIC speckle pattern that was applied in three passes. Local peaks in the measured height were visually confirmed to be large paint particles on the surface. While this experiment did not rigorously test the limits of the M-DIC technique, the accuracy was more than adequate to detect tows on composite specimens, which exhibited a typical peak-to-valley height of ~0.6 mm.

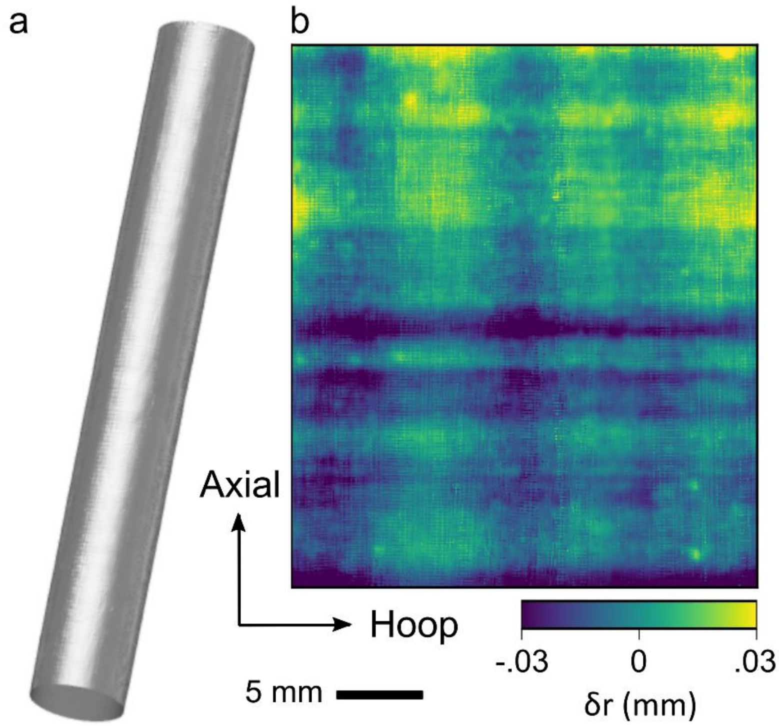

Fig. 4.3. Validation of M-DIC on Al rod.[7]

4. *Algorithms for measuring tow architecture variability*

Combined local measurements entailed a cloud of >1,000,000 surface measurement points. The data was reduced by fitting a cylinder to the point cloud via least squares, unwrapping the data along the cylinder axis into a rectangular coordinate system, and binning the data into a square grid with 0.1 mm pitch. Each cell in the grid contained multiple points with different measured radii due to noise in the DIC measurements. A single "height" was assigned to each cell by taking the median of all local heights $\delta r = r - r_{cylinder}$, where r is the measured cylinder radius, and

$r_{cylinder}$is the radius of the best-fit cylinder. Following this procedure, the condensed surface profile takes the equivalent form of an intensity image, enabling subsequent typical image processing analysis. To reconstruct the tow architecture of a composite, image processing algorithms must accurately extract the position of each tow from surface shape maps. Subsequently, the complete trajectories of individual tows are traced out by connecting measured tow centroids using knowledge of composite architecture, allowing reconstruction of the composite. The algorithms used to reconstruct the composite are developed in the following sections.

4.1. Tow search algorithm

Two composite systems were studied at separate times.[7,35] Therefore, modifications were made to this algorithm between the two datasets. Presented here is the logic of the most current procedure, which was implemented on the CFRP composites;[35] however, illustrations from both works will be used to avoid redundancy. For the older version of the algorithm, which was outlined by *Croom*, details can be found in *Heim et al.*[7] Notably, both procedures produce similar tow crown isolations and each has its own advantages and disadvantages. Notably, the later requires considerably less time to identify crown locations, which was convenient for implementation with quasi-static mechanical test DIC data.

A crown search algorithm which incorporates *a priori* knowledge of the tow architecture was used, as it was found subtle differences in tow crown height necessitated a structured search criterion. The algorithm utilizes average crown shape information and neighboring crown locations to search for the optimal crown location by automatically determining an initial location of suspected tow crown positions that are subsequently refined via a structured intensity maxima scheme. To accomplish this, a universal composite notation is established to model the tow geometry (Fig. 4.4). In this system, an idealized shape, such as an ellipse or rectangle, approximates the shape of each tow crown i (Fig. 4.4a). Each tow genus j is assigned a separate idealized shape parameterized by typical widths, aspect ratios and orientations (Fig. 4.4b).

Unit cell dimensions $U_{unit} = (U_{unit}, V_{unit})$, defined in Fig. 4.4c, are used to construct a library of intensity templates from experimental data. In a perfect composite with uniform tow spacing, the position of each crown in the virtual representation would fully overlap with the corresponding crown in the experimental composite, but deviations in the composite produce displacement vectors u_i for each crown. Theoretically, the search algorithm must compute both the geometry (size and orientation) as well as displacements of each crown, but it was found that by utilizing a searching shape corresponding to the smallest tow crowns, the minor deviations in observed crown geometry can be neglected without significant effect. Therefore, the crown segmentation algorithm simply should aim to measure the displacement vectors u_i, which is the minimum amount of information needed to represent the composite.

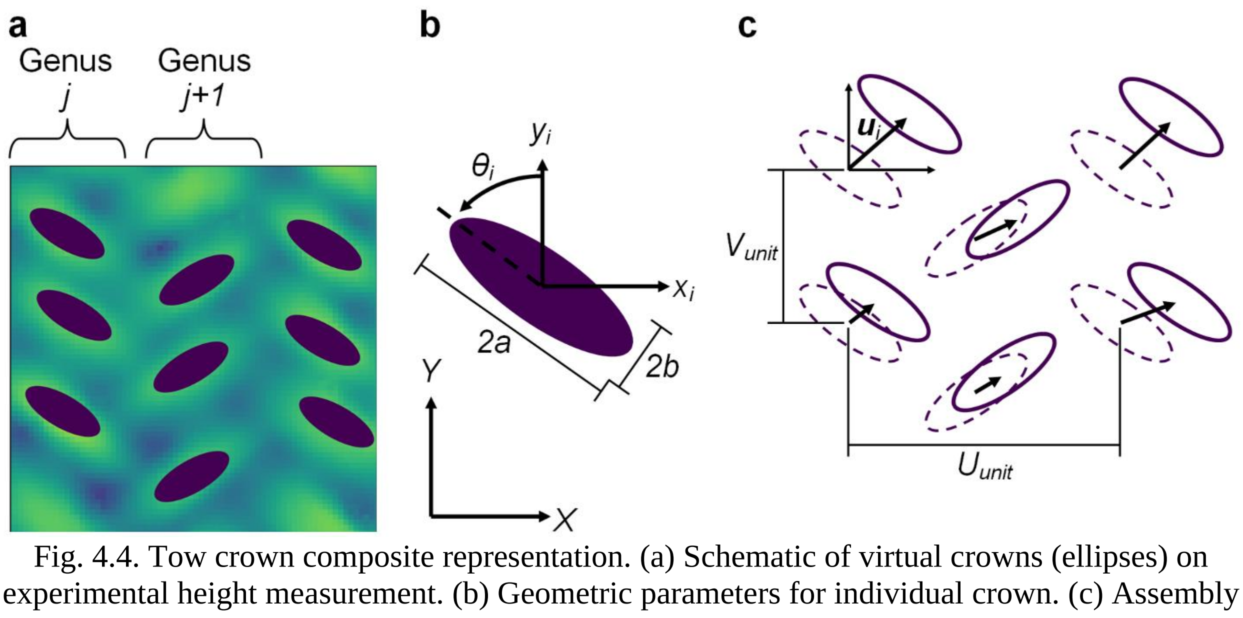

Fig. 4.4. Tow crown composite representation. (a) Schematic of virtual crowns (ellipses) on experimental height measurement. (b) Geometric parameters for individual crown. (c) Assembly of virtual composite by unit cell dimensions, as well as displacements u_i from ideal crown location (dashed outline) to experimental location (solid outline).[7]

An initial “coarse” crown centroid location was determined via a normalized cross-correlation template matching scheme,[36–38] leveraging the MATLAB normxcrosscorr2 function which determined spatial correlation coefficients according to: [37]

$$\gamma(u,v) = \frac{\sum_{x,y}[f(x,y)-\bar{f}_{u,v}][t(x-u,y-v)-\bar{t}]}{\sqrt{\left\{\sum_{x,y}[f(x,y)-\bar{f}_{u,v}]^2 \sum_{x,y}[t(x-u,y-v)-\bar{t}]^2\right\}}} \tag{4.9}$$

where $f(x,y)$ is the image, $\bar{f}_{u,v}$ is the mean of $f(x,y)$ under the template, $t(x,y)$ is the template and $\bar{t}$ is the mean of the template. The correlation value γ evaluated the similarity between the height profiles of the template and experimental height measurement and was locally maximized after finding a strong match. This correlation was done for a library of user-defined templates, in which the sum of the correlations was used to identify initial crown locations per tow genus (Fig. 4.4a). Notably, it was found that a template containing the intensity map of a single tow crown, was insufficient to accurately identifying unusually shaped or radially sunken tow crowns. Therefore, a template size of 3.5 mm x 2.5 mm was used for the CFRP composites, in which a multi-crown template was chosen such that the isolation of a single tow crown depended on intensity similarities between both the central crown and the four surrounding neighbor locations. An example result of the coarse search can be seen in Fig. 4.5a.

Subsequentially, a “fine” crown search strategy was used with a structured intensity maximation/minimization scheme coupled with a penalty to discourage non-physical tow locations. To this end, an objective function $f^{objective}$ was implemented, which is parameterized with respect to the crown displacements u_i, which allows the use of numerical maximation/minimization schemes to solve for the crown locations. The objective function consists of two components, including a search function f^{height} that tends to identify local maxima in the composite height map, and also a penalty function $f^{penalty}$ that constrains the search to enforce the known tow architecture,

$$f^{objective}(u_i) = f^{height}(u_i) + f^{penalty}(u_i) \tag{4.10}$$

In this definition, the crown positions are found as $u_i = \text{argmin}(f^{objective}(u_i))$.

The tow search using f^{height} begins by generating a virtual composite representation $g(x^{img}, u_i)$ which contains i crowns with displacements u_i and is of identical size as the experimental height image $h(x^{img})$. The virtual mask contains structuring geometries for each crown in $h(x^{img})$ according to the selected tow crown representation, described in Fig. 4.4. For different composite application, each tow crown was modeled as an ellipse or rectangle with representative dimensions and an orientation of $\pm 55°$ from the tube axis. All pixels within each unmasked crown were assigned equal weights of unity. The search function is evaluated by summing the element-wise multiplication of the two arrays,

$$f^{height}(x_i^{tow}) = \sum_{x^{img}} -g(x^{img}, u_i) \cdot h(x^{img}) \tag{4.11}$$

Which, as defined, is locally minimized when the measured crown positions u_i correspond to maxima in $h(x^{img})$.

Without a penalty function to constrain the search, it was observed that the intensity scheme would cause identified crown locations to converge on a single “high” feature. The addition of virtual, nonlinear springs between the crowns via $f^{penalty}(u_i)$ encourages moderately uniform spacing and prevents non-physical arrangement of crowns. The contributions of each spring are summed to evaluate the penalty function,

$$f^{penalty}(u_i) = \sum_i f_i^{penalty}(u_i)$$

$$f_i^{penalty} = \begin{cases} 0 & \text{if } \|\delta u_i\| < u_{max} \\ k(\|\delta u_i\| - u_{max})^2 & \text{else} \end{cases} \tag{4.12}$$

where the nonlinear spring between adjacent crowns is structured as a piecewise function $f_i^{penalty}$, $\|\delta u_i\| = \|u_{i+1} - u_i\|$ is the Euclidian relative displacement (spring extension) between adjacent crowns, k is a spring constant, and u_{max} is the upper bound of unconstrained motion. With this particular formulation, $f^{penalty}$ does not penalize minor relative motion of crowns for $\|\delta u_i\| < u_{max}$, but severely discourages extreme crown displacements that may cause non-viable crown arrangements since $f_i^{penalty} \gg f_i^{height}$ for large $\|\delta u_i\|$. Therefore, k and u_{max} should be selected to encompass reasonable variation in crown spacing. For each crown the position with the minimum score $f^{objective}$ was chosen. The best crown location was converged to over several iterations of $f^{objective}$ to a theoretical sub-pixel accuracy. An example result of the fine search can be seen in Fig. 4.5a.

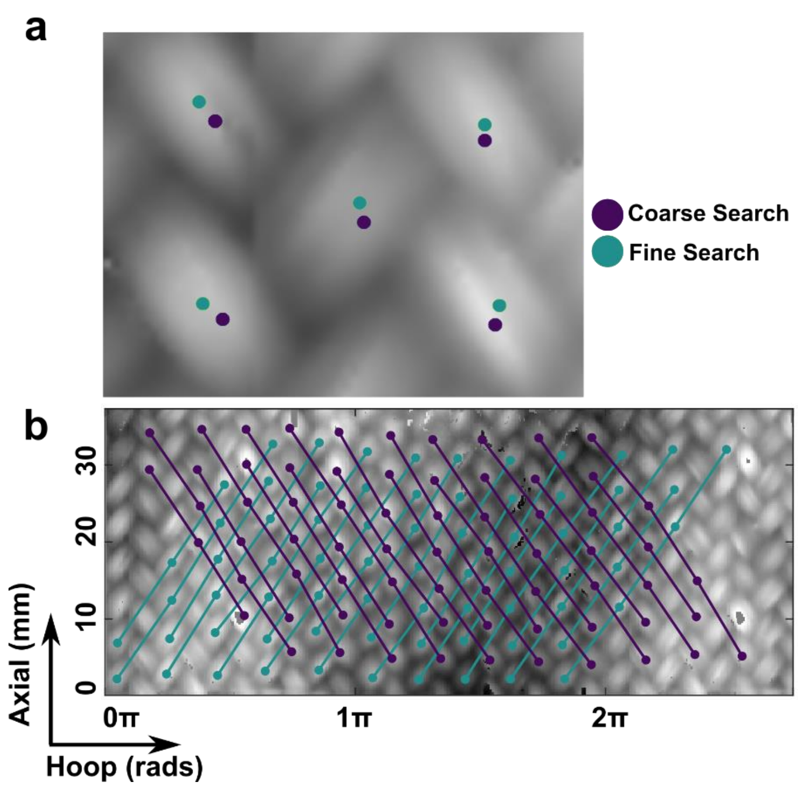

Fig. 4.5. Demonstration of tow centroid isolation for CFRP tubes. (a) The coarse-fine searching process to determine the centroid of each tow crown. (b) The tow tracing algorithm uses knowledge of the unit cell dimensions to connect the crowns and reconstruct the path of each tow.

4.2. *Tow tracing algorithm*

The final step in reconstructing the composite is connecting the segmented crowns to map the trajectory of each fiber bundle. Using knowledge of the unit cell geometry, it is easy to predict of the path of each tow, as schematically depicted in Fig. 4.6. For ideal composites, the next crown location will be positioned a constant, integer number of unit cells away from the current tow location. Due to composite variability, the actual location of the unidentified tow will lie some distance δu_i away from the predicted point, and a search is performed to find the closest crown location. Mathematically, this search is expressed as,

$$x_{i+1} = x_i + U_{unit} + \delta u_i \tag{4.13}$$

where x_i is the current tow location, x_{i+1} predicted location of the next crown on the tow, U_{unit} is the predicted spacing based on average unit cell dimensions, and δu_i is previously defined. Therefore, the connected tow is found as $x_{i+1} = \text{argmin}(\|\delta u_i\|)$, which is the closest tow centroid to the predicted position. This process is repeated for all tow locations in the image, creating a map of each tow (Fig. 4.5b)

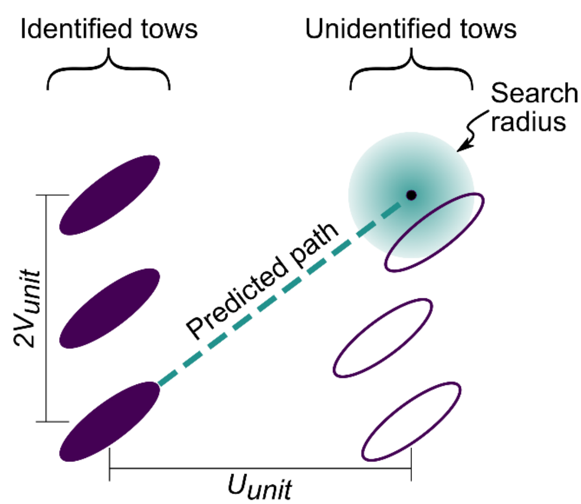

Fig. 4.6. Schematic describing tow tracing algorithm.

4.3. *Tow variability measurements*

After the tubes were reconstructed and analyzed by M-DIC, which identified the centroid locations of all tow crowns in each composite, the average unit cell dimensions X_{avg} and Y_{avg} were calculated for each tube. Subsequentially, ideal tow crown locations X_i^{ideal} and Y_i^{ideal} were predicted based on a uniform grid of tow positions. The displacement of each tow crown from the ideal unit cell location is defined as:

$$\begin{aligned} U_i &= X_i^{ideal} - X_i \\ V_i &= Y_i^{ideal} - Y_i \end{aligned} \tag{4.14}$$

The spatial variation in the composite was evaluated according to the methods outlined by Rossol.[31] To discern local variations in tow architecture from systematic displacements, the derivatives of U_i and V_i were calculated. These spatial derivatives can be represented as pseudo-strains δ_{xx}, δ_{yy}, and δ_{xy}. These "pseudo-strains" were then displayed as percentages for simpler viewing.

$$\begin{aligned} \delta_{xx} &\approx \frac{\partial U}{\partial x} \\ \delta_{yy} &\approx \frac{\partial V}{\partial y} \\ \delta_{xy} &\approx \frac{1}{2}\left(\frac{\partial U}{\partial y} + \frac{\partial V}{\partial x}\right) \end{aligned} \tag{4.15}$$

The derivatives were computed numerically at each crown using a central difference scheme that accounted for the periodicity in the hoop direction. Derivatives were not computed at the top and bottom edges of each composite.

5. *Materials and methods*

5.1. *CFRP*

The M-DIC technique was used to quantify the irregular unit cell geometry of two nominally identical carbon fiber-reinforced composite tubes; separate tubes were analyzed to assess the consistency of the braiding process. The tubes (supplied by Dragonplate) featured an inner unidirectional composite layer with 0° fiber orientation, and an outer, biaxially braided layer with nominal fiber orientations of ±45°; the tubes had nominal dimensions of 7.3 mm inner diameter (ID), 10.5 mm outer diameter (OD), and 300 mm length. Both tubes were visually dissimilar (seen in Chapter 1), with one appearing to have excess epoxy on the outer surface ("epoxy-rich"), and the other with a rougher surface ("epoxy-lean"). Per manufacturer specifications, the epoxy matrix comprises ~50 % of the total weight per tube.

The tubes were sectioned with a water-cooled diamond saw into smaller specimens for M-DIC analysis. The epoxy-rich tube was cut into "long" sections, while the epoxy-lean tube was cut into "short" sections; different specimen lengths were used to support mechanical testing for a forthcoming paper. While the longer cut tubes were nominally 88.9 mm (3.5 in) in axial length, only the inner 50.8 mm (2 in) region was studied; the full axial length was studied for short specimens. Physical dimensions of the specimens are summarized in Table 4.1, with each measurement obtained by averaging three separate measurements using calipers with an accuracy of ±0.02 mm. Interestingly, the outer braid layer was found to have an orientation of ±55° from the tube axis.

Table 4.1. Actual specimen dimensions, each dimension taken as the average of three measurements.

Short Specimen ID	**Length (mm)**	**Average OD (mm)**	**Average ID (mm)**
Exp S1	18.45	10.42	7.29
Exp S2	19.50	10.45	7.31
Exp S3	19.24	10.51	7.30
Exp S4	20.54	10.51	7.29
Exp S5	20.30	10.47	7.28
Exp S6	19.54	10.49	7.31
Long Specimen ID	**Length (mm)**	**Average OD (mm)**	**Average ID (mm)**

Exp L1	89.10	10.50	7.31
Exp L2	90.94	10.55	7.32
Exp L3	88.08	10.56	7.32
Exp L4	88.38	10.53	7.29
Exp L5	86.38	10.55	7.27

The full-field reconstruction was composed of 16 different fields of view per cylindrical specimen. After combining the local surface measurements, the surface profile was unwrapped along the circumference of the tube to create a 2D radial height map. The data was down-sampled by dividing the data into 0.1 mm square bins, and computing the median height of each bin. All experimental measurements were gathered with two FLIR Grasshopper 3 GS3-U3-50S5M-C digital CMOS cameras with Schneider 21-100197 50 mm compact lenses, and were correlated using commercial 3D-DIC software (Vic-3D 8, Correlated Solutions). 3D-DIC analysis was performed with uniformly weighted subsets of size 13 pixels and a step size of 1 pixel using an optimized 8-tap and zero-normalized squared differences correlation scheme.

5.2. SiC/SiC

Six braided CMC tubes (General Atomics) with nominal diameters of 9.8 mm and lengths of 70 mm were similarly prepared for M-DIC measurement. The composites consisted of two layers of triaxially braided Hi-Nicalon type S fiber tows, pyrolytic carbon interface and CVI SiC matrix, with nominal fiber orientations of 0°/±35° (from hoop). Both families of biased tows were visible from the exterior surface as they crossed over the underlying axial tows.

Local surface measurements of the specimens were acquired with typical 3D-DIC measurement procedures, using dual 5 megapixel CCD cameras with 50 mm lenses, diffuse white LED lighting, and commercial 3D-DIC software (Vic-3D, Correlated Solutions) with a subset size of 29 and step size of 2. The subset size was smaller than the width of individual tows, allowing accurate measurements of the surface profile. The specimens were mounted axially on a rotary stage and rotated in 24° increments to image the entire surface, producing a set of 15 image pairs. Image pairs were then processed and combined, producing a cloud of ~1,000,000 surface measurements. The data was reduced by fitting a cylinder to the point cloud via least squares, unwrapping the data along the cylinder axis into a rectangular coordinate system, and binning the data into a square grid with 0.1 mm pitch. Each cell in the grid contained multiple points with different measured radii due to noise in the DIC measurements. A single "height" was assigned to each cell by taking the median of all local heights $\delta r = r - r_{cylinder}$, where r is the measured cylinder radius, and $r_{cylinder}$is the radius of the best-fit cylinder. All post-DIC processing and analysis was done with Python and MATLAB.

6. Results

All results will be discussed in pairs to independently include both CFRP and SiC/SiC composites. Comparison of the results between the braids will be included in the final discussion section. Importantly, CFRP tubes contain a regular biaxial braid (Fig. 4.7a), and SiC/SiC tubes contain a regular triaxial braid (Fig. 4.7b). Differences in tow structure, include the addition or subtraction of axial tows and fiber-tow density. Tow widths differ, with ~1.4 mm and ~0.9 mm for SiC/SiC and CFRP, respectively.

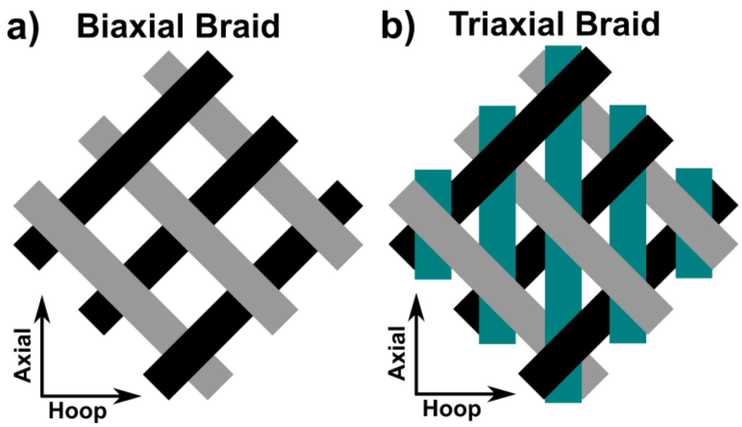

Fig. 4.7. Schematics of braid structures. (a) Regular biaxial braid. (b) Regular triaxial braid.

6.1. Nonuniformity in experimentally measured unit cells

6.1.1. CFRP

The tow tracing algorithm was used to extract the dimensions of every unit cell as well as the orientation of the biased tows in the reconstructed surface profiles. The statistical distributions of these metrics are presented as normal probability plots in Fig. 4.8 for all CFRP specimens. Critically, the probability plots showed that the placement was not uniform, but significantly varied in each composite by roughly ±1 mm in the axial and hoop directions. The linear trends observed for each specimen revealed that the variation of the unit cell dimensions closely obeyed a normal distribution, and that the measurements were very similar for all specimens. Noting that the "short" (Fig. 4.8a) and "long" (Fig. 4.8b) specimens were obtained from different tubes, the similarity in the unit cell dimensions indicated a consistent braiding process. The mean and standard deviation of these metrics used in the ideal model for each composite are summarized for each specimen in Table 4.2.

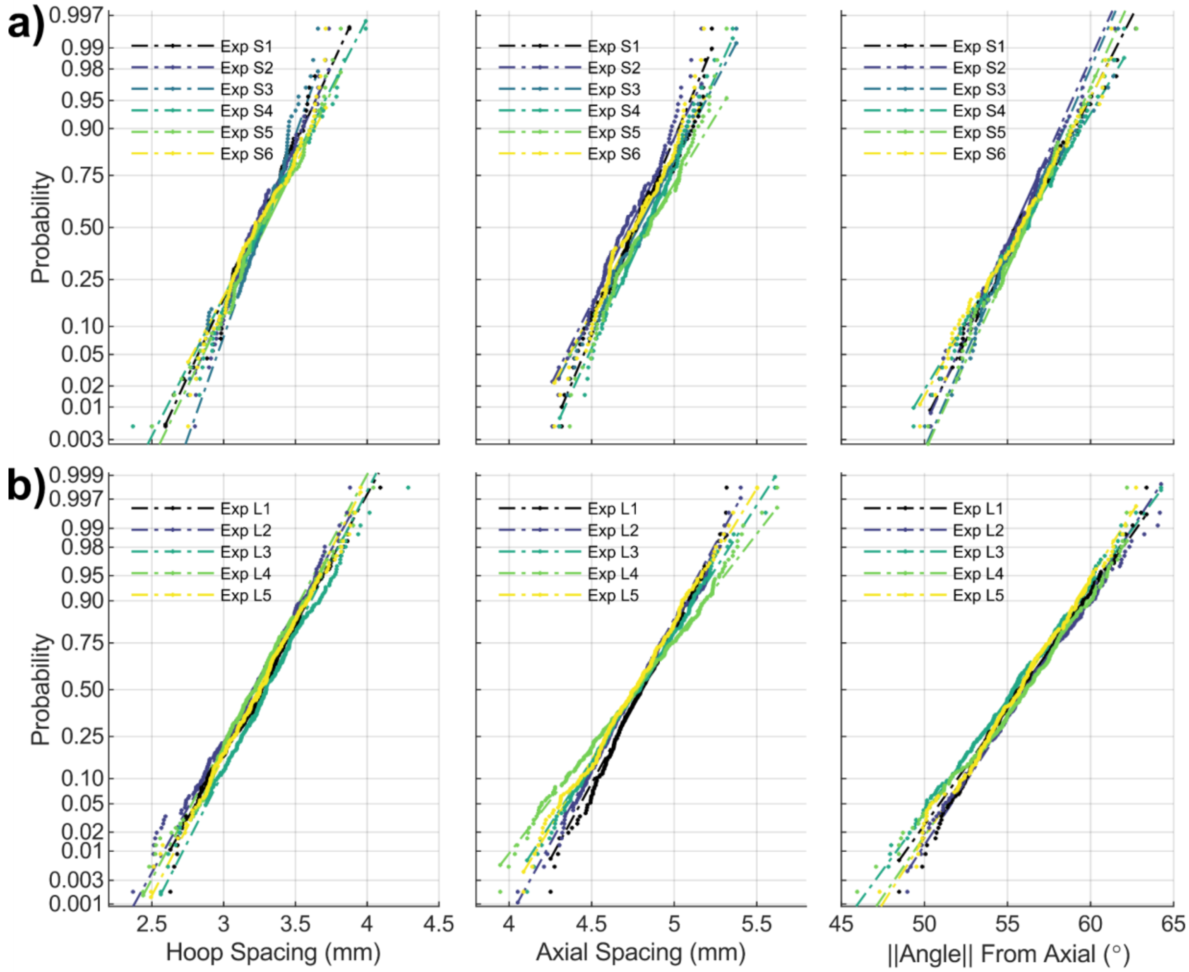

Fig. 4.8. Tow crown spacings and tow angle normal probability plots. (a) Short specimens. (b) Long specimens. Note, y-axis scales are different between (a) and (b).

Table 4.2. Average and standard deviation for hoop spacing, axial spacing, and ||angle|| from axial for each specimen.

Specimen ID	Hoop Spacing (mm) Mean ± Std.	Axial Spacing (mm) Mean ± Std.	||Angle|| (deg.) Mean ± Std.
Exp S1	3.275 ± 0.231	4.776 ± 0.224	55.86 ± 2.481
Exp S2	3.239 ± 0.218	4.712 ± 0.205	55.50 ± 2.306
Exp S3	3.234 ± 0.218	4.801 ± 0.221	56.03 ± 2.311
Exp S4	3.270 ± 0.267	4.825 ± 0.202	55.89 ± 2.633
Exp S5	3.268 ± 0.259	4.840 ± 0.230	55.99 ± 2.258
Exp S6	3.246 ± 0.243	4.758 ± 0.211	55.70 ± 2.572
Short Average	3.29 ± 0.239	4.785 ± 0.215	55.83 ± 2.427
Exp L1	3.257 ± 0.268	4.807 ± 0.213	55.89 ± 2.764

Exp L2	3.200 ± 0.275	4.773 ± 0.237	56.16 ± 2.939
Exp L3	3.302 ± 0.272	4.780 ± 0.263	55.36 ± 3.025
Exp L4	3.216 ± 0.264	4.765 ± 0.318	55.95 ± 3.078
Exp L5	3.246 ± 0.262	4.754 ± 0.252	55.68 ± 2.739
Long Average	3.244 ± 0.268	4.776 ± 0.256	55.81 ± 2.910

6.1.2. SiC/SiC CMC

By measuring 6 independent samples that were produced with the same manufacturing process, it was also possible to assess whether the unit-cell distortions exhibited the same statistical distributions. This was performed by computing the spacing between sequential crowns for each biased tow in the composite, mathematically expressed as $U_{unit} + \delta u_i$ in the hoop direction and $2V_{unit} + \delta v_i$ in the axial direction. The distributions for both the hoop and axial spacing for all CMCs are visually summarized in normal-probability plots for each specimen (Fig. 4.9), which show that the variance in spacing actually differed substantially between the sample of composite specimens. The deviations from a straight line (path of a normal distribution) indicated fewer extreme values compared to a Gaussian distribution. The difference between specimens was confirmed using a k-sample Anderson–Darling test, emphasizing that the six distributions of the tow spacing were not statistically similar (Table 4.3). Notably, this test put more emphasis on the tails of the cumulative density function than other similar tests.

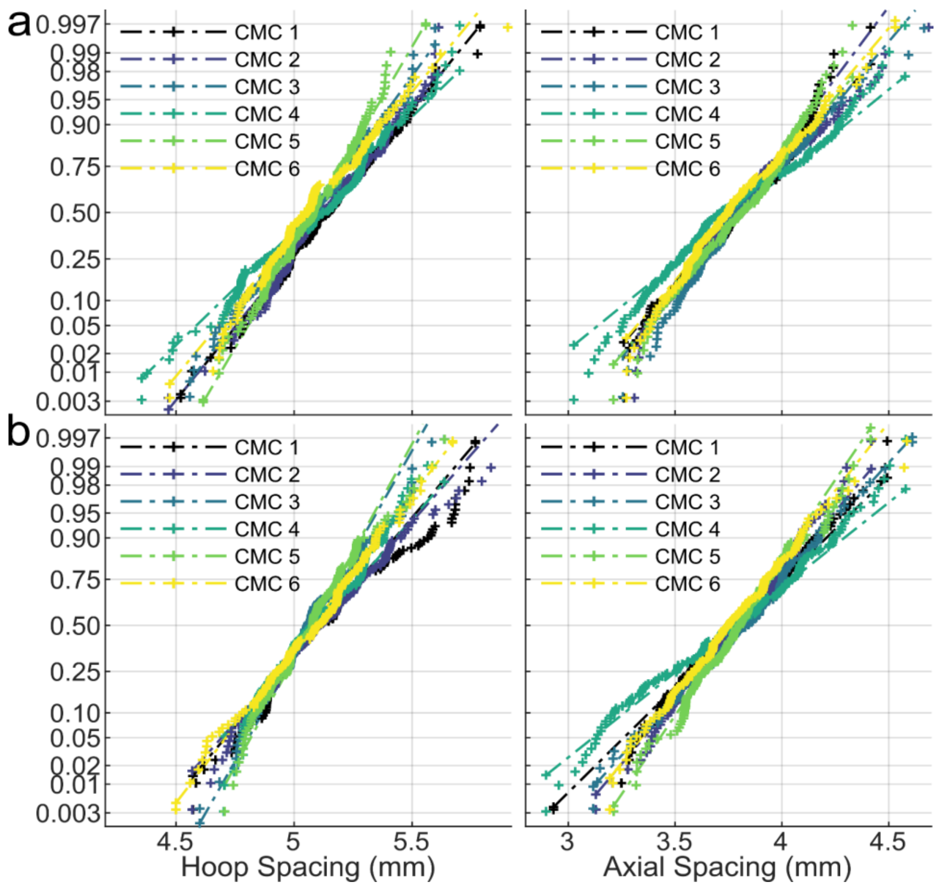

Fig. 4.9. Normal probability plots for 6 CMC specimens. (a) Hoop unit cell variation, axial unit cell variation for positive tow family. (b) Hoop unit cell variation, axial unit cell variation for negative tow family.

Table 4.3. Statistical summary of local tow trajectories (mean ± σ), and results from k-sample Anderson-Darling statistical analysis (k=6). Statistical significance: *p<0.05, **p <0.001. Note angle here is from horizontal.

	Hoop Spacing (mm)		***Axial Spacing (mm)***		
Specimen	***+35°***	***-35°***	***+35°***	***-35°***	***n***
CMC 1	5.15±0.23	5.14±0.26	3.79±0.25	3.79±0.29	144
CMC 2	5.13±0.22	5.16±0.26	3.80±0.28	3.79±0.25	144
CMC 3	5.08±0.22	5.08±0.19	3.83±0.26	3.82±0.29	138
CMC 4	5.09±0.28	5.09±0.21	3.77±0.34	3.76±0.37	156
CMC 5	5.08±0.17	5.08±0.18	3.80±0.24	3.80±0.23	156
CMC 6	5.07±0.23	5.08±0.23	3.77±0.26	3.76±0.26	144
A^2	5.46	2.9	3.76	4.63	
P-value	0.0002^{**}	0.0125^{*}	0.0036^{**}	0.0009^{**}	

6.2. Deviations from average unit cell dimensions

Deviations in the tow crown position from their theoretical positions can be understood colloquially as tow displacements. For purposes of this work, we present two classes of tow displacements (Fig. 4.10). First, I define *long-range defects* as the collective motion of adjacent tows, which produces large regions of similar non-zero displacement. On the other hand, I define *short-range defects* as the high-frequency oscillatory variation in spatial displacement fields, which identifies the independent motion of tows.

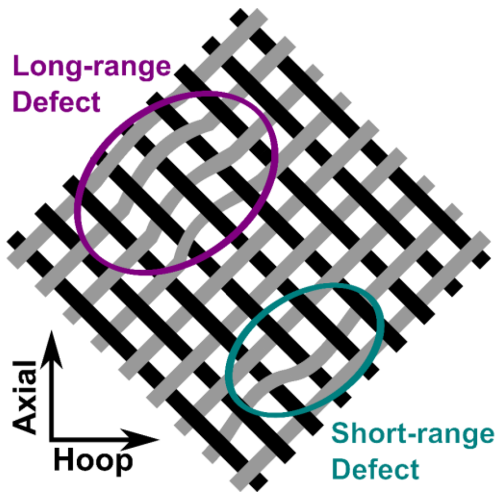

Fig. 4.10. Schematic of biaxial braid illustrating a comparison between a long-range defect, which propagates over much of the surface and a short-range defect, which is contained to a single or few tows.

6.2.1. **CFRP**

Displacement fields are plotted in Fig. 4.11 for the short composites, and Fig. 4.12 for the long composite tubes. Significant long-range distortion of up to 1 mm in magnitude was observed in both the hoop and axial directions; qualitatively, the magnitude of displacement was slightly larger in the hoop direction. The most prominent direction of variation in both the U and V displacement fields was in the hoop direction, indicating both normal (*e.g.*, Exp S2 & Exp S4) and shear (*e.g.*, Exp S1 & Exp S5) deformations in the braid, respectively. On top of these low-frequency distortions, we observed high-frequency variations in the hoop directions for both the

U and V displacements; these were particularly prominent in the large specimens (Fig. 4.12).

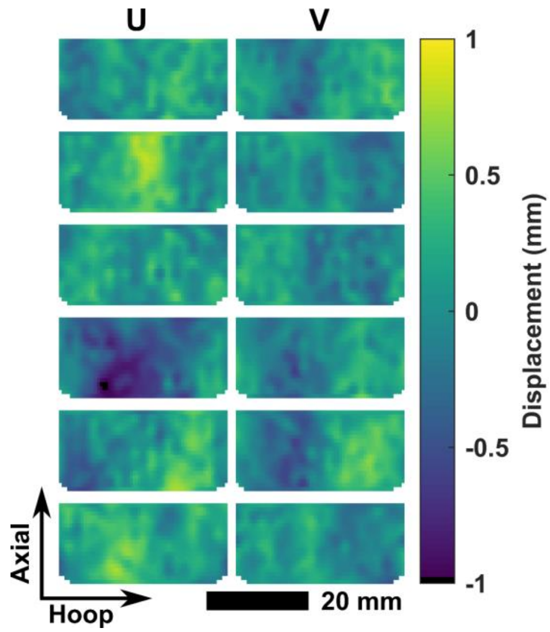

Fig. 4.11. Hoop (U) and axial (V) direction CFRP tow crown displacements from ideal composite model for short specimens, corresponding to Exp S1 through Exp S6 from top to bottom.

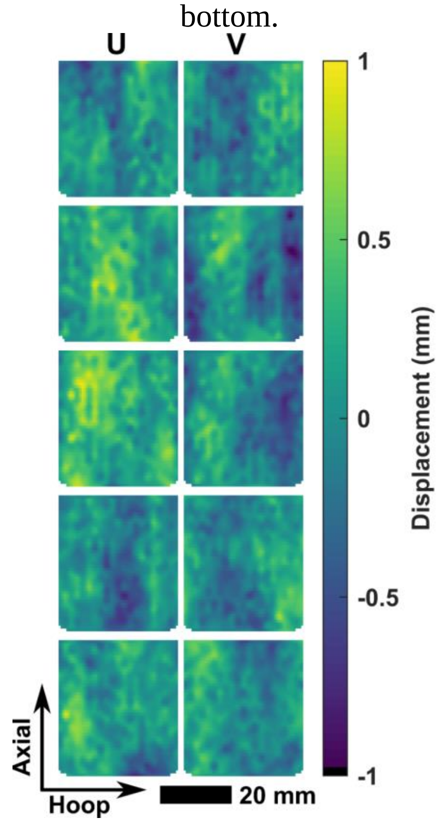

Fig. 4.12. Hoop (U) and axial (V) direction CFRP tow crown displacements from ideal composite model for long specimens, corresponding to Exp L1 through Exp L5 from top to bottom.

6.2.2. SiC/SiC CMC

Displacements in tow location from the ideal geometry are presented in Fig. 4.13 for both the hoop U and axial V directions. In general, the U displacement fields showed alternating positive and negative displacements in the hoop direction, indicating that adjacent axial tows tended to cluster together in pairs. Variation in the axial direction was limited and exhibited small wavelengths, suggesting that the axial tows constrained the motion of biased tows in the hoop direction. In contrast, the V displacement fields exhibited systematic distortion of up to 1 mm caused by the collective sliding of neighboring biased tows in the axial direction. In some specimens, this variation was observed over the entire area of interest (height of 75 mm). This behavior produced systematic tow waviness with a wavelength equal to the circumference of the cylinder and amplitude near 0.5 mm.

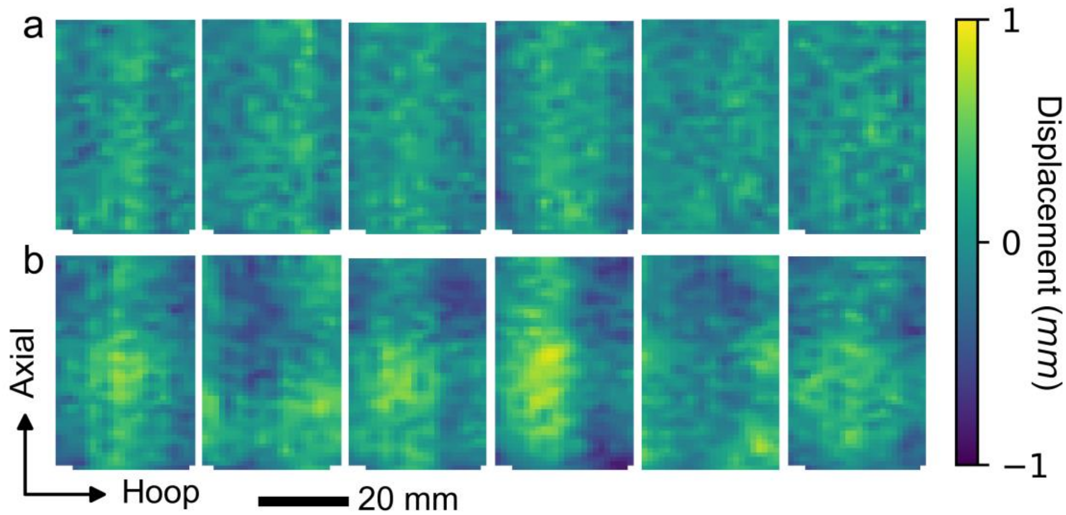

Fig. 4.13. Spatial displacement maps of the 6 CMC specimens. (a) Hoop displacements U. (b) Axial displacements V.

6.3. Gradient analysis of unit cell irregularity

6.3.1. CFRP

The variations in tow placement are best visualized through the derivatives or "pseudo-strains" δ_{xx}, δ_{yy}, and δ_{xy}, which isolates both short-range defects due to motion of individual tows, as well as the boundaries of long-range defects due to collective motion of tows. These pseudo-strains are presented in Fig. 4.14 for the short specimens and in Fig. 4.15 for the long specimens. The most prominent trend is vertical stripes of large δ_{xx} that oscillate along the hoop direction and are most discernable in the long composites; this implies that the hoop coordinate of each unit cell closely resembles the coordinate of the unit cell on the preceding row, with this pattern propagating down the tube axis. Moderately strong diagonal stripes are observed in both the δ_{xx} (*e.g.*, Exp S1) and the δ_{yy} (*e.g.*, Exp L1*)* measurements, which identified the pairwise clustering of adjacent biased tows. Finally, there are some vertical stripes in the δ_{xy} plots, which identify collective shearing of the composite in the axial direction (*e.g.*, Exp S1).

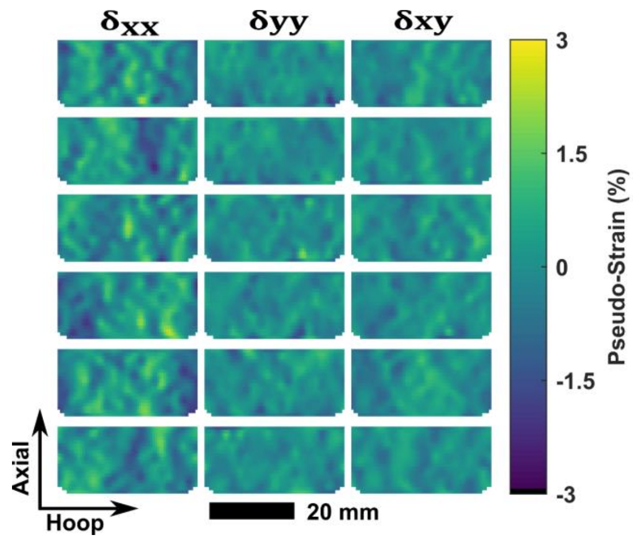

Fig. 4.14. Spatial pseudo-strains for short CFRP specimens, where x corresponds to the unwrapped hoop direction and y corresponds to the unwrapped axial direction.

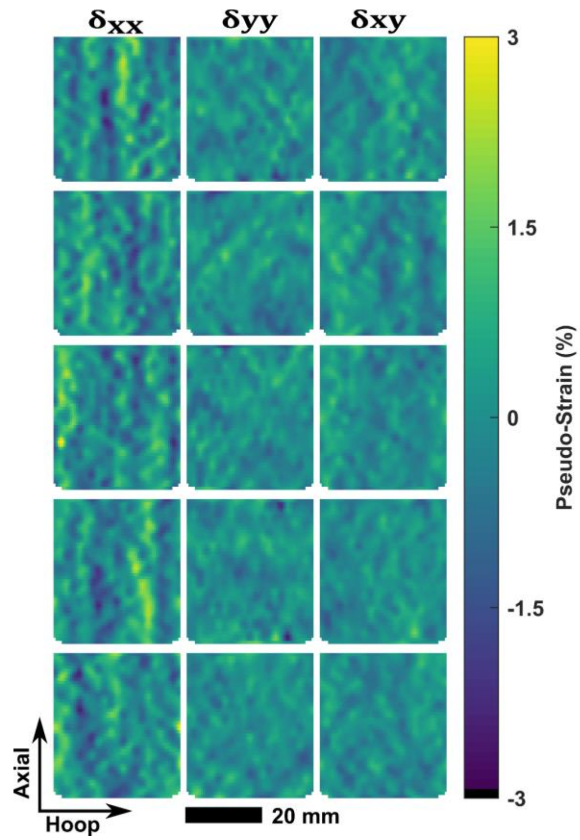

Fig. 4.15. Spatial pseudo-strains for long CFRP specimens, where x corresponds to the unwrapped hoop direction and y corresponds to the unwrapped axial direction.

The relative prominence of the short-range and long-range braid distortion can be calculated using the discrete Fourier transform (DFT) of the δ_{xx}, δ_{yy}, and δ_{xy} pseudo-strain fields. The amplitude of each frequency component is computed individually for each composite, and then averaged across the populations of short and long specimens; these results are presented in Fig. 4.16. In this figure, amplitude (color) represents the fractional prominence of each frequency component. Overall, the amplitudes are highest in intensity for the δ_{xx} power spectrum compared to the δ_{yy} and δ_{xy} power spectra, which indicates that the primary direction of tow motion is along the hoop direction. This is further supported by the prominent horizontal stripe of frequency components in the δ_{xx} spectrum. In all three spectra, moderate intensity frequency components exist in the diagonal lobes, which correspond to the directions of the biased tows.

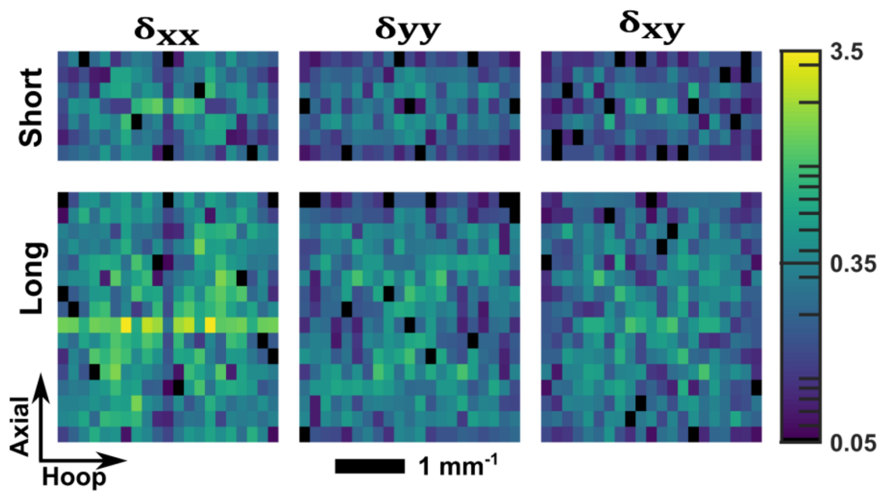

Fig. 4.16. 2D DFT amplitude of pseudo-strains δ_{xx}, δ_{yy}, δ_{xy}, for both short and long CFRP specimens. The frequencies of the DFTs are shifted such that the origin at the plot center indicates a zero frequency.

6.3.2. SiC/SiC CMC

Spatial derivatives of the displacement fields are able to distinguish variation in unit cell dimensions. The resulting *"pseudo-strain"* fields (Fig. 4.17) highlight the roles of the three different families of tows on the composite distortion; arrows are used to emphasize the pattern directionalities relevant to each strain field. Hoop pseudo-strains δ_{xx}, (Fig. 4.17a) varied strongly in the hoop and moderately in the diagonal directions, implying that hoop strains were primarily caused by systematic clustering of axial tows and secondarily by local shifts in the crown position for biased tows. In contrast, axial pseudo-strains δ_{yy} (Fig. 4.17b) showed strongest variation in the axial direction and moderate variation along the biased tow directions; axial variation suggested that individual rows of biased tows shifted collectively along the specimen axis. Finally, shear pseudo-strains δ_{xy}. (Fig. 4.17c) showed predominantly long-range variation in the hoop direction, indicative of tow waviness and the collective changes in axial displacement across the hoop direction observed in Fig. 4.17b.

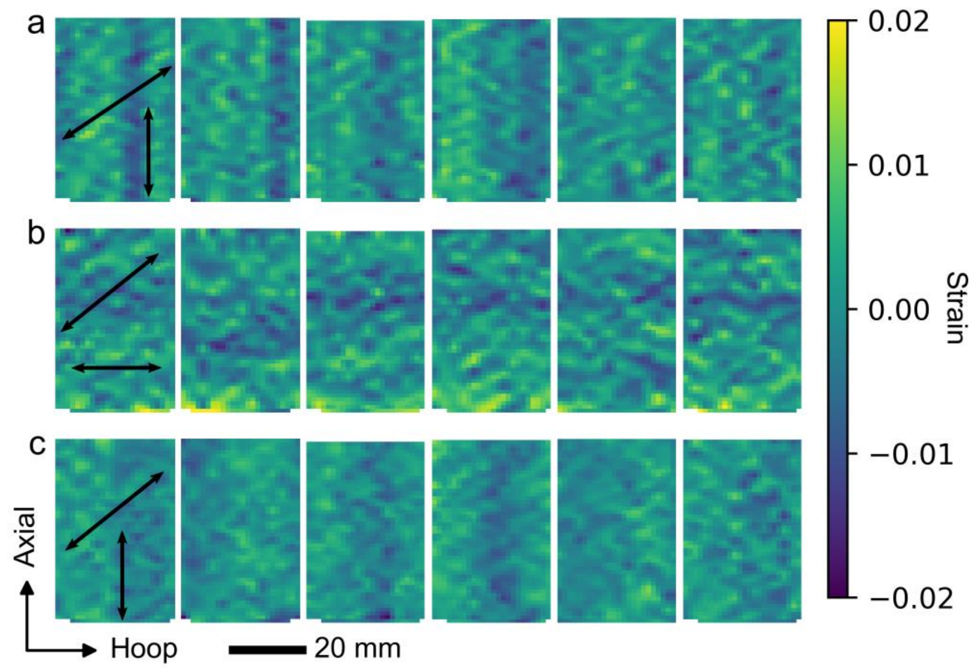

Fig. 4.17. Spatial derivatives of displacements of the 6 CMC specimens. (a) Hoop pseudo-strain δ_{xx}. (b) Axial pseudo-strain δ_{yy} . (c) Shear pseudo-strain δ_{xy}. Arrows highlight dominant directionalities.

Two-dimensional discrete Fourier transforms (DFT) of the pseudo strain fields were used to characterize the disorder in the composites. DFTs were computed individually for the 6 specimens for both hoop and axial strains, and the *averaged* amplitudes are presented in Fig. 4.18; ovals are used to emphasize the location of relevant frequency information. These frequency spectra confirmed the trends observed in Fig. 4.18, namely that hoop strain δ_{xx} and shear strain δ_{xy} varied predominantly in the hoop direction, and that axial strain δ_{yy} varied most strongly in the axial direction, which was consistent with prior measurements by Rossol on 2D woven composites.[31] However, significant diagonal lobes in Figs. 4.18a-c revealed that short-range disorder also propagated along biased tows (as indicated by higher-frequency terms), which implied that the variation could not be fully captured with one-dimensional DFTs along the hoop and axial directions. These lobes were not reported for planar harness-weave[31] or twill-weave[39] composites, where variation was restricted to the orthogonal warp and weft directions.

In other words, the additional tow interactions introduced by the triaxial braid caused more complex unit cell distortions.

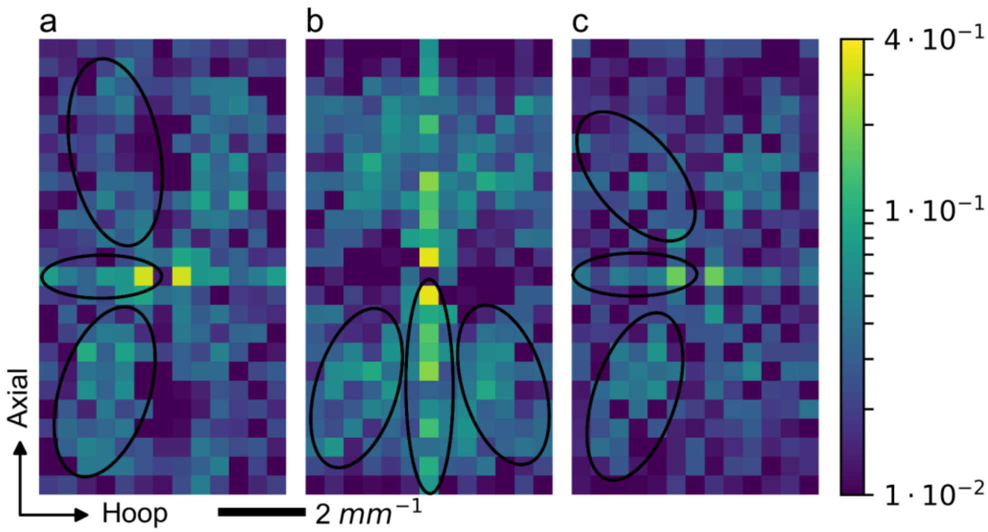

Fig. 4.18. Average DFT amplitudes for composite pseudo-strain frequencies. (a) $\bar{A}_{\delta_{xx}},$ hoop pseudo- strain, (b) $\bar{A}_{\delta_{yy}}$ axial pseudo-strain, and (c) $\bar{A}_{\delta_{xy}}$ shear pseudo-strain.

7. Discussion

The robust and scalable M-DIC and tow segmentation algorithms developed in this work enabled the assessment of "in-plane" tow variation of biaxially braided CFRP and triaxially braided CMC components with complex geometries, which has several advantages compared to alternative methods. For example, results are presented for over 36 cm of CFRP tube and 42 cm of braided CMC nuclear fuel cladding, which would not be possible with previous techniques due to the cylindrical geometry. Additionally, the automated M-DIC reconstruction and tow analysis techniques facilitate inspection of exceptionally large CMC structures, such as fuel cladding tubes that are commonly several *meters* in length. In the future, this framework can be applied to other non-planar CMC components, such as complex airfoils used in gas turbines. This technique could reveal if manufacturing processes introduce curvature-specific defects in the tow architecture, particularly molded components.

Analysis of variation in tow arrangement for the braided CMC tubes provided insight into the formation of tow packing defects in braided composites. At a high level, the variation could be categorized as either “intrinsic” defects that exhibited only short-range order due to braid constraints, or “systematic” defects that exhibited long-range order over the entire composite (in either the axial or hoop directions). The explicit distinction between these types of defects was not possible in prior measurements on [0°/90°] woven composites, since the tow directions aligned with the processing directions.[31,39] Accurate reconstruction of braided “virtual specimens” requires the modeling of both types of defects. A straightforward approach is the generation of statistically-representative 2D amplitude and phase spectra based on a population of experimental measurements, which can be converted to pseudo-strain fields by inverse DFT.

7.1. Biaxial tow placement variability in CFRP

The results indicate that the local width of the unit cell (along the hoop) of the tubes incurs substantially more nonuniformity than the height (along the axial). In fact, short-range axial defects are marginal. However, long-range shearing in the axial direction is prevalent. Angled tows tend to cluster in pairs and prefer to slide along each other, promoting high frequency waviness that tends to be displayed as distortion in the unit cell slanted with the biased tow angle. These observations and the measurements taken enable an explanation for much of this behavior.

A comparison between the DFTs of δ_{xx} and δ_{yy} in Fig. 4.16 illustrates that deviations from an ideal unit cell have a strong correspondence with the hoop direction and negligible correspondence with the axial direction. Furthermore, results show that the typical biased tow angle is roughly ±55° from the tube axis, instead of the nominal orientation of ±45°. Both observations support a long-range axial relaxation or trellising effect of the braid during manufacturing, in which an equilibrium was reached once tension in the braid was released prior to epoxy impregnation. However, this relaxation was not uniform along the circumference causing the low frequency shearing seen in δ_{xy} of Fig. 4.16 and the same behavior more clearly defined in Fig. 4.14, likely due to sliding friction with the inner layer or braid twisting. Additionally, the high frequency angular components of the DFT of δ_{yy} indicates that since the biaxial braid is not axially constrained, the displacements in the axial direction likely only stem from biased tows clustering as well as sliding along each other.

7.2. Triaxial tow placement variability in SiC/SiC CMC

Intrinsic defects emerged from the looseness of the triaxial braid, which allowed biased tows to slightly shift from their ideal position. These defects also displaced neighboring tows due to the interlocking fiber architecture, although these defects dissipated quickly over several unit cells because of the same interlocking constraint. These displacements typically occurred orthogonal to the biased tow directions, creating the diagonal lobes seen in the DFT-measured amplitudes (Fig. 4.18). These trends are not aligned with the stronger components in the processing directions; therefore, they can be clearly decoupled from systematic irregularities.

In contrast, the systematic defects were aligned with the primary processing directions (axial and hoop), and produced the largest amplitude components of the DFT analysis. We observed three types of systematic processing defects. First, hoop strain δ_{xx} revealed strong variation in tow density along the circumference, indicating paired clustering of adjacent underlying axial tows. This trend was not observed in woven CMCs, as the position of warp tows was tightly controlled by the loom. Second, circumferential bands of large axial strain δ_{yy} were likely caused by mismatched takeoff and braid velocities during processing, although they appeared to be less prominent than equivalent "beating up" defects in woven composites. Finally, periodicity in δ_{xy} was associated with the collective sliding of biased tows in the axial direction.

7.3. Comparison of tow placement in biaxial and triaxial braided composites

The measured variation in tow placement of the biaxially braided CFRP composites can be compared to measurements of triaxially braided SiC/SiC ceramic matrix composite. In contrast to the biaxially braided composite (Fig. 4.7a), the triaxially braided composite includes an additional family of axial tows (Fig. 4.7b). DFT-calculated power spectra, amplitude for the δ_{xx}, δ_{yy}, and δ_{xy} pseudo-strains in the triaxial composite are presented in Fig. 4.18, which are analogous to the results presented in Fig. 4.16 for the biaxial composite. This comparison therefore reveals the specific role of axial tows on the development of short- and long-range defects in the braid.

Several similarities in the DFT results identify common defect-generation mechanisms for the biaxial and triaxial braid architectures. In particular, both show strong low-frequency components in δ_{xx} along the hoop direction, as well as moderate high-frequency diagonal variation in δ_{xx}, δ_{yy} and δ_{xy}. The low-frequency variation of δ_{xx} in both composites is caused by large collectively displaced regions of unit cells along the hoop direction, which indicates that the hoop-wise positioning of tow crowns was poorly regulated. On the other hand, high-frequency diagonal components in δ_{xx}, δ_{yy} and δ_{xy} is associated with the sliding of biased tows along underlying biased tows. Given their appearance in both types of braid architectures, these mechanisms seem intrinsic to the braiding process.

Differences originating from the influence of each braid architecture can also be identified from the DFTs. Overall, the biaxial composites exhibit substantially higher magnitude of variation compared to the triaxial composites, as evident in the intensity ranges. Additionally, the δ_{yy} variation is very different for the two braid architectures: there is only moderate variation in the axial direction in the biaxial composite, but a very prominent band of substantial long-range, low-frequency defects in the triaxial composite. These differences are due to the axial tows, which limit the hoop-wise motion of tows associated with δ_{xx} and promote the systematic sliding of biased tows on the underlying axial tows associated with δ_{yy}. Therefore, both of these observations suggest that the addition of axial tows redirects the preferred direction of biased tow directional sliding towards the axial direction.

Finally, the braid architecture promotes unique correlations between the axial and hoop dimensions of each experimental unit cell; specifically, the irregularity in unit cell information from Fig. 4.8 and Fig. 4.9 can be compared (Fig. 4.19). In the biaxial braid, there exists a negatively-sloped linear relationship between the hoop and axial unit cell deviations, which is indicative of trellising. However, no such trend exists in the triaxial braid, indicating that the axial tows constrain the motion of the biased tows. Instead, the triaxial unit cells show a preference for particular discrete hoop dimensions, resulting in vertical stripes in Fig. 4.19b; this is caused jointly by the vertical sliding of biased tows on rigid axial tows, as well as the irregular positioning of axial tows in the composite. The distortion tendencies of both braids appear to greatly depend on the source of directional looseness, enabling sliding, intrinsic to the interlocking nature of each braid, and therefore, both have separate, unique distortions in unit cell dimensions.

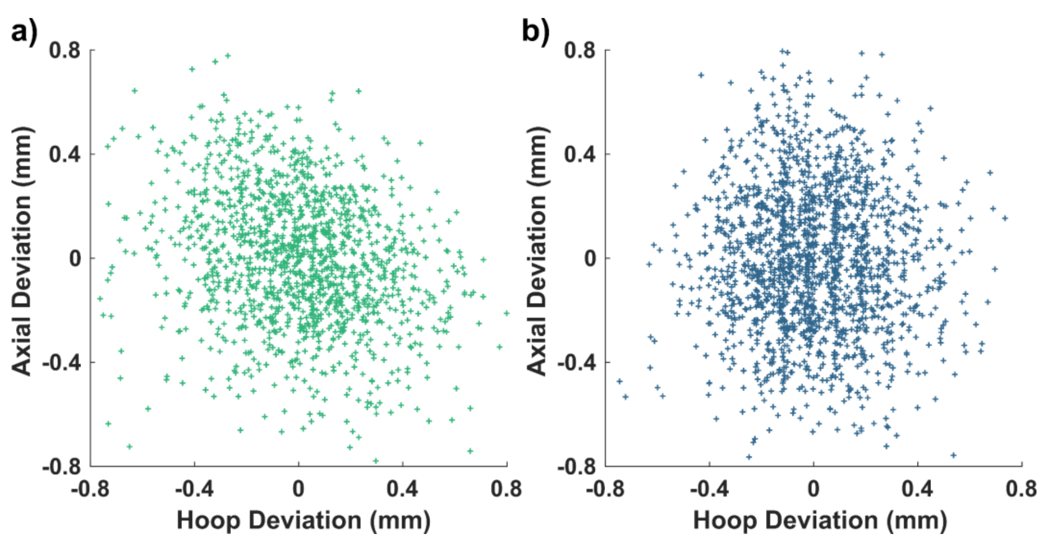

Fig. 4.19. Correlation between average centered or *deviations* from ideal in axial and hoop unit cell dimensions for (a) Biaxial, and (b) Triaxial braided composites.

7.4. *Development of realistic composite models*

The current measurements demonstrate that tow placement in composites is irregular and exhibits spatial relationships that are intrinsic to the specific braid architecture. These patterns must be incorporated in computational models to accurately predict the range of mechanical properties in the composite. In contrast, simple periodic architectures, or even periodic architectures with statistic-based irregularity added to each unit cell, are unable to capture the true spatial behavior of braid defects, which have been shown to depend on tow orientation and braid type.

In this chapter, two different routes toward numerical simulation are presented. First, 3D virtual models could be generated from experimental tow trajectories that were recovered from the M-DIC measurements. Creation of these models required few assumptions, and could easily be converted to computational models. These models could then be exported into finite element solvers to compute the mechanical response, which can subsequently be compared to experimental results. Second, the experimental analysis of tow placement defects can be used to generate statistically representative braid architectures, consistent with current statistical modeling. These models can then be used to investigate the criticality of specific combinations of unit cell dimensional distortions to isolate which significantly impact mechanical performance. This information could then be used to provide feedback in a manufacturing quality control system.

8. *Conclusions*

A scalable technique for full-field surface metrology based on digital image correlation was used to quantify the irregular tow placement in biaxially braided CFRP composite tubes. Using the recently developed M-DIC methodology, it was possible to efficiently determine the positions of surface tow crowns and reconstruct the trajectories of individual tows. Analysis of the experimental derived unit cell dimensions revealed significant spatial variation in tow placement. Biaxial braid results were compared to triaxial results to determine braid specific defect formation mechanisms as well as those intrinsic to in the braiding process. Key scientific contribution and conclusions include:

- A new set of algorithms was developed to infer the arrangement of tows from periodic height variation in the measured surface. These measurements were then compared to the ideal unit cell geometry to unveil spatial variations in tow packing density.
- The triaxial composites exhibited long-range systematic distortions in the axial and hoop direction created by processing equipment, as well as short-range intrinsic defects that aligned with the biased tow directions.
- Analysis of the biaxial braid experimental unit cell geometries revealed both long- and short-range defects in tow placement. Long-range defects in tow placement were most prominent in the hoop direction, while short-range defects most prominent in the biased direction.
- Stochastic measurements are presented to facilitate the development to of statistically-representative virtual composites for accurate modeling of triaxially and biaxially braided composite behavior.
- Braid architecture significantly affects the irregular placement of tows in the composite. Unit cells in the biaxial braid show extensive trellising, and the unit cells dimensions varied most significantly in the hoop direction. In contrast, triaxial data showed the introduction of comparatively rigid axial tows inhibited tow motion in the hoop direction and redirected this motion to align with the axial tows. Overall, the variation in unit cell dimensions was smaller for the triaxial braid than for the biaxial braid.

9. References

[1] Pankow M, Justusson B, Riosbaas M, Waas AM, Yen CF. Effect of fiber architecture on tensile fracture of 3D woven textile composites. Compos Struct 2019;225. doi:10.1016/j.compstruct.2019.111139.

[2] Berbon MZ, Rugg KL, Dadkhah MS, Marshall DB. Effect of Weave Architecture on Tensile Properties and Local Strain Heterogeneity in Thin-Sheet C-SiC Composites. J Am Ceram Soc 2002;85:2039–48. doi:10.1111/j.1151-2916.2002.tb00401.x.

[3] Melenka GW, Bruni-Bossio BM, Ayranci C, Carey JP. Examination of voids and geometry of bio-based braided composite structures. {IOP} Conf Ser Mater Sci Eng 2018;406:12012. doi:10.1088/1757-899x/406/1/012012.

[4] Melenka GW, Carey JP. Experimental analysis of diamond and regular tubular braided composites using three-dimensional digital image correlation. J Compos Mater 2017;51:3887–907. doi:10.1177/0021998317695418.

[5] Melenka GW, Carey JP. Development of a generalized analytical model for tubular braided-architecture composites. J Compos Mater 2017;51:3861–75. doi:10.1177/0021998317695421.

[6] Bruni-Bossio B, Ayranci C, Carey JP, Omonov T, Curtis J. Experimental testing of the tensile elastic properties of cellulose braided composites. Compos Part B Eng 2019;166:542–8. doi:10.1016/J.COMPOSITESB.2019.02.052.

[7] Heim FM, Croom BP, Bumgardner C, Li X. Scalable measurements of tow architecture variability in braided ceramic composite tubes. J Am Ceram Soc 2018;101:4297–307. doi:10.1111/jace.15564.

[8] Greenhalgh ES, editor. 7 - Defects and damage and their role in the failure of polymer composites. Fail. Anal. Fractography Polym. Compos., Woodhead Publishing; 2009, p. 356–440. doi:https://doi.org/10.1533/9781845696818.356.

[9] Boisse P, Hamila N, Madeo A. Modelling the development of defects during composite reinforcements and prepreg forming. Philos Trans A Math Phys Eng Sci 2016;374:20150269. doi:10.1098/rsta.2015.0269.

[10] Vanaerschot A, Cox BN, Lomov S V, Vandepitte D. Multi-scale modelling strategy for textile composites based on stochastic reinforcement geometry. Comput Methods Appl Mech Eng 2016;310:906–34. doi:https://doi.org/10.1016/j.cma.2016.08.007.

[11] Cox BN, Bale HA, Begley M, Blacklock M, Do B-C, Fast T, et al. Stochastic Virtual Tests for High-Temperature Ceramic Matrix Composites. Annu Rev Mater Res 2014;44:479–529. doi:10.1146/annurev-matsci-122013-025024.

[12] Rinaldi RG, Blacklock M, Bale H, Begley MR, Cox BN. Generating virtual textile composite specimens using statistical data from micro-computed tomography: 3D tow representations. J Mech Phys Solids 2012;60:1561–81. doi:10.1016/J.JMPS.2012.02.008.

[13] Das S, Warren J, West D, Schexnayder SM. Global Carbon Fiber Composites Supply Chain Competitiveness Analysis n.d. doi:10.2172/1260138.

[14] Kier ZT, Salvi A, Theis G, Waas AM, Shahwan K. Estimating mechanical properties of 2D triaxially braided textile composites based on microstructure properties. Compos Part B Eng 2015;68:288–99. doi:10.1016/j.compositesb.2014.08.039.

[15] Lightfoot JS, Wisnom MR, Potter K. Defects in woven preforms: Formation mechanisms and the effects of laminate design and layup protocol. Compos Part A Appl Sci Manuf 2013;51:99–107. doi:10.1016/J.COMPOSITESA.2013.04.004.

[16] Mills A. Automation of carbon fibre preform manufacture for affordable aerospace applications. Compos Part A Appl Sci Manuf 2001;32:955–62. doi:10.1016/S1359-835X(00)00154-8.

[17] Carey JP, Melenka GW, Hunt A, Cheung B, Ivey M, Ayranci C. Braided composites in aerospace engineering. Adv Compos Mater Aerosp Eng 2016:175–212. doi:10.1016/B978-0-08-100037-3.00006-7.

[18] Ansar M, Xinwei W, Chouwei Z. Modeling strategies of 3D woven composites: A review. Compos Struct 2011;93:1947–63. doi:10.1016/J.COMPSTRUCT.2011.03.010.

[19] Holmes J, Hafiz Y, Stachurski Z, Das R, Kalyanasundaram S. Surface topography evolution of woven thermoplastic composites under deformation. Compos Part B Eng 2020:107880. doi:10.1016/J.COMPOSITESB.2020.107880.

[20] Rossol MN, Shaw JH, Bale H, Ritchie RO, Marshall DB, Zok FW. Characterizing Weave Geometry in Textile Ceramic Composites Using Digital Image Correlation. J Am Ceram Soc 2013;96:2362–5. doi:10.1111/jace.12468.

[21] Rossol MN, Fast T, Marshall DB, Cox BN, Zok FW. Characterizing In-Plane Geometrical Variability in Textile Ceramic Composites. J Am Ceram Soc 2015;98:205–13. doi:10.1111/jace.13275.

[22] Shaw JH, Rossol MN, Marshall DB, Zok FW. Effects of Tow-Scale Holes on the Mechanical Performance of a 3D Woven C/SiC Composite. J Am Ceram Soc 2015;98:948–56. doi:10.1111/jace.13389.

[23] Rossol MN, Rajan VP, Zok FW. Effects of weave architecture on mechanical response of

2D ceramic composites. Compos Part A Appl Sci Manuf 2015;74:141–52. doi:10.1016/J.COMPOSITESA.2015.04.003.

[24] Chen M, Blacklock M, Zhang D, Gong J. Effects of stochastic tow waviness on stiffness and strength of plain-weave ceramic matrix composites. Adv Mech Eng 2017;9:1–10. doi:10.1177/1687814017727973.

[25] Yang QD, Rugg KL, Cox BN, Marshall DB. Evaluation of Macroscopic and Local Strains in a Three-Dimensional Woven C/SiC Composite. J Am Ceram Soc 2005;88:719–25. doi:10.1111/j.1551-2916.2005.00156.x.

[26] Rossol MN, Rajan VP, Zok FW. Effects of weave architecture on mechanical response of 2D ceramic composites. Compos Part A Appl Sci Manuf 2015;74:141–52. doi:10.1016/j.compositesa.2015.04.003.

[27] Croom BP, Li X, Deck CP, Xu P, Lahoda EJ. Quantifying the three-dimensional damage and stress redistribution mechanisms of braided SiC/SiC composites by in situ volumetric digital image correlation. Scr Mater 2016;130:238–41. doi:10.1016/j.scriptamat.2016.12.021.

[28] Bale H, Blacklock M, Begley MR, Marshall DB, Cox BN, Ritchie RO. Characterizing Three-Dimensional Textile Ceramic Composites Using Synchrotron X-Ray Micro-Computed-Tomography. J Am Ceram Soc 2012;95:392–402. doi:10.1111/j.1551-2916.2011.04802.x.

[29] Straumit I, Lomov S V., Wevers M. Quantification of the internal structure and automatic generation of voxel models of textile composites from X-ray computed tomography data. Compos Part A Appl Sci Manuf 2015;69:150–8. doi:10.1016/j.compositesa.2014.11.016.

[30] Desplentere F, Lomov S V., Woerdeman DL, Verpoest I, Wevers M, Bogdanovich A. Micro-CT characterization of variability in 3D textile architecture. Compos Sci Technol 2005;65:1920–30. doi:10.1016/j.compscitech.2005.04.008.

[31] Rossol MN, Fast T, Marshall DB, Cox BN, Zok FW. Characterizing in-plane geometrical variability in textile ceramic composites. J Am Ceram Soc 2015;98:205–13. doi:10.1111/jace.13275.

[32] Blacklock M, Bale H, Begley M, Cox B. Generating virtual textile composite specimens using statistical data from micro-computed tomography: 1D tow representations for the Binary Model. J Mech Phys Solids 2012;60:451–70. doi:10.1016/j.jmps.2011.11.010.

[33] Rinaldi RG, Blacklock M, Bale H, Begley MR, Cox BN. Generating virtual textile composite specimens using statistical data from micro-computed tomography: 3D tow representations. J Mech Phys Solids 2012;60:1561–81. doi:10.1016/j.jmps.2012.02.008.

[34] Arun KS, Huang TS, Blostein SD. Least-Squares Fitting of Two 3-D Point Sets. IEEE Trans Pattern Anal Mach Intell 1987;PAMI-9:698–700. doi:10.1109/TPAMI.1987.4767965.

[35] Heim FM, Daspit JT, Holzmond OB, Croom BP, Li X. Analysis of tow architecture variability in biaxially braided composite tubes. Compos Part B Eng 2020;190:107938. doi:https://doi.org/10.1016/j.compositesb.2020.107938.

[36] Lewis JP. Fast Template Matching. Vis Interface 1994;95.

[37] Lewis JP. Fast Normalized Cross-Correlation. Ind Light Magic 2001;10.

[38] Haralick, Robert M. and Sharpio LG. Computer and Robot Vision. Volume 2. Addison-Wesley; 1992.

[39] Vanaerschot A, Cox BN, Lomov S V., Vandepitte D. Stochastic Characterisation of the In-Plane Tow Centroid in Textile Composites to Quantify the Multi-scale Variation in Geometry. Multiscale Model. Uncertain. Quantif. Mater. Struct., Cham: Springer International Publishing; 2014, p. 187–202. doi:10.1007/978-3-319-06331-7_12.

CHAPTER 5: QUANTIFYING THE EFFECT OF TOW ARCHITECTURE VARIABILITY ON THE PERFORMANCE OF BIAXIALLY BRAIDED COMPOSITE TUBES

1. Introduction

Continuous-fiber reinforced, braided composites often consist of numerous micron sized fibers bundled into tows and braided around a preform to achieve a desired shape, prior to matrix application and infiltration.[1] It is commonly accepted that mechanical properties, such as strength and stiffness, are intrinsically dependent on the structure of the reinforcing tows, most notably braid angle and tow width.[2–4] Furthermore, it has been demonstrated, over multiple length scales, that measurable irregularity in the as-manufactured tow architecture is present.[5–8] While it is expected that local irregular tow-tow contact or spacing degrades mechanical performance and fatigue properties,[9,10] it has been challenging to quantify this nonuniformity over the full specimen and directly observe its effects during mechanical loading, beyond the use of X-ray tomography methods with a small range of observable volume.[3,8]

Three-dimensional digital image correlation (3D-DIC)[11] is often used to study the spatial strain response of anisotropic materials[12] and composites[13,14] during mechanical loading and entails a physically calibrated, 3D triangulation of the specimen surface, with which deformation is temporally correlated.[15] Because 3D-DIC is often used with tests of macroscale composite samples, it is exceptionally poised to provide the basis of a scalable quantification of tow structure.[16,17] Full-field defects in tow architecture have been quantified for samples of triaxially[18] and biaxially[6] braided composite tubes in Chapter 4 using surface undulations or "crowns" through digital image correlation (DIC). Importantly, it was found that defects in the tow structure spacing tend to have a spatial relationship. For example, it was found that axial tows constrained hoop-wise displacement of contacting biased tows, and therefore, promoted short-range variation in tow spacing following the axial tow path.

For braided composites with complex failure there is a current trend of implementing more representative finite element models by incorporating stochastic tow structure variation within experimentally defined statistical ranges.[19] In literature, [20–24] measurements of internal defects in both the matrix and tow architecture, for improved virtual unit cell generation, are largely based from X-ray computed tomography (XCT), as these systems are exceptionally suited to quantify spatial defects in all three dimensions at that scale. Because of the cost, complexity and limited microscale sampling region of XCT measurements, macroscale defects which may operate at periods larger than the unit cell, are hidden. Therefore, a combination of surface DIC and XCT should be used to obtain realistic tow architecture variability for numerical modeling.

In Chapter 4, it has been shown that the magnitude of tow spacing variability tends to vary per hoop and axial direction for tubular composites. As braided composites have a wide range of applications, they are subjected to manifold loading conditions. It is suspected that tow reinforcement defects which directionally align with loading mode could potentially produce the most significant effect on mechanical properties. If this behavior could be observed, it would assist in determining the necessary tow structure defect information for accurate and efficient numerical modeling. Herein, this subject has been evaluated and discussed for the polymer matrix composite specimens of Chapter 4, which have a record of their full-field, surface tow architecture irregularity.

2. *Material and methods*

2.1. *Specimens*

Carbon fiber-reinforced polymer/epoxy (CFRP) composite tubes were evaluated in this work. The sample set includes all of the "short" and several of the "long" specimens previously studied with the mosaic digital image correlation (M-DIC) and tow crown segmentation technique, in Chapter 4. Mechanical and numerical evaluation was performed on "short" tubes; while only numerical evaluation was performed on three of the five "long" tubes. The tubes (purchased from Dragonplate) featured an inner, unidirectional composite layer with 0° fiber orientation and an outer, biaxially braided layer with a measured orientation of ±55° from the tube axis. Two tubes were sectioned by a water-cooled diamond saw. Sample specific dimensions were included in the past chapter. Table 5.1 and Table 5.2 show a summary of the irregular tow "crown" placement previously found, for "short" and "long" tubes respectively.

Table 5.1. Average, standard deviation, and range of experimentally measured tow placement parameters for "short" specimens.

ID	**Hoop Spacing (mm)** Mean ± Std.	**Axial Spacing (mm)** Mean ± Std.	**||Angle|| (deg.)** Mean ± Std.	**U Disp. (mm)** Range	**∂U/∂x Derv. (mm/mm)** Range	**∂V/∂y Derv. (mm/mm)** Range
S1	3.275 ± 0.231	4.776 ± 0.224	55.86 ± 2.481	0.866	4.036e-2	3.356e-2
S2	3.239 ± 0.218	4.712 ± 0.205	55.50 ± 2.306	1.092	4.144e-2	2.305e-2
S3	3.234 ± 0.218	4.801 ± 0.221	56.03 ± 2.311	0.828	4.105e-2	3.268e-2
S4	3.270 ± 0.267	4.825 ± 0.202	55.89 ± 2.633	1.352	4.576e-2	2.563e-2
S5	3.268 ± 0.259	4.840 ± 0.230	55.99 ± 2.258	1.308	3.764e-2	2.905e-2
S6	3.246 ± 0.243	4.758 ± 0.211	55.70 ± 2.572	1.116	3.317e-2	2.707e-2
Average	3.290 ± 0.239	4.785 ± 0.215	55.83 ± 2.427	1.094 ± 0.217	3.990e-2 ± 0.421e-2	2.851e-2± 0.408e-2

Table 5.2. Average, standard deviation, and range of experimentally measured tow placement parameters for "long" specimens.

ID	**Hoop Spacing (mm)** Mean ± Std.	**Axial Spacing (mm)** Mean ± Std.	**||Angle|| (deg.)** Mean ± Std.	**U Disp. (mm)** Range	**∂U/∂x Derv. (mm/mm)** Range	**∂V/∂y Derv. (mm/mm)** Range
L2	3.200 ± 0.275	4.773 ± 0.237	56.16 ± 2.939	1.331	4.846e-2	4.440e-2
L3	3.302 ± 0.272	4.780 ± 0.263	55.36 ± 3.025	1.29	5.803e-2	3.394e-2
L4	3.216 ± 0.264	4.765 ± 0.318	55.95 ± 3.078	1.222	4.053e-2	3.646e-2
Average	3.244 ± 0.268	4.776 ± 0.256	55.81 ± 2.910	1.281 ± 0.055	4.901e-2 ± 0.876e-2	3.827e-2± 0.546e-2

2.2. Mechanical experiments

To evaluate the role of tow structure irregularity, as measured by tow "crown" locations, mechanical tests were performed on the "short" specimens previously studied. In the past chapter, it was found for the tubes that the magnitude of irregularity was greatest along the hoop orientation; therefore, this is the targeted direction of mechanical loading. Applied internal radial expansion by expanding rubber plug tests (Fig. 5.1) are documented in ASTM C1819 – 15 and literature[12,25,26] and are commonly used to evaluate pressure vessels for energy applications. Notably, expanding plug tests are subject to a slight gradient in loading along the tube axis;[25] therefore short sections (<25 mm) of tubular specimens are recommended.

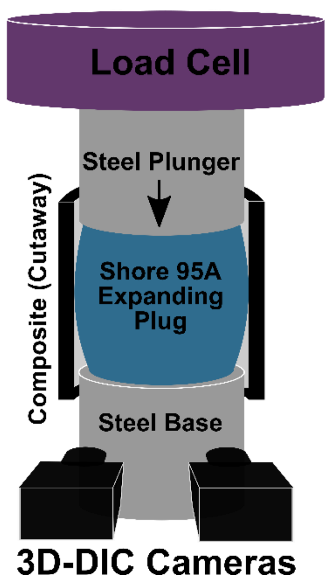

Fig. 5.1. Schematic of expanding plug setup and camera orientation.

All tests were conducted at room-temperature using an Admet eXpert 2611 table-top, universal testing machine with an 8.9 kN load cell (Admet 1210AJ-2K-B). A Shore 95A rubber plug was used with steel plungers, slightly undersize of the composite inner diameter. Past work with custom expanding plug fixtures serves to validate the present test procedure.[12] *In situ* 3D-DIC was used to measure spatial strain field development and matrix failure initiation and propagation during loading (Fig. 5.1). All samples were prepared with a random, black and white speckle pattern using conventional, matte-finish spray paints. All experimental measurements were gathered with two FLIR Grasshopper 3 GS3-U3-50S5M-C digital CMOS cameras with Schneider 21-100197 50 mm compact lenses, and were correlated using commercial 3D-DIC software (Vic-3D 8, Correlated Solutions). 3D-DIC analysis was performed with gaussian-weighted, 39 pixel subsets with a step size of 3 pixels using an optimized 8-tap and zero-normalized squared differences correlation scheme. Notably, cylindrical specimens tend to have considerable errors towards edges of the area of interest along the hoop. This was accounted for by maximizing the depth of field for the given setup via reduction of lens aperture and subsequent cropping of potentially less reliable DIC data using best judgment. Hoop-wise cropping near crown locations was performed to maintain a similar number of rows per column, which varied from 7 to 4 columns due to DIC correlation quality and continuity.

For expanding plug tests, typically hoop strain is estimated by the change in dimensions along the radial direction of the tube by averaging four radial displacement or strain sensors.[26,27] By this method, reported strains correspond to the peak hoop strain incurred on the outer diameter. This definition of hoop strain was matched for analysis with DIC correlated surface strains.[12] Therefore, singular hoop strain values per DIC correlation are reported as the average of the top 95th to 100th percentile of radial expansion strain. Hoop stress was calculated according to the isotropic thick-walled equation:[28]

$$\sigma_{Hoop} = \frac{F}{A}\frac{2*r_{in}^2}{r_{out}^2-r_{in}^2} \tag{5.1}$$

where F is the applied compressive load on the rubber plug, A is the cross-sectional area of the plug, r_{in} is the inner radius of the tube, and r_{out} is the outer radius of the tube.

2.3. Numerical models

2.3.1. Digital reconstruction of experimentally measured tow structure

Virtual models of the CFRP composites were reconstructed from the experimentally measured tow trajectories of Chapter 4 using MATLAB. To isolate the effects of tow path irregularity, "ideal" uniform tow trajectories were also reconstructed for each "short" CFRP specimen using an identical procedure. These trajectories utilize the "ideal" tow crown locations used to measure tow placement variation, detailed in Chapter 4.

As M-DIC and tow segmentation measurements only provided the locations of surface tow "crowns", several assumptions were required to render the 3D tow trajectories. First, the valleys of the tows (*i.e.,* where the tow is beneath other surface-visible tows) were assumed to be located halfway between tow crowns, and at a radial depth equal to twice the tow thickness. Second, the tow trajectories were interpolated using a cubic fit between the crowns, implemented to ensure C^1 smoothness at the locations of crowns and valleys as well as fix the location of crown and valley. Finally, the average least-squares fitted cylinder radius of 5.24 mm was used to rewrap the tow trajectories into a cylinder. The wrapped 3D tow trajectories for S1 can be seen in Fig. 5.2a. Reconstruction of the full measured tow length would lead to models containing uneven tow termination points along the axial length; therefore, the axial length was trimmed to be even with the shortest tow segment.

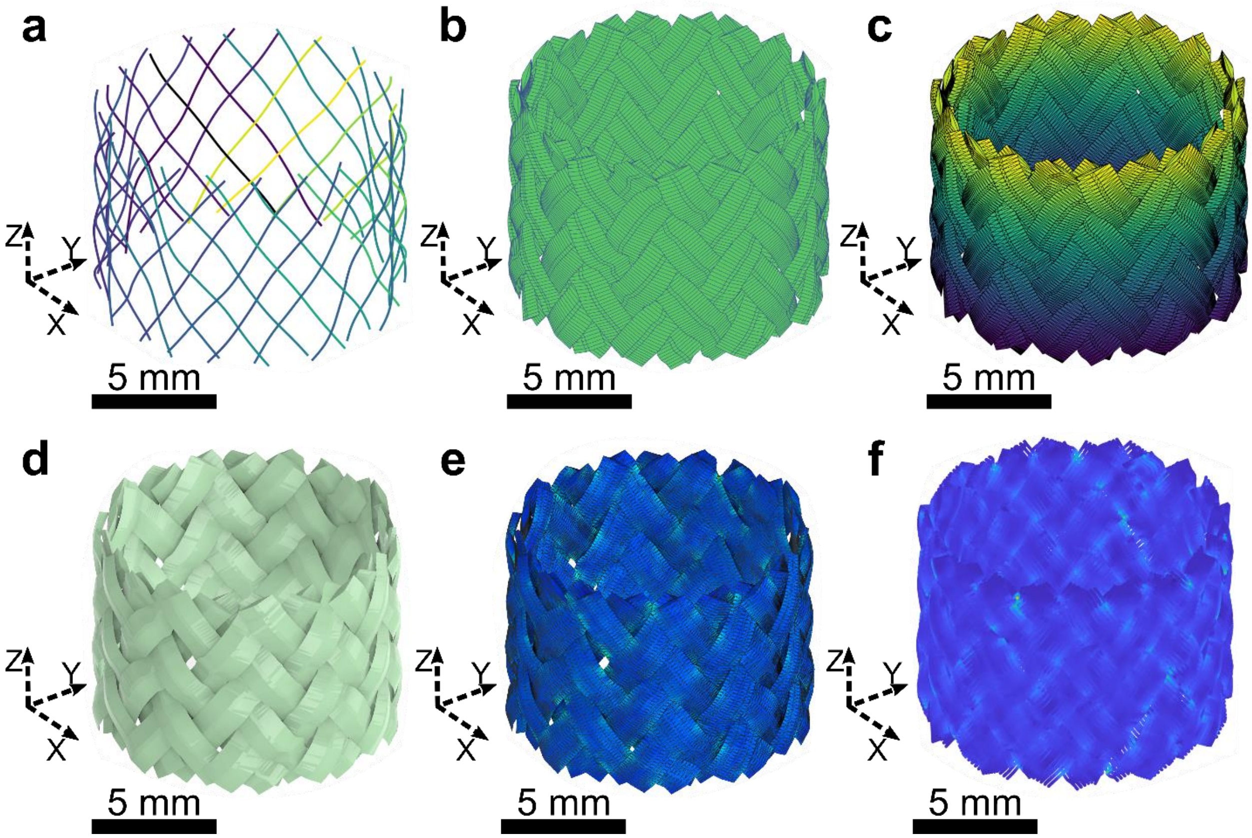

Fig. 5.2. Depictions of S1 during the sequential stages of computational processing. (a) 3D tow trajectories as lines. (b) Nonintersecting tow structure with hexagon cross-section and quadrilateral faces. (c) Triangulated tow structure. (d) Tow structure meshed as solid elements. (e) Solid tow structure with applied loading. (f) Numerical simulation output for post-processing.

The carbon fiber tow cross-section with an average thickness $(2a)$ of 0.27 ± 0.02 and width $(2b)$ of 1.4 ± 0.02 mm, defined at starred locations in Fig. 5.3a, was modeled as a hexagon with nonuniform edge lengths defined by c in Fig. 5.3a. The selected hexagonal tow cross-section j was projected down the tow trajectory $j+1$ using connected quadrilateral face components (Fig. 5.3b), inspired by other work concerning the meshing of tubes.[29] The number of hexagonal sections j comprising a single tow i was equivalent to the quantity of interpolated values N along the length of each tow; therefore, a uniform spacing was maintained between each $j, j+1, \dots j+N-1$. The influence of the magnitude of this spacing on numerical simulation results was studied and will be discussed later. Normality of each section $j, j+1, j+N-1$ was maintained towards the center of each tube (Fig. 5.3a), which is physically representative of braided tows laying on a smooth inner ply layer or mandrel.

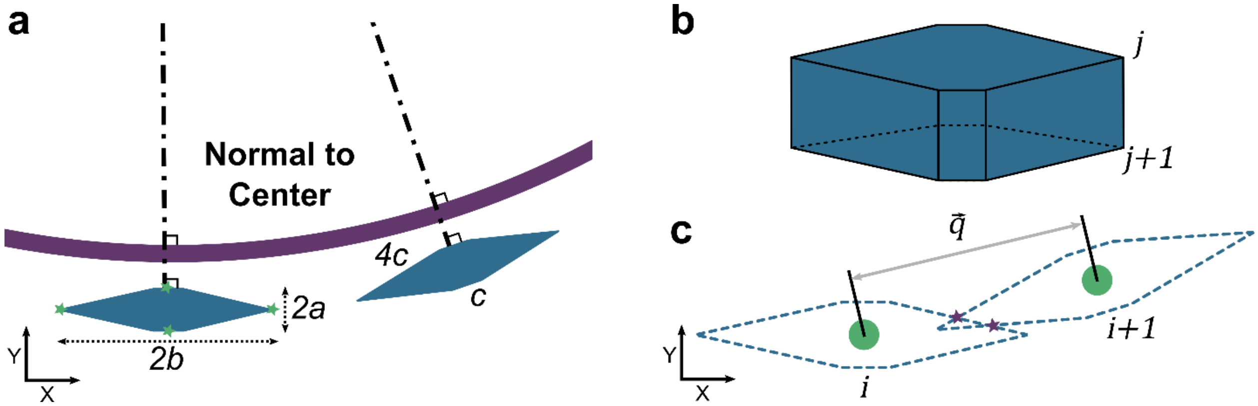

Fig. 5.3. Illustrations of parameters used to digitally reconstruct the tow structure of each composite. (a) Size and orientation of tow cross-sections. (b) Tow structure elements used in digital reconstruction. (c) Tow-face intersection mitigation scheme.

The intersection of digitally modeled tow faces was detected using an edge intersection scheme. The algorithm used was a modified implementation of the fast triangle-triangle intersection test developed and outlined by *Möller* [30]. This triangle-triangle intersection test algorithm was coded into a MATLAB function by *Tusynski* [31], who's function was modified for quadrilaterals and used here. The output of the modified intersection test included the index of intersecting faces of neighboring tows i and $i + 1$ (Fig. 5.3c).

The majority of face intersections occurred at the crossover sections of the biased tows. All quadrilateral face intersections were addressed by an iterative corrective algorithm. Mitigation of intersecting faces was implemented at the centroid of local hexagonal sections, depicted as green circles in Fig. 5.3. The Euclidean vector $\vec{q}$ was defined between the centroids of neighboring tow sections (Fig. 5.3c), which was used to define a unit vector with direction parallel to $\vec{q}$. An equal but opposite displacement of both centroids per tow i and tow $i + 1$ was applied along this direction with a magnitude which was equivalent to and could be controlled by a "shifting" factor G. Effectively, the "shifting" factor controlled the aggressiveness of the corrective displacement between intersecting tow section j per iteration. Additionally, a "smoothing" factor H was utilized to implement a similar shift of local hexagonal sections $j - H \ldots j + H$ with a displacement magnitude proportional to their proximity to j to encourage a smooth relocation of hexagonal sections. For the results with a j to $j + 1$ spacing of 0.1 mm presented here, $G = 0.001\, mm$ and $H = 1.4\, mm$.

During each iteration every tow was checked for intersections between adjacent tows for a total of 800 unique comparisons. Per iteration, a single corrective displacement was applied per hexagonal section j regardless of the number of edges detected to intersect in j, including sections moved by the "smoothing" factor, to avoid excessive relocation. The quantity of iterations of the corrective algorithm was controlled by the number of unique intersections detected per iteration. Therefore, deep intersections were corrected over multiple iterations. After zero intersections were detected from the modified intersection test algorithm, the corrective algorithm was stopped with a final result for S1 displayed in Fig. 5.2b. Using a MATLAB built-in function, the quadrilateral geometry was triangulated and exported to a stereolithography (.stl) format (Fig. 5.2c).

2.3.2. Numerical simulation parameters

The output files containing the triangulated surfaces coordinates of each tow were imported into the Ansys AIM suite as solids and meshed (Fig. 5.2d). The epoxy matrix was not modeled. A mesh size study was done with results presented in Fig. 5.4. This work included adjusting the j to $j + 1$ spacing (Fig. 5.3b) in MATLAB and maximum element length in Ansys. All other model parameters were held constant, according to values listed later. It was determined that a j to $j + 1$ spacing of 0.1 mm and a maximum mesh element length of 0.6 mm provided reasonable convergence of mechanical outputs with the least number of nodes. These mesh parameters implemented on S1 can be seen in Fig. 5.5.

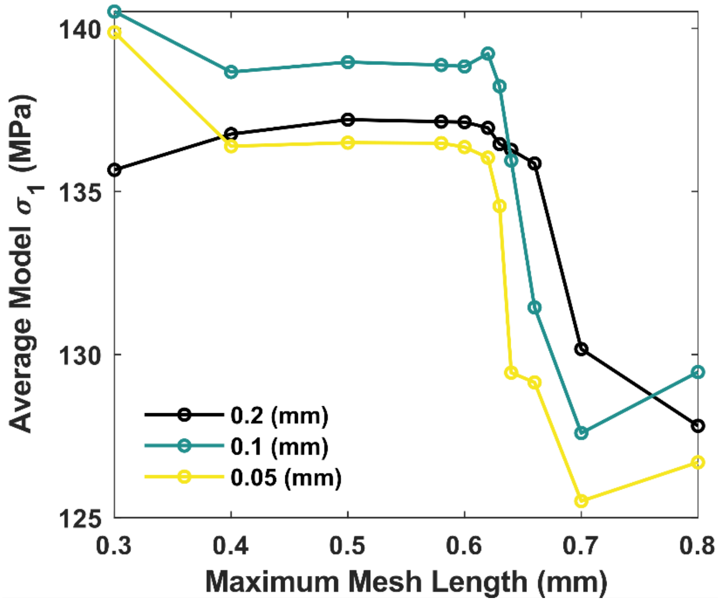

Fig. 5.4. Plot of mesh size study. Legend values correspond to distances between interpolated values of experimental tow trajectories, which is equivalent to the quantity of hexagonal sections which were used to form a tow in MATLAB. Maximum element mesh length corresponds to the largest distance between any two nodes forming an element. Reasonable convergence was found with a hexagonal section spacing of 0.1 mm and a maximum mesh length of 0.6 mm.

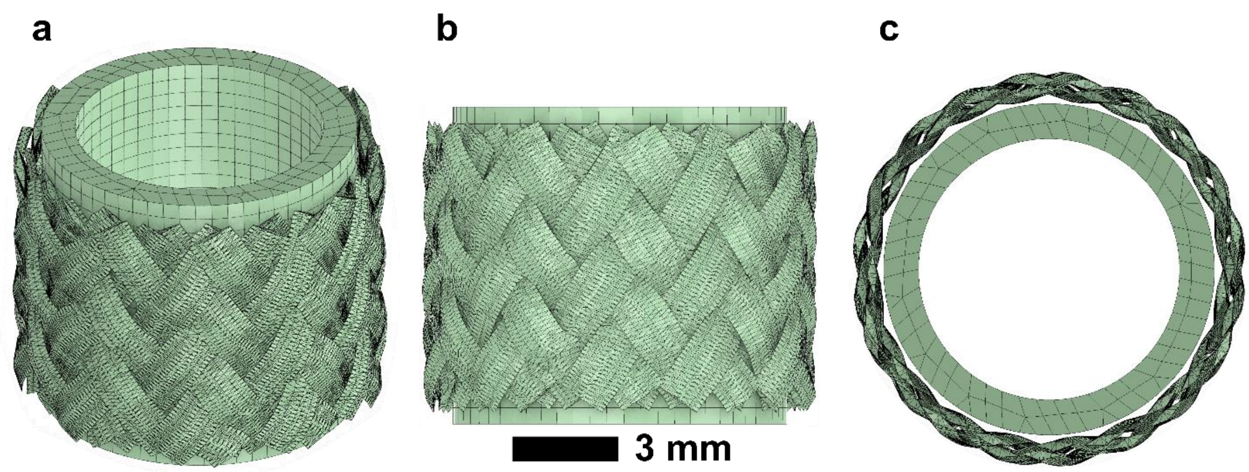

Fig. 5.5. Multiview of S1 tow structure and rubber shell numerical model. (a) Isometric view. (b) Side view. (c) Top view.

A rubber shell (Fig. 5.5a) was modeled with an outer diameter of 9.48 mm and wall thickness of 1 mm with a maximum element length of 0.5 mm. Both the rubber shell ($E = 30\ MPa, v = 0.49$) and carbon fiber tows ($E = 227.5\ GPa, v = 0.23$) were modeled as isotropic with all model contacts bonded, which is only representative for the elastic regime. Bonded contact was defined with a pinball diameter of 1 mm, which ensured that the rubber shell and all tow crossover regions were initially in contact. The outer edges of both ends of the rubber shell, which extend beyond the tow structure (Fig. 5.5b) were fixed as a support with zero movement, and a pressure of 8.6 MPa was applied normal to the rubber shell along the inner surface, which is similar to experimental conditions near the end of the elastic regime. Model outputs for each specimen include first principal stress (Fig. 5.2e), which was used in a relative manner to measure inhomogeneous responses of each specimen. These values at each node were exported into MATLAB (Fig. 5.2f) for post-processing.

Numerical results were post-processed in a manner similar to 3D-DIC outputs previously detailed.[6] Briefly, the cylindrical information was unwrapped and binned in 0.1 mm increments. Because unwrapped model outputs have depth, compared to the strictly surface-based outputs of DIC, binning was done to capture the outer, maximum surface radial height as well as the stresses at these outer locations; once binned, typical image processing techniques could be used. Examples of the binned numerical results for S1, including the nonuniform, experimentally measured trajectories (Fig. 5.6a) and uniform, "ideal" trajectories (Fig. 5.6b) are provided.

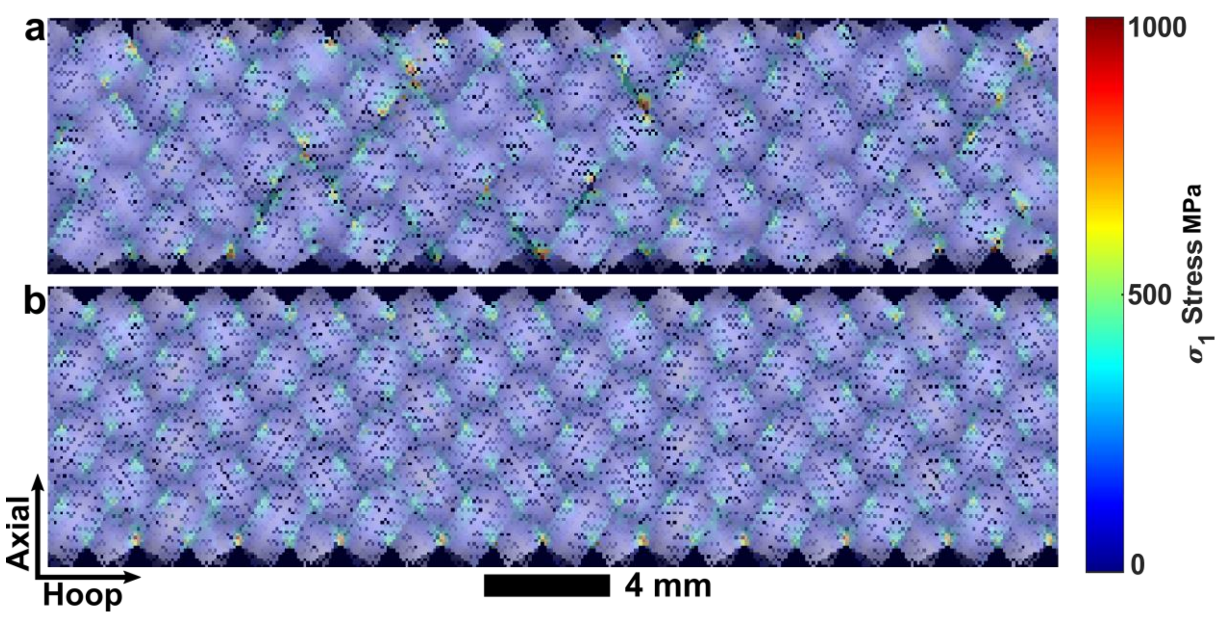

Fig. 5.6. Unwrapped and binned numerical results for S1. Maximum radial is shown in grayscale; a jet colormap, partially transparent overlay of the first principal stress is also included, which enables a direct visual comparison of outer diameter tow structure and the corresponding spatial stress response. Any blank bins were filled with NaN values which have no contribution to post-processed results. (a) Result for S1 using nonuniform, experimentally tow trajectories. (b) Result for S1 using uniform, "ideal" tow trajectories. Note that local stress concentrations are apparent near irregular tow path positions.

2.4. Measurements of tow structure nonuniformity

In past the past chapter, the tow structure irregularity was quantified by the measured centroid locations of surface tow "crowns". This process is summarized here. The average unit cell dimensions X_{unit} and Y_{unit} were calculated for each tube, depicted in Fig 5.7a. Subsequentially, ideal tow crown locations X_i^{ideal} and Y_i^{ideal} were predicted over the entire surface using a uniform grid of tow positions. The displacement of each tow crown *i* from the ideal unit cell location was calculated, according to:

$$\begin{aligned} U_i &= X_i^{ideal} - X_i \\ V_i &= Y_i^{ideal} - Y_i \end{aligned} \tag{5.2}$$

To discern local variations in tow architecture from collective displacements, the derivatives of U_i and V_i were calculated using a central differences scheme. These spatial derivatives can be represented as δ_{xx}, δ_{yy}, and δ_{xy}. The derivatives were calculated as:

$$\begin{aligned} \delta_{xx} &\approx \frac{\partial U}{\partial x} \\ \delta_{yy} &\approx \frac{\partial V}{\partial y} \\ \delta_{xy} &\approx \frac{1}{2}\left(\frac{\partial U}{\partial y} + \frac{\partial V}{\partial x}\right) \end{aligned} \tag{5.3}$$

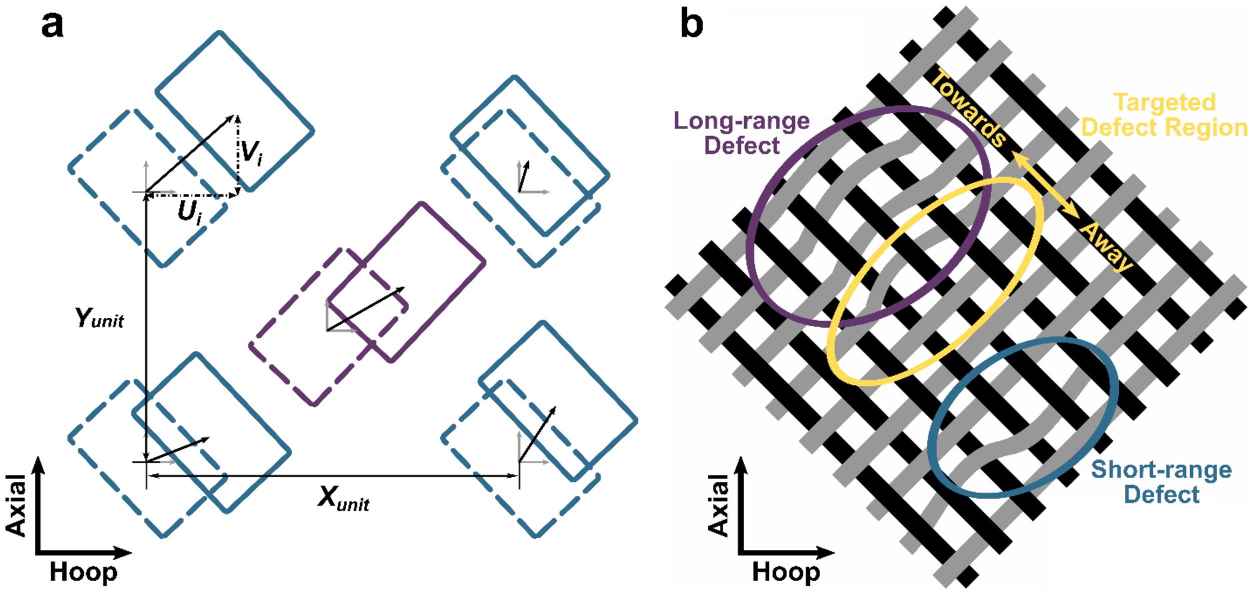

Fig. 5.7. Illustrations defining tow structure irregularity. (a) Schematic defining average unit cell dimensions and displacement from ideal location components. (b) Schematic depicting long-range, collective tow positional variation and short-range defects, which affect only a single or few tows. The yellow region highlights the regions targeted by the DIC cameras during mechanical loading.

2.5. Comparing tow structure nonuniformity and local surface strain/stress

Using the spatial derivative profiles, surface locations exhibiting a significant gradient in δ_{xx}, were manually identified. These regions of interest for mechanical loading experiments were selected as the boundaries of long-range, collective shifts in tow position, as depicted in Fig. 5.7b, and are the hypothesized locations which may have the largest impact on mechanical performance and strain progression. The approximate orientation between the digital surface profile and the physical tube was coordinated by three unique cuts in the DIC speckle pattern, which could be clearly identified in the digital surface. The position of the two DIC cameras was located to capture the targeted significant δ_{xx} gradient per sample. Therefore, a comparison between local surface strains, during internal expansion loading, and tow structure irregularity at these locations could be made. Furthermore, a comparison with tow structure irregularity profiles and numerical results was also directly possible via a coordinate transformation.

To quantify the local strain (experimental measurements) or local stress (numerical measurements) per tow crown *i* at any given load state within an elastic regime a bounding box mask was defined (Fig. 5.8). The centroid of each box, which best encompassed the crown and surrounding matrix, was determined using an identical procedure to the scheme used to determine tow crown locations over the entire composite surface. Due to the spacing between crowns and braid irregularity, several boxes contained regions of overlap with their neighbors. Additionally, a small proportion of the total matrix was not included in any bounding box. The length and width for each bounding box were set as 2.8 mm and 1.7 mm, respectively (Fig. 5.8). While the maximum strain/stress constrained within each box could correspond to local inhomogeneities, noise intrinsic to DIC and potential overlap between boxes warrants the use of an averaged value. Therefore, the local, first principal strain $\overline{\varepsilon_1^{L_i}}$ and stress $\overline{\sigma_1^{L_i}}$ was defined as the average of the 50th to 100th percentile of tensile, first principal strain/stress contained within each crown bounding box *i*.

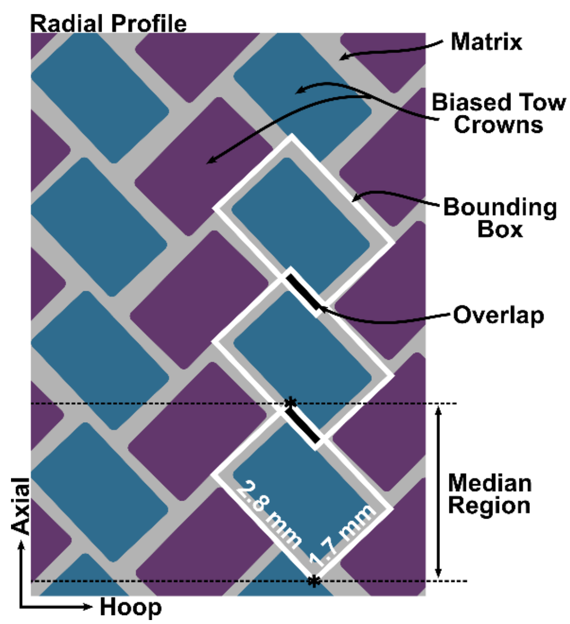

Fig. 5.8. Schematic depicting features used in normalizing local principal strain/stress per tow crown. Note, the matrix was not numerically modeled.

Because expanding plug tests are known to impart a slight gradient in radial expansion along the axial length of the tube,[25] the local measurement must be normalized relative to a nominal strain/stress measurement per a given axial location. Furthermore, by comparing a local measurement to a representative bulk measurement, the significance of tow irregularity on spatial strain/stress concentration can be determined. Here, the median value of first principal strain $\widetilde{\varepsilon_1^{H_i}}$ or stress $\widetilde{\sigma_1^{H_i}}$ over the entire DIC correlated or numerically modeled hoop region was taken with identical axial bounds as the local bounding box. This region is schematically depicted in Fig. 5.8, where the axial bounds are indicated by black asterisks. Therefore, the hoop-wise normalized local, first principal strain $\varepsilon_1^{N_i}$ and stress $\sigma_1^{N_i}$ values per crown bounding box *i*, are defined as:

$$\varepsilon_1^{N_i} = \overline{\varepsilon_1^{L_i}} \Big/ \widetilde{\varepsilon_1^{H_i}} \tag{5.4}$$

$$\sigma_1^{N_i} = \overline{\sigma_1^{L_i}} \Big/ \widetilde{\sigma_1^{H_i}} \tag{5.5}$$

Using ε_1^N and σ_1^N a comparison between local strain/stress magnitudes and spatial derivatives of tow placement irregularity can be made for every tow crown reliably observable by a single pair of digital cameras during mechanical loading or from numerical simulations of a full surface.

3. Results

Results are presented and discussed comparing experimental and numerical results stemming from the "S" short and "L" long specimens previously discussed. For clarity, the addition of "Exp" (experimental) or "Num" (numerical) is used to indicate the source of a result. For experimental results ε_1^N strain is used to demonstrate the mechanical response near each tow crown location, while σ_1^N stress is used in numerical results. While these two measures should clearly not be equal in absolute magnitude, it is proposed that within the elastic regime they should be proportional and can therefore, be used in a relative manner to identify a locally concentrated strain/stress region. Furthermore, for future practical applications, the positive or negative nature of tow irregularity measurements depends on the measured direction and is *arbitrary*, rather it is important that the measured direction is *consistent* to allow a meaningful comparison per specimen or dataset.

3.1. Expanding plug experiments

Six CFRP, biaxially braided composite tubes were loaded to failure via internal expansion. These composites exhibited three distinct failure regimes, (Fig. 5.9) including: (1) a linear elastic region, (2) fracture of the inner unidirectional 0° ply, and (3) debonding failure of the outer braided ply. While the inner unidirectional layer is exceptionally strong in tension, it is highly vulnerable to nonaxial loading, hence the relatively low deviation from linearity (DFL) stress of these composites, seen at the end of (1); these properties are listed later in Table 5.3. While some composites experienced higher stresses than others, prior to inner layer fracture, this behavior would not be expected to depend on the outer layer tow structure.

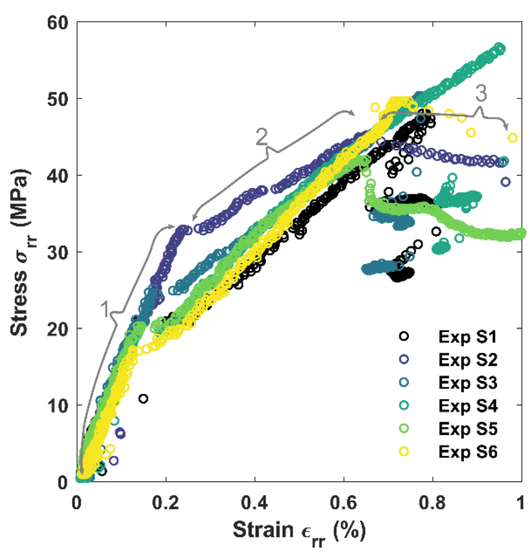

Fig. 5.9. Hoop stress and hoop strain relationship for braided CFRP composites. Gray arrows indicate distinct failure regions, where (1) is the elastic regime, (2) indicated the failure of the internal unidirectional layer, (3) indicates the failure of outer braided layer.

3.2. *Experiments for relating tow irregularity and local strain magnitude*

Stereoscopic DIC measurements were targeted at the interfaces of long-range defect locations of each CFRP tube during internal expansion loading. The normalized first principal strain, which is representative of the local strain state surrounding a tow crown, can then be compared to tow structure irregularity. It was found that δ_{xx} and ε_1^N tend to have a decreasing linear relationship (Fig. 5.10a), meaning a rapid hoop-wise change in tow structure serves to alter the local surface strain response experience in the CFRP braid, which is quantified here for the first time. Direct visualization of the tow structure U displacement (Fig. 5.10b), δ_{xx} derivative (Fig. 5.10c), and ε_1^N normalized strain (Fig. 5.10d) at each tow crown location observed by DIC can be seen in Fig. 5.10.

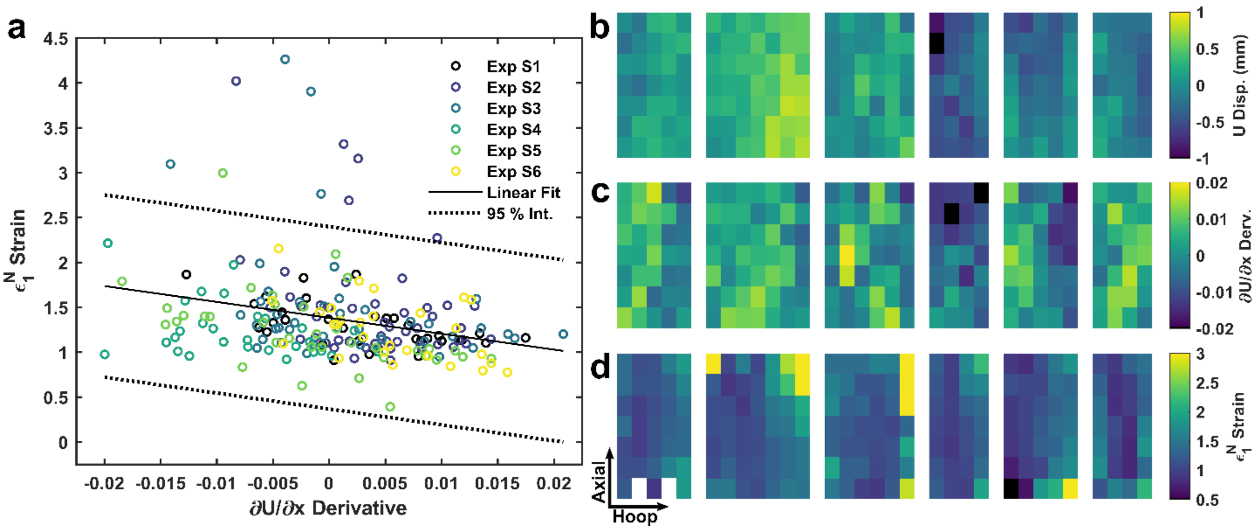

Fig. 5.10. Plot and spatial profiles depicting measurements of tow structure irregularity and normalized local strain measurements. (a) Scatter plot illustrating linear relationship between δ_{xx} (∂U/∂x derivative) and normalized, local first principal strain ε_1^N. (b) Hoop direction tow crown displacements from ideal, uniform locations. (c) Spatial derivative δ_{xx} taken along hoop. (d) Normalized, local first principal strain ε_1^Nat tow crown locations. For b-d), each pixel corresponds to a single tow crown and left to right blocks corresponds to S1 to S6.

To prove the statistical significance of the trend, Pearson correlation coefficient tests were performed (Table 5.3), where the null hypothesis is that no linear relationship exists and the alternative hypothesis is that a linear relationship exists. For all short specimens, the p-values indicated a rejection of the null hypothesis between ε_1^N and δ_{xx} to the 95 % confidence level, with several significant to the 99 % confidence level. Interestingly, a similar result was not seen for the U displacement (Table 5.3), from which δ_{xx} (∂U/∂x derivative) stems, with correlation coefficients varying widely and zero p-values significant to the 0.05 level. This result indicates that gradients in tow structure are more damaging to mechanical performance than the magnitude of displaced tow position. Notably, large shifts in δ_{xx} were targeted in these experiments, and no other past measures (U, V, δ_{yy}, δ_{xy}) of tow irregularity tended to have any correspondence to the local strain response observed at each tow crown. However, more experiments would need to be performed to prove their insignificance.

Table 5.3. DFL stress and strain values per specimen and Pearson correlation coefficient with associated p-values, * significant to 95 % confidence, ** significant to 99 % confidence.

Specimen ID	**DFL Stress (MPa)**	**DFL Strain (%)**	**ε_1^N - δ_{xx} Correlation**		**ε_1^N - U Correlation**	
			R	P-value	R	P-value
Exp S1	20.86	0.1408	-0.5563	0.0008**	0.1694	0.346
Exp S2	32.25	0.2292	-0.3761	0.0077**	0.2374	0.1005
Exp S3	25.16	0.1698	-0.3213	0.0380*	0.0171	0.9145
Exp S4	20.14	0.1431	-0.3759	0.0487*	0.3453	0.0719
Exp S5	20.3	0.1447	-0.4866	0.003**	0.1794	0.3024
Exp S6	17.16	0.1257	-0.4976	0.0071**	-0.0619	0.7544
Average	22.65	0.1589	-0.4356		0.1478	

3.3. Numerical simulations for relating tow irregularity and local stress magnitude

Numerical simulations of the expanding plug experiments utilizing representative tow trajectories, constructed from past DIC-based measurements of tow crown positions for each composite, provides a basis to explore the relationship between heterogenous stress/strain response and nonuniform tow structure. Using an identical normalization procedure for outer surface stress, exported from numerical modeling simulations, a similar trend can be seen for both the "short" (Fig. 5.11a) and "long" (Fig. 5.11b) specimens modeled. Critically, both batches of CFRP tubes agree well with experimental results. Furthermore, "ideal" composite models demonstrated a globally uniform stress response per bounding box region (Fig. 5.6), with a nominal slope of zero between σ_1^N and δ_{xx}. Direct visualization of the tow structure U displacement (Fig. 5.12a), δ_{xx} derivative (Fig. 5.12b), and σ_1^N normalized stress (Fig. 5.12c) at each tow crown location contained in each simulation can be seen in Fig. 5.12. An example of the relative agreement between experimental and numerical results can clearly be seen in S2, where the central region of Fig. 5.12a corresponds to the location in Fig. 5.10b. The Pearson correlation coefficient test between δ_{xx} and σ_1^N was repeated for Num S1-Num S6 to reveal a strong significance, disproving the null hypothesis for each numerically simulated CFRP composite to a minimum of 99.95 % confidence level. The lack of a correlation between U displacement and σ_1^N was reaffirmed by numerical simulations, with a nominally zero slope, seen in Fig. 5.13.

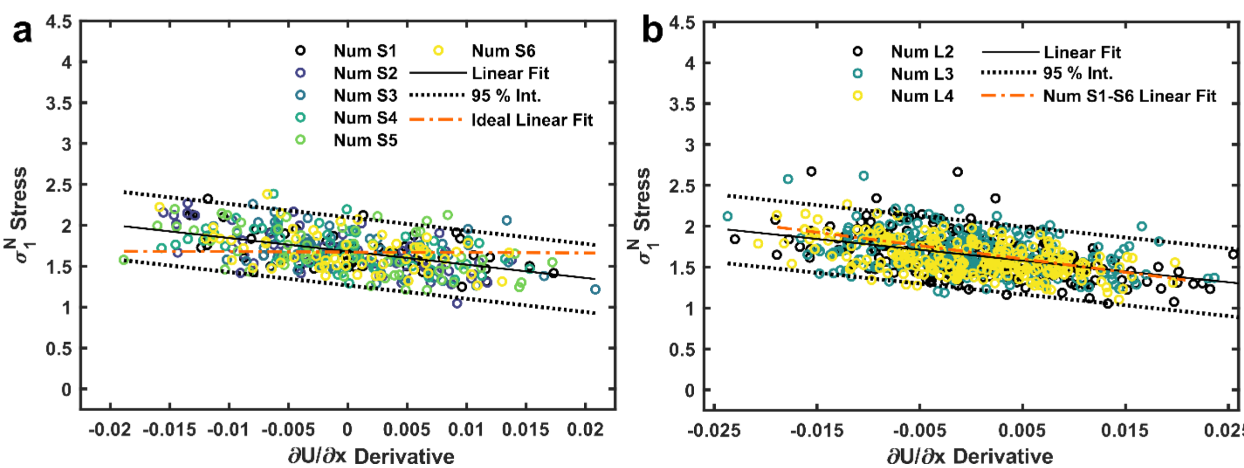

Fig. 5.11. Scatter plots of δ_{xx} and normalized, local first principal stress exhibited in numerical model of expanding plug experiments. (a) Plot illustrating linear relationship for "short" specimens between δ_{xx} (∂U/∂x derivative) and normalized, local first principal stress σ_1^N. (b) Plot illustrating linear relationship for "long" specimens between δ_{xx} (∂U/∂x derivative) and normalized, local first principal stress σ_1^N.

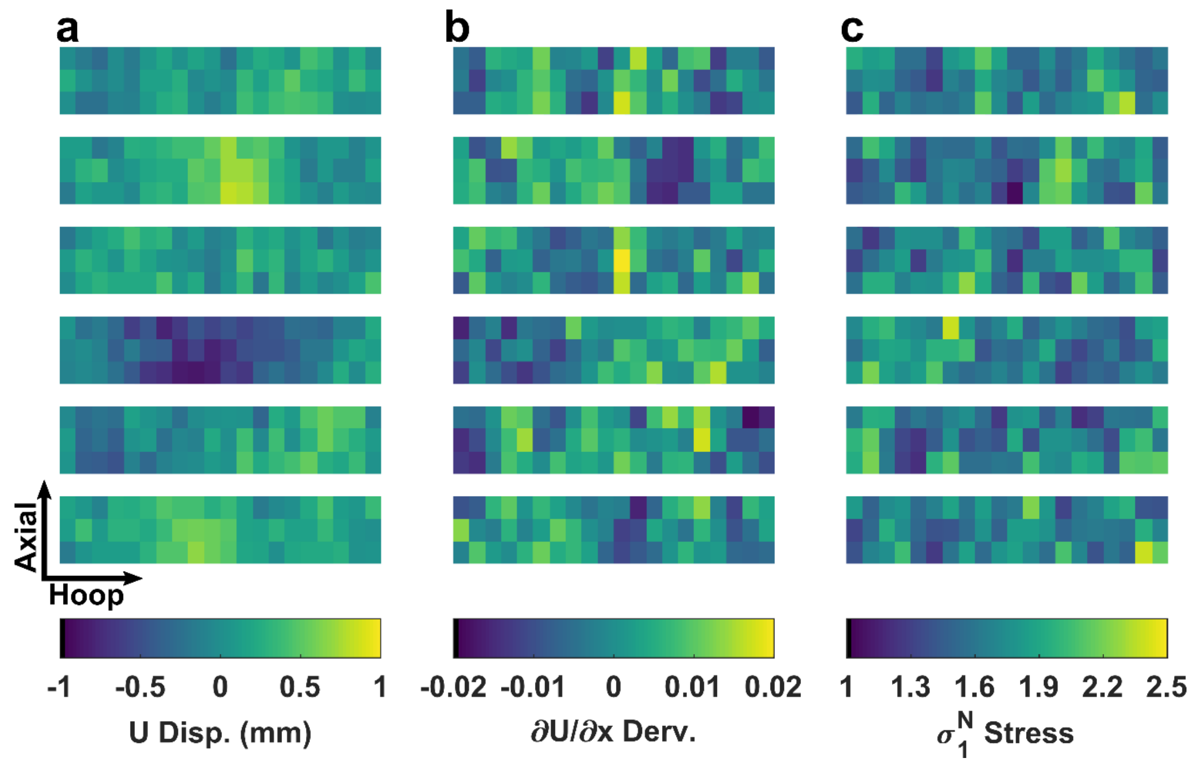

Fig. 5.12. Spatial profiles depicting measurements of tow structure irregularity and normalized local stress. (a) Hoop direction tow crown displacements from ideal, uniform locations. (b) Spatial derivative δ_{xx} taken along hoop. (c) Normalized, local first principal stress σ_1^N at tow crown locations. For all, each pixel corresponds to a single tow crown and top to bottom blocks correspond to Num S1 to Num S6.

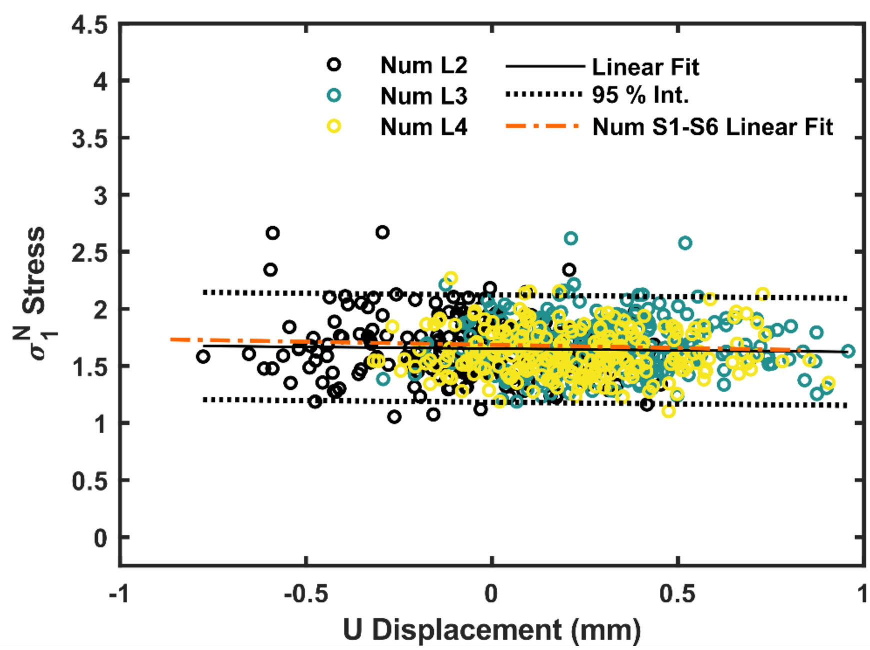

Fig. 5.13. Post processed numerical result plot relating *U Displacement* (hoop-wise movement of tow crown locations) to *normalized first principal stress* for “long” specimens. Similar results for

the “short” specimens are summarized by the orange line. The slope of this relationship is nominally zero and is statistically insignificant. This numerical result was also reflected by experimental results.

While the top and bottom axial portions of past measurements necessitated trimming within numerical models, the central region provides a large sample of measurements (60/short model and 240/long model) around the full circumference, which allows exploration of remaining tow nonuniformity parameters beyond δ_{xx}. A comparison in Chapter 4 of the hoop and axial spacing for these biaxially braided CFRP composites indicated that a proportional relationship between axial and hoop tow crown spacing existed. Here, this observation is supported by observing a proportional relationship (Fig. 5.14) between δ_{yy} ($\partial V/\partial y$ derivative) and normalized, local first principal stress σ_1^N, with a minimum confidence level of 99.3 % from the Pearson correlation test. Notably, the range of δ_{yy} is substantially less with a similar variation of the σ_1^N stress.

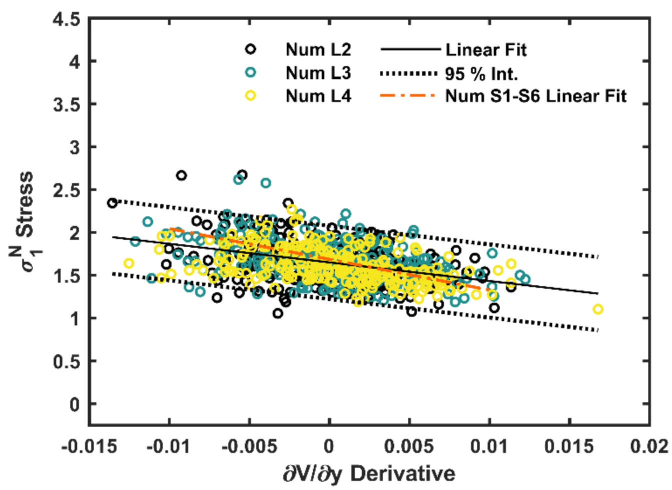

Fig. 5.14. Scatter plot illustrating a linear relationship for “long” specimens between δ_{yy} ($\partial V/\partial y$ derivative) and normalized, local first principal stress σ_1^N.

4. Discussion

Targeted expanding plug experiments were performed which demonstrated a linear relationship between hoop-wise tow placement derivative δ_{xx} and tow crown local strain with an average slope of -17.71. Numerical simulations of similar experiments were performed using virtual models developed using experimentally measured tow trajectories from the same composites, and a similar relationship over a large portion of the composite surface was found between δ_{xx} and tow crown local stress with an average slope of -16.28. Additionally, from the numerical simulations a linear relationship between axial-wise tow placement derivative δ_{yy} and tow crown local stress was found with an average slope of -35.80, which is approximately twice as steep. The regular biaxial braid features a surface pattern which shifts 1 unit along the hoop while shifting 2 units along the axis; therefore, it is likely δ_{xx} and δ_{yy} are coupled in this particular braid style. Interestingly, from combined experimental results and numerical simulations, only δ_{xx} and δ_{yy} were found to possess any correspondence to the local mechanical response of the composites. This observation supports the conclusion that for this braid the rate or gradient at which tow structure varies is substantially more critical to failure than the magnitude in which they vary.

The slopes of these trends relative to models utilizing an "ideal" uniform tow structure can be used to explain some of the stress redistribution mechanisms exhibited by the biaxial braid structure (Fig. 9a). Notably, the local stress magnitude appears to be conserved, such that certain local variations in tow structure serve to increase the magnitude of the local stress, while others within the same composite serve to reduce the stress. For these CFRPs, local heterogenous stress responses with increased magnitude may serve to exceed the strength of the neighboring matrix and promote failure initiation and debonding. Within the ranges of local tow irregularity observed in the "short" tubes, this increase could be as high as 18 % in a single ply braid, which demonstrates the importance of maintaining a non-defective, uniform tow structure.

In the past chapter braid structure irregularity has been shown to be spatially related to constituent tow family orientation, and here, the stress/strain redistribution to defective tow structure regions has been quantified for a single ply. Understanding how defects are positioned and how they affect performance is the first step to mitigation. The information presented here can serve as a guide for manufacturers of defect sensitive braided composites for use in extreme or structural applications, such as seen in the aerospace, nuclear energy, or automotive industries. While braid intrinsic defects, such as tow crimp/waviness, likely cannot be corrected, others involving mismatch in braiding velocity, mandrel or preform layer friction, braid relaxation, braid twist, or handling can be optimized to produce an ideal reinforcement structure to support an even redistribution of stress and predictable failure criteria.

5. Conclusions

Using past tow-based measurements of biaxially braided composite architecture defects to perform targeted mechanical testing experiments and develop similar numerical simulations with virtual models containing realistic as-manufactured tow trajectories. Expanding elastomer insert tests of the tubes were coupled with stereoscopic digital image correlation to resolve surface strain response. A methodology to directly compare local surface strain/stress surrounding tow trajectory radial peaks or "crowns" to past measures of tow structure nonuniformity is presented and used to demonstrate statistical correlations. Using the past proposed method of generating virtual models of each braided specimen via experimentally measured tow paths, numerical simulations are performed to replicate the 3D response of each specimen. Numerical results are processed similar to experimental results, and a comparison is performed within the elastic regime. Numerical results demonstrate similar correlations of increased strain/stress concentration surrounding surface areas of defective tow structure. Ideal tow structure virtual models and numerical simulations were also performed, which enabled a quantification of the difference in stress redistribution mechanisms.

Finally, the numerical model results are used to explore the significance of other nontargeted measured of tow structure variability. The information presented here demonstrates the sensitivity of local mechanical response to braid irregularity and has far reaching implications for defect sensitive composite materials used in extreme and structural applications, including pressure vessels, high temperature seals, and turbine components. Key scientific contributions and conclusions include:

- A route for converting full-field surface tow measurements into virtual models is presented and utilized.
- A scalable method to relate local tow structure and local mechanical response is demonstrated for macro-sized composites tubes.
- Results show that the rate or gradient at which tow structure varies is substantially more critical to failure than the magnitude in which they vary.
- By comparing numerical results for uniform, "ideal" biaxial braids and as-manufactured, nonuniform braids, the stress redistribution increase due to variation in tow placement can be estimated to be as great as 18 %.

6. References

[1] Carey JP. 1 - Introduction to braided composites. In: Carey JP, editor. Handb. Adv. Braided Compos. Mater., Woodhead Publishing; 2017, p. 1–21. doi:https://doi.org/10.1016/B978-0-08-100369-5.00001-5.

[2] Melenka GW, Carey JP. Experimental analysis of diamond and regular tubular braided composites using three-dimensional digital image correlation. J Compos Mater 2017;51:3887–907. doi:10.1177/0021998317695418.

[3] Melenka GW, Ayranci C. Advanced measurement techniques for braided composite structures: A review of current and upcoming trends. J Compos Mater 2020:0021998320903105. doi:10.1177/0021998320903105.

[4] Melenka GW, Carey JP. Development of a generalized analytical model for tubular

braided-architecture composites. J Compos Mater 2017;51:3861–75. doi:10.1177/0021998317695421.

[5] Heim FM, Croom BP, Bumgardner C, Li X. Scalable measurements of tow architecture variability in braided ceramic composite tubes. J Am Ceram Soc 2018;101. doi:10.1111/jace.15564.

[6] Heim FM, Daspit JT, Holzmond OB, Croom BP, Li X. Analysis of tow architecture variability in biaxially braided composite tubes. Compos Part B Eng 2020;190:107938. doi:https://doi.org/10.1016/j.compositesb.2020.107938.

[7] Desplentere F, Lomov S V., Woerdeman DL, Verpoest I, Wevers M, Bogdanovich A. Micro-CT characterization of variability in 3D textile architecture. Compos Sci Technol 2005;65:1920–30. doi:10.1016/j.compscitech.2005.04.008.

[8] Croom BP, Li X, Deck CP, Xu P, Lahoda EJ. Quantifying the three-dimensional damage and stress redistribution mechanisms of braided SiC/SiC composites by in situ volumetric digital image correlation. Scr Mater 2016;130:238–41. doi:10.1016/j.scriptamat.2016.12.021.

[9] Tate JS, Kelkar AD. Stiffness degradation model for biaxial braided composites under fatigue loading. Compos Part B Eng 2008;39:548–55. doi:https://doi.org/10.1016/j.compositesb.2007.03.001.

[10] Xiao S, Wang P, Soulat D, Legrand X, Gao H. Towards the deformability of triaxial braided composite reinforcement during manufacturing. Compos Part B Eng 2019;169:209–20. doi:https://doi.org/10.1016/j.compositesb.2019.04.017.

[11] Sutton MA, Orteu JJ, Schreier HW. Image Correlation for Shape, Motion and Deformation Measurements. Boston, MA: Springer US; 2009. doi:10.1007/978-0-387-78747-3.

[12] Roache DC, Jarama A, Bumgardner CH, Heim FM, Walters J, Romero J, et al. Unveiling damage mechanisms of chromium-coated zirconium-based fuel claddings by coupling digital image correlation and acoustic emission. Mater Sci Eng A 2020. doi:10.1016/j.msea.2019.138850.

[13] Bumgardner CH, Heim FM, Roache DC, Jarama A, Xu P, Lu R, et al. Unveiling hermetic failure of ceramic tubes by digital image correlation and acoustic emission. J Am Ceram Soc 2019. doi:10.1111/jace.16854.

[14] Bumgardner C, Croom BP, Li X. High-temperature delamination mechanisms of thermal barrier coatings: in-situ digital image correlation and finite element analyses. Acta Mater 2017;128:54–63. doi:10.1016/j.actamat.2017.01.061.

[15] McNeill SR, Sutton MA, Miao Z, Ma J. Measurement of surface profile using digital image

correlation. Exp Mech 1997;37:13–20. doi:10.1007/BF02328744.

[16] Rossol MN, Shaw JH, Bale H, Ritchie RO, Marshall DB, Zok FW. Characterizing Weave Geometry in Textile Ceramic Composites Using Digital Image Correlation. J Am Ceram Soc 2013;96:2362–5. doi:10.1111/jace.12468.

[17] Rossol MN, Fast T, Marshall DB, Cox BN, Zok FW. Characterizing In-Plane Geometrical Variability in Textile Ceramic Composites. J Am Ceram Soc 2015;98:205–13. doi:10.1111/jace.13275.

[18] Heim FM, Croom BP, Bumgardner C, Li X. Scalable measurements of tow architecture variability in braided ceramic composite tubes. J Am Ceram Soc 2018;101:4297–307. doi:10.1111/jace.15564.

[19] Okereke MI, Akpoyomare AI, Bingley MS. Virtual testing of advanced composites, cellular materials and biomaterials: A review. Compos Part B Eng 2014;60:637–62. doi:https://doi.org/10.1016/j.compositesb.2014.01.007.

[20] Rossol MN, Rajan VP, Zok FW. Effects of weave architecture on mechanical response of 2D ceramic composites. Compos Part A Appl Sci Manuf 2015;74:141–52. doi:10.1016/j.compositesa.2015.04.003.

[21] Desplentere F, Lomov SV, Woerdeman DL, Verpoest I, Wevers M, Bogdanovich A. Micro-CT characterization of variability in 3D textile architecture. Compos Sci Technol 2005;65:1920–30. doi:10.1016/J.COMPSCITECH.2005.04.008.

[22] Nikishkov G, Nikishkov Y, Makeev A. Finite element mesh generation for composites with ply waviness based on X-ray computed tomography. Adv Eng Softw 2013;58:35–44. doi:https://doi.org/10.1016/j.advengsoft.2013.01.002.

[23] Rinaldi RG, Blacklock M, Bale H, Begley MR, Cox BN. Generating virtual textile composite specimens using statistical data from micro-computed tomography: 3D tow representations. J Mech Phys Solids 2012;60:1561–81. doi:10.1016/J.JMPS.2012.02.008.

[24] Blacklock M, Bale H, Begley M, Cox B. Generating virtual textile composite specimens using statistical data from micro-computed tomography: 1D tow representations for the Binary Model. J Mech Phys Solids 2012;60:451–70. doi:10.1016/j.jmps.2011.11.010.

[25] Jiang H, Wang J-AJ. Methodology for mechanical property testing of fuel cladding using an expanding plug wedge test. J Nucl Mater 2014;446:27–37. doi:https://doi.org/10.1016/j.jnucmat.2013.11.026.

[26] Jacobsen GM, Stone JD, Khalifa HE, Deck CP, Back CA. Investigation of the C-ring test

for measuring hoop tensile strength of nuclear grade ceramic composites. J Nucl Mater 2014;452:125–32. doi:https://doi.org/10.1016/j.jnucmat.2014.05.002.

[27] Jiang H, Wang J-AJ. Methodology for mechanical property testing of fuel cladding using an expanding plug wedge test. J Nucl Mater 2014;446:27–37. doi:10.1016/J.JNUCMAT.2013.11.026.

[28] Mosley K. The Stressing for Test Purposes of Materials in Tubular Form Using Elastomeric Inserts—Experimental and Theoretical Development. Proc Inst Mech Eng 1982;196:123–39. doi:10.1243/PIME_PROC_1982_196_014_02.

[29] Bertolazzi E, Trento U of. Knots & Tubes 2020.

[30] Möller T. A Fast Triangle-Triangle Intersection Test. J Graph Tools 1997;2:25–30. doi:10.1080/10867651.1997.10487472.

[31] Tuszynski J. Surface Intersection 2020.

CHAPTER 6: SPATIAL INVESTIGATION OF SIC/SIC CERAMIC MATRIX COMPOSITE FAILURE

1. Introduction

In recent years, significant effort has been placed on developing next-generation accident tolerant nuclear fuel systems and robust materials to extend reactor design safety to include non-ideal, extreme reactor conditions, addressing the critical safety concerns following the Fukushima incident.[1–4] While there are several leading, material-based solutions addressing concerns with current fuel claddings, one of the more auspicious and heavily investigated is silicon carbide (SiC) continuous fiber-reinforced SiC matrix (SiC/SiC) composites. SiC ceramic matrix composites (CMC) are favored due to their high temperature strength, chemical inertness, irradiation tolerance, and improved damage tolerance, all of which indicate a general compatibility with the harsh environment within a nuclear reactor.[5–7] Furthermore, SiC CMCs have been rigorously tested within the aerospace community, where high temperature properties and corrosion resistance are critical requirements of many materials.[8–10] In a reactor environment, the onset of matrix microcracking coupled with the loss of cladding hermeticity can allow the escape of radiative fuel and gases with potentially disastrous consequences, even though the cladding may still possess full load bearing capabilities.[11,12] In order for these CMCs to be accepted by the stringent nuclear community, they must be exhaustively evaluated and examined through a suite of investigations to elucidate their full failure behavior.

While other options are being studied, it is common for the SiC matrix to be grown via chemical vapor infiltration (CVI) and the interphase to be pyrolytic carbon (PyC); these distinctions can lead to subtle but unique performance differences compared to aerospace CMCs.[6] However, like aerospace CMCs, the manufacturing geometry requirements are potentially coupled with failure mechanisms. This relationship is critically pertinent for light water reactor (LWR) cladding materials,[13] which have challenging physical requirements for CMC processing, namely a tubular geometry with a small outer diameter (~10 mm) and thin walls (~1 mm). Thus, it is necessary to extensively investigate the mechanical performance of these CMCs. Performing this evaluation under ambient conditions to establish the baseline relationships between CMC manufacturing geometry, microstructure, and failure mechanisms is a logical and cost-effective approach prior to expensive irradiation and high temperature evaluation.

Mechanical testing of SiC CMCs nuclear fuel cladding is greatly complicated by several factors: (i) anisotropy of both mechanical and thermomechanical properties; (ii) complex, multiscale failure mechanisms induced from the fiber-matrix structure; (iii) a laminated, thin-walled cylindrical geometry; and (iv) the relatively small failure strains of monolithic SiC.[14,15] Furthermore, these factors contribute to a convoluted definition of failure, where matrix cracking, fiber cracking, loss of hermeticity, and loss of load-bearing function may occur at distinctly different strains. Currently, this relationship between microcracking and gas tightness remains unresolved as available *ex situ* hermetic evaluations are unable to account for likely microcrack closing upon mechanical unloading.[13,16] Therefore, the *in situ* hermetic failure behavior under loading must be thoroughly addressed to progress the implementation of advanced CMC materials for use in extreme applications;[7,16,17] this unknown hermeticity behavior is one of the subjects addressed in this work.

In this chapter, planar and tubular of SiC/SiC CMCs were evaluated at ambient, room temperature conditions, under different loading conditions, including tension and four-point bending. Custom-designed fixtures for CMC testing were developed for each loading mode and were coupled with three-dimensional digital image correlation (3D-DIC) to reveal spatial strain development and cracking behavior during the slow failure of each composite. Specific work was done to validate deviations from typical four-point bending loading contact points. Mechanical properties are presented to be representative of the current state of SiC/ SiC CMCs developed for nuclear applications. Scanning electron microscopy (SEM) was performed postmortem to determine the influence of microstructural features on failure.

2. Experimental methods

2.1. Custom experimental setups

2.1.1. Tension

To aid in accurate tensile evaluation of few ply or thin SiC/SiC CMCs a custom tensile stage was constructed, which is schematically depicted in Fig. 6.2. A total of three variable points ensured proper alignment of the tensile specimens. Tension specimens were epoxied (3M Scotch-Weld 2214) on both faces to steel tab adapters, which were pinned into a custom-designed, double universal joint fixture with a free-floating base mount (Fig. 6.2). Universal joint hinges were lubricated to minimize friction.

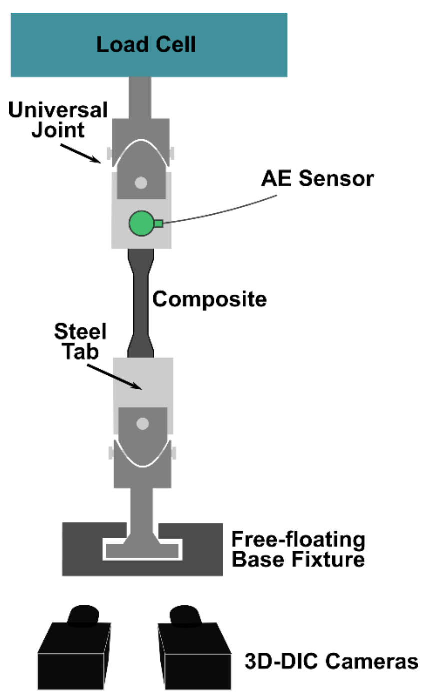

Fig. 6.1. Depiction of custom-made tensile stage.

2.1.2. Four-point bending setup

Here, with equal contributions from *Bumgardner*,[18] we demonstrate a novel, *in situ* helium hermeticity monitoring setup utilizing three-dimensional digital image correlation (3D-DIC) and acoustic emission (AE) detection to investigate the relationship between microcracking and spatial damage with the hermetic seal of SiC CMC fuel claddings. This experimental setup was evaluated on brittle ceramics and glasses, and we report preliminary, *in situ* hermeticity results for SiC/SiC CMCs. This methodology represents the world's first conglomeration of comprehensive sensors (helium leak detection, AE detection, and 3D-DIC), designed to sequentially determine the onset of cracking, loss of hermeticity, and ultimate failure while at the same time accommodating SiC/SiC fuel claddings without the need for special modification or specimen dependent gripping section. This setup is schematically depicted in Fig. 6.2.

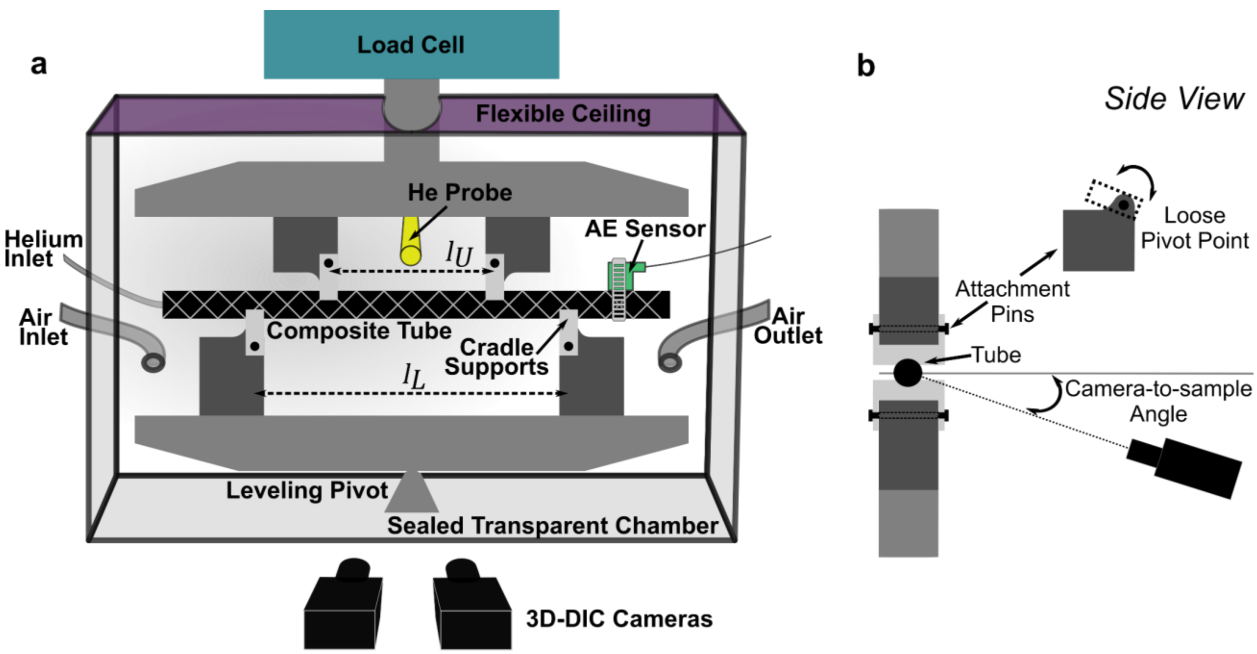

Fig. 6.2. Depiction of developed four-point bend setup for cladding. (a) Front view. (b) Side view.

Four-point bending is the most logical choice for investigating hermetic failure as it concentrates compressive and tensile strains at known orientations, providing simple He sensor positioning and a route to internal pressurization through non-obstructed specimen ends,[19,20] unlike conventional tension or compression testing. Extending the design template described in ASTM C1684 – 18 for bending of brittle rods, custom-designed, load-distributing cradles were fabricated and utilized to reduce contact point stresses.[21] Composites have historically presented a challenge for experimentalists due to their highly non-uniform stress state, which produces spatial strain gradients that cannot be accurately determined using conventional strain gauges.[22,23] Addressing this challenge, 3D-DIC was leveraged to measure spatial strain fields over a targeted area of interest with sufficient resolution to track local strain concentrations associated with composite architectural features.[23,24] AE monitoring was used to identify the strains at the onset and progression of cracking, leading up to loss of He gas tightness.[25–27]

Inspiration for the design of the loading fixtures originated from the Idaho National Laboratory.[19] Specimens were supported using four cylindrical cradles, which were sized such that the cradle width matched the roller diameter as specified in ASTM C1684-18. Support span distances of $l_U/l_L = $ 42/84, 50/100, and 33/100 mm/mm were used; selection of these spans was guided by the recommendation of $l_U/l_L = $ 40/80 mm/mm in ASTM C1684-18 for ceramic rods with diameters in the range of 4 to 12 mm. The cradles were machined to a diameter of 10.4 mm to accommodate the diameter of the tubes and rotate at the support to maintain contact throughout specimen bending (Fig. 6.2). It should be noted that a nominally smooth tube surface with less than 0.2 mm deviations is ideal to prevent point concentrations at the cradles. It was discovered during early testing that free cradles would move and alter the load distribution; to counter this, the pivot points were secured with pins to prevent the cradles from sliding during loading. Support pivot points were lubricated to minimize any frictional effects.

For coupled hermetic mechanical testing, each test specimen, pressurized with 2 atm (30 psi) of internal pressure, were contained in a sealed, plastic chamber with a transparent, polycarbonate front window through which optical images for DIC analysis could be acquired. A flexible chamber ceiling was constructed from a thin, plastic veil that was sealed at the base of the load cell and on the chamber walls, enabling the upper loading fixture to move within the sealed environment. Air inlet and outlet ports were included to rapidly purge He from the chamber after specimen failure. A combination of clay and masking tape were utilized to provide a temporary seal at the chamber window edges, which could be quickly removed to provide access to the specimen and loading fixtures. This sealed chamber presented two key advantages: (i) it isolated the test environment from ambient helium, and (ii) it could be rapidly purged to enable quick successive testing.

2.1.3. General experimental setup

All tests were conducted at room temperature and ambient conditions using an Admet eXpert 2611 table-top, universal testing machine with an Admet 1210AJ-2K-B, 8.9 kN load cell using a loading rate of 0.5 mm/min. Mechanical loading fixtures were attached according to the desired testing procedure.

Acoustic emissions were acquired by a Mistras 1283 USB AE Node at a rate of 1MHz with a threshold of 10 dB throughout the duration of testing. The AE sensor was secured directly to the specimen by an adjustable hose clamp. Helium leak rate was recorded by an Inficon Protec P3000 Helium Sniffer Leak Detector at a rate of 10 Hz with a minimum leak rate of 1 $*10^{-7}$ mbar l/s and a reaction time of ~400 ms with the probe directly above the bending center. In order to account for sensor reaction time and to ensure that the leak rate and acoustic activity could be directly correlated with mechanical strain with minimal error, a stepped displacement profile was used, which displaced the crosshead at a rate of 0.5 mm/min in 0.01 mm increments with a 2 second hold period. This intermittent displacement profile is considered equivalent to a typical quasi-static rate.

Digital images were acquired with two FLIR Grasshopper 3 GS3-U3-50S5M-C digital CMOS cameras equipped with Schneider 21-100197 50 mm compact lenses at a capture rate of 5 to 20 Hz. Another similar set of cameras with Schneider 21-100621 35 mm lenses was used to capture the opposing face of select specimens and helped to identify final fracture initiation locations. 3D-DIC analysis was performed using a commercial correlation software, Correlated Solutions VIC-3D 8. For each analysis, an ideal subset size and step size were chosen based on the applied speckle pattern size. Typical subset sizes ranged from 13 to 35 pixels, and step sizes ranged from 2 to 9 pixels. All VIC-3D datasets were processed with a calibration of at least 30 images and rigid body motion removal via built-in functions. Data graphing and calculations were done in Python 3.6 and MATLAB. Scanning electron microscope (SEM) images were taken by a FEI Quanta 650 Scanning Electron Microscope equipped with a Circular Backscatter Detector (CBS)

2.2. Materials

For the work reported here, some materials were evaluated with the addition of helium leak sensing and acoustic emissions to determine hermetic performance, while other CMC specimens were evaluated solely to determine mechanical performance and cracking mechanisms. For clarity, these two groups of materials will be separated in discussion. Batch A are materials where He and AE data were not presented; these are more recently developed SiC/SiC CMCs from General Atomics in 2020. Batch B are materials where He and AE data were available; these are representative of older SiC/SiC CMCs from General Atomics and were provided by Westinghouse Electric Company in 2018.

2.2.1. Mechanical failure materials (Batch A)

Two types of SiC/SiC CMC specimens were examined to determine mechanical performance. They were both purchased from General Atomics and consisted of reinforcing SiC fibers, a pyrocarbon fiber/matrix interphase (~100 - 150 nm), and a SiC matrix produced via CVI. The planar CMCs consisted of three layers of plain weave (PW) made from Tyranno SA3 fibers with a nominal gauge length, width, and thickness of 50 mm, 6.38 mm, and 0.89 mm, respectively. The tubular CMCs contained 3 plies of Hi-Nicalon type-S fibers in a diamond pattern biaxial braid orientation of ± 50° from the tube axis and a chemical vapor deposition (CVD) SiC outer coating with an inner and outer diameter of 8.4 mm and 10.1 mm, respectively. The SiC/SiC samples are prototypes of SiC-based nuclear energy structural materials currently under development. Prior to testing, all specimens were coated with a thin speckle pattern layer of matte white and black paint (spray can) for DIC correlation.

2.2.2. Hermetic failure materials (Batch B)

Table 6.1 lists the specifications of the four different materials tested using the four-point bend hermeticity setup, including outer diameter (OD) and inner diameter (ID). Alumina (96-99.8 % purity), borosilicate glass, and 4130 steel tubes were purchased from McMaster-Carr. Diameter sizes were limited to commercial availability and were selected to be similar to the diameter of the CMCs. Single layer, chemical vapor infiltrated (CVI) SiC/SiC tubular CMCs (consisting of Hi-Nicalon Type S fibers and pyrocarbon fiber/matrix interphase) with a nominal, tri-axial braid orientation of ± 55° from the tube axis were purchased from General Atomics; notably, the CMC tubes were coated with a SiC coating with the outer diameter ground smooth. These SiC/SiC samples are prototypes of SiC-based nuclear fuel cladding currently under development and are not necessarily representative of a fully optimized SiC cladding. Specimens were cut to a 152 mm (6 in) length using a water-cooled, circular-bladed diamond saw. To establish an internal, He pressure with potential to exceed 2 atm, both specimen ends were sealed with a urethane adhesive (3M Scotch-Weld 2214 epoxy adhesive) with one end containing a high-pressure plastic tube in which He was infused. Prior to testing, all specimens were coated with a thin, speckle pattern layer of matte white and black paint (spray can) to provide a trackable surface pattern for DIC.

Table 6.1. Tubular specimen properties.

Material	Specimen Identifier	OD (mm/in)	ID (mm/in)	Vendor
Alumina	A	9.53 / 0.375	6.35 / 0.250	McMaster-Carr
Borosilicate Glass	B	9.53 / 0.375	5.59 / 0.220	McMaster-Carr
4130 Steel	S	9.53 / 0.375	8.00 / 0.315	McMaster-Carr
SiC CMC	CMC	9.53 / 0.375	7.15 / 0.281	General Atomics

2.3. Post-processing of multiple data streams for performance curves

As previously described, multiple data streams were acquired from the universal test frame, the DIC cameras, the AE sensor, and the leak detector within a single test. All sensor data was temporally aligned via an average of several comparison points, enabling alignment and correlation of events detected by individual data streams.

The normalized cumulative acoustic energy (NC-AE) is a metric frequently used to evaluate the initiation, progression, and frequency of cracking events in ceramic composites.[28,29] Acoustic data was normalized by the total cumulative acoustic energy within each individual test; normalizing the acoustic energy minimizes variation in sensor sensitivity between consecutive tests, which stems from varying sensor contact pressure.[30]

Strain data was exported from VIC-3D for every pair of images acquired. Each strain profile provided full-field measurements within a global coordinate system in millimeters, including x, y, and z position; u, v, and w displacements; and ε_{xx}, ε_{yy}, and ε_{xy} strains at every pixel location. The conversion of spatial DIC strains to singular values and the calculation of relevant stress per test is described in the next sections. The Young's modulus was calculated as the slope of a linear fit to the initial region of the stress-strain curves prior to the point of deviation from linearity. Where applicable, the proportional limit or the deviation from linearity strain (DFLS) values were calculated by shifting the linear fit over by 0.005% strain and finding the intersection point with the stress-strain curves.

2.3.1. Tension

For tension tests, strain values were calculated by taking the average of all ε_{yy}, DIC measurements within the gauge section. Engineering tensile stress was calculated according to:

$$\sigma = \frac{F}{A} \tag{6.1}$$

where F is the tensile load for tension, and A is the cross-sectional area of the specimen.

2.3.2. Four-point bending

For bend tests, DIC processing and mechanical property analysis was implemented courtesy of *Bumgardner*, whom outlined the following procedure to retrieve conventional mechanical properties, which is included here for continuity.[18] For bending DIC profiles were cropped to only include data within the inner load points associated with pure bending and subsequently analyzed to extract the camera-to-sample angle; to view the location of maximum bending tensile strains, the camera was located below horizontal (Fig. 6.2b). Relative to the camera, vertical test frame displacements have *y* and *z* dimensions. The angle of the cameras was derived by the following equation:

$$\theta_i = \tan^{-1}(\frac{w_i}{v_i}) \tag{6.2}$$

where θ_i is the camera angle at every time step, and v_i and w_i are the specimen displacements in *y* and *z*, respectively. The camera angle converged to a value over time, which is the true camera-to-sample angle. Each cropped profile was rotated about the camera-to-sample angle such that all displacements of the specimen occurred in the loading direction.

The strain data was analyzed to determine surface bending strain. Extracting such parameters was necessary to convert the spatial strains collected from DIC to singular points to use for conventional stress-strain curves and modulus calculations. For every *y* position down the cross-section of the specimen, all the strains were averaged down the length of the bending zone. Strain at the lowest cross-sectional position (referred to as peak strain) was extracted and used for stress-strain curves and modulus calculations as the maximum tensile strain due to bending.

The maximum bending stress experienced of tubular specimens was calculated as follows:

$$\sigma = \frac{M(OD)}{2I} \tag{6.3}$$

where *M* is the bending moment and *I* is the moment of inertia. *M* and *I* are given by:

$$M = \frac{1}{4}F(l_L - l_U) \tag{6.4}$$

$$I = \frac{\pi(OD^4 - ID^4)}{64} \tag{6.5}$$

In Eqn. 4, l_L and l_U are the spans between the outer load points and inner load points, respectively; *F* is the applied load, and *OD* and *ID* represent the outer and inner diameters, respectively.

2.4. Digital image correlation crack analysis

A DIC-based analysis was performed in MATLAB on the DIC displacement profiles to reveal discontinuities associated with crack locations. To accomplish this a subset size was chosen to be the smallest value with acceptable levels of uncorrelated regions, generally this was between 11 and 13 px. A central differences scheme was used to compute the spatial derivatives $\frac{\partial U}{\partial x}$ of the displacements U along the direction of loading x (Fig. 6.3). The derivatives have been used by other researchers[23,24,31,32] to find the edges of cracks from DIC. A scalar, intensity threshold I was applied to the spatial derivatives to isolate the crack edges in the final f DIC correlation.

The threshold was chosen to account for the median $\frac{\widetilde{\partial U}}{\partial x}$ and standard deviation σ of the initial *i* (prior to any applied load) Gaussian noise present in DIC measurements and was defined as:

$$I = 3 * \sigma_i - \frac{\widetilde{\partial U}}{\partial x_i} + \frac{\widetilde{\partial U}}{\partial x_f} \tag{6.6}$$

It should be noted that $\frac{\widetilde{\partial U}}{\partial x_i} \cong 0$.The subset, step, and strain filter parameters used to estimate crack locations were 15 px, 2 px, and 15 points, respectively, for the tensile specimens and 11 px, 3 px, and 15 points respectively, for the bending specimens.

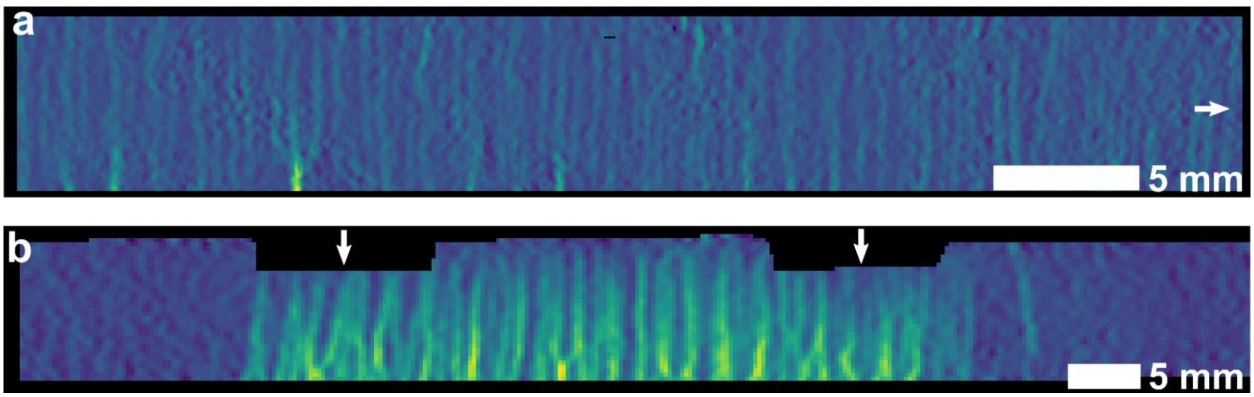

Fig. 6.3. Example of spatial derivative profile prior to thresholding. a) T01. b) B02. Arrows indicate loading fixture displacement directions.

3. *Validation of hermeticity four-point bend setup*

3.1. *Numerical model*

The four-point bending fixture presented here represents a slight modification to the accepted standard (ASTM C1684-18) concerning four-point bending of brittle rods at ambient temperatures. This alteration allows the fixture to consist only of rigid, metal components, which potentially qualifies the fixture for future higher temperature conditions. The alteration entails a different, yet functionally equivalent method of cradle attachment (see standard for more details). Past designs have relied on rubber bands or springs to secure the cradles, which are balanced against / upon pins and are guided by slots in the fixture such that they are free to rotate only about an axis perpendicular to the specimen length, with minimal opportunity to translate (Fig. 6.4a). By using pins to secure the cradle pivot points, our design enables the cradle to constrain itself to allow only the same rotation as the specimen while also providing a loose means of attachment to the main fixture (Fig. 6.4b), which was necessary to prevent cradle translation during bending. Additionally, the new cradles have an internal radius customized for nuclear fuel cladding diameters; this radius provides a more uniform specimen contact area and is an accepted option in ASTM C1684-18 for contact sensitive specimens.

Given the changes to the four-point bending fixture, it must be demonstrated that these modifications do not promote significant strain concentrations or unwanted constraints under the expected bending conditions for SiC CMCs and other high stiffness materials. Therefore, a three-dimensional numerical model was developed to replicate the experimental four-point bending fixture, which is shown for a steel tube in Fig. 6.4c. This fixture model was implemented for alumina, borosilicate, and 4130 steel tubes with correct geometry, including results for three different span measurements ($l_U/l_L\ =\ $ 42/84, 50/100, and 33/100 mm/mm). An extensive study to verify minimal strain concentration formation in regions underneath the grips and outside of the view of the 3D-DIC analysis was done for the three materials at strains measured via DIC. The steel tube is more ductile than the CMCs seen in this study and presents a case of extreme deflection or rotation of the cradles to ensure that no strain concentrations associated with wedging stresses form before 0.5% strain, which surpasses the anticipated strains incurred by the CMCs. Thus, it can be demonstrated that the modified fixture and attachment pins will not induce any undesirable constraint on the free rotation of the cradles during this range of bending deformation. We do note the possibility of a bending constraint past the deformation experienced by CMCs, but the deformation when this would occur is dependent on the diameter of the pins that loosely attach the cradle to the support fixture and therefore, is capable of being changed if needed. Hence, this fixture should be used carefully when testing ductile materials to extended strains, as is the case with the ASTM standard fixture, which is noted only for ceramics and glasses.

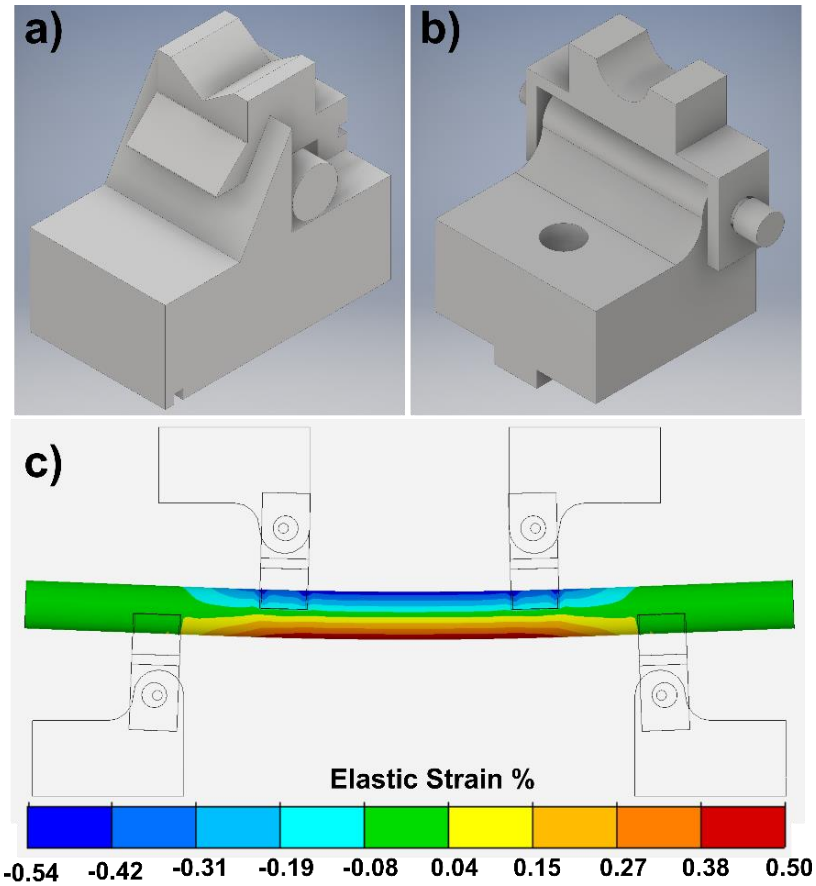

Fig. 6.4. Computer-aided design model of (a) similar ASTM standard and (b) improved bend cradles. (c) Numerical model of the bend setup with a steel tube confirms lack of strain concentrations with an even bending profile. Here l_U = 42 mm and l_L = 84 mm.

The numerical model of our four-point bend setup was created using Autodesk Inventor and then imported into ANSYS AIM 18.0. A thorough investigation of model parameters was done to include a range of coefficients of friction from 0.01 to 0.5 at both the cradle pivot points and tube contacts as well as varied mesh sizes, which converged to the following parameters and were used in Fig. 6.4. Maximum mesh generation sizes were set to 4 mm, 2 mm, and 1 mm for the supports, cradles, and tube, respectively. The supports were almost fully constrained such that only the inner supports could translate vertically. Cradle attachment pin locations and cylindrical support to cradle contact regions were modeled to have a coefficient of friction of 0.1. Contact between the tube and cradles was modeled to have a slightly higher coefficient of friction of 0.3. Mechanical properties for alumina, borosilicate glass, and 4130 steel were taken from the retailer McMaster-Carr and used as isotropic constants.

3.2. Experiments with steel, alumina, and borosilicate glass tubes

3.2.1. Steel

SiC CMCs are expected to exhibit pseudo-plasticity and survive to several percent strain. Therefore, steel tubes were tested on the custom four-point bend fixture to investigate the effects of high bending deformation on the reliability of the cradles to evenly distribute the loading force and prevent localized damage, which can be compared to the above numerical model. Individual properties derived from 3D-DIC and the universal testing machine are presented in Table 6.2, while individual stress-strain curves and a representative DIC strain profile at 0.5 % bending strain are presented in Fig. 6.5.

Measured Young's modulus and yield strength data all agreed well with the expected properties. Most encouragingly, the DIC profile maintained a uniform, Euler-Bernoulli strain profile across the bending zone for each specimen for a range of strains through 0.5 % (slightly greater than the largest strain achieved by a CMC specimen). There were no indicators of strain concentrations, which might hint to any imposed constraint by the setup. These physical observations combined with the numerical model validate the test methodology for the range of motion necessary for accurate testing of CMC tubes.

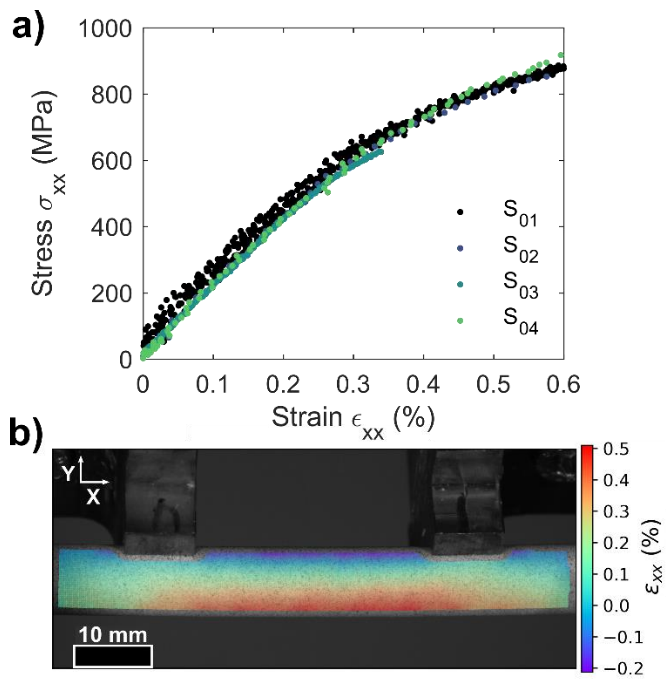

Fig. 6.5. **(**a) Plot of stress-strain responses. (b) Typical DIC profile for steel tube, S_04.

Table 6.2. Summary of 4130 steel experimental properties. Expected values were provided from the retailer McMaster-Carr. Spans are in mm.[18]

Specimen ID	Material	l_U	l_L	Expected Young's Modulus (GPa)	Young's Modulus (GPa)	Expected Yield Strength (MPa)	Yield Strength (MPa)
S_01	Steel	42	84	190-205	195	435-485	525
S_02	Steel	42	84	190-205	202	435-485	444
S_03	Steel	42	84	190-205	195	435-485	473
S_04	Steel	42	84	190-205	204	435-485	445

3.2.2. Alumina and borosilicate glass

Six alumina and six borosilicate glass specimens were tested as previously described using two different support span ratios (l_U/l_L= 34/100 and 50/100 mm/mm). Representative DIC strain profiles immediately prior to fracture are presented in Fig. 6.6, and a summary of measured moduli, fracture strength, and strain is provided in Table 6.3. Despite the brittle fracture exhibited by both alumina and borosilicate specimens, DIC processing could distinguish a conventional Euler-Bernoulli bending profile with compressive strains along the upper region of the specimen and tension underneath. Borosilicate glass specimens failed at a higher bending strain than alumina, 0.19 % compared to 0.09 % strain on average. The borosilicate specimens exhibited a profile more clearly reflective of the expected Euler-Bernoulli trend, yet the strain profiles of the alumina specimens showed relatively substantial variation. However, the individual properties derived from the DIC and mechanical tester fell within expected ranges, demonstrating the fundamental accuracy of this methodology.

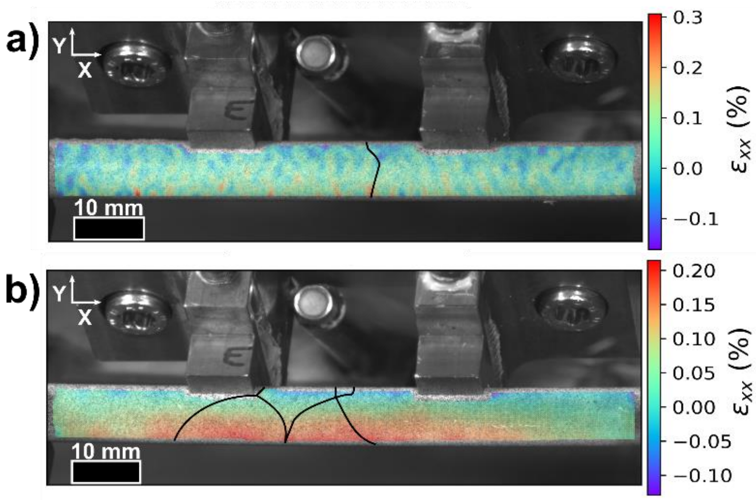

Fig. 6.6. Spatial bending ε_{xx} strain (%) profile of (a) a representative alumina and (b) borosilicate tube immediately prior to fracture with the overlaid corresponding fracture patterns in black.

Table 6.3. Summary of alumina and borosilicate glass experimental properties. Expected values derive from the retailer McMaster-Carr and literature.[33–35] Spans are in mm.

Specimen ID	**Material**	l_U	l_L	**Expected Young's Modulus (GPa)**	**Young's Modulus (GPa)**	**Expected Fracture Strength (MPa)**	**Fracture Strength (MPa)**	**Failure Strain (%)**
A_01	Alumina	34	100	340-370	358	210-350	252	0.062
A_02	Alumina	34	100	340-370	382	210-350	279	0.065
A_03	Alumina	34	100	340-370	389	210-350	281	0.067
A_04	Alumina	50	100	340-370	366	210-350	351	0.095
A_05	Alumina	50	100	340-370	372	210-350	353	0.086
A_06	Alumina	50	100	340-370	363	210-350	353	0.093

B_01	Borosilicate	34	100	60-65	62	69-340	116	0.155
B_02	Borosilicate	34	100	60-65	61	69-340	145	0.198
B_03	Borosilicate	34	100	60-65	56	69-340	121	0.187
B_04	Borosilicate	50	100	60-65	61	69-340	129	0.181
B_05	Borosilicate	50	100	60-65	62	69-340	117	0.165
B_06	Borosilicate	50	100	60-65	61	69-340	136	0.188

The brittle fracture nature of both alumina and borosilicate specimens is best illustrated in the stress-strain, NC-AE, and He leak rate plots (Fig. 6.7). The stress-strain plots indicate only a linear, elastic regime before an abrupt fracture, supported by the occurrence of a single acoustic event at fracture. Despite some noise, generally $<10^{-6}$ mbar l/s, leak rate data also indicates a single event. It comes as no surprise that the alumina and borosilicate specimens failed by fast fracture, where onset of cracking immediately propagated to relieve all stress and release all pressurized gas at once. While the sharp acoustic profile would seemingly indicate a concentrated crack network as observed on alumina (Fig. 6.6a), borosilicate specimens tended to shatter (Fig. 6.6b) with a network of cracks spanning out along the length of the specimens. We note the fracture patterns of the borosilicate specimens closely resembled those depicted in ASTM C1684-18, where initial fracture occurs at the bottom of the “V-like” intersection of the fracture line at the region of maximum tensile strain seen in Fig. 6.6b.

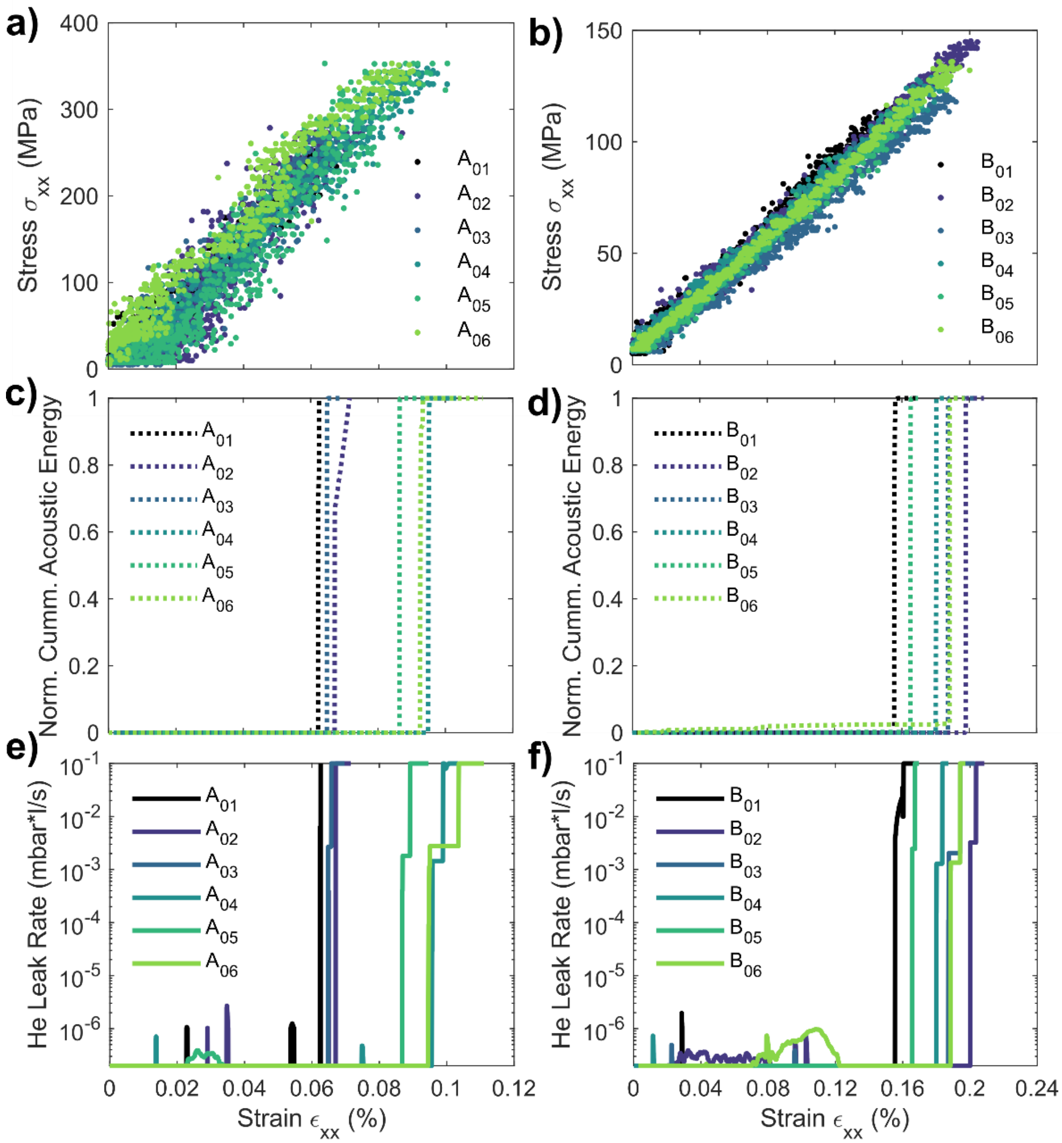

Fig. 6.7. (a,b) Stress-strain curves, (c,d) NC-AE, and (e,f) leak rate over increasing strain of all alumina (left) and borosilicate glass tubes (right), covering two span distances/ratios.

The critical finding of the testing on alumina and borosilicate specimens is that the sensors and analysis procedures developed were capable of capturing the fast fracture event of brittle ceramics. Furthermore, the initial fracture locations of all 12 brittle specimens occurred within the inner bending zone, indicating a high repeatability of successful tests. Therefore, this methodology is more than adequate to reliably capture the prolonged fracture events of CMC failure.

4. Results and discussion

4.1. Mechanical performance

Mechanical properties derived from experimental measurements (2 per test type) are listed for each test in Table 6.4. Proportional limit values, or the deviation from linearity (DFL), were calculated from a 0.005 % strain offset. Generally, published properties of CMCs vary greatly as they depend on many factors, including fiber type, interphase thickness, tow architecture, loading mode, *etc*.[13,36–38] Mechanical properties of the CMCs evaluated here fall within typical ranges; these expected ranges were derived from mechanical testing of similarly structured CMCs in tension and bending respectively. Some deviation from these ranges may be expected due to the specific fiber architecture used in this testing, but the general agreement between results of this testing and those presented in literature supports a high degree of confidence in the results despite the use of only two samples per loading mode. These properties were derived from DIC stress-strain analyses of the specimen deformation (Fig. 6.8).

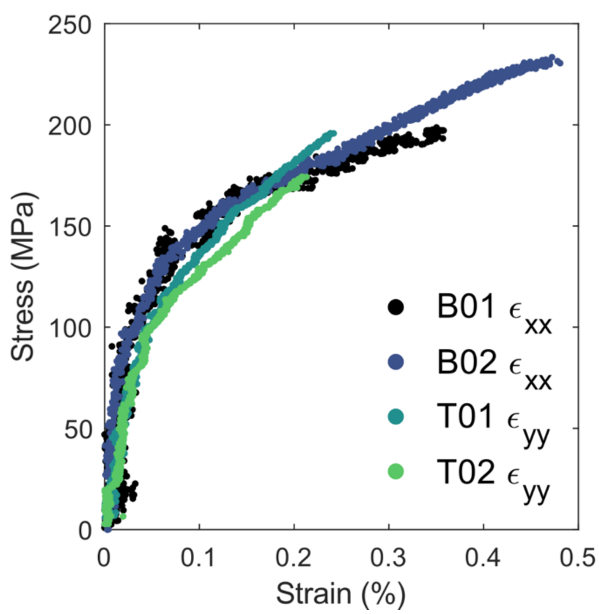

Fig. 6.8. Stress-strain response of CMCs. Strains correspond to their respective test type, including bending and tensile.

When compared to plain weave CMCs of a similar composition, the tension results agree well with past reported properties.[13,38,39] Young's modulus and DFL stress, which are more closely related to matrix properties, are representative of typical values stemming from PW CMCs produced via CVI.[39,40] Ultimate failure strength and strain are relatively low, which may be related to the interphase thickness.[39] Furthermore, the majority of PW specimens studied in literature exceed 2 mm in gauge thickness with an average ply thickness of ~0.25 mm,[38,41] which is over twice the gauge thickness of the planar CMCs studied here (~0.89 mm). It is suspected that gauge thickness below 1 mm would increase sensitivity to tow architecture or internal porosity/gap defects, which may reduce the ultimate strain of the CMCs.[41,42] Additionally, thin CMC samples and those with surface texture are prone to an increased percentage of dimensional measurement error, which could potentially reduce ultimate failure stress.

Few measurements of tubular bending properties exist in literature,[43,44] so expected values must be derived from both relevant bending literature sources when available and tubular tension test results. Results for similar tubular SiC/SiC CMCs under identical four-point bending are reported later and in Bumgardner, CH, Heim, FM, *et al.*[18] There is a slight increase in the reported Young's modulus compared to past results and expected values for similar tubular specimens; this increase may be attributed to more consistent outer CVI matrix coating compared to past claddings.

Table 6.4. Summary of CMC experimental properties and literature properties.[13,37–40]

ID	Test Type	Young's Modulus (GPa)	Expected Young's Modulus (GPa)	Ultimate Strength (MPa)	Expected Ultimate Strength (MPa)	Ultimate Strain (%)	DFL Stress (MPa)	DFL Strain (%)
T01	Tension	265	200-280	196	150-250	0.240	90.4	0.039
T02	Tension	246	200-280	174	150-250	0.211	92.1	0.042
B01	4pt. Bend	292	173-248	199	230-270	0.358	109.5	0.042

B02	4pt. Bend	268	173-248	233	230-270	0.473	120	0.044

4.2. Hermetic performance under four-point bending

Three CMC specimens were tested at ambient conditions; CMC_01 and CMC_03 were tested until complete loss of load bearing capability, while CMC_02 was tested until significant leaking was detected. Future testing is being conducted to characterize the damage mechanisms of these specimens, but here, we assessed the capability of the test methodology to capture certain mechanisms and stages in the progression of CMC failure. Mechanical performance properties are listed in Table 6.5.[18] All specimens were found to have a modulus and fracture strength within typical literature values; however, a direct comparison is impossible without an identical architecture, which often convolutes the performance of experimental CMC materials. All CMCs deviated from an elastic response (DFL) around 0.04 to 0.05 % strain.

Table 6.5. Summary of CMC experimental properties and literature properties.[5,14,35,36] Spans are in mm

ID	l_U	l_L	Expected Young's Modulus (GPa)	Young's Modulus (GPa)	Expected Ultimate Strength (MPa)	Ultimate Strength (MPa)	Ultimate Strain (%)	DFL Stress (MPa)	DFL Strain (%)
CMC_01	42	84	230-250	238	220-300	178	0.156	139	0.043
CMC_02	42	84	230-250	265	220-300	N/A	N/A	162	0.055
CMC_03	42	84	230-250	260	220-300	265	0.457	132	0.043

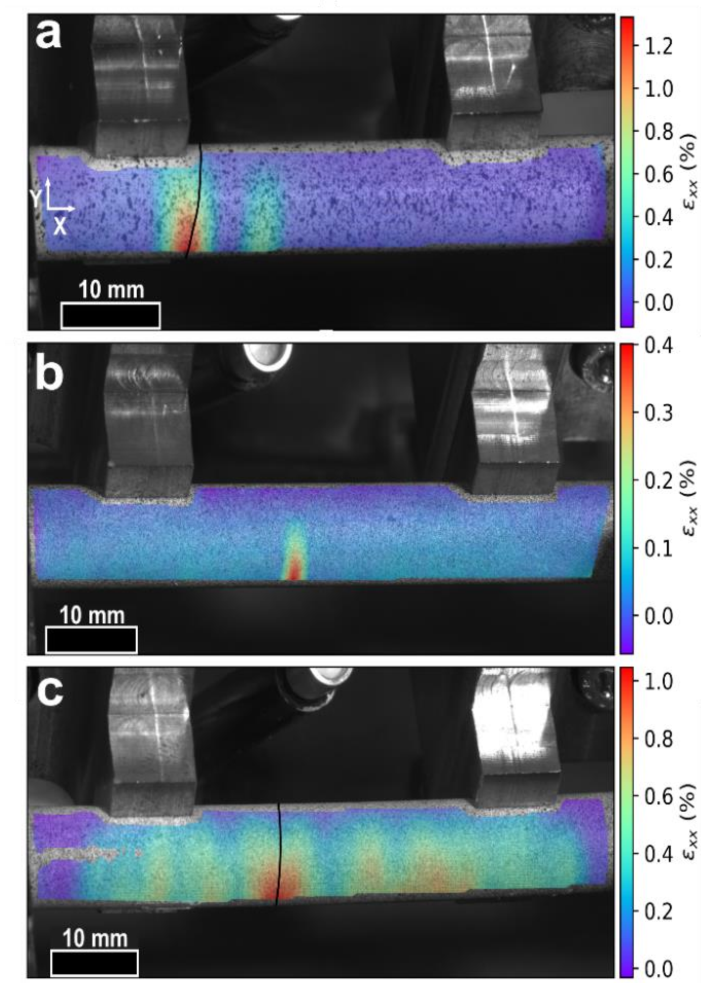

Fig. 6.9. Strain bending profiles for all three CMC specimens, showing immediately prior to (a) loss of load-bearing capability for CMC_01, (b) initial He leakage of CMC_02, and (c) loss of load-bearing capability for CMC_03. Note varied color scales.

Fig. 6.9 presents the complete DIC strain profiles immediately prior to the test end. Notably all specimens began cracking within the bending zone; specimens CMC_01 and CMC_02 exhibited one or two prominent cracks while CMC_03 showcased a distribution of cracks down the bending zone. Single or few crack failure of SiC/SiC CMCs can be attributed to several sources, namely matrix or tow structure defects or inadequate interphase properties. While CMC_02 was not loaded to failure but rather the onset of He leaking, a comparison with Fig. 6.10b of CMC_03 at a similar strain indicates that CMC_02 was likely to fracture by a single or few crack like CMC_01. Therefore, 2 out of 3 for the measured CMCs exhibited unacceptable failure behavior.

Fig. 6.10 displays the DIC correlated data for the stress-strain curve analysis, using a moderately sized subset and step size. Looking closely at the buildup of strain within CMC_03 (Fig. 6.10), it is possible to see a relatively uniform bending profile early in the test; corresponding stress-strain locations of the images seen in Fig. 6.10 are labeled in Fig. 6.11a. As acoustic events were detected, large strain concentrations appeared along the bending zone, indicating that cracking had initiated (Fig. 6.10a). Eventually, the cracks penetrated the matrix, forming a narrow channel for gas to begin to slowly escape (Fig. 6.10b). The progressive increase in deformation opened up more cracks and widened any penetrating cracks, initiating the first, large jump in He leak rate around 0.09% bending strain (Fig. 6.10c). Two more sequential jumps in He leak rate (Fig. 6.10d-e) were caused by additional crack opening before final loss of load-bearing capacity of CMC_03.

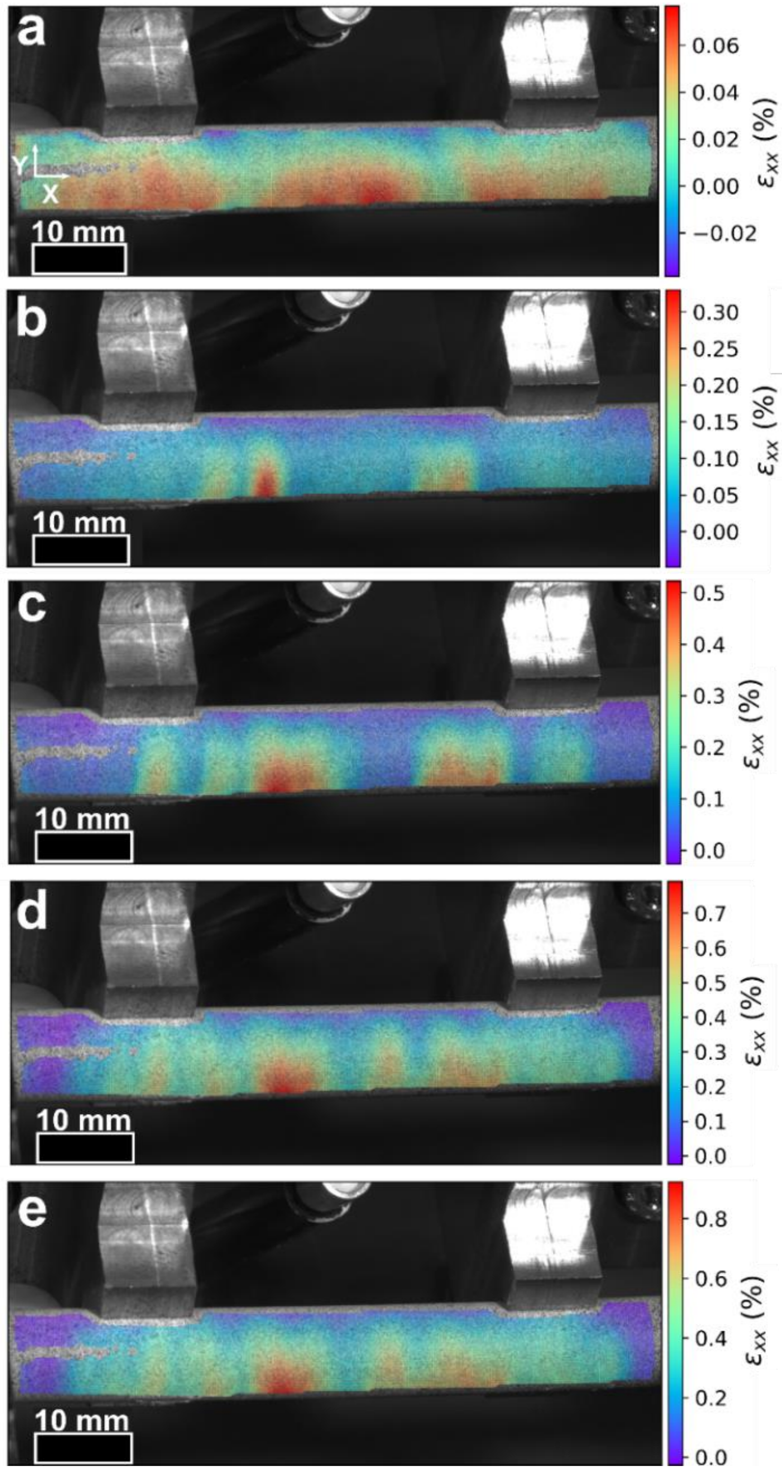

Fig. 6.10. Strain bending profile of CMC_03 (a) at the onset of increased NC-AE, (b) at the onset of increased He leak rate, (c) at the first large increase of He leak rate, (d) at the second large increase of He leak rate, (e) at the third large increase of He leak rate up to sensor saturation. Note varied color scales and strain ranges are without the 90th percentile filter.

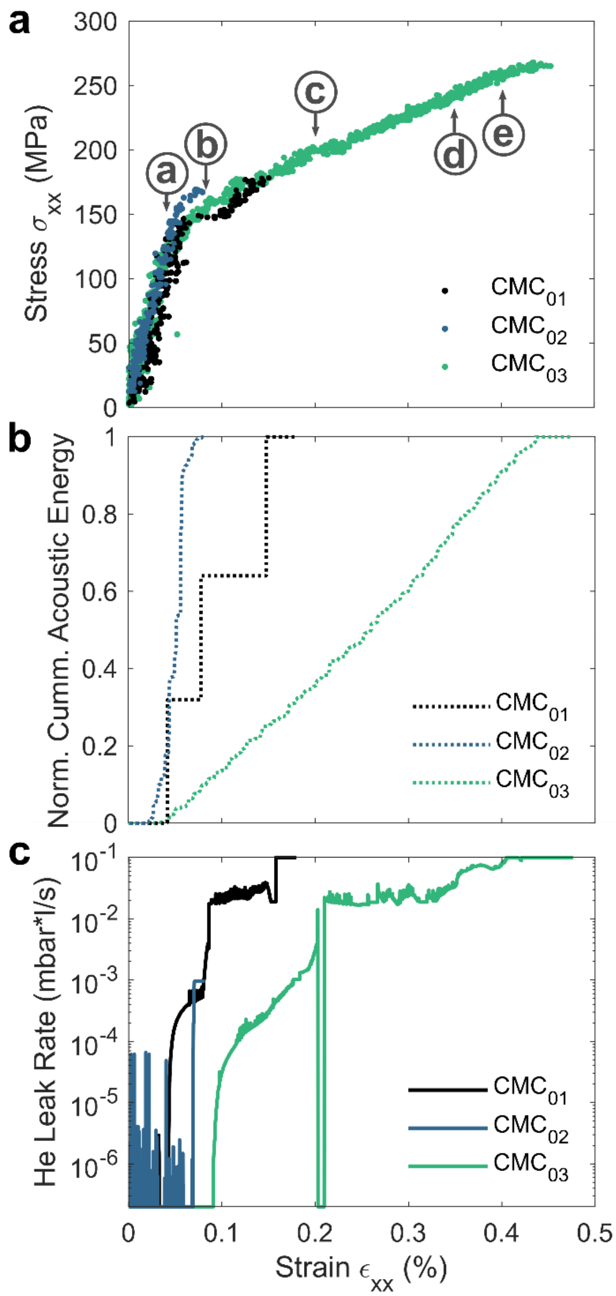

Fig. 6.11 **(**a) Four-point bending stress-strain curves, (b) AE, and (c) He leak rate response over bending strain of CMC tubes. The circled lettering corresponds directly to the labeled strain profiles seen in Fig. 6.10.

The elastic response of each CMC specimen aligned well (Fig. 9a), but the continued response beyond the DFLS highlighted the differences between the specimens. CMC_02, which was removed at the onset of leaking, only achieved a strain just past the DFLS. CMC_01 obtained a slightly higher strain, while CMC_03 achieved the highest strength and strain before fracture.

From AE (Fig. 9b), it is clear that the DFLS point is nearly concurrent with the onset of acoustic activity (0.042 %), signaling that these acoustic events correspond to matrix microcracking and the transfer of load to the fiber tows. Leaking from CMC_01 began shortly after the DFLS point as well, corresponding to 0.043 % strain, but was delayed for CMC_02 and CMC_03 at 0.069 % and 0.090 % strains, respectively. The delayed leaking of CMC_03 is an interesting behavior that likely stems from the more distributed cracking of this CMC and is the desired failure format for CMC claddings.

Of the two specimens taken to loss of load bearing capability, the acoustic and leak data trends were quite different. For CMC_01, the buildup of acoustic and leak rate data followed the same trend, occurring in stages and associated with onset of matrix microcracking and initial leaking, the onset of fiber cracking and opening of matrix channels, and the final fracture of the tows. In contrast, the leak rate of CMC_03 followed a similar three-stage trend, but the buildup of acoustic activity was very linear without any distinct stages. This linear increase of acoustic activity reflects the greater occurrence of distributed cracking down the length of the bending zone and is the expected behavior for an ideal CMC cladding. From the higher fracture strain of CMC_03, it is apparent that the uniform distribution of cracks effectively distributes stresses.

4.3. Measurements of surface matrix cracking by stereoscopic digital image correlation

4.3.1. **Cracking and failure behavior in Batch A**

High resolution DIC measurements can be used to identify and measure cracks, which can be compared to fracture surfaces viewed under SEM. The DIC images at the maximum recorded stress were re-correlated with a fine subset and step size to reveal large crack locations, as previously mentioned. Representative profiles are shown in Fig. 6.12. In Fig. 6.12a-b, out-of-plane height is added to the image background to reveal the tow architecture. The location of the final fracture of both specimens is marked in black.

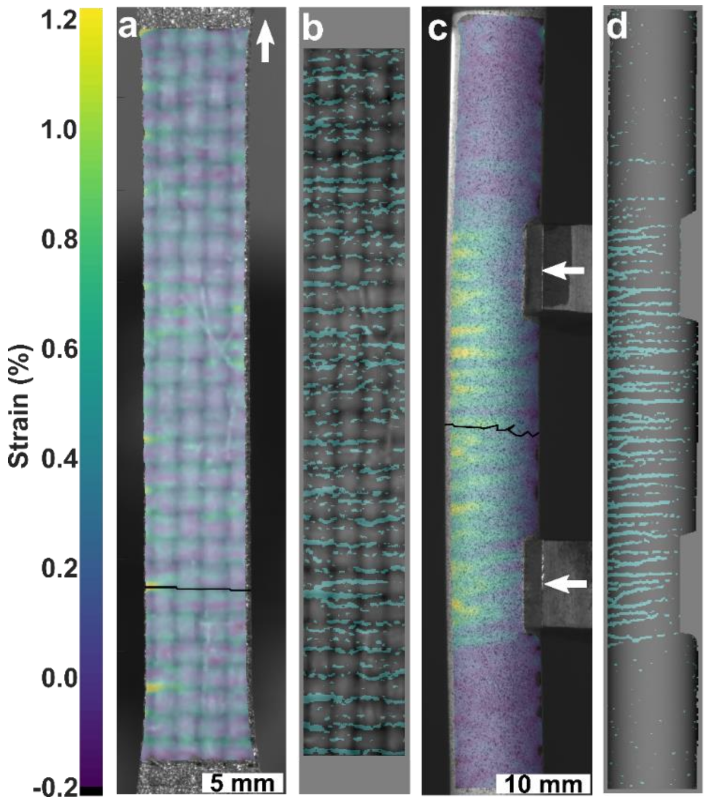

Fig. 6.12. 3D-DIC profiles at maximum stress. (a) T01 tensile strain (out-of-plane topology added to background). (b) Potential cracks revealed by thresholding for T01. (c) B02 bending strain (image rotated 90° clockwise). (d) Potential cracks revealed by thresholding for B02. For all, arrows indicate loading direction and black lines indicate the final fracture path.

Rear cameras capturing the opposing face revealed that for T01, cracking initiated in the ply facing the front camera set with DIC correlation presented in Fig. 6.12a. Numerous cracks existed down the gauge length of T01 (Fig. 6.12b) with two larger cracks initiating within the cut axial tow, shown in Fig. 6.12a as regions with yellow shading, demarked as high strain. Threshold analysis (Fig. 6.12b) indicates cracks in the outer matrix, ran across the full width of the gauge section at numerous points along the gauge length, with many occurring at the edges of transverse tows. In fact, for both PW CMCs, it was found via threshold analysis that, prior to final fracture, every observable transverse-axial tow contact line within the gauge section contained some instance of DIC measurable cracking.

Cross-sectional SEM images (Fig. 6.13a) of the DIC-indicated final fracture initiation site were taken. From examining the fracture surface, it is clear that final fracture initiated at and propagated along the contact points between axial and transverse tow, as few remains of the transverse tows were seen on this half of the tension specimen. Notably, a large gap between the plies was found directly adjacent to the DIC indicated final fracture initiation location. Additionally, cracks were also found to run along the axial direction, as indicated in Fig. 6.13b with arrows. These cracks were not visible via DIC analysis and either may have been produced during the rapid final fracture event or were too small to detect with present resolution.

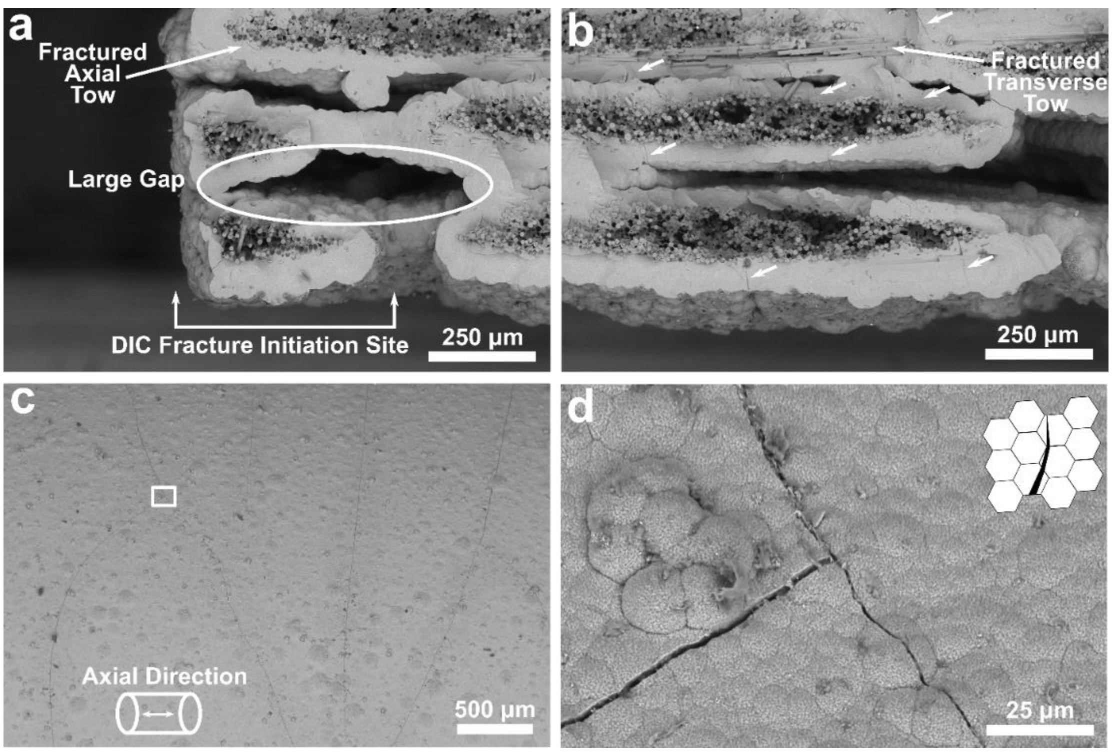

Fig. 6.13. Backscatter SEM images (a) T01 cross-sectional fracture surface of DIC indicated final facture initiation site (double arrows) (b) T01 fracture surface adjacent from (a), which shows axial cracking along axial tows (indicated by short white arrows). (c) B02 outer diameter cracking within bending region. (d) Inset location from (c) revealing cracking (schematic). SEM images acquired by David Roche.

Fig. 6.12c shows the maximum strain profile of B02 before failure, with final fracture location highlighted in black. Widespread cracking (Fig. 6.12d) occurred largely within and below the central supports. These DIC displacement indicated cracks were measured to an average spacing of ~1 mm along the 0° location with maximum tensile bending. The crack spacing at 0° was examined from SEM images, which indicated an average crack spacing of 1.14 mm. The magnitudes of DIC and SEM measured crack spacing down the length of the bending zone between the inner loading points indicates crack initiation sites are likely microstructure dependent. Tow crossover spacing (Fig. 6.14) was measured from select regions, which contained visible surface tows from DIC data. Single biased tow spacing was found to be 0.81 mm (standard deviation of 0.03 mm). Considering the measured crossover spacing and the tensile fracture locations, which occurred at contact points between axial and transverse tows, it is surmised these bending crack locations occur where the braided tows contact beneath the typical outer SiC coating, as has been documented in other expanding plug[11] and bending[19] studies with SiC/SiC CMCs. This contact interaction likely provides a sufficient local stress concentration to initiate a crack, or a local cluster of multiple cracks, within the outer SiC coating.

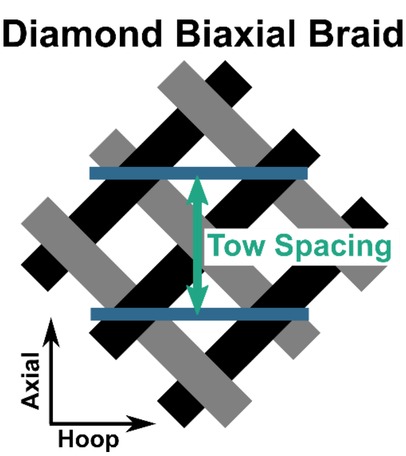

Fig. 6.14. Schematic of diamond biaxial braid pattern and measured tow spacing.

The potential crack map (Fig. 6.12d) indicates many cracks propagate through the initial neutral axis of bending (located at 90° where 0° is the bottom most, under greatest tensile strain surface of the specimen) and into the upper, assumedly compressive region of the bending specimen (between 90 and 180°). While the DIC strains and crack analysis are limited to the visible regions, under SEM these cracks can be traced through continuous hairline fractures along the entire circumference. A few instances of crack coalescence were observed in the crack position map (Fig. 6.12d) and under SEM (Fig. 6.13c-d), where several cracks growing from the underside of the specimen were observed to intersect at the neutral axis where the tension driving crack propagation decreased. The surface micrographs clearly reveal the trans-globular cracking behavior of the SiC matrix, as also documented in other literature.[45,46] Unlike the tensile specimens, the outer SiC coating prevented direct visualization of tow structure features to crack propagation, but observable cracking features are indicative of a tow structure dependent failure of these tubes in bending. The tension under bending initiates cracking along the bending zone within the outer coating matrix, marking the DFL point in the stress-strain curve. These cracks progress, leading to circumferential cracking across the tubular specimen, and eventually, fiber tow fracture leads to final failure of the specimen.

4.3.2. **Cracking and failure behavior of Batch B**

The nominal cracking behavior of Batch B SiC/SiC CMCs is inconsistent from Batch A. Two of three CMCs in Batch B exhibited single dominate crack failure, and only CMC_03 exhibited distributed cracking similar to Batch A. This inconsistent behavior likely stems from manufacturing variations and is to be expected with experimental SiC/SiC claddings. However, CMC_03 can be used to make some observations on the cracking and hermetic performance of these and future SiC/SiC claddings in bending.

DIC subset size has been proven to be linked with noise in 3D-DIC measurements (artificial displacements) in literature[22] and in previous sections of this dissertation. While it may be generally better to use a larger subset to minimize noise when calculating conventional mechanical properties, a small subset increases measurement resolution and can be used to better identify matrix crack locations in CMCs.[24] Fig. 6.15 is analogous to Fig. 6.10 , except the use of a 13 px subset, which is less than half of that used in Fig. 6.10.

The progressive cracking behavior of CMC_03 can be seen in Fig. 6.15. In Fig. 6.15a, NC-AE has risen above nominal zero, but no cracks in the outer SiC coating are detected via 3D-DIC. In Fig. 6.15b, CMC_03 has begun to leak internally pressurized helium. Fig. 6.15e shows the surface cracking prior to leak inhiation; however, the cracks rapidly penetrate through the tube wall. In a reactor environment, this leak would include helium and potentially radioactive fuel particles, which would be released into the surrounding water coolant and working fluid for the steam turbines. These results indicate that shortly following the average DFL stress of 144 MPa and strain of 0.047 % the hermetic integrity of the SiC/SiC CMC claddings is lost, and they have effectively failed their design mission. It should be further noted that these values ignore the potential effects of the fuel pellets during bending.

Work done in *Cockeram et al.*[47] with flexural tests of chemical vapor deposited (CVD) monolithic silicon carbide beams can be used as a useful comparison point to reflect on for the performance of SiC/SiC CMCs and a similar composition of monolithic SiC. Cockeram's work includes a statistically relevant sample size of monolithic SiC, which can be considered in the elastic regime. Average values of the CVD SiC for ultimate (here, equivalent to DFL) stress and strain are 408 MPa and 0.118 %, respectively. While the mechanical performance of CVD SiC was found to greatly depend on the grinding/polishing of the beams, these results indicate that finely polished monolithic SiC exhibits potentially better hermetic stress/strain performance than current (notably, experimental) SiC/SiC CMCs due to the underlying tow architecture in bending. SiC/SiC CMC claddings exhibit vastly superior failure strains (> 0.4%) and a graceful loss of load bearing capacity, which is necessary for practical applications. Given the complexity of the underlying braid tow structure contact points, it may prove advantageous to switch to a filament wound CMC architecture.

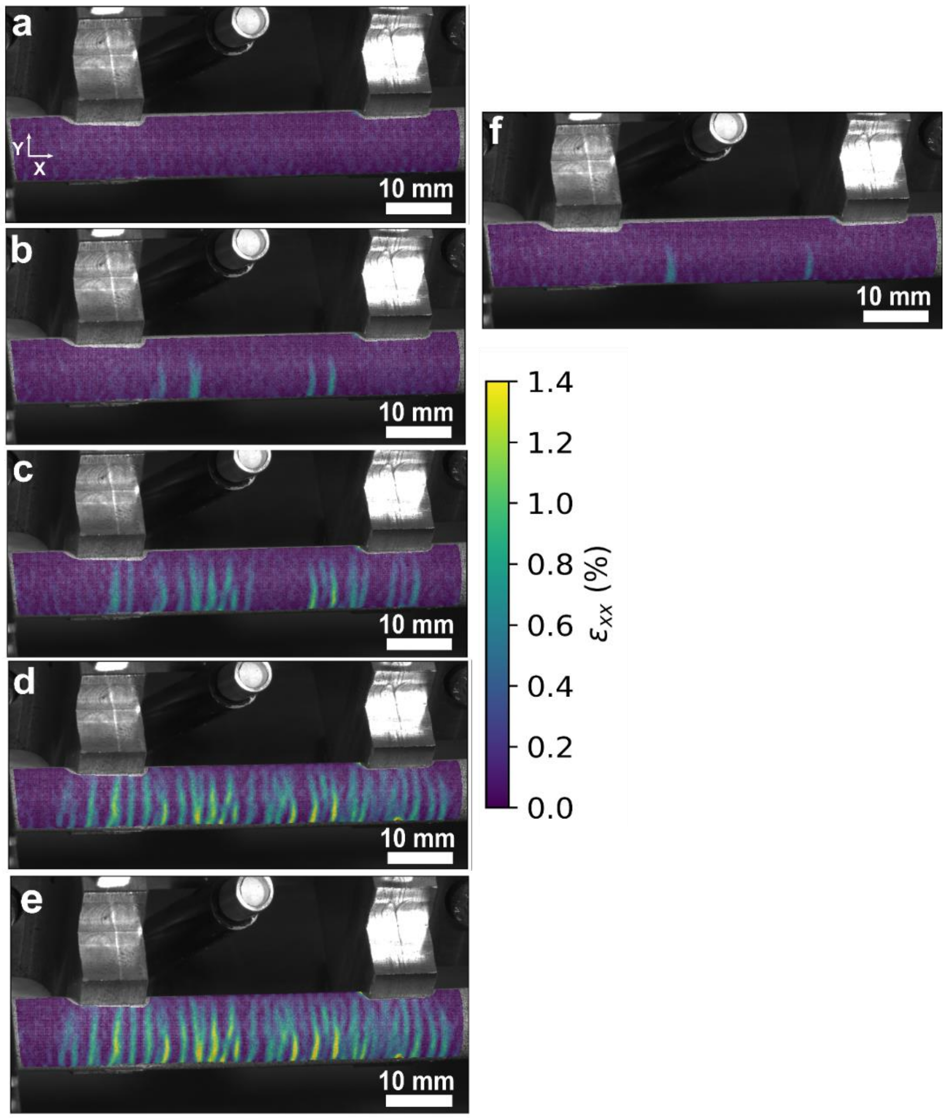

Fig. 6.15. Strain bending profile of CMC_03, analyzed with a small DIC subset of 13 px to increase strain resolution. Results are a mirror of Fig. 6.10. (a) at the onset of increased NC-AE, (b) at the onset of increased He leak rate, (c) at the first large increase of He leak rate, (d) at the second large increase of He leak rate, (e) at the third large increase of He leak rate up to sensor saturation, (f) between onset of NC-AE and onset of He leaking (between (a) and (b)).

4.3.3. Tow structure analysis of plain weave SiC/SiC CMCs

Failure of CMCs can often be attributed to internal or tow architecture defects.[10,11]

Since the planar CMCs studied here consisted of only three plies with no overcoating, they are ideal to study the effects of plain weave tow architecture on final failure location. Cracking and high DIC strains were observed to occur along transverse tows. While it has been reported that failure often initiates within tows perpendicular to loading,[40] it is currently unclear if transverse tow angle variation could significantly alter crack initiation and fracture sites.

Using the programmatic methods detailed in Heim, *et.al.*,[48,49] the centroid location of tow peaks or "crowns" (Fig. 6.16a) were robustly isolated for both axial and transverse tows from the DIC triangulation surface data. Tow crown isolation was performed on all faces k with measurements gathered prior to loading. Linear fits were applied to tow centroid coordinates for each transverse tow $i \dots n$, such that each transverse tow angle θ_i (Fig. 6.16a) could be determined from horizontal. Global tow tilt of each face k from the DIC setup or misalignment in manufacturing cutting path was removed by subtracting out the average transverse tow angle $\overline{\theta_k}$, which was nominally <2°. It is anticipated that a high local gradient in tow angle could concentrate stress; therefore, the change in neighboring transverse tows angle was defined as:

$$\Delta\theta_i = [\theta_i - \overline{\theta_k}] - [\theta_{i+1} - \overline{\theta_k}] \text{ for } i = 1 \dots n-1. \tag{6.9}$$

With the combined front and back face from each CMC, over 100 transverse tows were measured. The statistical probability distribution of $\Delta\theta$ is presented in Fig. 6.16b. The $\Delta\theta$ values at the location of final fracture are indicated with black arrows, where F and B correspond to the face of each CMC. It should be noted that DIC indicated final failure initiation occurred in $T01_F$ and $T02_B$. Dominate crack locations were found to occur between transverse tows with $\Delta\theta$ well within a single standard deviation of the mean $\Delta\theta$, indicating that the local variation in transverse tow angle does not have a significant effect on final failure location, for transverse tows with $\Delta\theta$ in the range of $\pm 4°$ from a sample average.

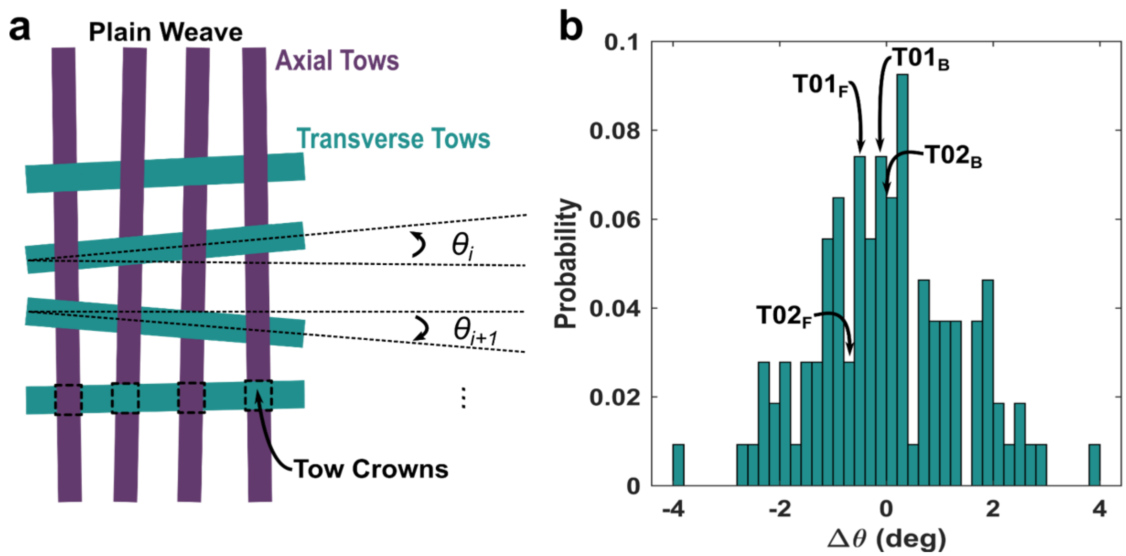

Fig. 6.16. (a) Plain weave schematic defining $\theta_{i...n}$. (b) Probability histogram plot of change in angle between transverse tows $\Delta\theta_i$.

5. *Conclusions*

Custom-designed fixtures for SiC/SiC CMC testing were developed and coupled with 3D-DIC to evaluate plain weave, planar CMCs in tension and biaxially-braided, tubular CMCs in four-point bending at ambient, room temperature conditions. Mechanical properties fall within expected ranges and demonstrate the stress redistribution mechanism of CMCS. High resolution DIC strain measurements and spatial derivative analyses of DIC displacement measurements reveal crack initiation sites and provide insight into stress redistribution mechanisms. SEM was performed postmortem to determine the influence of microstructural features on failure. For plain weave planar CMCs tested in uniaxial tension, it was determined that fracture initiated at tow crossover, with potential to propagate along transverse tows. It was also determined that for the range measured ($\pm 4°$), subtle variations in local transverse tow variation did not have a significant effect on final fracture location. For tubular biaxially braided CMCs with SiC coating tested in four-point bending, cracking was found to initiate due to tensile strains, with a percentage of cracks propagating along the full circumference prior to final fracture, as crack growth led to local stress redistribution towards the upper, originally compressed region of the specimen. Crack spacing was measured i*n situ* by stereoscopic image correlation and confirmed by SEM measurements to relate to underlying tow-tow crossing points for tubular CMC under bending.

Using a triad of complementary sensors, including 3D-DIC, AE, and He leak rate detection, the spatial strains at critical fracture events could be investigated for CMC fuel cladding tubes, including the onset of matrix cracking, loss of hermitic seal, and loss of load-bearing capability. Matrix cracking was well defined by the DFL at strains ranging from 0.04 - 0.06 % and was shortly followed by initial loss of hermetic seal by 0.09 % bending strain. Leaking increased in distinct steps over a span of 0.1- 0.2 % bending strain. The slower, stepped progression of NC-AE events and He leak rate demonstrated the graceful, delayed failure behavior characteristic of CMCs over four distinct steps. These test methodologies and techniques were developed to progress the standardization of critical nuclear reactor components and to resolve the mechanisms that control these distinct steps of CMC failure.

6. References

[1] Hirano M, Yonomoto T, Ishigaki M, Watanabe N, Maruyama Y, Sibamoto Y, et al. Insights from review and analysis of the Fukushima Dai-ichi accident. J Nucl Sci Technol 2012;49:1–17. doi:10.1080/18811248.2011.636538.

[2] Karoutas Z, Brown J, Atwood A, Hallstadius L, Lahoda E, Ray S, et al. The maturing of nuclear fuel: Past to Accident Tolerant Fuel. Prog Nucl Energy 2018;102:68–78. doi:10.1016/j.pnucene.2017.07.016.

[3] Kurata M. Research and Development Methodology for Practical Use of Accident Tolerant Fuel in Light Water Reactors. Nucl Eng Technol 2016;48:26–32. doi:10.1016/j.net.2015.12.004.

[4] Yvon P, Carré F. Structural materials challenges for advanced reactor systems. J Nucl Mater 2009;385:217–22. doi:10.1016/j.jnucmat.2008.11.026.

[5] Bacalski CF, Jacobsen GM, Deck CP. Characterization of SiC-SiC accident tolerant fuel cladding after stress application. Top Fuel 2016 LWR Fuels with Enhanc Saf Perform 2016:843–8.

[6] Deck CP, Khalifa HE, Sammuli B, Hilsabeck T, Back CA. Fabrication of SiC–SiC composites for fuel cladding in advanced reactor designs. Prog Nucl Energy 2012;57:38–45. doi:10.1016/J.PNUCENE.2011.10.002.

[7] Deck CP, Jacobsen GM, Sheeder J, Gutierrez O, Zhang J, Stone J, et al. Characterization of SiC–SiC composites for accident tolerant fuel cladding. J Nucl Mater 2015;466:667–81. doi:10.1016/J.JNUCMAT.2015.08.020.

[8] Morscher GN, Pujar V V. Design guidelines for in-plane mechanical properties of SiC fiber-reinforced melt-infiltrated SiC composites. Int J Appl Ceram Technol 2009;6:151–63. doi:10.1111/j.1744-7402.2008.02331.x.

[9] Gyekenyesi JZ, Bansal NP. High Temperature Tensile Properties of Unidirectional Hi-Nicalon/Celsian Composites In Air 2000.

[10] Rossol MN, Rajan VP, Zok FW. Effects of weave architecture on mechanical response of 2D ceramic composites. Compos Part A Appl Sci Manuf 2015;74:141–52. doi:10.1016/j.compositesa.2015.04.003.

[11] Croom BP, Li X, Deck CP, Xu P, Lahoda EJ. Quantifying the three-dimensional damage and stress redistribution mechanisms of braided SiC/SiC composites by in situ volumetric digital image correlation. Scr Mater 2016;130:238–41. doi:10.1016/j.scriptamat.2016.12.021.

[12] Vasiliev V V., Morozov E V. Composite Pressure Vessels. Adv. Mech. Compos. Mater. Struct. 4th ed., Elsevier; 2018, p. 787–821. doi:10.1016/B978-0-08-102209-2.00012-8.

[13] Koyanagi T, Katoh Y, George J, Deck CP. Issue Update to LWR SiC/SiC Cladding Handbook of Properties. Oak Ridge, TN (United States): 2018. doi:10.2172/1479750.

[14] Ding D. 2 - Processing, properties and applications of ceramic matrix composites, SiCf/SiC: an overview. In: Low IM, editor. Adv. Ceram. Matrix Compos., Woodhead Publishing; 2014, p. 9–26. doi:https://doi.org/10.1533/9780857098825.1.9.

[15] Isaac M. Daniel OI. Engineering mechanics of composite materials. 2nd ed. New York: Oxford University Press; 2006.

[16] Katoh Y, Hu X, Koyanagi T, Singh GP. Determination of He and D permeability of neutron-irradiated SiC tubes to examine the potential for release due to micro-cracking. Oak Ridge, TN (United States): 2017. doi:10.2172/1394374.

[17] Singh G, Gonczy S, Deck C, Lara-Curzio E, Katoh Y. Interlaboratory round robin study on axial tensile properties of SiC-SiC CMC tubular test specimens. Int J Appl Ceram Technol 2018;15:1334–49. doi:10.1111/ijac.13010.

[18] Bumgardner CH, Heim FM, Roache DC, Jarama A, Xu P, Lu R, et al. Unveiling hermetic failure of ceramic tubes by digital image correlation and acoustic emission. J Am Ceram Soc 2019. doi:10.1111/jace.16854.

[19] Van Rooyen IJ, Lloyd WR, Trowbridge TL, Novascone SR, Wendt KJ, Bragg-Sitton SM, et al. SiC-CMC-Zircaloy-4 Nuclear Fuel Cladding Performance During 4- Point Tubular Bend Testing: LWR Fuel Performance Meeting/Top Fuel 2013. Idaho Natl. Lab., 2013.

[20] Vinogradov ML, Barchenko VT. Measurement of the gas permeation through the composite materials 2015:40–4. doi:10.1109/eiconrusnw.2015.7102228.

[21] Quinn G, T. Sparenberg B, Koshy P, K. Ives L, Jahanmir S, Arola D. Flexural Strength of Ceramic and Glass Rods. J Test Eval 2009;37:222–44. doi:10.1520/JTE101649.

[22] Schreier H, Orteu JJ, Sutton MA. Image correlation for shape, motion and deformation measurements: Basic concepts, theory and applications. Springer US; 2009. doi:10.1007/978-0-387-78747-3.

[23] Sutton MA. Three-dimensional digital image correlation to quantify deformation and crack-opening displacement in ductile aluminum under mixed-mode I/III loading. Opt Eng 2007;46:051003. doi:10.1117/1.2741279.

[24] Rajan VP, Rossol MN, Zok FW. Optimization of Digital Image Correlation for High-Resolution Strain Mapping of Ceramic Composites. Exp Mech 2012;52:1407–21. doi:10.1007/s11340-012-9617-1.

[25] Ojard G, Goberman D, Holowczak J. Acoustic emission as a screening tool for ceramic matrix composites. AIP Conf Proc 2017;1806. doi:10.1063/1.4974568.

[26] Munch E, Duisabeau L, Fregonese M, Fournier L. Acoustic emission detection of environmentally assisted cracking in Zircaloy-4 alloy. EUROCORR 2004 2004;36.

[27] Kral Z, Horn W, Steck J. Crack propagation analysis using acoustic emission sensors for structural health monitoring systems. Sci World J 2013;2013. doi:10.1155/2013/823603.

[28] Morscher GN, Yun HM, Dicarlo JA. In-plane cracking behavior and ultimate strength for 2D woven and braided melt-infiltrated SiC/SiC composites tensile loaded in off-axis fiber directions. J Am Ceram Soc 2007;90:3185–93. doi:10.1111/j.1551-2916.2007.01887.x.

[29] Morscher G, Gyekenyesi J. Room temperature tensile behavior and damage accumulation of Hi-Nicalon reinforced SiC matrix composites. 22nd Annu Conf Compos Adv Ceram Mater Struct 2009.

[30] Morscher GN. Modal acoustic emission source determination in silicon carbide matrix composites. AIP Conf Proc 2000;509. doi:10.1063/1.1306075.

[31] Nunes LCS, Reis JML. Estimation of crack-tip-opening displacement and crack extension of glass fiber reinforced polymer mortars using digital image correlation method. Mater Des 2012;33:248–53. doi:https://doi.org/10.1016/j.matdes.2011.07.051.

[32] Lai S, Shi L, Fok A, Li H, Sun L, Zhang Z. A New Method to Measure Crack Extension in Nuclear Graphite Based on Digital Image Correlation. Sci Technol Nucl Install 2017;2017:2416545. doi:10.1155/2017/2416545.

[33] Auerkari P. Mechanical and physical properties of engineering alumina ceramics. 1996.

[34] Asmani M, Kermel C, Leriche A, Ourak M. Influence of porosity on Youngs modulus and poisson's ratio in alumina ceramics. J Eur Ceram Soc 2001;21:1081–6. doi:10.1016/S0955-2219(00)00314-9.

[35] Nie X, Chen WW, Wereszczak AA, Templeton DW. Effect of loading rate and surface conditions on the flexural strength of borosilicate glass. J Am Ceram Soc 2009;92:1287–95. doi:10.1111/j.1551-2916.2009.03019.x.

[36] Bacalski CF, Jacobsen GM, Deck CP. Characterization of SiC-SiC accident tolerant fuel cladding after stress application. United States: American Nuclear Society - ANS; 2016.

[37] Singh G, Gonczy S, Deck C, Lara-Curzio E, Katoh Y. Interlaboratory round robin study on axial tensile properties of SiC-SiC CMC tubular test specimens. Int J Appl Ceram Technol 2018;15:1334–49. doi:10.1111/ijac.13010.

[38] Katoh Y, Ozawa K, Shih C, Nozawa T, Shinavski RJ, Hasegawa A, et al. Continuous SiC fiber, CVI SiC matrix composites for nuclear applications: Properties and irradiation effects. J Nucl Mater 2014;448:448–76. doi:10.1016/j.jnucmat.2013.06.040.

[39] Katoh Y, Ozawa K, Hinoki T, Choi Y, Snead LL, Hasegawa A. Mechanical properties of advanced SiC fiber composites irradiated at very high temperatures. J Nucl Mater 2011;417:416–20. doi:https://doi.org/10.1016/j.jnucmat.2011.02.006.

[40] Katoh Y, Snead LL, Nozawa T, Hinoki T, Kohyama A, Igawa N, et al. Mechanical Properties of Chemically Vapor-Infiltrated Silicon Carbide Structural Composites with Thin Carbon Interphases for Fusion and Advanced Fission Applications. Mater Trans - MATER TRANS 2005;46:527–35. doi:10.2320/matertrans.46.527.

[41] T Nozawa Y Katoh, Y Katoh, A Kohyama, A Kohyama, E Lara-Curzio, TH. Specimen Size Effects on Tensile Properties of 2D/3D SiC/SiC Composites. West Conshohocken, PA:

ASTM International; n.d. doi:10.1520/STP10828S.

[42] Nozawa T, Katoh Y, Kohyama A. Evaluation of Tensile Properties of SiC/SiC Composites with Miniaturized Specimens. Mater Trans - MATER TRANS 2005;46:543–51. doi:10.2320/matertrans.46.543.

[43] Heim FM, Zhang Y, Li X. Uniting Strength and Toughness of Al Matrix Composites with Coordinated Al3Ni and Al3Ti Reinforcements. Adv Eng Mater 2018;20:1700605. doi:10.1002/adem.201700605.

[44] Rooyen IJ van, Lloyd WR, Trowbridge TL, Novascone SR, Wendt KJ, Rooyen IJ Van, et al. SiC-CMC-Zircaloy-4 Nuclear Fuel Cladding Performance During 4- Point Tubular Bend Testing. LWR Fuel Perform Meet Fuel 2013 2013.

[45] Wade J, Ghosh S, Claydon P, Wu H. Contact damage of silicon carbide ceramics with different grain structures measured by Hertzian and Vickers indentation. J Eur Ceram Soc 2015;35:1725–36. doi:10.1016/j.jeurceramsoc.2014.12.030.

[46] Gavalda Diaz O, Axinte DA, Butler-Smith P, Novovic D. On understanding the microstructure of SiC/SiC Ceramic Matrix Composites (CMCs) after a material removal process. Mater Sci Eng A 2019;743:1–11. doi:10.1016/j.msea.2018.11.037.

[47] Cockeram BV. Fracture Strength of Plate and Tubular Forms of Monolithic Silicon Carbide Produced by Chemical Vapor Deposition. J Am Ceram Soc 2002;85:603–10. doi:10.1111/j.1151-2916.2002.tb00139.x.

[48] Heim FM, Croom BP, Bumgardner C, Li X. Scalable measurements of tow architecture variability in braided ceramic composite tubes. J Am Ceram Soc 2018;101:4297–307. doi:10.1111/jace.15564.

[49] Heim FM, Daspit JT, Holzmond OB, Croom BP, Li X. Analysis of tow architecture variability in biaxially braided composite tubes. Compos Part B Eng 2020;190:107938. doi:https://doi.org/10.1016/j.compositesb.2020.107938.

CHAPTER 7: SUMMARY AND OUTLOOK

1. Summary

The properties of composites are tunable via the constituents, but failure is often related to nonuniformity of the constituents, including irregular size, shape, density or orientation. To improve performance and safety in extreme material applications, many classically metallic structural components are set to be replaced by new textile composites featuring continuous fiber reinforcements, bundled into tows. The complex manufacturing process of braided and woven composites produces inconsistency in both the microstructure and mechanical properties, particularly, along the length of long components. Some of this variability is attributed to nonuniform reinforcement placment, producing systematic and stochastic distortions in the tow trajectories, causing unit cells of irregular shape and size, and ultimately, influencing stress redistribution behavior. Much information about these nonperiodic defects is unknown, including how they are spatially distributed, how the specific braid/weave architecture or local geometry influences their development, and how they influence local mechanical failure. To address this need, stereoscopic digital image correlation (DIC) was utilized in an unconventional manner to develop a multitude of scalable systems to quantify nonuniform reinforcement distributions and investigate the reinforcement architecture dependency of failure for textile composites.

In Chapter 1, motivation for this study is provided, concerning the complex failure of many composite materials and the failure relationship to the local placement of reinforcing phases/fibers. Necessary background information on the two examined composite systems: SiC/SiC ceramic matrix composites (CMC) and carbon fiber reinforced polymer (CFRP) composites is given, as well as a brief description of typical manufacturing procedures, in which tow structure defects likely arise. Finally, a detailed overview of the procedure and sources of error in stereoscopic digital image correlation (DIC) is given.

In Chapter 2, hybrid aluminum composites were fabricated in a novel manner to characteristically induce a layer-wise aligned distribution of micro-scale Al_3Ni and Al_3Ti reinforcing intermetallic particles, which were formed *in situ* within a ductile Al matrix. The developed Rolling of Randomly Orientated Layer-wise Materials (RROLM) manufacturing methodology enables microstructural tailoring of the intermetallic reinforcing particles to prescribe enhanced crack tip deflection caused by the complex interaction of local veins of reinforcement particles, in an effort to overshadow the classical loss of toughness in large-particle reinforced composites. *In situ* scanning electron microscopy, three-point bending observations combined with a local strain field analysis demonstrate the crack deflection mechanisms exhibited by the composite. This specialized composite exhibits both strengthening and toughening simultaneously, over control samples. The investigated design strategy and model material served as inspiration for the work compiled for textile composites and will assist materials development towards light-weight, stronger, and tougher materials through intelligent placement and design of the reinforcement phases of composite systems.

In Chapter 3, a high resolution, high accuracy, and noncontact surface reconstruction and metrology technique was developed to measure complexly/arbitrarily shaped geometries, termed mosaic digital image correlation (M-DIC). As the core focus of this chapter, fundamental and numerical experiments were performed to demonstrate that M-DIC's intrinsic measurement errors can be quantified and significantly reduced to improve upon the base accuracy and precision of the technique. Speckle patterning methods and quality assessment were also addressed. This chapter lays out the groundwork needed to develop and validate M-DIC measurements for use in the practical applications in following chapters.

In Chapter 4, full-field M-DIC measurements were used to quantify the irregular tow placement in biaxially braided CFRP tubes and triaxially braided SiC/SiC CMC nuclear fuel claddings. The surface texture peaks of these composites, corresponding to the tow path's radial maximum or "crowns", were used as fiducial markers to measure the surface tow structure. Analysis included the reconstructed tow paths and tow crown spacings. A comparison between the biaxial and triaxial braid results indicated axial tows work to constrain unit cells dimensions along the hoop direction. It was found that braid type significantly affected the irregular placement of tows in the composite. Unit cells in the biaxial braid show extensive trellising, and the unit cells dimensions varied most significantly in the hoop direction. In contrast, triaxial data showed the introduction of comparatively rigid axial tows inhibited tow motion in the hoop direction and redirected this motion to align with the axial tows. Overall, the variation in unit cell dimensions was smaller for the triaxial braid than for the biaxial braid. Finally, a route toward numerical simulation of the composite response is proposed by developing a 3D model of the composite using the measured tow trajectories.

In Chapter 5, using measurement of regular biaxial braid tow structure variability gathered in Chapter 4 for carbon-fiber reinforced polymer tubes, targeted experiments were performed with stereoscopic digital image correlation to measure the effects of braid irregularity on the local surface strain response during internal expansion loading. Virtual models containing experimentally measured nonuniform tow structure and corrected, "ideal" virtual models of the outer braid of each specimen were generated and integrated into numerical simulations similar to experiments. Experimental and numerical results agreed well. Numerical simulations are used to study the influence of untargeted measures of nonuniform tow paths. Statistical tests are used to support observed correlations between select measures of braid variation. A route for converting full-field surface tow measurements into virtual models is presented and utilize. A scalable method to relate local tow structure and local mechanical response is demonstrated for macro-sized composites tubes. Results show that the rate or gradient at which tow structure varies is substantially more critical to than the magnitude in which they vary. By comparing numerical results for uniform, "ideal" biaxial braids and as-manufactured, nonuniform braids, the stress redistribution increase due to variation in tow placement can be estimated to be as great as 18 %.

In Chapter 6, plain weave planar and braided tubular SiC/SiC CMCs are evaluated in tension and four-point bending, respectively, at ambient conditions. Custom-designed fixtures for CMC testing are developed for each loading mode and are coupled with three-dimensional digital image correlation. Select CMC claddings were evaluated in four-point bending for coupled hermetic seal, mechanical failure performance through the addition of acoustic emissions detection and helium leak detection sensors. Stereoscopic image correlation analysis reveals crack initiation and failure sites to provide insight into stress redistribution mechanisms. Scanning electron microscopy is performed postmortem to determine the influence of microstructural features on crack initiation and failure. Crack spacing is measured i*n situ* by stereoscopic image correlation and confirmed by SEM measurements to relate to underlying tow-tow crossing points. Triangulated surface heights of plain weave tow architecture are used to determine that subtle differences in neighboring transverse tow angle, which vary within a range of $\pm 4°$ from horizontal, have no significant effect on final fracture location. The results presented reaffirm the state of current SiC/SiC CMCs developed for energy applications and help to further improvements of SiC/SiC and other CMCs.

2. Recommendations and outlook

In general, this dissertation entails the development of novel DIC-based techniques to reveal new information about the surface state of composites in the as-manufactured configuration and during mechanical loading. These methods are applicable to countless composite systems to reveal informative measurements, which could be used to improve numerical model accuracy or manufacturing quality of those materials. The strengths of surface DIC measurements over other methods of characterization, such as X-ray computed tomography (XCT) or scanning electron microcopy (SEM), is the larger scale at which measurements can be made accurately, enabling a statistically significant sampling region. I believe the work developed here can provide the basis for several studies.

2.1. Relating the micro and macro scale

A limitation of surface measurements is the lack of information on the internal structure. However, for few ply composites, as in the case of ceramic matrix composite (CMC) nuclear fuel claddings, the new information provided in this dissertation indicates an increase or decrease in the local surface mechanical response of a braided composite can be measured and related to rapid gradients of nonuniformities in tow structure at the macro scale. This effect has been measured in the past at the micro level using XCT[1] but at the time no information on the long-range tow structure variability was known, so the measurements were performed at arbitrary locations. Both systems serve to complement each other, and their combined use should be investigated to perform targeted experiments on highly defect sensitive materials, such as CMCs. Potentially, mosaic digital image correlation (M-DIC) techniques could be used to determine spatial location of excess defect, and these locations could be viewed and quantified via XCT,[2] either as-manufactured or during loading (Fig. 7.1). Furthermore, a relationship can be found for cylindrical composites between full-specimen DIC-based measurements of the surface and unit cell scale XCT-based measurements of internal structure, similar to what has been done for planar CMCs.[3]

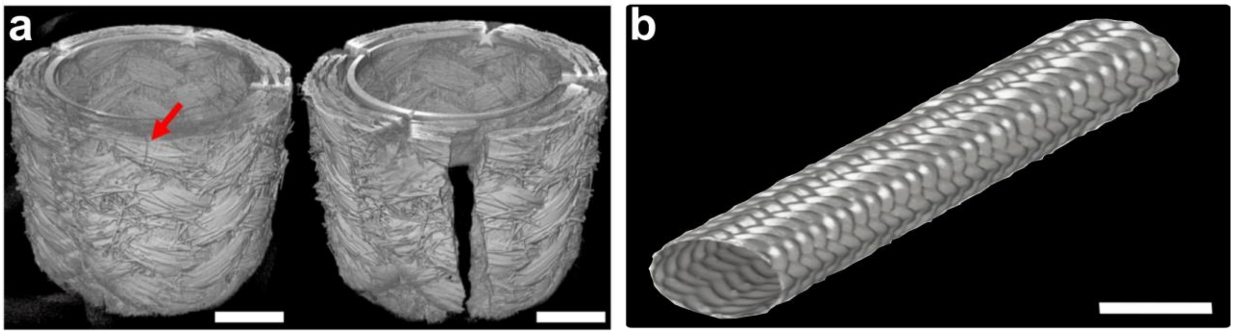

Fig. 7.1. Experimental reconstructions of SiC/ SiC CMCs. (a) XCT. (b) M-DIC technique. Scale bars are (a) 3 mm and (b) 9 mm.

2.2. Combing local, tow-based surface measurements and surface measurements of cracking for ceramic matrix composites

In this dissertation, carbon-fiber reinforced polymer (CFRP) braided composites, which have distinct interface/interphase failure mechanisms CMCs, were studied via tow crown segmentation analysis coupled with applied mechanical loading. Therefore, it was not possible to decouple the effects of matrix cracking and irregular tow structure on the local stress/strain within the material. It is likely that irregular tow structure serves to promote initiation of matrix cracking; however, once cracking has occurred the stress/strain state of the local material likely changes considerably. This concept is depicted in Fig. 7.2. Tow crowns could serve as markers with spatial strain profiles from DIC can be condensed. Through this method it is likely the spatial stress/strain response could be directly quantified.

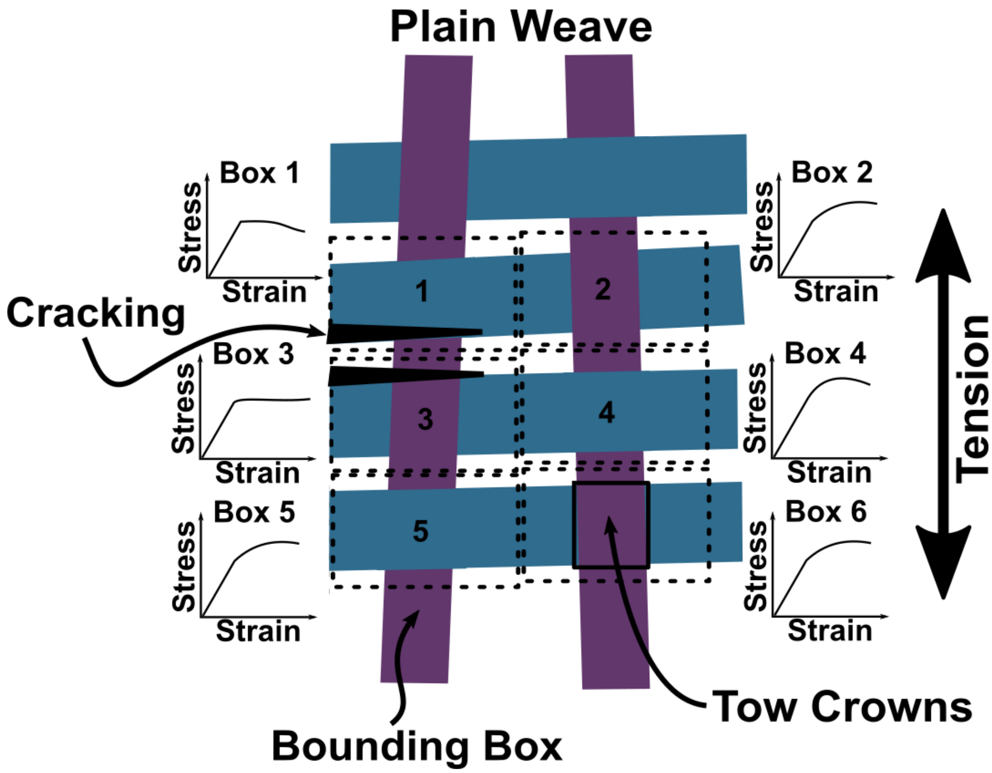

Fig. 7.2. Schematic depicting a tow crown centered, spatial analysis of the strain redistribution mechanism likely exhibited by CMCs during matrix cracking.

In a preliminary study with two plain weave SiC/SiC CMCs, which are featured in Chapter 6, a relationship (Fig. 7.3) between the axial tow spacing gradient δ_{yy} and the final, average normalized tensile strain ε_{yy} prior to fracture was found to be significant to the 95 % confidence level. Typical segmented tow irregularity profiles can be seen in Fig. 7.4. This trend indicates that particular gradients in axial spacing tended to increase the local strain response of the material, immediately prior to failure. Such a trend exists with cracking present; therefore, it is currently unclear if the axial tow spacing gradient δ_{yy} is related to real strain or matrix cracking. Decoupling this behavior could be useful for relating tow structure and crack initiation and propagation at the macro scale with DIC. Furthermore, additional samples would need to be correlated to support this preliminary result.

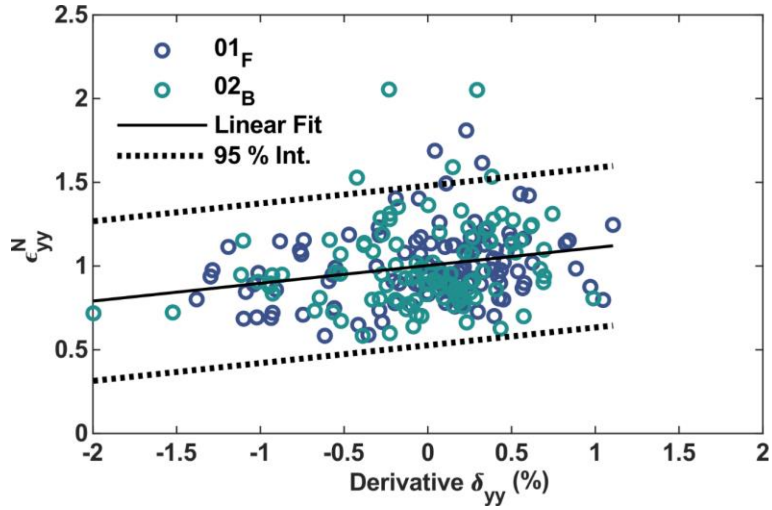

Fig. 7.3. Scatter plot demonstrating a possible linear relationship between the axial tow spacing derivative δ_{yy} and the final tensile strain ε_{yy}

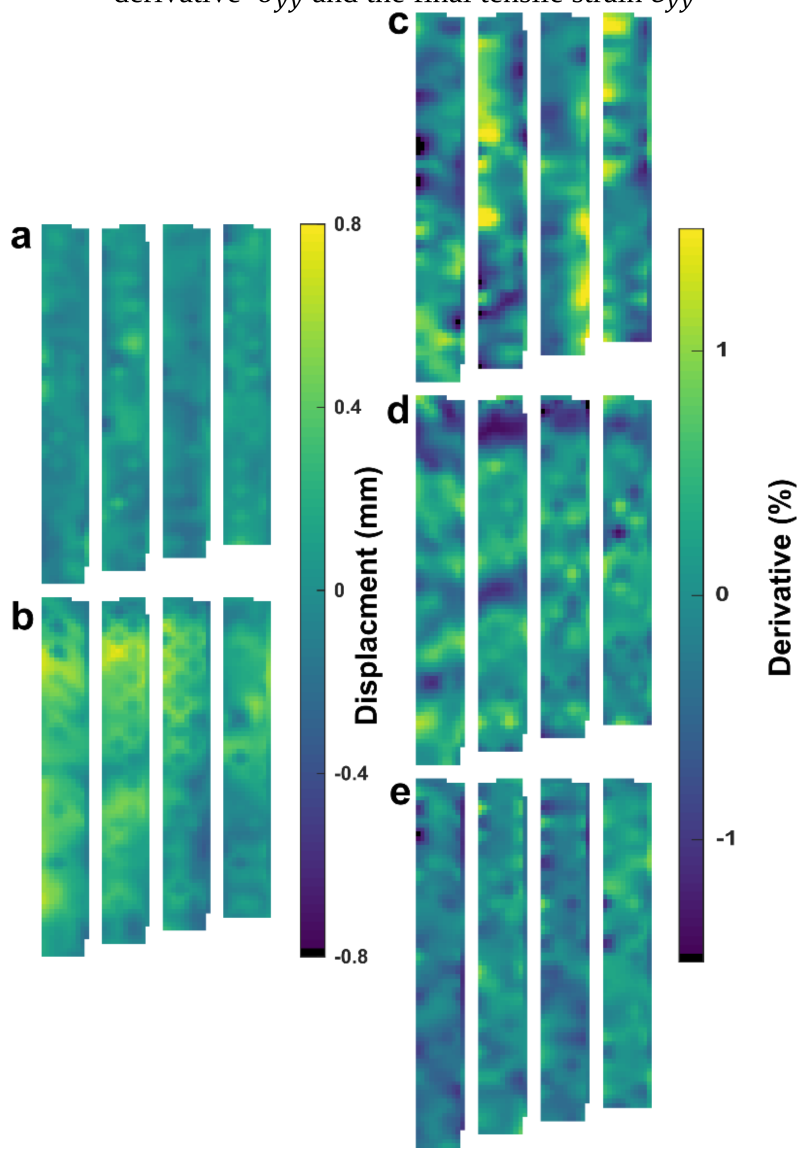

Fig. 7.4. Spatial profiles of tow irregularity in SiC/SiC plain weave CMC. Left to right includes 01-Back, 01-Front, 02-Back, 02-Front. a) U (transverse) displacement. b) V (axial) displacement. c) Transverse tow spacing gradient δ_{xx} d) Axial tow spacing gradient δ_{yy}. e) Shear tow spacing gradient δ_{xy}.

2.3. Revealing manufacturing mechanisms

Another possible avenue that is supported by the work in this dissertation is the development of a system capable of monitoring the tow structure of a full-length (4 m) SiC/SiC CMC cladding tube during and after manufacturing. This would serve several purposes. The chemical vapor infiltration (CVI) process may relocate tows during infiltration, and this could be quantified. Furthermore, in Chapter 4 the sensitivity of M-DIC measurements was found to be great enough to visually identify regions of excess paint in the surface speckle pattern. Therefore, it might be also possible to measure the deposition rate of the SiC. Finally, a pedigree of the tow structure irregularity would be possible along the full cladding and could be linked to the history and performance of each cladding. All of these would serve to improve the reliability of manufacturing quality, which is necessary prior to using these CMCs in extreme structural applications where safety is critical.

3. References

[1] Croom BP, Li X, Deck CP, Xu P, Lahoda EJ. Quantifying the three-dimensional damage and stress redistribution mechanisms of braided SiC/SiC composites by in situ volumetric digital image correlation. Scr Mater 2016;130:238–41. doi:10.1016/j.scriptamat.2016.12.021.

[2] Rossol MN, Shaw JH, Bale H, Ritchie RO, Marshall DB, Zok FW. Characterizing Weave Geometry in Textile Ceramic Composites Using Digital Image Correlation. J Am Ceram Soc 2013;96:2362–5. doi:10.1111/jace.12468.

[3] Shaw JH, Rossol MN, Marshall DB, Zok FW. Effects of Tow-Scale Holes on the Mechanical Performance of a 3D Woven C/SiC Composite. J Am Ceram Soc 2015;98:948–56. doi:10.1111/jace.13389.